Interferentie door onvoldoende cyclische prefix en padverlies voor IEEE 802.11-systemen in een multipad-indooromgeving

Interference Due to Insufficient Cyclic Prefix and Path Loss for IEEE 802.11 Systems in a Multipath Indoor Environment

Frédéric Heereman

Promotoren: prof. dr. ir. W. Joseph, prof. dr. ir. L. Martens
Proefschrift ingediend tot het behalen van de graad van
Doctor in de Ingenieurswetenschappen: Elektrotechniek

Vakgroep Informatietechnologie
Voorzitter: prof. dr. ir. D. De Zutter
Faculteit Ingenieurswetenschappen en Architectuur
Academiejaar 2015 - 2016

UNIVERSITEIT
GENT

ISBN 978-90-8578-888-1
NUR 959
Wettelijk depot: D/2016/10.500/20

Acknowledgments

Graag wou ik een aantal mensen oprecht bedanken die bijgedragen hebben tot mijn doctoraatsonderzoek. In de eerste plaats bedank ik mijn promotoren, prof. Wout Joseph en prof. Luc Martens, voor hun wetenschappelijke ondersteuning en hun vertrouwen. Bij uitbreiding dank ik de hele onderzoeksgroep WAVES (tot voor kort WiCa) voor de jarenlange open en aangename werksfeer. Er is een hele lijst van (ex-)collega's, maar ze zijn elk een vermelding waard: Adrian, Aliou, Amine, Arno, Brecht, David, Divya, Emmeric, Francis, Günter, Isabelle, Jens, Karien, Kris, Leen, Margot, Marina, Matthias, Mostafa, Ning, Quintin, Reza, Roel, Said, Sam, Simon, Toon, Xu and Yue. Enkele collega's wou ik nog in het bijzonder bedanken voor technische en/of wetenschappelijke ondersteuning: David, Emmeric (prof. E. Tanghe), Kris, Leen en Margot.

Maar de steun die ik afgelopen jaren genoten heb gaat nog verder. Een eerste deel van mijn onderzoek kwam tot stand in het kader van OMUS (Optimizing MUltimedia Service Delivery), een project ondersteund door het toenmalige Interdisciplinair Instituut voor Breedbandtechnologie (IBBT) of heden iMinds. Verder wens ik het Agentschap voor Innovatie door Wetenschap en Technologie (IWT) te bedanken voor het uitreiken van een "doctoraatsbeurs van strategisch basisonderzoek".

Ook bedank ik volgende personen voor technische ondersteuning, wetenschappelijk advies of inspirerende discussies: prof. M. Moeneclaey (UGent), prof. J. O. Nielsen (Aalborg University), prof. H. Steendam (UGent), Wim De Ketelaere (Excentis), prof. J. Bauwelinck (UGent) en prof. M. Moonen (KU Leuven). Ook een woord van dank voor John Gesquiere (Televic), Cedric Mélange (Televic), Karel Six (ICC Gent) en Peter Guns (UGent) voor technische ondersteuning of het ter beschikking stellen van indoor-ruimtes voor metingen. Tenslotte bedank ik ook nog Maarten Steenhuyse (destijds UGent) en Nicolas Letor (destijds UAntwerpen) voor de medewerking in de (intensieve) meetcampagne in Straatsburg.

Tenslotte dank ik ook van harte mijn familie en vriendenkring. De steun die ik gekregen heb gaat van een kleine aanmoediging of een goeie babbel tot concrete hulp. Hoewel ik geen volledige oplijsting geef, vergeet ik die kleine en grote dingen niet...

Ghent, April 2016
Frédéric Heereman

Table of Contents

Acknowledgments **i**

Samenvatting **xxxiii**

Summary **xxxix**

1 Introduction **1**
- 1.1 Context and motivation of the dissertation . . . 2
  - 1.1.1 Interference due to insufficient cyclic prefix . . . 2
  - 1.1.2 Path loss modeling . . . 11
- 1.2 Approach and goals of the dissertation . . . 14
  - 1.2.1 Interference due to insufficient cyclic prefix . . . 14
  - 1.2.2 Path loss and shadowing in large conference rooms: approach and goals . . . 19
- 1.3 State-of-the-art and comparison with the dissertation's approach . 20
  - 1.3.1 Channel-based analysis of interference due to insufficient CP . . . 20
  - 1.3.2 Determination of the interference due to insufficient CP: measurement techniques . . . 22
- 1.4 Novelties of the dissertation . . . 26
- 1.5 Outline of the dissertation . . . 27
- 1.6 Publications . . . 29
  - 1.6.1 A1 . . . 29
  - 1.6.2 P1 . . . 29
  - 1.6.3 C3 . . . 30

2 Interference due to insufficient CP: channel-based analysis **31**
- 2.1 OFDM signal model . . . 33
  - 2.1.1 Transmitter and channel . . . 33
  - 2.1.2 Receiver . . . 35
  - 2.1.3 Near-optimal FFT window positioning . . . 36
- 2.2 Channel-based analysis of the interference due to insufficient CP . 39
  - 2.2.1 CIR-based weighting functions for the interference coefficient . . . 39

2.2.2 Generalized representation of Fourier-type interference coefficient - Error vector with neglecting the aliasing effect . 43
2.3 Interference coefficients for IEEE 802.11 OFDM 48
2.4 Comparison with APDP-based weighting function for total interference power proposed in [1] 49
2.5 SINR due to insufficient CP 51
2.6 Conclusions 52

3 Determination of the interference coefficient from frequency-domain channel sounding: theory 53
3.1 Introduction and overview of the chapter 54
3.2 Interference coefficient in relation with the channel frequency response 59
3.3 General computation procedure of the interference coefficient . . . 61
3.4 Definition of different windowing methods 64
3.4.1 Type I method 65
3.4.2 Type II method 65
3.4.3 Type III method 65
3.5 Error analysis 68
3.5.1 Error due to a time-domain cut-off and due to measurement noise 68
3.5.2 Error analysis of the remaining error 68
3.5.3 Overall error 73
3.6 Relative error power versus dB-scaled deviation 75
3.6.1 Spectral interference power 75
3.6.2 Total interference power 77
3.6.3 Conclusion 78
3.7 APDP-based expression for the frequency-averaged interference power 79
3.8 Error power due to a time-domain cut-off 81
3.9 Error power due to a non-zero time resolution and leakage 83
3.9.1 Calculation method of the error power due to resolution and leakage 83
3.9.2 Theoretical estimation of the error power due to resolution: analysis in terms of the reverberation time 84
3.9.3 Theoretical estimation method of the error power due to direct and aliased leakage 89

4 Performance analysis of different windowing methods: required measurement range 91
4.1 Experimental setup and measurements 93
4.2 Convergence analysis method 96
4.3 Measured frequency range requirement 101
4.3.1 Methods using a Hann window 102
4.3.2 Methods using a rectangular window 111

4.3.3 Methods using Hann window correction 115
4.3.4 Required measurement range for the determination of the total interference 117
4.4 Measured interference power 124
4.5 Conclusions 126

5 Limitations for windowing methods due to time resolution and leakage 127
5.1 Validation of the theoretical estimation of the error power due to resolution and leakage 128
5.1.1 Results for error power due to resolution 129
5.1.2 Results for error power due to direct and aliased leakage . 131
5.2 Limiting error types for methods III-Hann and I-rect: time resolution and leakage 133
5.2.1 Error power due to direct and aliased leakage 133
5.2.2 Limiting error type for measurement range requirement . . 137
5.3 SIR limitations due to leakage 141
5.3.1 SIR limitations for determination of spectral interference . 141
5.3.2 SIR limitations for determination of total interference . . . 144
5.3.3 Implications on measurement range requirement 144

6 Processing time and measurement noise for different windowing methods - Time-domain cut-off requirement 147
6.1 Processing time 148
6.1.1 Experimental processing time 148
6.1.2 Theoretical analysis of the processing time 148
6.1.3 Experimental validation 151
6.1.4 Discussion of the processing time for different windowing method types 151
6.2 Measurement noise 154
6.2.1 Influence of the windowing method on the error power due to measurement noise 154
6.2.2 Error power due to measurement noise 157
6.2.3 Measurement noise reduction by averaging 160
6.3 Validation of the time-domain cut-off requirement 162

7 Interference due to insufficient CP: effective noise factor and analysis as a function of the reverberation time 165
7.1 Determination of the loss factor due to multipath noise: concept of an effective AWGN 166
7.1.1 Multipath noise described in terms of a packet-dependent AWGN 166
7.1.2 Multipath noise described in terms of an *effective* AWGN . 167
7.2 Analysis of the spectral interference power and the effective noise factor in terms of the reverberation time 169

7.2.1 Determination of the effective noise factor in terms of the interference coefficient . . . 169
7.2.2 APDP-based expressions for the effective interference power and the effective noise factor . . . 169
7.2.3 Analytical expressions for the interference power and the effective noise factor . . . 170
7.2.4 Per-packet complex Gaussian behavior of the error vector due to multipath noise . . . 172
7.2.5 Closed-form analytical expression for the effective noise factor . . . 173
7.3 Measurements and data processing . . . 174
7.4 Experimental validation with respect to the concept of an effective AWGN . . . 176
7.5 Experimental validation with respect to the APDP-based and the analytical determination method . . . 178
7.5.1 Validation of the frequency-independence of the packet-averaged interference power . . . 178
7.5.2 Validation of the APDP-based and the analytical method for the determination of the effective interference power . 179
7.6 Effective noise factor and loss factor for IEEE 802.11 in large conference rooms . . . 181
7.7 Conclusions . . . 183

8 Path loss model and prediction of range, power and throughput for IEEE 802.11 in large conference rooms 185
8.1 Measurement configurations and setups . . . 187
8.1.1 Path loss measurement . . . 187
8.1.2 PL measurement in a university auditorium . . . 188
8.2 Path loss model . . . 189
8.2.1 Development of the path loss model . . . 189
8.2.2 Path loss model: results and discussion . . . 189
8.2.3 Influence of humans on the PL model . . . 192
8.3 Range, power consumption and throughput of IEEE 802.11n in large conference rooms . . . 195
8.3.1 Calculation of the range, number of access points and power consumption . . . 195
8.3.2 Results and discussion . . . 196
8.3.3 Summary . . . 200
8.4 Conclusions . . . 201

9 Conclusions, applications and future work 203
9.1 Conclusions . . . 204
9.1.1 Interference due to insufficient CP: detection methodology based on frequency-domain channel sounding . . . 204

9.1.2 Interference due to insufficient CP: effective noise and relation with reverberation time 206
9.1.3 Path loss modeling in large indoor environments 206
9.2 Applications and future work 208
9.2.1 Characterization of the interference due to insufficient CP 208
9.2.2 Implications to link budget analysis 209
9.2.3 Implications to channel modeling 210
9.2.4 Implications to frequency-domain equalization 211
9.2.5 Future research 211

A Derivation of CIR-based weighting functions for the interference coefficient due to insufficient CP 221
A.1 Weighting function for Fourier series coefficients (*Fourier-type interference coefficient*) 224
A.1.1 $Z_{k',i';k,i;A}$ 224
A.1.2 $Z_{k',i';k,i;B}$ 224
A.1.3 $Z_{k',i';k,i;C}$ 225
A.1.4 Determination of $Y_{k',i';k,i;\mathrm{Four}}$ 225
A.2 Weighting function for the correction term, $Y_{k',i';k,i;\mathrm{corr}}$ (*correction-type interference coefficient*) 226
A.3 Error vector due to insufficient CP 226

List of Figures

1.1 Principle of CP-OFDM: replicas of the transmit OFDM signal with an excess delay ($\Delta\tau$) smaller than the cyclic prefix (CP) length do not result into intersymbol or intercarrier interference assuming proper FFT window positioning. 3

1.2 Schematical top view illustration of indoor multipath propagation. The transmit signal (at Tx) reaches the receiver (Rx) via distinct propagation paths, resulting into a delay spread of the channel. . . 4

1.3 Schematical illustration of the room electromagnetics theory, stating an exponentially decaying APDP tail. The decay time is referred to as reverberation time (τ_{r}). 5

1.4 The interference due to insufficient CP is composed of different interference processes characterized by the subcarrier separation, Δi, and the separation of the OFDM symbol index, Δk. Interference processes with $\Delta k = 0$ and $\Delta k \neq 0$ are referred to as intercarrier and intersymbol interference, resp. (ICI/ISI). 8

1.5 Schematical illustration of the (normalized) spectral interference power profile for a fixed OFDM symbol separation. The spectral interference width indicates how many subcarriers are (on average) involved in interference due to insufficient CP in a non-negligible way. 10

1.6 Schematical illustration of the measured (delay-discrete) CIR (depicted in normalized power), where the time resolution, time window and dynamic range are indicated. The weighting function (depicted in squared magnitude) determines to which extent each channel component contributes to the interference coefficient. . . . 15

1.7 A windowing method is applied on the measured channel frequency response samples prior to IDFT computation. Besides conventional windowing, a novel windowing method is studied where the window is positioned around source and detecting subcarrier (of the interference coefficient) separately. 16

2.1 Block diagram of the OFDM transmitter. 34

2.2 Block diagram of the OFDM receiver. 35

2.3 Schematical (linear-scaled) envelope of two successive OFDM symbols as transmitted and as received time signals. The near-optimal FFT window positioning proposed is given by $\Delta t_{\mathrm{win},0} = \tau_{\min} + D_{\mathrm{FFT}}\, N_{\mathrm{sample}}^{-1}$. 37

2.4 Schematical illustration of transmitted and received OFDM symbols. The received signal is a superposition of replicas of the transmit signal with different delays, which are classified into 3 subintervals types depending on the extent of overlap with the FFT window: type A (left-hand partial overlap), type B (complete overlap) and type C (right-hand partial overlap). 40

2.5 Weighting functions (in absolute value) for correction-type and Fourier-type interference coefficient, $g_{\mathrm{corr}}(\tau)$ and $g_{\mathrm{Four},\Delta i}(\tau)$, respectively, for different subcarrier separation Δi. All functions are depicted at scale, except $g_{\mathrm{corr}}(\tau)$. Subintervals (2), (3) and (4) correspond to the subintervals of type A, B and C, resp., of the interference delay interval. 42

3.1 The part of the frequency-domain that is physically relevant to accurately determine the interference coefficient is concentrated around the source subcarrier frequency (ω_{s}) and the detecting subcarrier frequency (ω_{d}). The frequency width is related to the inverse duration of the interference delay interval. 60

3.2 To determine the interference for a subcarrier separation $\pm|\Delta i|$ over a given calculation range (Δf_{calc}), 3 windowing method types can be used. Type I applies a fixed window centered over the measurement range (Δf_{meas}). Type II uses a moving window centered around the detecting subcarrier (f_{d}). Type III applies a moving window to determine the generalized interference coefficient centered around both source and detecting subcarrier frequency (f_{s} and f_{d}). The window centre ranges over Δf_{calc} for type II and over the zero-excess measurement range ($\Delta f_{\mathrm{meas},0}$) for type III. Finally, the excess measurement range ($\Delta f_{\mathrm{meas,exc}}$) is indicated. . 64

3.3 Channel impulse response (CIR) in aliased form, measured over a time window of 2 µs. The CIR is normalized to the total power. Weighting functions with a rectangular ("rect", solid) and a linear ("lin", dash) profile are shown for an interference delay interval for 800 ns CP. Different error types due to a non-zero time resolution and leakage ("LK") are indicated: (i) direct leakage, (ii) aliased leakage, (iii) resolution error ("RS") (including near leakage) for both weighting function profiles. 72

3.4 The mean (normalized) energy ($R_{\mathrm{M}}(\gamma)$) and the (normalized) time width ($\Delta\tau_{\mathrm{RS}} \times \Delta f_{\mathrm{win}}$) are analytically determined as a function of $1-\gamma$ for a Hann and a rectangular window. The trend proportional to $(1-\gamma)^{-1}$ is added for comparison. 88

4.1 Block scheme of the measurement setup. At the Rx side: network analyzer (VNA) and Rx antenna, at the Tx side (remote): amplifier ("AMP") and Tx antenna. 93
4.2 "Minneplein" room in International Convention Center (ICC, Ghent) with measurement setup. 94
4.3 Floor plan (to scale) of "Minneplein" room (first floor). There are two stair wells leading to the "Arteveldeforum" (ground floor), which is separated from the "Pedro de Gante" room by glass doors (dash-dot line). The walls of the first and the ground floor are depicted in solid and dash line, respectively. The Tx and Rx positions of the channel measurement are indicated. 95
4.4 Required measurement range (Δf_{meas}) for **400 ns CP** as a function of the subcarrier separation (Δi) for different windowing methods. This is based on a $241\ \mathrm{MHz}$ calculation range and a relative error power of $-14\ \mathrm{dB}$. The requirement is given for both interference coefficient types, (a) y_{corr} and (b) y_{Four}. The zero-excess measurement range ($\Delta f_{\mathrm{meas},\,0}$) is added for comparison. 103
4.5 Required measurement range (Δf_{meas}) for **800 ns CP** as a function of the subcarrier separation (Δi) for different windowing methods. This is based on a $241\ \mathrm{MHz}$ calculation range and a relative error power of $-14\ \mathrm{dB}$. The requirement is given for both interference coefficient types, (a) y_{corr} and (b) y_{Four}. The zero-excess measurement range ($\Delta f_{\mathrm{meas},\,0}$) is added for comparison. 104
4.6 From a convergence analysis for $800\ \mathrm{ns}$ CP, the required excess measurement range for a varying calculation range (CR1 – CR4) is determined for both coefficient types. 107
4.7 Required measurement range (Δf_{meas}) for $800\ \mathrm{ns}$ CP as a function of the subcarrier separation (Δi) for different windowing methods. This is based on a $241\ \mathrm{MHz}$ calculation range and a $-14\ \mathrm{dB}$ error ratio. The requirement is given for interference coefficient type y_{Four}. The zero-excess measurement range ($\Delta f_{\mathrm{meas},\,0}$) is added for comparison. 113
4.8 Schematical illustration of the windowing methods in the case of a fixed zero-excess measurement range ($\Delta f_{\mathrm{meas},0}$). For all source and detecting subcarrier frequencies (f_{s} and f_{d}, resp.) lying both in this frequency band, the interference due to insufficient CP is determined. In this case, the calculation range (Δf_{calc}) falls together with the zero-excess measurement range. The measurement range (Δf_{meas}) and the excess measurement range ($\Delta f_{\mathrm{meas,exc}}$) are indicated as well. 118
4.9 For a frequency band centered at $3.8\ \mathrm{GHz}$ and with a $241\ \mathrm{MHz}$ width, the (normalized) spectral interference power is determined as a function of the subcarrier separation (Δi) from a measured channel for $400\ \mathrm{ns}$ and $800\ \mathrm{ns}$ CP. 124

4.10 The (normalized) total interference power as a function of the detecting subcarrier frequency is determined from a measured channel for $400\ \mathrm{ns}$ and $800\ \mathrm{ns}$ CP. The (normalized) signal and thermal noise level are added. The latter refers to a transmit power of $30\ \mathrm{dBm}$ at a $160\ \mathrm{MHz}$ bandwidth. 125

5.1 The theoretical estimation of the relative error powers due to resolution ("RS"), direct and aliased leakage ("LK"), are compared with the real error power. This is determined as a function of the subcarrier separation, Δi, based on method III-Hann, $800\ \mathrm{ns}$ CP and a $75\ \mathrm{MHz}$ window width. The real relative error power due to all window-related error types ("all") is added too. Both coefficient types, y_{corr} (a) and y_{Four} (b), are considered. 130

5.2 Relative error ratio as a function of the subcarrier separation for **method III-Hann** for a measurement range of $450\ \mathrm{MHz}$ (i.e., a $50\ \mathrm{MHz}$ window width). The (estimated) error powers due to resolution ("RS"), direct and aliased leakage ("LK") are shown. The (real) error power due to all window-related errors ("all") is added for comparison. Both interference coefficient types are considered, y_{corr} ("corr.") and y_{Four} ("Four."). The required accuracy level is set at $-14\ \mathrm{dB}$. Both $400\ \mathrm{ns}$ CP (a) and $800\ \mathrm{ns}$ CP (b) are considered. 134

5.3 Relative error ratio as a function of the subcarrier separation for **method I-rect** for a measurement range of $450\ \mathrm{MHz}$ (i.e., a $450\ \mathrm{MHz}$ window width). The (estimated) error powers due to resolution ("RS"), direct and aliased leakage ("LK") are shown. The (real) error power due to all window-related errors ("all") is added for comparison. Both interference coefficient types are considered, y_{corr} ("corr.") and y_{Four} ("Four."). The required accuracy level is set at $-14\ \mathrm{dB}$. Both $400\ \mathrm{ns}$ CP (a) and $800\ \mathrm{ns}$ CP (b) are considered. 135

5.4 SIR limitation ($\mathrm{SIR}_{\mathrm{max}}$ [dB]) due to direct and aliased leakage as a function of the measurement range (Δf_{meas}) for methods III-Hann and I-rect. These values refer to a relative error power threshold of $-14\ \mathrm{dB}$ and apply to the determination of the *spectral* interference. $\mathrm{SIR}_{\mathrm{max}}$ values are given for $400\ \mathrm{ns}$ CP (a) and $800\ \mathrm{ns}$ CP (b) and for both coefficient types, y_{corr} ("corr.") and y_{Four} ("Four."). 143

6.1 Experimental processing time as a function of the measurement range (Δf_{meas}) for the calculation of the channel impulse response ("i.r.") and the interference coefficient ("coef."). The total processing time is also added. This is given for windowing method types I, II and III. 149

6.2 The relative error power ($\tilde{E}_{\alpha',\mathrm{MN-av}}$) due to measurement noise after averaging over 80 sweeps is experimentally determined as a function of the subcarrier separation (Δi). This is given for both coefficient types y_{corr} ("corr.") and y_{Four} ("Four.") and for 400 ns and 800 ns CP. 158

6.3 Averaged power delay profile (APDP) and the corresponding error power due to measurement noise after averaging over 80 sweeps. The error power consists of a flat and a multiplicative component. All power profiles are normalized to the total APDP power. 159

6.4 The relative error power ($\tilde{E}_{\alpha',\mathrm{MN-av}}$) due to measurement noise is experimentally determined as a function of the number of sweeps (N_{sweeps}) for averaging. This is given for (i) the spectral interference at a zero subcarrier separation for coefficient types y_{corr} ("corr.") and y_{Four} ("Four.") and (ii) for the total interference. From the one-sweep point, the error power is also extrapolated inversely proportionally to N_{sweeps} (dash lines). 161

6.5 The relative error power due to a time-domain cut-off is experimentally determined as a function of the subcarrier separation (Δi) for a cut-off interval duration of 6.6 times the reverberation time. This is given for both interference coefficient types, y_{corr} and y_{Four}. 163

7.1 The Fourier-type effective spectral interference power (normalized to the zero subcarrier separation term) is calculated analytically (solid line). The tail of the interference profile is well described by the theoretical inverse-square law (Eq. 7.19) (dash line). The frequency width of the spectral interference is of the order of the inverse of the reverberation time. 172

7.2 Floor plan of room A. The conference table is indicated by (3). Measurements were executed at Tx/Rx positions 1 – 3. 174

7.3 Conference room A 175

7.4 Floor plan of conference room B. The conference table is indicated by (1). Tx is set at position 1 and the Rx array is placed at positions 2 and 3, respectively. 175

7.5 Based on a virtual SIMO measurement, the CDF of $\mathrm{SINR}_{m,0}$ (curve (1)) is determined for 800 ns CP. For an outage probability smaller than 50%, an excellent agreement is found with the CDF based on the effective noise factor ($F_{\mathrm{delay,eff}}$) (curve (2)). CDF (3) is determined assuming a decorrelation between the packet-dependent noise factor ($F_{\mathrm{delay},m,0}$) and the channel response. 177

7.6 The complementary CDF (CCDF) of the ratio between $F_{\mathrm{delay},m,0}$ and its average (solid line) is determined for 800 ns CP. This is compared with the theoretical CCDF (dashed line) assuming $F_{\mathrm{delay},m,0}$ as an exponentially distributed variable. 177

7.7 The packet-averaged interference power terms, $\langle |y_{\mathrm{corr},m}(\omega_\mathrm{s})|^2 \rangle_m$ and $\langle |y_{\mathrm{Four},i'-i,m}(\omega_\mathrm{s})|^2 \rangle_m$, are experimentally determined as a function of the frequency for a subcarrier separation ($|i'-i|$) of $0,\ 5,\ 10$ and 15. Only a small variation over the considered frequency band is found. 178

7.8 The Fourier-type spectral interference power, $\langle |y_{\mathrm{Four},i'-i,m}(\omega_\mathrm{s})|^2 \rangle_{m,\omega_\mathrm{s}}$, is experimentally determined as a function of the subcarrier separation ($|i'-i|$) based on the samples-based, APDP-based and analytical method, showing good agreement. The theoretical inverse-square law is also included. 180

8.1 Plan of a conference room in the European Parliament (Brussels), where path loss measurements were carried out. 187

8.2 Plan of a university auditorium where path loss measurements were carried out. 188

8.3 Measured PL and PL model in a large conference room (at 5.4 GHz, Tx position at the side). Percentiles based on the measured PL samples show that the PL can be described accurately by a one-slope model with a single standard deviation. For clarity, only PL samples of positions separated by 10λ are shown. 191

8.4 Comparison of proposed PL models (PL median), developed for conference rooms, with the TGn PL models for 'Large office' and 'Large space (indoors - outdoors)' at 2.4 GHz. 193

8.5 PL model in a university auditorium in the absence of humans and during a lecture at 2.4 GHz and 5.4 GHz. 194

8.6 Total radiated power consumption (P) as a function of the transmit power (P_T) at the 2.4 GHz and 5.5 GHz band. The calculation is based on the **TGn model**. An overall stagnating or increasing trend of P vs. P_T is found. The dotted line indicates the overall trend (P [mW] proportional to $P_\mathrm{T}^{-2/n+1}$). 199

8.7 Total radiated power consumption (P) as a function of the transmit power (P_T) at the 2.4 GHz and 5.5 GHz band. The calculation is based on the **proposed PL model**. An overall decreasing relation of P vs. P_T is found. The dotted line indicates the overall trend (P [mW] proportional to $P_\mathrm{T}^{-2/n+1}$). The grey line indicates that the PL model is out of the region where the PL could be experimentally determined. 199

9.1 A schematical plot of the range (R) as a function of the transmit power (P_T) based on link budget analysis without and including the loss factor due to multipath noise (L_delay). The range increases with P_T according to the path loss exponent (n). As a result of the loss factor, there is a stagnation of the range from a certain transmit power ($P_{\mathrm{T,max}}$). 210

A.1 Transmit and received OFDM signal corresponding to data symbols $\tilde{X}_{k,i}$ and $\tilde{X}_{k',i'}$ are schematically shown. The received signal is a superposition of replicas of the transmit signal with different delays, which are classified into 3 subintervals types depending on the extent of overlap with the FFT window: type A (left-hand partial overlap), type B (complete overlap) and type C (right-hand partial overlap). 222

List of Tables

2.1 The weighting function $g_{\mathrm{corr}}(\tau)$ defined per subinterval (1)-(5). . . 42

2.2 The weighting function $g_{\mathrm{Four},\Delta i}(\tau)$ defined per subinterval (1)-(5). 42

3.1 Parameters for the generalized representation of the Fourier-type interference coefficient for $\Delta i \neq 0$ and the correction-type interference coefficient. 66

3.2 Parameters of the time-domain resolution error at the edge of a rectangular weighting function: (i) the mean (M), minimum (MIN) and maximum (MAX) of the normalized energy, $R(\beta, \gamma)$, and (ii) the normalized time width. This is given for a Hann and a rectangular window and as a function of γ, indicating the position of the evaluation frequency with respect to the window. 88

4.1 Overall required measurement range (Δf_{meas} [MHz]) to determine the spectral interference for all subcarrier separations ($|\Delta i| \leq 255$) using different windowing methods. This is based on a $241\ \mathrm{MHz}$ calculation range, a maximum subcarrier frequency separation of $80\ \mathrm{MHz}$ and a relative error power of $-14\ \mathrm{dB}$. The requirement is given for interference coefficient types y_{corr} and y_{Four}, as well as for the composed type y_{tot}. 105

4.2 Experimental $a_{\mathrm{I-Hann}}$ values (dimensionless) are determined based on calculation range CR1 – CR4 and $-255 \leq \Delta i \leq 255$. Mean (M), standard deviation (SD), minimum (MIN) and maximum (MAX) are given for different CP lengths and both coefficient types (y_{corr} and y_{Four}). 108

4.3 Experimental $a_{\mathrm{II-Hann}}$ values (dimensionless) are determined based on higher $|\Delta i|$ values, where the convergence of method II-Hann is restricted by non-uniform windowing. Mean (M), standard deviation (SD), minimum (MIN) and maximum (MAX) are given for different CP lengths and both coefficient types (y_{corr} and y_{Four}). . 109

4.4 Theoretical estimations of the maximum relative error power due to direct and aliased leakage ($\tilde{E}_{\mathrm{LK,\,dir}}$ and $\tilde{E}_{\mathrm{LK,\,dir}}$, resp.) for method III-Hann. This is given for a window width ranging from $25\ \mathrm{MHz}$ to $75\ \mathrm{MHz}$ and for both coefficient types (y_{corr} and y_{Four}). 111

4.5 This table presents the excess measurement range ($\Delta f_{\mathrm{meas,\,exc}}$) [MHz] required to determine the spectral and the total interference over a 241 MHz frequency band for a 160 MHz bandwidth. The relative error power is -14 dB. For the spectral interference, the requirement is also given specifically for the y_{corr} and y_{Four} type interference terms forming the composed type, y_{tot}. 120

5.1 The minimum ("MIN") and maximum ("MAX") deviation [dB] of the theoretical versus the real error power are determined over all subcarrier separations (Δi) and over different window widths. Both coefficient types, y_{corr} and y_{Four}, are considered. This table confirms the validity of the theoretical error power estimations as (i) an order estimation for the resolution error power, apart from the cancellation effect for y_{Four} (at a small Δi) and as (ii) an upper envelope for the error power types due to leakage. 131

5.2 The relative error power due to direct and aliased leakage ($\tilde{E}_{\mathrm{LK,\,dir}}$ and $\tilde{E}_{\mathrm{LK,\,al}}$, resp.) for method III-Hann and I-rect is given in terms of the mean (M) [dB] for coefficient type y_{corr} and in terms of the out-of-peak mean (M) [dB] and the peak maximum (MAX) [dB] for the y_{Four} type. Values are given for a measurement range (Δf_{meas}) of 450 MHz and 800 MHz. 136

5.3 SIR limitations ($\mathrm{SIR}_{\mathrm{max}}$ [dB]) due to direct and aliased leakage over a wide range of the applied window width (Δf_{win}) for methods III-Hann and I-rect. These values refer to the y_{Four} type coefficient and to a relative error power threshold of -14 dB. $\mathrm{SIR}_{\mathrm{max}}$ values are given based on the spectral ("S") as well as the total ("T") interference. 145

6.1 Experimental values of the proportionality factor (b) in Eqs. 6.1-6.6 (i.e., $b_{\mathrm{I,ir}}$,...), for the processing time needed for the calculation of the channel impulse response ("i.r.") and the interference coefficient ("coef."). The mean (M) and standard deviation (SD) are only determined based on a measurement range higher than Δf_{meas}. 151

6.2 Processing time ([s]) corresponding to the measurement range required to achieve a -14 dB relative error power. This is given for the calculation of the channel impulse response ("i.r.") and the interference coefficient ("coef."). The total processing time is also added. 153

6.3 The deviation between the actual and the reference error power due to measurement noise is studied over the range of convergence of different windowing methods. The maximum deviation, $\Delta E_{\alpha',\mathrm{MN-av}}$ [dB], is determined for the spectral interference over all subcarrier separations, based on which the mean (M), standard deviation (SD), minimum (MIN) and maximum (MAX) are determined. This is given for both interference coefficient types, y_{corr} and y_{Four}. 156

7.1 Measured APDP tail parameters: reverberation time (τ_{r}) and proportionality factor (I_{diff}) 179
7.2 The effective noise factor ($F_{\mathrm{delay,eff}}$) is determined for a transmit power (P_{T}) of 20 dBm using the (i) samples-based and (ii) analytical method. The loss factor (L_{delay}) is given for a transmit power of $20 - 30$ dBm. 182

8.1 Parameters of PL model, based on PL measurements in a large conference room. 190
8.2 Parameters of PL model in a university auditorium in the absence of humans and during a lecture at 2.4 GHz and 5.4 GHz. 193
8.3 The effect of different link parameters on #AP, total radiated power consumption (P) (expressed by a multiplication factor) and $\mathrm{TP}_{\mathrm{max}}$, assuming a fixed range of 30 m (unless otherwise mentioned). This calculation is based on the **TGn model** for environment 'E' and 'F', resp. (indicated by (1)). 196
8.4 The effect of different link parameters on #AP, total radiated power consumption (P) (expressed by a multiplication factor) and $\mathrm{TP}_{\mathrm{max}}$, assuming a fixed range of 30 m (unless otherwise mentioned). This calculation is based on the **proposed PL model** for the two Tx positions: in front and at the side, resp. (indicated by (1)). . . . 196

List of Acronyms

0-9

4G 4^{th} Generation

A

A/D Analog-to-Digital
ADC Analog-to-Digital Convertor
AGC Automatic Gain Control
APDP Averaged Power Delay Profile
AWGN Additive White Gaussian Noise

B

BER Bit Error Rate
bps bits per second
BPSK Binary Phase-Shift Keying

C

CCDF Complementary Cumulative Distribution Function
CDF Cumulative Distribution Function

CIR Channel Impulse Response
CP Cyclic Prefix
CPU Central Processing Unit
CR Calculation Range

D

D/A Digital-to-Analog
DAC Digital-to-Analog Convertor
DFT Discrete Fourier Transform
DSL Digital Subscriber Line

E

EIRP Equivalent Isotropically Radiated Power
EVM Error Vector Magnitude

F

FEQ Frequency-domain EQualization
FFT Fast Fourier Transform

G

GPS Global Positioning System

I

ICI Intercarrier Interference

IDFT Inverse Discrete Fourier Transform
IEEE Institute of Electrical and Electronics Engineers
IFFT Inverse Fast Fourier Transform
I/Q In-phase and Quadrature
ISI Intersymbol Interference
ISM Industrial, Scientific, and Medical

L

LAN Local Area Network
LOS Line Of Sight

M

MAC Medium Access Control
MCS Modulation and Coding Scheme
MIMO Multiple Input Multiple Output

O

OFDM Orthogonal Frequency Division Multiplexing

P

PC Personal Computer
PDP Power Delay Profile
PER Packet Error Rate
PL Path Loss

PLC Power Line Communication
P/S Parallel-to-Serial

Q

QAM Quadrature Amplitude Modulation

R

RAM Random-Access Memory
rms root-mean-square
Rx receiver

S

SER Symbol Error Rate
SIMO Single Input Multiple Output
SINR Signal-to-Interference-plus-Noise Ratio
SIR Signal-to-Interference Ratio
SISO Single Input Single Output
SNR Signal-to-Noise Ratio
S/P Serial-to-Parallel

T

TGac Task Group ac
TGn Task Group n
Tx transmitter

V

VNA	Vector Network Analyzer
VGA	Variable Gain Amplifier
VSA	Vector Signal Analyzer
VSG	Vector Signal Generator

W

Wi-Fi	Wireless Fidelity
WLAN	Wireless Local Area Network
WPAN	Wireless Personal Area Network
WSSUS	Wide-Sense Stationary Uncorrelated Scattering

List of Symbols

a	proportionality factor for measurement range requirement due to non-uniform windowing (method mentioned in subscript) [ ]
$\#\mathrm{AP}$	number of access points [ ]
B	bandwidth [Hz]
$c(\,\cdot\,)$	channel impulse response [Hz]
$C(\,\cdot\,)$	channel frequency response (as a function of the angular frequency) [ ]
$\hat{c}(\,\cdot\,)$	channel impulse response under aliased form [Hz]
$c_{\mathrm{IDFT}}(\,\cdot\,)$	IDFT coefficients of (windowed) channel response samples [ ]
d	Tx-Rx distance [m]
d_{br}	Tx-Rx breakpoint distance [m]
D_{CP}	cyclic prefix length [s]
D_{FFT}	FFT period [s]
$\exp(\,\cdot\,)$	exponential function based on Euler's number
$\tilde{E}_{\mathrm{thresh}}$	accuracy threshold level for relative error power on the interference coefficient [ ]
$E_{\alpha'}$	absolute (frequency-averaged) error power on the interference coefficient (y_α) [ ]
$\tilde{E}_{\alpha'}$	relative (frequency-averaged) error power on the interference coefficient (y_α) [ ]
$\tilde{E}_{\alpha',\mathrm{CO}}$	relative error power on the interference coefficient due to cut-off [ ]
$\tilde{E}_{\alpha',\mathrm{LK,\,al}}$	relative error power on the interference coefficient due to aliased leakage [ ]
$\tilde{E}_{\alpha',\mathrm{LK,\,dir}}$	relative error power on the interference coefficient due to direct leakage [ ]
$\tilde{E}_{\alpha',\mathrm{MN}}$	relative error power on the interference coefficient due to measurement noise [ ]
$\tilde{E}_{\alpha',\mathrm{NU}}$	relative error power on the interference coefficient due to non-uniform windowing [ ]

$\tilde{E}_{\alpha',\mathrm{RS}}$	relative error power on the interference coefficient due to time resolution [ ]
f	frequency [Hz]
F_{AWGN}	noise factor due to AWGN (hardware-related and thermal noise) [ ]
F_{delay}	noise factor corresponding to multipath noise (insufficient CP) [ ]
$F_{\mathrm{delay,eff}}$	effective noise factor corresponding to multipath noise (insufficient CP) [ ]
G_{R}	Rx antenna gain [dBi]
G_{T}	Tx antenna gain [dBi]
$g_{\alpha}(\,\cdot\,)$	weighting function (as a function of the delay) [ ]
$\tilde{g}_{\alpha}(\,\cdot\,)$	generalized weighting function (as a function of the delay) [ ]
i	subcarrier index [ ]
$I(\,\cdot\,)$	overall (normalized) interference power from all OFDM symbols and all subcarriers (as a function of the angular frequency of the detecting subcarrier) [ ]
I_{diff}	normalized multipath intensity factor of exponential APDP decay [Hz]
$I_{\alpha',\mathrm{av}}$	frequency-averaged (normalized) interference power [ ]
j	imaginary unit
k_{B}	Boltzmann constant [J/K]
L_{delay}	loss factor as a result of interference due to insufficient CP [ ]
$\log(\,\cdot\,)$	logarithm to base of 10
L_{R}	Rx cable loss [dB]
L_{T}	Tx cable loss [dB]
M_{F}	fading margin [dB]
M_{S}	shadowing margin [dB]
n	path loss exponent [ ] (Chapter 8)
N_{rep}	number of measurement repetitions [ ]
N_{sample}	FFT size [ ]
N_{subc}	highest subcarrier index used for transmission [ ]
N_{sweeps}	number of sweeps [ ]
P	total radiated power [dBm]
PL	path loss [dB]
PL_0	path loss intercept [dB]
$\mathrm{PL}_{\mathrm{med}}$	median path loss [dB]

p_{out}	outage probability [%]
P_{R}	received power [dBm]
$P_{\mathrm{R,sens}}$	receiver sensitivity [dBm]
P_{T}	transmit power [dBm]
$P_{\mathrm{T,subc}}$	transmit power per subcarrier [dBm]
R	range [m]
R_{win}	normalization factor of window [ ]
t	time [s]
T	temperature [K]
TP	throughput [bps]
$t_{\mathrm{win},k}$	start time of receiver FFT window for kth OFDM symbol [s]
$w(\,\cdot\,)$	continuous inverse Fourier transform of window function ($W(\,\cdot\,)$) [Hz]
$W(\,\cdot\,)$	window function (as a function of the angular frequency) [ ]
$\tilde{X}$	normalized data symbol [ ]
y_{corr}	correction-type interference coefficient [ ]
$y_{\mathrm{Four},\Delta i}$	Fourier-type interference coefficient [ ]
$y_{\mathrm{total},\Delta i}$	total interference coefficient [ ]
$\tilde{y}$	generalized interference coefficient [ ]
Y	FFT output [ ]
$\tilde{Y}$	normalized (equalized) FFT output [ ]
α	index representation for interference coefficient type (“corr”, “Four” or “tot”) and subcarrier separation
α'	extended index representation for interference coefficient type (“corr”, “Four” or “tot”) and subcarrier separation (for spectral interference) or set of subcarrier separations (for total interference)
$\delta(\,\cdot\,)$	Dirac delta function
Δf_{calc}	frequency width of the calculation range [Hz]
Δf_{d}	frequency resolution of the computation of the interference coefficient [Hz]
Δf_{meas}	frequency width of the measurement range [Hz]
$\Delta f_{\mathrm{meas},0}$	frequency width of the zero-excess measurement range [Hz]
$\Delta f_{\mathrm{meas,exc}}$	excess measurement range [Hz]
Δf_{res}	frequency resolution of measured channel response [Hz]
Δf_{w}	spectral interference width in terms of frequency [Hz]

Δf_{win}	frequency width of the window [Hz]
Δi	subcarrier index separation [ ]
$\lvert\Delta i_{\mathrm{w}}\rvert$	spectral interference width in terms of subcarrier separation [ ]
$\Delta\tilde{Y}$	normalized (equalized) symbol error vector [ ]
$\Delta\tilde{Y}_{\mathrm{AWGN}}$	normalized symbol error vector due to conventional AWGN [ ]
$\Delta\tilde{Y}_{\mathrm{delay}}$	normalized symbol error vector due to insufficient CP [ ]
$\Delta\tilde{Y}_{\mathrm{therm}}$	normalized symbol error vector due to thermal noise [ ]
$\Delta y_{\alpha,\mathrm{AL}}$	error on interference coefficient (y_α) due to aliasing [ ]
$\Delta y_{\alpha,\mathrm{CM}}$	error on interference coefficient (y_α) due to commutation [ ]
$\Delta y_{\alpha,\mathrm{CO}}$	error on interference coefficient (y_α) due to cut-off [ ]
$\Delta y_{\alpha,\mathrm{LK,\,dir}}$	error on interference coefficient (y_α) due to direct leakage [ ]
$\Delta y_{\alpha,\mathrm{LK,\,al}}$	error on interference coefficient (y_α) due to aliased leakage [ ]
$\Delta y_{\alpha,\mathrm{MN}}$	error on interference coefficient (y_α) due to measurement noise [ ]
$\Delta y_{\alpha,\mathrm{NU}}$	error on interference coefficient (y_α) due to non-uniform windowing [ ]
$\Delta y_{\alpha,\mathrm{RS}}$	error on interference coefficient (y_α) due to time resolution [ ]
$\Delta\tau_{\mathrm{CO}}$	duration of interference delay interval after a cut-off [s]
$\Delta\omega_{\mathrm{d}}$	angular frequency separation between detecting subcarrier and window centre [Hz]
$\Delta\omega_{\mathrm{s}}$	angular frequency separation between source subcarrier and window centre [Hz]
$\Delta\omega_{\mathrm{subc}}$	angular frequency subcarrier spacing (i.e., $2\pi/D_{\mathrm{FFT}}$) [Hz]
λ	wavelength [m]
σ	standard deviation of shadowing [dB]
τ	delay [s]
$\tau_{\mathrm{int},0}$	$\tau_{\mathrm{int},1}$ plus FFT period [s]
$\tau_{\mathrm{int},1}$	start delay of interference delay interval [s]
$\tau_{\mathrm{int},2}$	end delay of interference delay interval or cut-off delay (if applicable) [s]
τ_{min}	delay of first arriving propagation path [s]
τ_{r}	reverberation time [s]
ω	angular frequency [Hz]
ω_{d}	angular frequency of the detecting subcarrier [Hz]
ω_i	angular frequency of ith subcarrier [Hz]
ω_{s}	angular frequency of the source subcarrier [Hz]

ω_{win}	angular centre frequency of the window [Hz]
$\cdot * \cdot$	convolution operator
$\langle \cdot \rangle_{\cdot}$	averaging operator over variable(s) mentioned in subscript

Samenvatting
– Summary in Dutch –

Orthogonal frequency-division multiplexing (OFDM) is opgenomen in een breed gamma van draadloze en bedrade standaarden om transmissie aan hoge datasnelheid te realiseren over frequentie-selectieve kanalen. De data-stroom wordt opgedeeld in meerdere parallelle deelstromen, die worden gemoduleerd op orthogonale draagsignalen, zgn. subdraaggolven of *subcarriers*. Het ontvangstsignaal kan gedemoduleerd worden door relatief eenvoudige frequentie-domein equalisatie na een *Fast Fourier Transform* (FFT), op voorwaarde dat de orthogonaliteit van de *subcarriers* behouden blijft over het FFT window. Door het intrinsiek tijdsdispersief karakter van frequentie-selectieve kanalen is het ontvangstsignaal echter vervormd, waardoor de orthogonaliteit aangetast wordt en verschillende OFDM symbolen overlappen. Dit resulteert resp. in *intercarrier*-interferentie (ICI) en intersymbool-interferentie (ISI). Om deze vervorming tegen te gaan maken de meeste OFDM systemen gebruik van een cyclische prefix (CP), een periodieke uitbreiding van het *baseband* OFDM zendsignaal naast de FFT periode.

De performantie van CP-gebaseerde OFDM systemen kan nog steeds aangetast worden over realistische kanalen door hun tijdsdispersief karakter. Ten eerste kan dit performantieverlies veroorzaakt worden door een symbool *timing offset* door distortie van het *training* signaal. Ten tweede kan de lengte van de kanaalimpulsrespons de CP lengte overschrijden. Hiernaar verwijst interferentie door onvoldoende CP.

Deze thesis is gericht op IEEE 802.11, een set fysische en MAC[1] laag specificaties voor WLAN[2] en ook bekend onder het certificatie-label Wi-Fi[3]. De focus ligt meer specifiek op de 11a/g/n/ac standaarden, die gebaseerd zijn op een FFT periode van 3.2 µs en een CP lengte van 800 ns (11a/g) en 400 / 800 ns (11n/ac). Door de relatief grote CP lengte ten opzichte van de rms-vertragingsspreiding[4] van indoorkanalen, worden IEEE 802.11a/g/n/ac systemen gewoonlijk ontwikkeld vanuit de onderstelling dat het kanaal geen distortie over het FFT window veroorzaakt. Bijgevolg wordt meestal een eenvoudige frequentie-domein equalisatie zonder specifieke interferentie-neutralisatie geïmplementeerd in realistische systemen. Een aanzienlijk performantieverlies door onvoldoende CP is echter mogelijk voor

[1] Medium Access Control
[2] Wireless Local Area Network
[3] Wireless Fidelity
[4] root-mean-square delay spread

realistische kanalen, i.h.b. in grote indoor omgevingen door multipad-propagatie.

Het grootste deel van deze thesis is gewijd aan interferentie door onvoldoende CP. De gevolgde aanpak is gebaseerd op frequentie-domein karakterisering van het propagatiekanaal en een analytisch kader in termen van de kanaal-impulsrespons op basis van een geïdealiseerd OFDM signaalmodel. De kanaal-componenten in het tijdsdomein worden bepaald door zgn. *windowing* in het frequentie-domein en inverse discrete Fourier transformatie. Nieuwe methoden voor dataverwerking worden ontwikkeld en geëvalueerd voor nauwkeurige detectie van de interferentie. Verder wordt de interferentie bestudeerd in relatie tot het propagatiekanaal. Meerdere analyses zijn doorgevoerd gebaseerd op de zgn. *room electromagnetics* theorie voor draadloze indoorkanalen, volgens dewelke het gemiddelde *power-delay*[5] profiel (APDP[6]) exponentieel afneemt vanaf voldoend grote tijdsvertraging of *delay* en waar de tijdsconstante *reverberatietijd* wordt genoemd. Het laatste deel van de thesis is gericht op het modelleren van padverlies in grote conferentieruimten. Modellering van padverlies en interferentie dragen gezamenlijk bij tot efficiëntere netwerkplanning en instelling van uitzendvermogen.

Een analytisch kader is ontwikkeld om de interferentie door onvoldoende CP te bepalen in relatie tot het propagatiekanaal. De symbool *error vector* door onvoldoende CP wordt bepaald in termen van een spectrale (d.i. *subcarrier*-specifieke) interferentie-coëfficiënt, die bepaald wordt op basis van de *continue* kanaal-impulsrespons via tijdsafhankelijke gewichtsfuncties. De zgn. signaal-interferentie-plus-ruis-verhouding (SINR[7]), die kan gezien worden als performantie-metriek, is in relatie gebracht met de interferentie-coëfficiënt. Naast een "Fourier"-type coëfficiënt, gerelateerd aan de Fourierreeks-decompositie van het ontvangstsignaal, wordt een "correctie"-type coëfficiënt geïntroduceerd om het effect van een discrete *sampling* periode in rekening te brengen. Voor IEEE 802.11a/g/n/ac is de ISI beperkt tot twee opeenvolgende OFDM symbolen en de ISI en de ICI zijn spectraal identiek.

Voor een nauwkeurige bepaling van de interferentie-coëfficiënt over een bepaalde frequentieband, dient de kanaal-impulsrespons gedetecteerd te worden met een voldoend kleine tijdsresolutie. Met frequentie-domein karakterisering impliceert dit dat de kanaalrespons gemeten wordt over een voldoend breed frequentiebereik. Dit zgn. *meetbereik* kan aanzienlijk groter zijn dan het frequentiebereik bepaald door alle betrokken bron- en detectie-*subcarriers* (d.i., die resp. interferentie veroorzaken en detecteren), het zgn. *exces-vrije meetbereik*. Indien de interesse ligt in de interferentie tussen alle *subcarriers* in de frequentieband, komt het exces-vrije meetbereik precies overeen met de frequentieband. Een groter meetbereik kan problematisch zijn omwille van een groter operationeel frequentiebereik van de meetapparatuur, interferentie met externe bronnen buiten de frequentieband, en een grotere meettijd. Het zgn. *meetbereik-exces* (d.i. het meetbereik versus het exces-vrije meetbereik) kan echter beperkt worden afhankelijk van de *windowing* methode. Andere belangrijke items zijn (i) een voldoend hoog dynamisch bereik,

[5] vermogen-tijdsvertraging
[6] average power-delay profile
[7] signal-to-interference-plus-noise ratio

(ii) beperking van de meetruis en (iii) een voldoend breed tijdswindow.

In deze thesis worden de volgende *windowing* methoden bestudeerd, ingedeeld volgens positionering en profiel. Methoden van type I en II zijn resp. gebaseerd op een vast en een variabel window en op een conventionele gewichtsfunctie, die afhangt van zowel de bron- als de detectie-*subcarrier* voor de Fourier-type interferentie-coëfficiënt. Voor methode-types I en II worden een Hann window (methode *I-Hann* en *II-Hann*) en een rechthoekig window (methode *I-rect* en *II-rect*) in beschouwing genomen. Ook wordt een Hann window met window-correctie bestudeerd, waarbij het niet-uniforme profiel wordt compenseerd door bijkomende deling van de coëfficiënt door de window-functie aan de bron-*subcarrier*.

De Fourier-type interferentie-coëfficiënt is fysisch gerelateerd aan de kanaalrespons rond zowel de bron- als de detectie-*subcarrier*. Bij methode-types I en II dient aldus het window systematisch zowel de bron- als de detectie-*subcarrier* correct te dekken, hetgeen problematisch kan zijn voor transmissiekanalen met een hoge bandbreedte. Methode-type III lost dit probleem op door de specifieke structuur te beschouwen van de gewichtsfunctie bij een *subcarrier*-separatie verschillend van nul. Hierdoor is een decompositie mogelijk in termen van een gegeneraliseerde (frequentie-afhankelijke) interferentie-coëfficiënt, die aan de bron- en detectie-*subcarrier* afzonderlijk geëvalueerd wordt. Deze gegeneraliseerde interferentie-coëfficiënt kan dan bepaald worden vanuit de opgemeten kanaalrespons door een variabel window. Voor methode-type III worden een Hann en een rechthoekig window bestudeerd (resp. methode *III-Hann* en *III-rect*).

Een complete foutenanalyse op de interferentie-coëfficiënt wordt uitgewerkt. Naast de fout door *cut-off*[8] in het tijdsdomein en door meetruis, wordt de resterende fout opgesplitst in een zgn. fout door (i) niet-uniforme *windowing*, (ii) een discrete tijdsresolutie, (iii) *directe lek*, (iv) *alias-gestuurde lek* en (v) *aliasing*. De direct lek is afkomstig van de set sterkste kanaal-componenten in het eigenlijke tijdswindow, terwijl alias-gestuurde lek afkomstig is van alias-componenten buiten het eigenlijke tijdswindow. De fout door *aliasing* is typisch inferieur ten opzichte van de fout door een *cut-off*. De fouten door niet-uniforme *windowing*, een discrete tijdsresolutie en lek zijn sterk afhankelijk van de *windowing* methode. De fouten door een *cut-off* en *aliasing* zijn sterk gerelateerd aan de frequentieresolutie van de gemeten kanaalrespons.

Voor IEEE 802.11, waarbij de FFT periode typisch veel langer is dan de reverberatietijd van een indoorkanaal, kan het *delay*-interval dat interferentie veroorzaakt ingekort worden door een *cut-off* van de gewichtsfunctie, wat resulteert in een minder breed vereist tijdswindow. Gebaseerd op de *room electromagnetics* theorie toont een parametrische analyse aan dat, om de relatieve fout (in vermogen) te beperken tot -14 dB, een *cut-off* dient toegepast te worden bij een *delay* van ten minste 6.6 maal de reverberatietijd na dan de CP lengte. Deze vereiste is meest kritiek bepaald door de Fourier-type interferentie-coëfficiënt bij een *subcarrier*-separatie gelijk nul, zijnde de belangrijkste spectrale interferentie-term. Ex-

[8] afkapping

perimentele validatie van deze theoretische vereiste wordt geleverd op basis van een opgemeten indoorkanaal.

Op basis van de *room electromagnetics* theorie wordt een schatting van de relatieve fout (in vermogen) t.g.v. een discrete tijdsresolutie afgeleid. Deze theoretische schatting dient als een referentie voor de Fourier-type coëfficiënt, waar de resolutiefout typisch sterk gereduceerd is voor een kleine *subcarrier*-separatie. Voor methoden op basis van een Hann window (zonder window-correctie) en methode III-rect blijkt de foutschatting omgekeerd evenredig met de reverberatietijd en de window-breedte. Voor methode III-Hann en III-rect wordt een evenredigheidsfactor van resp. -6.5 dB en -6.7 dB gevonden. Voor methoden I-rect en II-rect blijkt de resolutiefout echter eerder gerelateerd aan het exces van het window t.o.v. de evaluatie-frequentie, dan aan de window-breedte zelf. Een interessante vaststelling is dat de vereiste window-breedte kleiner wordt voor een grotere reverberatietijd, d.w.z. bij een sterkere interferentie. Experimentele verificatie gebaseerd op een opgemeten indoorkanaal toont aan dat de theorie een goede orde-schatting levert.

Op basis van een kanaalmeting in een grote expositieruimte wordt de performantie van de vermelde *windowing* methoden geëvalueerd m.b.t. het vereiste meetbereik voor een frequentieband van 241 MHz. Het vereiste meetbereik wordt bepaald d.m.v. een convergentie-analyse met een procedure specifiek voor window-gerelateerde fouten. Ook worden de limiterende fouttypes geïdentificeerd door inspectie van hun relatieve fout (in vermogen). Voor de detectie van de *spectrale* interferentie blijkt methode III-Hann het efficiëntst, i.h.b. voor een grotere bandbreedte (bv. 160 MHz). Het vereiste meetbereik-exces is bepaald door de resolutiefout en is van de orde van de omgekeerde reverberatietijd. Andere methoden gebaseerd op een Hann window vereisen een exces van de orde van de bandbreedte (methode II-Hann, I-HC en II-HC) of zelfs de frequentieband (methode I-Hann) door de fout t.g.v. niet-uniforme *windowing*. Evenredigheidsfactoren worden experimenteel bepaald. Methoden op basis van een rechthoekig window zijn beperkt door lek, i.h.b. voor een grote CP lengte, wat meest kritiek is voor de Fourier-type coëfficiënt bij een *subcarrier*-separatie gelijk nul. In het bestudeerde geval vereist methode I-rect een meetbereik-exces van 661 MHz voor 800 ns CP. Ook voor de detectie van de *totale* interferentie blijkt methode III-Hann zeer efficiënt. Methoden II-Hann en I-HC blijken tevens efficiënt, met een vereist meetbereik-exces van de orde van de spectrale interferentie-breedte. Deze is typisch van de orde van de omgekeerde reverberatietijd, zoals verder aangetoond. Methode I-HC is wel minder interessant voor de detectie van de frequentie-afhankelijke interferentie, omdat de fout niet uniform verdeeld is over de frequentieband. Andere methoden gebaseerd op een Hann window vereisen nog steeds een exces van de orde van de bandbreedte (methode II-HC) of zelfs de frequentieband (methode I-Hann). Methoden op basis van een rechthoekig window zijn beperkt door lek, i.h.b. voor een grote CP lengte. In het bestudeerde geval vereist methode I-rect een meetbereik-exces van 321 MHz voor 800 ns CP.

De limitaties m.b.t. het vereiste meetbereik t.g.v. lek wordt algemener bestudeerd in termen van een maximum meetbare signaal-interferentie-verhouding

($\mathrm{SIR}_{\max}$[9]), gedefinieerd op basis van de totale interferentie afkomstig van alle OFDM symbolen (inclusief ISI en ICI). Om interferentie tot op het thermisch ruisniveau te meten, mag $\mathrm{SIR}_{\max}$ niet kleiner zijn dan de signaal-ruisverhouding die werkelijk gedetecteerd wordt door de ontvanger. Om een $\mathrm{SIR}_{\max}$ van $100\ \mathrm{dB}$ te bekomen, vereist methode III-Hann voor $400\ \mathrm{ns}$ CP slechts een window-breedte van $79\ \mathrm{MHz}$ and $53\ \mathrm{MHz}$ t.g.v. resp. directe and alias-gestuurde lek en $46\ \mathrm{MHz}$ en $162\ \mathrm{MHz}$ voor $800\ \mathrm{ns}$ CP. De performantie van methoden op basis van een rechthoekig window is echter beperkt. Voor methode I-rect levert zelfs een extreme window-breedte van $1500\ \mathrm{MHz}$ slechts een $\mathrm{SIR}_{\max}$ van $65\ \mathrm{dB}$ en $60\ \mathrm{dB}$ t.g.v. resp. directe en alias-gestuurde lek voor $400\ \mathrm{ns}$ CP, en resp. $67\ \mathrm{dB}$ en $50\ \mathrm{dB}$ voor $800\ \mathrm{ns}$ CP.

De performantie van de *windowing* methoden wordt tevens geëvalueerd m.b.t. de rekentijd voor de detectie van de interferentie-coëfficiënt. Dit wordt zowel theoretisch als experimenteel bestudeerd. Het blijkt dat, i.h.b. voor een hoge bandbreedte, de totale rekentijd voor methode-type III beduidend lager is dan voor type I en II bij een realistisch meetbereik. Bij het *vereiste* meetbereik blijkt de rekentijd voor methode III-Hann in het algemeen twee grootte-orden lager dan voor andere methoden.

De invloed van de *windowing* methoden op de fout t.g.v. de meetruis wordt experimenteel onderzocht. Het blijkt dat in het convergentiegebied, d.i. voor een meetbereik groter dan vereist op basis van de window-gerelateerde fouten, er in het algemeen geen essentiële invloed bestaat. Vervolgens wordt de fout door meetruis spectraal bestudeerd, waarbij wordt aangetoond dat de Fourier-type interferentiecoëfficiënt bij een *subcarrier*-separatie gelijk nul meest kritiek is voor de reductie van meetruis door uitmiddeling van de kanaalrespons. Ook wordt een praktische procedure voor de bepaling van het vereiste aantal observaties voor uitmiddeling experimenteel geverifieerd.

Het effect van de variatie van zowel ontvangstsignaal als interferentie door onvoldoende CP over opeenvolgende OFDM pakketten wordt in rekening gebracht voor traag tijdsvariabele kanalen. De tijdsvariabele interferentie wordt beschreven door een tijdsinvariante, effectieve additieve Gaussische ruis, wat direct resulteert in een verliesfactor. Het wordt theoretisch en experimenteel gemotiveerd dat deze effectieve ruis overeenkomt met de tijdsgemiddelde van het (lineair geschaalde) interferentie-vermogen. Vervolgens worden de spectrale en totale interferentie geanalyseerd in functie van de reverberatietijd op basis van de *room electromagnetics* theorie. Het blijkt dat de frequentie-breedte van de spectrale interferentie typisch van de orde is van de omgekeerde reverberatietijd. Experimentele validatie wordt geleverd op basis van kanaalmetingen in een grote conferentieruimte. Een verliesfactor tot $19\ \mathrm{dB}$ wordt gemeten voor $800\ \mathrm{ns}$ CP en een uitzendvermogen van $30\ \mathrm{dBm}$, wat aantoont dat interferentie door onvoldoende CP de systeemperformantie aanzienlijk kan beperken.

Naast dit deel gericht op interferentie door onvoldoende CP, worden ook padverlies en zgn. *shadowing* bestudeerd op basis van kanaalmetingen in grote con-

[9] signal-to-interference ratio

ferentieruimten. Modellen voor padverlies worden ontwikkeld en de invloed van de aanwezigheid van mensen wordt bestudeerd. Op basis van dit padverlies-model wordt het effect van typische eigenschappen van IEEE 802.11n (zoals frequentie, bandbreedte en MIMO[10] antenne-configuratie) onderzocht op het vereiste aantal toegangspunten, energieverbruik (door straling) en (maximum) fysische datasnelheid. Dit wordt gedaan door zgn. *link budget* analyse op basis van het voorgestelde padverlies-model evenals het IEEE 802.11 TGn kanaalmodel. Uit deze evaluatie blijkt dat de twee modellen essentieel verschillende effecten voorspellen m.b.t. fysische datasnelheid en uitgestraald vermogen.

De onderzoeksresultaten van deze thesis hebben potentiële toepassingen op de volgende domeinen. Ten eerste is een complete meetprocedure op basis van frequentie-domein kanaal-karakterisering ontwikkeld voor accurate detectie van de interferentie door onvoldoende CP voor OFDM over realistische (tijdsdispersieve) kanalen. Dit laat de bepaling toe van typische karakteristieken, zoals (i) het (frequentie-gemiddelde) spectrale interferentie-profiel en (ii) de frequentie-afhankelijke monitoring van het totale interferentie-vermogen, de signaal-interferentie-verhouding of de verliesfactor, zelfs over een brede frequentieband. Deze karakteristieken kunnen verder gebruikt worden voor een beter OFDM design, zoals de selectie van de CP lengte, en het design van frequentie-domein equalisatie. Bovendien zijn padverlies en verliesfactoren door *shadowing* en interferentie belangrijke eigenschappen voor betere netwerkplanning en instelling van uitzendvermogen in grote indooromgevingen door *link budget* analyse. Ten tweede zijn er implicaties m.b.t. kanaalmodellering. I.h.b. voor grote indooromgevingen dienen kanaal-componenten met een *delay* groter dan de CP lengte beschreven te worden in kanaalmodellen. Ten derde zijn verschillende fysische inzichten, zoals de representatie van de interferentie in *windowing* methode type III en de relatie tussen de interferentie en de reverberatietijd, van groot belang voor het design van frequentie-domein equalisatie.

[10] multiple-input multiple-output

Summary

Orthogonal frequency-division multiplexing (OFDM) has been adopted to a wide range of wireless and wireline standards to provide a high-data-rate transmission over frequency-selective channels. The data stream is divided into a number of parallel substreams, which are modulated onto orthogonal carrier signals, referred to as subcarriers. The received signal can be demodulated by a relatively simple frequency-domain channel equalization after a Fast Fourier Transform (FFT), on condition that the subcarrier orthogonality is preserved over the FFT window. However, for a frequency-selective channel, which is intrinsicly time-dispersive, the received signal will be distorted, affecting the orthogonality between the subcarriers and causing overlap between different OFDM symbols. This results into intercarrier interference (ICI) and intersymbol interference (ISI), respectively. To counter the distortion, most OFDM systems make use of a cyclic prefix (CP), which refers to the periodical extension of the baseband transmit OFDM signal in addition to the FFT period.

The performance of CP-based OFDM systems may still be degraded over realistic channels due to the time-dispersive character. First, this performance loss can be caused by a symbol timing offset due to the distortion of the training signal. Second, the length of the channel impulse response may exceed the CP length in realistic scenarios. This is referred to as interference due to insufficient CP.

This dissertation is focused on IEEE 802.11, which is a set of physical and MAC[11] layer specifications for WLAN[12] and is also known under the trademark of Wi-Fi[13]. More specifically, the focus is on the 11a/g/n/ac standards, which are based on an FFT duration of $3.2\ \mu\mathrm{s}$ and a CP length of $800\ \mathrm{ns}$ (11a/g) or $400\ /\ 800\ \mathrm{ns}$ (11n/ac). Because of the relatively large CP length compared to the rms[14] delay spread of indoor channels, IEEE 802.11a/g/n/ac systems are usually designed in the assumption that the channel introduces no signal distortion over the FFT window. Therefore, a simple frequency-domain equalizer scheme without appropriate interference cancellation is typically implemented in realistic systems. However, a severe performance degradation due to insufficient CP is possible for realistic channels, especially in large indoor environments due to multipath propagation.

The dissertation's major part is dedicated to interference due to insufficient CP.

[11] Medium Access Control
[12] Wireless Local Area Network
[13] Wireless Fidelity
[14] root-mean-square

The approach followed is based on frequency-domain channel sounding and an analytical framework in terms of the channel impulse response based on an idealized OFDM signal model. The time-domain channel components are obtained by frequency-domain windowing and inverse discrete Fourier transformation. Novel data processing methods are developed and evaluated for accurate detection of the interference. The interference is further investigated in relation with the propagation channel. Several analyses are carried out based on the room electromagnetics theory for indoor wireless channels, according to which the tail of the averaged power delay profile (APDP) decays exponentially and where the decay time is referred to as the reverberation time. The last part of the dissertation reports on path loss modeling in large conference rooms. Path loss refers to the average signal attenuation at a certain transmitter-receiver separation. Path loss and interference modeling aid jointly to better network planning and transmit power control.

An analytical framework is developed to relate the interference due to insufficient CP to the propagation channel. The constellation error vector due to insufficient CP is determined in terms of a spectral (i.e., subcarrier-specific) interference coefficient, which is related to the *continuous* channel impulse reponse via time-domain weighting functions. The signal-to-interference-plus-noise ratio (SINR), which can be considered as a performance metric, is linked to the interference coefficient. Besides a "Fourier"-type of interference coefficient, related to the Fourier series decomposition of the received signal, a "correction"-type coefficient was introduced, to take into account the effect of a non-zero sampling period. For IEEE 802.11a/g/n/ac, it is found that typically only ISI between two consecutive OFDM symbols is relevant and that the ISI and ICI are spectrally identical.

For accurate determination of the interference coefficient over a given frequency band, the channel impulse response must be detected with a sufficiently small time resolution. Using frequency-domain channel sounding, this implies that the channel reponse is measured over a sufficiently wide frequency range. This *measurement range* may be considerably larger than the frequency range determined by all source and detecting subcarriers (i.e., causing and detecting interference, resp.) involved, referred to as the *zero-excess measurement range*. If the interest is in the interference between all subcarriers within the frequency band, the zero-excess measurement range just corresponds to the frequency band. A larger measurement range may be problematic because of a higher operating frequency range of the measurement equipment, interference with external sources outside the frequency band and a larger measurement time. However, the *excess measurement range* (i.e., measurement range versus zero-excess measurement range) can be reduced depending on the windowing method. Other issues are (i) the requirement of a large dynamic range, (ii) the suppression of the measurement noise and (iii) the requirement of a sufficiently large time window.

In this dissertation, the following windowing methods are considered, classified depending on the positioning and the profile. Methods of type I and II are based on a fixed and moving window, resp., and on a conventional weighting function, which is dependent on both source and detecting subcarrier for the Fourier-type interference coefficient. For method types I and II, a Hann window (method

I-Hann and *II-Hann*, resp.) and a rectangular window are considered (method *I-rect* and *II-rect*, resp.). In addition, a Hann window with window correction is studied (method *I-HC* and *II-HC*, resp.), where the non-uniform window profile is compensated by additionally dividing the interference coefficient by the window function at the source subcarrier.

The Fourier-type coefficient is physically related to the channel response around the source as well as the detecting subcarrier. Hence, for method types I and II, the window must systematically cover properly both the source and the detecting subcarrier frequency, which may be problematic for a high bandwidth. Method type III tackles this problem by consideration of the specific structure of the weighting function for a non-zero subcarrier separation. This allows decomposition in terms of a generalized (frequency-dependent) interference coefficient, which is evaluated at the source and detecting subcarrier separately. This generalized interference coefficient can then be determined from a measured channel response by applying a moving window. For method type III, a Hann and a rectangular window are considered (*III-Hann* and *III-rect*, resp.).

A complete error analysis on the interference coefficient is carried out. Besides the error due to a time-domain cut-off and due to measurement noise, the remaining error is divided up into an error due to (i) non-uniform windowing, (ii) a non-zero time resolution, (iii) direct leakage, (iv) aliased leakage and (v) aliasing. The direct leakage originates from the set of strongest channel components in the actual time window, whereas aliased leakage from the aliased components outside the actual time window. The error due to aliasing is typically inferior to the error due to a cut-off. The error due to non-uniform windowing, resolution and (direct and aliased) leakage are strongly dependent on the windowing method. The error due to a cut-off and aliasing are strongly related to the frequency resolution of the measured channel response.

For IEEE 802.11, where the FFT duration is typically much larger than the reverberation time of an indoor channel, the delay interval causing interference can be shortened by cutting off the weighting function, resulting into a smaller required time window. Based on the room electromagnetics theory, a parametric analysis shows that, to suppress the relative error power below -14 dB, the cut-off must be applied at a delay exceeding the CP length by at least 6.6 times the reverberation time. This requirement is most critically determined by the Fourier-type interference coefficient at a zero subcarrier separation, which is the most important spectral interference term. Experimental validation of this theoretical requirement is provided based on a measured indoor channel.

For the error due to a non-zero time resolution, an estimation for the relative error power is derived for the correction-type coefficient based on the room electromagnetics theory. This theoretical error power serves as a reference for the Fourier-type coefficient, where the resolution error power is typically strongly reduced for a small subcarrier separation. Using a Hann window (without window correction) or method III-rect, the resolution error power is found inversely proportional to the reverberation time and the window width. For method III-Hann and III-rect, the proportionality factor is -6.5 dB and -6.7 dB, respectively. How-

ever, for methods I-rect and II-rect, the resolution error power is rather determined by the excess of the window with respect to the evaluation frequency, than to the window width itself. Interestingly, the window width required to suppress the resolution error becomes smaller when the reverberation time is larger, i.e., when the interference becomes more significant. Experimental verification based on a measured indoor channel shows that the theoretical error power is a good order estimation.

Based on a channel measurement in a large exposition hall, the performance of the aforementioned windowing methods is evaluated with respect to the required measurement range for a $241\ \mathrm{MHz}$ frequency band. The required measurement range is determined from a convergence analysis procedure specifically for the window-related error types only. In addition, the limiting error types are identified through inspection of the type-specific error power. To determine the *spectral* interference, method III-Hann is found most appealing, especially for a higher bandwidth (e.g., $160\ \mathrm{MHz}$). Only an excess measurement range due to the resolution error is required, which is of the order of the inverse of the reverberation time. Other Hann window-based methods require an excess of the order of the bandwidth (methods II-Hann, I-HC, II-HC) or even the frequency band (method I-Hann) due to the error of non-uniform windowing. Proportionality factors are determined experimentally. Methods using a rectangular window suffer from leakage for a higher CP, which is most critically determined by the spectral Fourier-type interference coefficient at a zero subcarrier separation (i.e., the most important spectral term). In the case studied, method I-rect requires an excess measurement range of $661\ \mathrm{MHz}$ for $800\ \mathrm{ns}$ CP. To determine the *total* interference, method III-Hann is also very attractive. Methods II-Hann and I-HC are very useful too, requiring an excess measurement range of the order of the spectral interference width. Typically, this is of the order of the inverse of the reverberation time, as further shown. Note that method I-HC is less attractive to determine the interference as a function of the frequency because of a non-uniformly distributed error. Other Hann window-based methods still require an excess of the order of the bandwidth (method II-HC) or the frequency band (method I-Hann). Methods using a rectangular window may suffer from leakage, especially at a higher CP. In the case studied, method I-rect requires an excess measurement range of $321\ \mathrm{MHz}$ for $800\ \mathrm{ns}$ CP.

The limitations on the measurement range requirement through leakage are more generally investigated in terms of a maximum measurable signal-to-interference ratio ($\mathrm{SIR}_{\max}$), defined based on the total interference power originating from any OFDM symbol (i.e., including ISI and ICI). To measure an interference power as low as the thermal noise level, $\mathrm{SIR}_{\max}$ must not be smaller than the signal-to-noise ratio (SNR) that is actually detected by the OFDM receiver. To reach a $\mathrm{SIR}_{\max}$ of $100\ \mathrm{dB}$, method III-Hann requires for $400\ \mathrm{ns}$ CP a window width of $79\ \mathrm{MHz}$ and $53\ \mathrm{MHz}$ for direct and aliased leakage, resp., and $46\ \mathrm{MHz}$ and $162\ \mathrm{MHz}$ for $800\ \mathrm{ns}$ CP. In contrast, the performance of methods using a rectangular window is dramatically poor and the improvement through increasing the window width is slight. For method I-rect, even an extremely high window width

of 1500 MHz results into $\mathrm{SIR}_{\max}$ limitations of 65 dB and 60 dB due to direct and aliased leakage, resp., for 400 ns CP and 67 dB and 50 dB, resp., for 800 ns CP.

The performance of the windowing methods is also investigated with respect to the processing time required to determine the interference coefficient. This is done both theoretically and experimentally. It is found that especially for a high bandwidth, the total processing time for method type III is much lower than for type I and II at a realistic measurement range. At the *required* measurement range, the processing time for method III-Hann is found to be largely two orders of magnitude lower than for other methods.

The influence of the windowing methods on the error power due to measurement noise is investigated experimentally. It is found that in the range of convergence (i.e., for a measurement range larger than the requirement based on window-related errors), there is largely no essential influence. Further, the measurement error is investigated spectrally, showing that the Fourier-type interference coefficient at a zero subcarrier separation is most critical to suppress the measurement noise by averaging of the channel reponse. Finally, a practical procedure to determine the required number of sweeps for averaging is experimentally verified.

The effect of variations of both the received signal and the interference due to insufficient CP over subsequent OFDM bursts is taken into account for slowly time-varying channels. The time-varying interference is described as a time-invariant, effective additive Gaussian noise, which directly results into a loss factor. It is theoretically and experimentally motivated that this effective noise corresponds to the linear-scaled time-average of the interference power. Further, the spectral and the total interference are analytically described in terms of the reverberation time based on the room electromagnetics theory. It is found that the frequency width of the spectral interference is typically of the order of the inverse of the reverberation time. Experimental validation is performed based on channel sounding in a large conference room. A loss factor up to 19 dB is found for 800 ns CP and a 30 dBm transmit power, showing that the interference due to insufficient CP may severely affect the system performance.

Besides interference due to insufficient CP, path loss and shadowing is investigated based on channel measurements in large conference rooms. Path loss models are developed and the influence of the presence of humans is studied. Based this path loss model, the effect of typical IEEE 802.11n features (including frequency, bandwidth and MIMO[15] antenna configuration) on the required number of access points, total power consumption (due to radiation) and (maximum) physical data rate is investigated. This is done by link budget analysis, based on the proposed path loss model as well as the IEEE 802.11 TGn channel model. In this evaluation, it is found that the two path loss models predict some essentially different effects concerning data rate and radiated power.

This dissertation's research has potential applications in the following areas. First, a complete measurement procedure based on frequency-domain channel

[15] multiple-input multiple-output

sounding is developed for accurate detection of the interference due to insufficient CP for OFDM over realistic (time-dispersive) channels. This allows determination of typical characteristics such as (i) the (frequency-averaged) spectral interference profile, (ii) the frequency-dependent monitoring of the total interference power, signal-to-interference ratio or loss factor, even over a large frequency band. These characteristics can further be used for better OFDM design, such as CP length selection, and frequency-domain equalization design. Moreover, path loss and shadowing and interference loss factors are key properties for better network planning and transmit power control in large indoor environments via link budget analysis. Second, there are implications on channel modeling. Especially for large indoor environments, channel components with a delay larger than the CP length should be included in channel modeling. Thirdly, several physical insights, such as the interference representation in windowing method type III and the relation of the interference with the reverberation time, are also highly important to frequency-domain equalization design.

1
Introduction

1.1 Context and motivation of the dissertation

The first and major part of the dissertation is dedicated to interference due to insufficient cyclic prefix for *Orthogonal Frequency-Division Multiplexing* (OFDM) systems over time-dispersive channels. Although partly applicable to general OFDM systems, this research is focused on the IEEE 802.11 OFDM physical standard and on large indoor environments. In a second part, the dissertation centres on the modeling of path loss (including large-scale fading) for IEEE 802.11 links in large conference rooms. This section gives for both parts a description of the context and the motivation for the research conducted.

1.1.1 Interference due to insufficient cyclic prefix

1.1.1.1 CP-OFDM over time-dispersive channels

Orthogonal Frequency-Division Multiplexing (OFDM) is a modulation scheme adopted to a wide range of wireless and wireline physical standards to provide a high-data-rate transmission over frequency-selective channels [2]. *Frequency-selective* refers to a frequency-varying magnitude of the channel response. In OFDM, the data stream is divided into a number of parallel substreams, which are modulated onto orthogonal carrier signals, referred to as *subcarriers* or *tones*. The total transmit signal consists of a stream of *OFDM symbols*, which are each periodic over the inverse of the subcarrier frequency spacing. The received signal can be demodulated by a relatively simple frequency-domain channel equalization after a Fast Fourier Transform (FFT) [2], on condition that the orthogonality between the subcarrier signals is preserved over the receiver's *FFT window*. The FFT window refers to the FFT time interval and has a duration of the inverse of the subcarrier frequency spacing.

A frequency-selective channel is intrinsicly ***time-dispersive***, which refers to a time-domain (or delay-domain) spread of the channel impulse reponse. As a result, the received signal is a superposition of replicas of the transmit OFDM signal, each with a different delay. Considering an OFDM symbol duration of the FFT period, the orthogonality between the subcarrier signals as detected over the FFT window is lost, as "late" replicas do not completely overlap with the FFT window. This causes interference between different subcarriers of the same OFDM symbol, referred to as *intercarrier interference* (ICI). Moreover, "late" replicas from preceding OFDM symbols overlap with the FFT window, which causes interference between different OFDM symbols, referred to as *intersymbol interference* (ISI). To counter these adverse effects, most OFDM systems make use of a ***cyclic prefix*** (CP), which refers to the periodical extension of the baseband transmit OFDM signal in addition to the FFT period. The principle of CP-based OFDM is illustrated in Fig. 1.1. Due to the OFDM symbol duration being longer than the FFT

window, “late” replicas also show a complete overlap with the FFT window, preserving the orthogonality of the subcarrier signals and avoiding any overlap with “late” replicas from preceding OFDM symbols. The channel equalization can then be performed by a one-tap frequency-domain equalization scheme. This situation of proper OFDM operation without ISI nor ICI applies if (i) the channel’s maximum *excess delay* (i.e., the difference between the delay and the minimum delay), is smaller than the CP length and (ii) on condition of proper FFT window positioning. Besides CP-based OFDM, zero-padding OFDM employs a guard interval (i.e., waiting time against intersymbol interference) padded with zeros, which provides some equalization advantages [3]. However, most practical OFDM systems are CP-based, which is the focus of this dissertation.

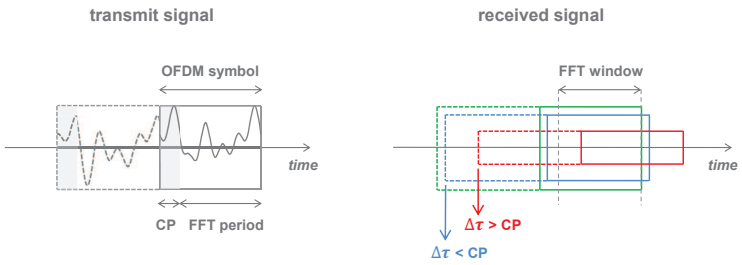

Figure 1.1: Principle of CP-OFDM: replicas of the transmit OFDM signal with an excess delay ($\Delta\tau$) smaller than the cyclic prefix (CP) length do not result into intersymbol or intercarrier interference assuming proper FFT window positioning.

Despite the CP insertion, realistic OFDM systems over time-dispersive channels may still suffer from ICI and ISI. First, this may be caused by a symbol timing offset, which refers to an improper FFT window positioning. The timing synchronization is typically accomplished by correlation between a (known) training signal and its received version. The latter may be distorted by the time-dispersive channel. The resulting timing offset has been related to the channel’s rms[1] delay spread [4]. Second, the maximum excess delay of the channel impulse response may exceed the CP length in realistic scenarios. In this case, ICI and ISI can no longer be avoided, even with a proper FFT window positioning. This is illustrated in Fig. 1.1 for a channel component with an excess delay larger than the CP length. The replica of the OFDM signal does not completely overlap with the FFT window, causing ICI. Moreover, there is an overlap with the replica of the preceding OFDM symbol, which causes ISI. This situation is realistic, as standardized CP lengths are selected based on a general trade-off between the spectral efficiency loss due to overhead and the interference power. This interference is referred to as ***interference due to insufficient CP*** and is the focus of this dissertation. However,

[1] root-mean-square

there is no physical difference between the interference due to insufficient CP and due to a timing offset.

1.1.1.2 Multipath propagation and room electromagnetics theory

For wireless propagation channels, the frequency-selective or time-dispersive character is mainly caused by ***multipath propagation***, which is illustrated in Fig. 1.2. The OFDM signal is transmitted by the transmit antenna (Tx) as an electromagnetic wave and reaches the receiver antenna (Rx) via different propagation paths as a result of interactions with the environment. These interactions concern reflection and diffraction at structures such as walls, the ceiling, the floor and furniture for an indoor scenario and buildings, the ground and mountains outdoors. As a result, the received signal is a superposition of replicas of the transmit OFDM signal, each with a different delay being the path length divided by the speed of light. This is reflected in the channel impulse response as a set of different channel components, each arising at the corresponding delay. Besides multipath propagation, the time-dispersive nature of the propagation channel can also be caused by a frequency-selective behavior of interaction processes with the environment (reflection, transmission, diffraction and absorption) or the antenna radiation pattern.

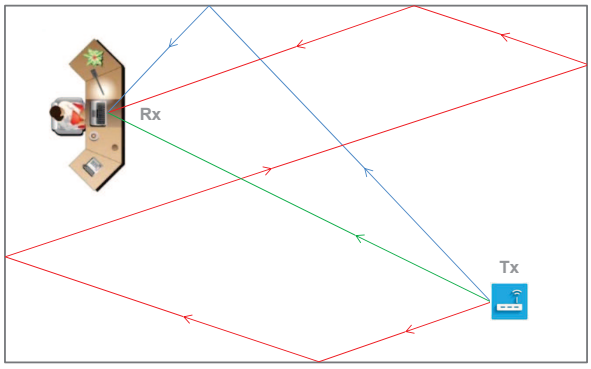

Figure 1.2: Schematical top view illustration of indoor multipath propagation. The transmit signal (at Tx) reaches the receiver (Rx) via distinct propagation paths, resulting into a delay spread of the channel.

In this dissertation, several analyses are carried out based on the ***room electromagnetics*** theory for indoor wireless channels [5]. According to this theory, the tail of the averaged *power delay profile* (APDP) decays exponentially and the decay time is referred to as the ***reverberation time***, which is illustrated in Fig. 1.3. The power delay profile or multipath intensity profile refers to the squared magni-

tude of the channel impulse response in time-discrete passband form. As indicated in Fig. 1.3, the exponential APDP decay implies a decrease in power of about $4.3\ \mathrm{dB}$ if the delay increases with the reverberation time. In the APDP, the average is taken over a varying small-scale position of the transmit and receive antenna. This theory was introduced in [5], where a 16×32 MIMO channel measurement with a $100\ \mathrm{MHz}$ bandwidth and a $200\ \mathrm{ns}$ time window was executed in a large office environment. The APDP was found to decay exponentially from a delay of about $75\ \mathrm{ns}$ with a reverberation time of $24\ \mathrm{ns}$. Moreover, it was found that the power of the time-domain channel components was exponentially distributed and that the APDP tail was approximately the same for most Tx and Rx locations in the room. These observations have been described by a model where a uniform energy density, remaining a certain time after signal transmission, decays exponentially as a result of loss processes, i.e., transmission (through the walls, floor or ceiling) or absorption.

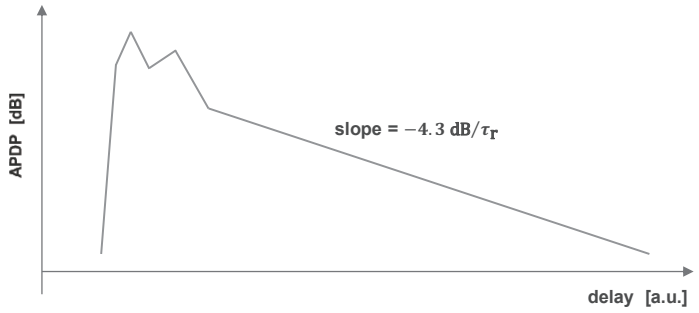

Figure 1.3: Schematical illustration of the room electromagnetics theory, stating an exponentially decaying APDP tail. The decay time is referred to as reverberation time (τ_r).

For an indoor channel, it can be motivated that from a sufficiently large delay, the time-domain channel is composed of a dense set of physically distinct propagation paths with a gain that on average decreases exponentially with the delay. The latter is based on the fact that the concerning paths arrive at the receiver typically after a series of attenuations through reflection or diffraction in the room [6]. Note that *dense* is meant relative to the time resolution of the power delay profile. Thus, the room electromagnetics theory is applicable if the channel bandwidth is much larger than the inverse of the power-delay decay time, but much smaller than the path inter-arrival time. In this situation, the time-domain components are composed of a large number of physically distinct propagation paths, resulting into their power being exponentially distributed over a varying small-scale position. This was also experimentally found in [7].

In literature, experimental values of the reverberation time are provided for

various indoor environments. In [8], a reverberation time between 15 ns and 25 ns is observed in the delay range of $[40, 140]$ ns in an aircraft environment (with and without passengers) at $3.5 - 3.7$ GHz. A reverberation time of $22 - 28$ ns in a delay range of about $[100, 500]$ ns was found in a seminar room (with dimensions of 8×6 m) at 2.3 GHz in [9]. In [10], a reverberation time of $17 - 19$ ns was found over a delay range of about $[25, 150]$ ns in small meeting and office rooms (with dimensions up to 5×5 m) at 5.2 GHz. An overview of experimental reverberation times from literature was presented in [8], yielding values between 8 ns and 26 ns for small- to medium-size office and meeting rooms (up to dimensions of 11×20 m) at frequencies in the range of $[1, 60]$ GHz.

An important implication of the room electromagnetics theory is that propagation paths with an excess delay larger than the CP length cannot be avoided. Hence, CP selection is always a trade-off between interference due to insufficient CP and channel capacity loss due to overhead. This is most critical in high-multipath environments, which have large room dimensions and/or weak loss processes as a result of highly reflective structures and the absence of highly absorptive objects. In this case, propagation paths with a large excess delay appear with a non-negliglible gain, resulting into a large reverberation time.

1.1.1.3 Interference due to insufficient CP for various OFDM technologies

The interference caused by insufficient CP may substantially affect the system performance, as reported for several wireless communication technologies. In [11–13], a significant effect on the bit rate or bit error rate was found for IEEE 802.11a. This is a physical standard for Wireless Local Area Networks (WLAN), specifying an 800 ns CP and operating at 5 GHz [14]. Typical WLAN environments are a.o. homes, offices, industrial halls, trains and airplanes. In [15], a significant interference due to insufficient CP was experimentally found for IEEE 802.11ad and IEEE 802.15.3c in a hospital environment. These are standards for short-range point-to-point links (up to 10 m) for multi-gigabit data- and video-applications and operating at 60 GHz. They feature an OFDM mode with a CP length of 48.4 ns [16] and 24.24 ns [17], respectively.

In [18], the interference due to insufficient CP is experimentally studied for fourth-generation (4G) mobile cellular networks at 3.7 GHz in urban and suburban environments. Orthogonal Frequency-Division Multiple Access (OFDMA), which is an OFDM-based frequency-division multiple access scheme, is used in the 4G standards of Long Term Evolution-Advanced (LTE-A) for downlink transmission [19] and IEEE 802.16m (WiMAXv2) for both downlink and uplink [20]. The CP length over different modes is of the order of 10 µs [2,20]. The issue of insufficient CP has also been reported for OFDM underwater acoustic communication [21] and wireline OFDM technologies, such as Digital Subscriber Line (DSL) [22], power line communication (PLC) [23] and fiber-optic communication [24].

This dissertation is in particular focused on IEEE 802.11, which is a set of physical and MAC[2] layer specifications for WLAN and is also known under the trademark of Wi-Fi[3]. More specifically, the focus is on the 11a/g/n/ac standards [14] - [27], which are based on comparable OFDM parameters and are operating in the 2.4 GHz (11g/n) and 5 GHz (11a/n/ac) band. The FFT duration is specified at 3.2 µs with a CP length of 800 ns. A short CP option of 400 ns is added to 11n/11ac. While 11a/11g operates at a 20 MHz bandwidth, higher bandwidth modes are included in 11n (20 / 40 MHz) and 11ac (20 / 40 / 80 / 160 MHz). Conventional WLAN has been extended by IEEE 802.11ad to provide short-range and point-to-point links at multi-gigabit throughput in the unlicensed 60 GHz band. The standard specifies a 2640 MHz bandwidth, a 194 ns FFT period and a 48.4 ns CP length [16].

Because of the relatively large CP length compared to the delay spread of indoor channels, IEEE 802.11a/g/n/ac systems are usually designed in the assumption that the channel introduces no signal distortion over the FFT window. Therefore, a simple frequency-domain equalizer scheme without appropriate interference cancellation is implemented in realistic systems. However, a severe performance degradation due to insufficient CP is possible for realistic channels, especially in large indoor environments due to multipath propagation.

1.1.1.4 Motivation of the research conducted on interference due to insufficient CP

Considering the significance of the interference due to insufficient CP and its dependence on the actual physical channel, **accurate experimental determination of the interference power for realistic channels is of great importance for system designers and integrators**. In this section, this is motivated for interference characteristics based on the *total* interference power (interference from *any* OFDM symbol and *any* subcarrier) as well as the interference between individual subcarriers and OFDM symbols. This is illustrated in Fig. 1.4, showing the different interference processes characterized by a separation of the OFDM symbol index, Δk, and a separation of the subcarrier index, Δi. In general, the *source subcarrier* refers to the subcarrier from which the interference process originates, while the *detecting subcarrier* refers to the subcarrier where the interference is received. Interference processes with $\Delta k = 0$ and $\Delta k \neq 0$ are referred to as intercarrier and intersymbol interference, respectively. Finally, arguments are provided for investigating the analytical relationship between the interference power and the reverberation time on the basis of the room electromagnetics theory.

[2] Medium Access Control
[3] Wireless Fidelity

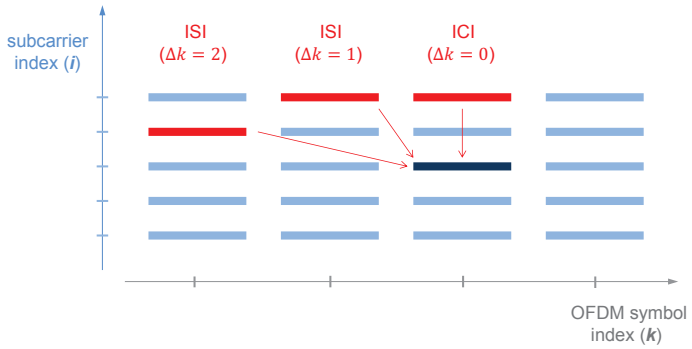

Figure 1.4: The interference due to insufficient CP is composed of different interference processes characterized by the subcarrier separation, Δi, and the separation of the OFDM symbol index, Δk. Interference processes with $\Delta k = 0$ and $\Delta k \neq 0$ are referred to as intercarrier and intersymbol interference, resp. (ICI/ISI).

Total interference power

The ***signal-to-noise-plus-interference ratio*** (SINR), which is the ratio between the useful signal power (at the receiver) and sum of the (thermal and hardware-related) noise and the interference power, acts as a performance metric for the *channel capacity*, which is the physical information data rate. The interference power due to insufficient CP comprises interference from *any* OFDM symbol and *any* subcarrier, as illustrated in Fig. 1.4. Considering the frequency-selective nature of the channel, the interference power due to insufficient CP may strongly vary over different subcarriers. Therefore, it should be possible to experimentally determine the (total) interference power present per individual subcarrier.

By measuring the per-tone signal power and the per-tone interference power for a given set of data transmission channels, the following **performance characteristics** can be detected:

- the SINR
- the *signal-to-interference ratio* (SIR):
  The SIR serves as an upper limit for the SINR, which is achieved for a sufficiently large transmit power. This is because the signal power and the interference power are both proportional to the transmit power. Contrary to the SINR, the SIR does not depend on the transmit power and the noise factor and is therefore an interesting characteristic.
- the *SINR degradation* or *loss factor* due to insufficient CP:
  The SINR degradation due to insufficient CP is defined as the SINR loss in reference with the situation of an infinitely large CP length. The loss factor

due to insufficient CP is a loss margin[4] to be implemented in link budget analysis and corresponds to the SINR degradation.

Experimental determination of these performance characteristics is very useful for a **wide range of purposes**:

- This may help integrators to **identify potential reception problems** related to interference due to insufficient CP. This thesis actually originates from such a practical case, where an industrial designer and integrator repeatedly experienced reception problems with an IEEE 802.11a audio conference system in a *specific* large conference room. The base station was positioned in line-of-sight up to $10\ \mathrm{m}$ from the terminals at the conference table, in which case a sufficiently high signal-to-noise ratio is expected. After spectral analysis, the reception problems could neither be attributed to external interference sources. Although there was a strong indication that the reception issues were related to the environment, the manufacturer did not succeed to identify the problem. The loss factor due to insufficient CP in this room is experimentally determined in Chapter 7 in order to link the poor reception performance to the interference due to insufficient CP.

- Experimental determination of the performance characteristics also allows to **optimize network integration**. In the practical case mentioned, the integrator spent great efforts to optimize the base station position and the antenna type. A substantial improvement was reportedly noticed using a directional antenna, where the beam was directed towards a glass wall to limit reflection. Experimental detection of the SINR allows to quantify the system performance and provides an adequate approach to optimize network integration.

- Experimental SINR detection also contributes to **better OFDM design**. Especially the selection of the CP length is an important matter for most OFDM technologies. This can be carried out by optimization of the channel capacity as a function of the CP length [18]. The channel capacity is dependent on the CP length via the loss factor due to CP-related overhead and the SINR.

Interference between individual subcarriers and OFDM symbols

Whereas the *total* interference power due to insufficient CP is important with respect to the system performance, experimental determination of the interference between individual subcarriers and OFDM symbols is of great importance to the

[4] the actual system performance is described on the basis of a reference situation with an infinite CP length and a transmit power reduced by the loss factor

design of frequency-domain channel equalization. In this equalization scheme, the interference is cancelled out by a matrix operation on the FFT output (at the receiver), giving the undisturbed transmitted data symbols. Knowledge on the structure of the equalization matrix, such as the required number of taps for per-tone equalization, is important for better equalization design. This information is directly revealed by measuring the interference between individual subcarriers and OFDM symbols. An important characteristic is the ***spectral interference profile***, which is the frequency-averaged interference power as a function of the subcarrier separation (Δi) for a given OFDM symbol separation. The ***spectral interference width***, which is the profile width covering a large percentage of the total profile power, is an indicator of the required number of taps. These characteristics are schematically illustrated in Fig. 1.5.

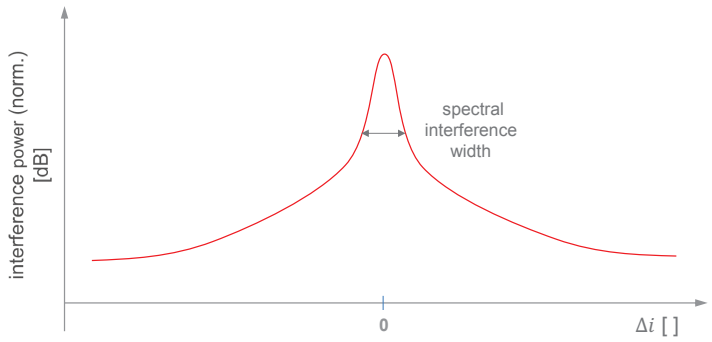

Figure 1.5: Schematical illustration of the (normalized) spectral interference power profile for a fixed OFDM symbol separation. The spectral interference width indicates how many subcarriers are (on average) involved in interference due to insufficient CP in a non-negligible way.

Analytical relationship between interference power and reverberation time

The interference due to insufficient CP originates from channel components with an excess delay larger than the CP length. In this delay region, the APDP decays exponentially according to the room electromagnetics theory, which is realistic for IEEE 802.11 indoor channels. Therefore, the reverberation time is an important propagation characteristic with respect to the interference due to insufficient CP. This indicates that, where the room electromagnetics theory is applicable, several interference characteristics, such as the (averaged) total interference power and the spectral interference profile, can be analytically determined as a function of the reverberation time. This would be interesting for different reasons:

- physical insight is gained in the relation between the interference due to

insufficient CP and the propagation channel

- possibility to perform a parametric study of the interference
- a simplified interference measurement technique is provided, based on the experimental determination of the room electromagnetics parameters (namely the reverberation time and the intensity factor of the APDP tail)

1.1.2 Path loss modeling

1.1.2.1 Path loss and shadowing

When a signal is transmitted at a given frequency, the signal is received with a certain attenuation in power. For wireless channels, the actual signal attenuation can be described as a result of different physical processes.

- ***path loss***: Path loss refers to the signal attenuation corresponding to the averaged received power around a fixed Tx-Rx separation after de-embedding the antenna gain. As proposed in [28], this is based on the line-of-sight transmitter and receiver gain. In free space, the path loss follows an inverse-square law as a function of the Tx-Rx separation due to the spheric wave propagation. In a real-world scenario, the path loss generally follows a modified trend due to the interaction with the specific environment. The path loss is usually modeled by a deterministic law dependent on the Tx-Rx distance.
- ***large-scale fading***: Large-scale fading or *shadowing* refers to the variation of the received power as averaged over a local region with a dimension of about 10 times the wavelength [2]. The variation is caused by a different multipath structure per local region. This is a result of the interaction of the propagation wave with the local environment, such as furniture or humans in an indoor scenario, causing local regions where propagation paths are blocked or added by reflection. The deviation of the large-scale-averaged received power is usually described as a statistical (typically Gaussian) process.
- ***small-scale fading***: Small-scale fading refers to the variation of the receiver signal power due to a Tx/Rx movement over a distance of the order of the wavelength. This is caused by interference of distinct propagation paths in the case of multipath propagation. Small-scale fading is usually described as a statistical variable, where various distributions, such as a Nakagami-*m*, Rayleigh, or lognormal distribution, are proposed in literature [7].
- ***temporal fading***: Temporal fading refers to the time-variation of the channel due to a change of the environment, such as moving humans or objects.

This variation is usually described by a statistical variable, following e.g. a Ricean distribution (or Rayleigh distribution in particular) [7].

1.1.2.2 Motivation of the research conducted on path loss modeling

As the channel capacity is related to the SINR, the attenuation of the signal strength is an important factor determining the maximum achievable data rate. For wireless networks, this is reflected in the limitation of the Tx-Rx range where, using a given transmit power, preset requirements on the data rate and the link reliability are met. Therefore, modeling the different mechanisms of signal attenuation described above is highly important for integrators of wireless networks. These models allow network planners to predict the Tx-Rx range, based on which the base stations are positioned and configured.

Considering that the attenuation processes outlined above depend on the specific environment, there is a need for appropriate models for different types of environment. For IEEE 802.11 scenarios, **different aspects of the environments may have an effect on the path loss and large-scale fading** in particular:

- Large indoor environments such as exposition halls, train stations or factory halls are expected to have different characteristics compared to small indoor environments such as office rooms or residential environments [7].
- The line-of-sight link condition is mentioned as an elementary factor [2]. Under non-line-of-sight conditions, the path loss is reported to decrease faster with the Tx-Rx distance [29]. This results into different characteristics for open environments such as large conference rooms (e.g., parliament hemicycles) compared to factory halls with a lot of machinery units.
- The environment is also characterized by the type of materials. E.g., highly reflective structures such as a metal wire-mesh integrated in the floor or ceiling may have an influence, or the massive presence of people in exposition halls (due to absorption).

In literature, various propagation models have been reported for Wireless LAN in different indoor environments [30] - [36]. However, **almost no path loss models can be found which are specifically applicable for large conference rooms**. The IEEE 802.11 TGn channel model could be applicable [29]. However, this model applies to very different types of environment (from residential to large space (indoors - outdoors)), and possibly does not take into account the specific geometry of large conference rooms (e.g., parliament hemicycles). The path loss modeling in the TGac channel model is taken over from the TGn channel model [37].

In this dissertation, the path loss and shadowing is modeled for the specific environment of a **large, open conference room** with a line-of-sight condition,

such as a parliament hemicycle. The influence of the presence of humans during a meeting is studied as well.

1.2 Approach and goals of the dissertation

1.2.1 Interference due to insufficient cyclic prefix

1.2.1.1 Methodology for experimental detection of the interference coefficient

Detection of the interference due to insufficient CP implies that the constellation error vector caused by an insufficient CP length is inspected. This constellation error vector[5] is a result of different interference processes and is a linear combination[6] of the transmitted data symbols of the OFDM symbols and/or subcarriers causing interference (see Fig. 1.4). The coefficients in this linear combination are referred to as ***interference coefficients*** and describe the interference due to insufficient CP between individual OFDM symbols and/or subcarriers. These interference coefficients are dependent on the transmission channel and the OFDM signal processing. Methodology for experimental detection of the interference coefficients is needed in order to determine various interference characteristics (Section 1.1.1.4).

In this dissertation, the detection of the interference coefficient is accomplished by **experimental characterization of the transmission channel** and a **channel-based analysis of the interference coefficient**. In this analysis, the interference coefficient is analytically related to the channel impulse response on the basis of a general, standard OFDM signal model. In the dissertation's analysis, the channel impulse response is considered time-invariant and continuous (non-discrete in the delay domain). The interference coefficient is connected with the channel impulse reponse by means of a weighting function, which refers to a delay-domain function that determines the contribution of each channel component with a certain delay to the interference coefficient. The interference coefficient is then obtained as the inverse Fourier transform of the channel impulse response multiplied by the weighting function and evaluated at the frequency of the source subcarrier. This is schematically illustrated in Fig. 1.6.

Practical channel sounder systems do not yield the exact continuous CIR, but a delay-discrete (passband) representation with a finite *time window*. The time window refers to the range in the delay-domain (also referred as time-domain), starting at a zero delay, where channel components can be detected by the channel sounder system. The interference coefficient can be computed by a delay-discrete form of the Fourier transform and using the experimental delay-discrete CIR. However, the interference detection involves **particular issues on proper CIR detection**:

[5] the deviation between the received and the transmitted complex-valued data symbol in the constellation diagram

[6] assuming a linear receiver signal model

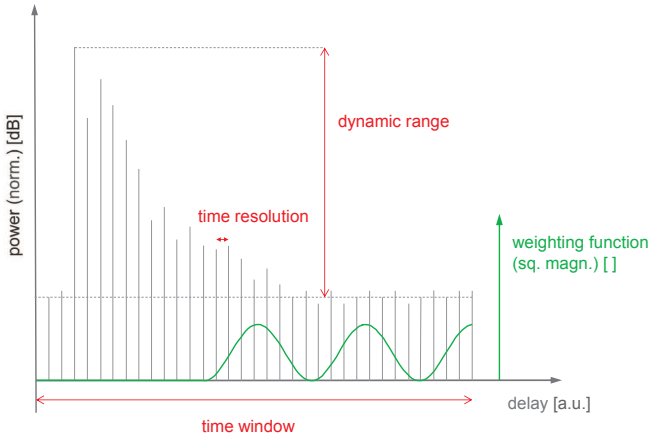

Figure 1.6: Schematical illustration of the measured (delay-discrete) CIR (depicted in normalized power), where the time resolution, time window and dynamic range are indicated. The weighting function (depicted in squared magnitude) determines to which extent each channel component contributes to the interference coefficient.

- The ***time resolution*** of the measured CIR, which refers to the delay spacing of the delay-discrete channel components, should be sufficiently small to allow proper delay-domain discretization. In particular, the required time resolution depends on the coherence width of the weighting function.
- The measured CIR should have a sufficiently large ***dynamic range***, which refers to the ratio in power between the strongest channel component and the weakest measurable one. The dynamic range of practical channel sounders is limited by measurement noise as well as spurious-free causes related to the signal processing of the channel sounding. The dynamic range caused by measurement noise can be improved by averaging of the measured CIR components over a series of acquisitions.
- The **time window** should be large enough to capture all relevant channel components with respect to the interference coefficient. Consequently, the required time window is larger than the CP length and also depends on the channel's power-delay profile and the profile of the weighting function.

In this dissertation's approach, the CIR is experimentally determined based on **frequency-domain channel sounding**. This can be performed by a low-cost narrowband channel sounding setup using a vector network analyzer (VNA). A detailed comparison with other channel sounding techniques is provided in Section 1.3.2.1. In a frequency-domain channel sounding system, the channel (frequency) response is measured over a limited frequency range, referred to as the

measurement range, and with a non-zero frequency spacing, referred to as the *frequency resolution*. The delay-discrete CIR representation is obtained as an inverse discrete Fourier transform (IDFT) of the measured channel response samples. The time resolution and the spurious-free dynamic range can be improved by appropriate windowing of the measured channel response samples prior to IDFT computation. The spurious-free dynamic range is caused by delay-domain leakage introduced by the frequency-domain windowing, which cannot be avoided due to the finite measurement range. Different *windowing methods* can be applied, depending on (i) the positioning of the window centre frequency with respect to the source subcarrier and the detecting subcarrier and (ii) the window profile. Furthermore, a sufficiently large time window can be directly obtained by selecting a sufficiently small frequency resolution.

This dissertation provides an in-depth study of different **windowing methods** with respect to the time resolution and the dynamic range. A novel windowing method is developed, based on a generalized representation of the interference coefficient. While for more conventional windowing methods, the window systematically covers both the source subcarrier and the detecting subcarrier, the novel windowing method centres a window around the source subcarrier and the detecting subcarrier separately. This is illustrated in Fig. 1.7. In general, the non-zero time resolution and the limited dynamic range result into an error on the obtained interference coefficient. For each windowing method, this error can be suppressed by taking a sufficiently large *window width*, which refers to the frequency width of the applied window. In this dissertation, a theoretical error analysis is carried out to relate the windowing method and the window width to the error on the interference coefficient.

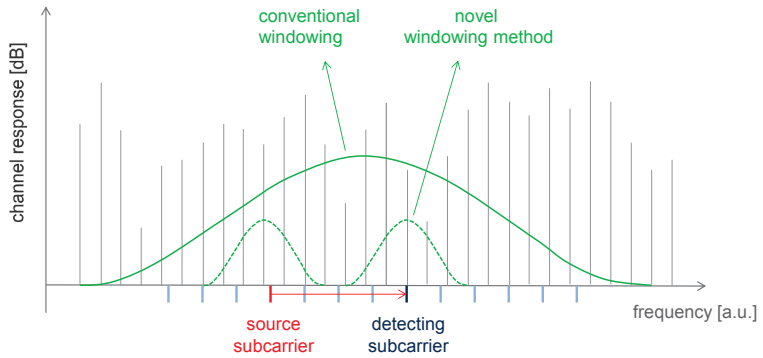

Figure 1.7: A windowing method is applied on the measured channel frequency response samples prior to IDFT computation. Besides conventional windowing, a novel windowing method is studied where the window is positioned around source and detecting subcarrier (of the interference coefficient) separately.

In this dissertation, the performance of the windowing methods with respect to the time resolution and the dynamic range is also experimentally evaluated based on an indoor channel measurement and for IEEE 802.11 OFDM parameters. The **performance evaluation** is conducted at a fixed accuracy level of the interference coefficient. To determine the interference coefficient over a given frequency range of the detecting subcarrier, a certain measurement range is needed as a result of the window width requirement to achieve sufficient time resolution and dynamic range. It is practically important to limit the measurement range because of higher hardware requirements on the measurement system, possibly additional external interference sources and a larger measurement time. Besides the measurement range, the windowing methods are also evaluated on their processing time and their sensitivity to the measurement noise.

1.2.1.2 Determination of the loss factor due to insufficient CP

By definition, the loss factor due to insufficient CP describes the actual system performance on the basis of a reference situation, being the actual situation with an infinite CP length, and a transmit power reduction by the loss factor. As reported before, this loss factor is an important characteristic that can be integrated in link budget analysis. For a static channel, the loss factor is determined by the ratio between the noise plus interference power (due to insufficient CP) and the noise power. However, for a slowly time-varying channel, which can be considered as static during each single OFDM packet[7], the interference power is time-varying as well, which complicates the determination of the loss factor. The dissertation's approach to this problem consists of two steps:

1. The actual system performance is described based on the reference situation and a **per-packet (time-dependent) additional noise factor**, which is proportional to the interference power due to insufficient CP. Considering the static behaviour of the channel within a single OFDM packet, this description is reasonable if the number of interference processes is sufficiently large, so that the constellation error vector due to insufficient CP can be statistically perceived as thermal noise.

2. The actual system performance is described based on the reference situation and an additional *effective* (time-constant) noise factor. The determination of the **effective noise factor** from the (time-dependent) noise factor is investigated theoretically and experimentally by evaluation of the SINR statistics.

[7] OFDM frame containing a series of OFDM symbols

1.2.1.3 Analysis of the interference power due to insufficient CP in relation to the reverberation time

To relate the interference power due to insufficient CP to the reverberation time, which is a characteristic of the APDP, **APDP-based expressions for the interference power** are to be determined. Using these expressions, the interference power can be analytically determined as a function of the reverberation time, if the **room electromagnetics theory** is applicable. The APDP-based and analytical (reverberation time-based) expressions are experimentally validated on the basis of indoor channel measurements and for typical IEEE 802.11 OFDM parameters. The analytical expressions are then further investigated to determine (i) a simplified closed-form expression for the effective noise factor and (ii) the importance of the reverberation time with respect to the spectral interference profile.

1.2.1.4 Goals of the dissertation on the interference due to insufficient CP

In the thesis' approach just outlined to study the interference due to insufficient CP, the specific goals can be listed as follows:

- analytical determination of the interference coefficient by means of **CIR-based weighting functions**
- windowing methods for experimental detection of the interference coefficient from frequency-domain channel sounding:
  - development of a **novel windowing method** based on a generalized representation of the interference coefficient
  - error analysis of novel and more conventional windowing methods
- **experimental performance evaluation of various windowing methods**:
  - evaluation of the required measurement range to achieve appropriate time resolution and spurious-free (leakage-related) dynamic range
  - evaluation of the processing time
  - evaluation of the sensitivity to the measurement noise
- investigation of the **required time window** for CIR-based experimental detection of the interference coefficient
- investigation of the **required number of acquisitions** for measurement noise averaging
- investigation of the **concept of the effective noise factor** due to insufficient CP

- analysis of the effective noise factor and the spectral interference profile in **relation to the reverberation time**
- experimental determination of the effective noise factor and the **loss factor in several large indoor environments for IEEE 802.11 OFDM**

1.2.2 Path loss and shadowing in large conference rooms: approach and goals

In this dissertation, the path loss and shadowing are modeled according to an ***empirical* approach.** In this approach of channel modeling, the channel is *experimentally* characterized by detection of a transmitted sounding signal [7]. Besides empirical modeling, another approach is *deterministic* modeling, where the physical propagation mechanisms are computationally simulated (e.g., by ray-tracing) to determine the channel characteristics [7, 38]. Considering the complexity of the environment of large conference rooms (such as unknown material properties and the presence of humans), the empirical approach is followed in this dissertation.

The channel is experimentally characterized by narrowband channel sounding, where a monochromatic signal is transmitted. The received power is measured by a spectrum analyzer. Realistic antenna types with an omnidirectional radiation pattern are used to capture possible multipath propagation in a representative way. The large-scale-averaged received power is modeled by regression, where the path loss is modeled as a function of the Tx-Rx separation and the shadowing as a stochastic process.

The dissertation's part on path loss and shadowing aims at the following specific **goals**:

- modeling of the path loss and shadowing in large conference rooms for IEEE 802.11
- investigation of the influence of people present during a meeting

1.3 State-of-the-art and comparison with the dissertation's approach

1.3.1 Channel-based analysis of interference due to insufficient CP

In literature, the interference due to insufficient CP is usually analyzed based on delay-domain weighting functions describing the contribution of each delay component of the channel impulse response. In [39], weighting functions were proposed for the spectral error vector (i.e., interference between individual subcarriers) due to insufficient CP and a Doppler shift (i.e., time-varying channel). For a slowly fading channel (i.e., static during one OFDM symbol), the time-averaged total interference (i.e., from all subcarriers jointly) was described in [40] by a weighting function based on the time-averaged power delay profile (PDP).

In [1], a two-dimensional weighting function was proposed to relate the (time-averaged) total interference due to insufficient CP and a Doppler shift due to the time-dependent channel impulse response. It was shown that the ISI is not dependent on the channel's time-correlation properties and that the ICI is approximately composed of two interference terms due to the delay- and frequency-selective character of the channel, respectively. The latter term and ISI were each linked to the time-averaged PDP by a delay-domain weighting function. This work was extended in [41] including a (hardware-related) frequency offset. Based on [1], a time-varying channel with a line-of-sight (LOS) component was considered in [42] to investigate optimization of the CP length and the FFT period. Where the aforementioned studies use a discrete channel impulse reponse, a continuous form was used in [43, 44] assuming an infinitely small receiver sampling period, though the relation found between the (time-averaged) total interference and the (time-averaged) PDP essentially coincides with [1]. All studies mentioned are based on the wide-sense stationary uncorrelated scattering (WSSUS) fading model [45], which states that different delay components are uncorrelated and that the time-correlation properties are time-invariant.

Another approach is presented for a time-invariant channel in [46], where the interference is analyzed per time sample of the transmit signal and weighted with the discrete Fourier transform (DFT) of the tail of the channel impulse response. Further, a closed-form analytical expression for the interference power as a function of the CP length, the rms delay spread and the FFT period has been presented in [47] as an upperbound. An analytical framework for the calculation of the interference due to insufficient CP as well as timing and frequency offset is given in [48]. While all these references are focused on a SISO (single-input single-output) system, the interference due an insufficient CP length is studied for

a cellular network MIMO[8] system in [49], taking multi-user interference due to asynchronous signal transmission into account.

Comparison with the thesis' approach

In the dissertation's approach, the interference coefficient is analytically determined using CIR-based weighting functions. This is based on a static, continuous CIR and a general, standard OFDM signal model. This includes the following aspects:

- **CIR-based** weighting function for the **interference coefficient**:
  In [1, 42], the weighting function is based on the APDP, which is essentially only applicable to determine the frequency-averaged and/or time-averaged interference power. Furthermore, while [1, 42] present a weighting function to determine the total interference power, the weighting function in this dissertation determines the interference coefficient, which allows to measure the spectral interference profile in addition. A CIR-based weighting function for the interference coefficient was already derived in [39], but not for general OFDM parameters (CP length and FFT time).

- **continuous** CIR:
  While most earlier studies analyze the interference based on an OFDM signal model featuring a delay-discrete CIR representation, this dissertation determines the interference coefficient based on the continuous CIR. The continuous CIR contains all physical information of the channel, based on which the error on the interference coefficient can be theoretically analyzed for various windowing methods.

- **static** channel per OFDM packet:
  In the dissertation's channel-based analysis of the interference, the channel is assumed to be static per OFDM packet. As just mentioned, a number of earlier studies also consider a channel that is time-varying during an OFDM packet, which results into intercarrier interference through a Doppler shift. According to [1], the interference due to insufficient CP and due to the Doppler shift can be studied separately based on the delay-dispersive properties (beyond the CP length) and the time-selective channel properties, respectively. The latter falls out of the scope of the dissertation, which is focused on interference due to insufficient CP.

[8] multiple-input multiple-output

1.3.2 Determination of the interference due to insufficient CP: measurement techniques

This section provides an overview of different measurement techniques to determine the interference power due to insufficient CP (Section 1.3.2.1). Further, available studies providing experimental interference characterics are given (Section 1.3.2.2). Finally, a comparison is made with the approach followed in this dissertation (Section 1.3.2.3).

1.3.2.1 Overview of measurement techniques

In a **first approach**, the constellation error vector is detected by an **error vector magnitude** (EVM) measurement [50, 51]. The actual OFDM signal is generated by a Vector Signal Generator (VSG) and the received signal, which is distorted through the propagation channel, is detected by a vector signal analyzer (VSA). This signal is fed into an OFDM receiver simulator to evaluate the symbol error vector. Timing and frequency synchronization between VSG and VSA may be required [2]. A first disadvantage is that the measurement is specific for essential OFDM parameters such as the CP length and the FFT period. As a second disadvantage, the detected error vector is due to interference from any OFDM symbol (ISI and ICI) and from any subcarrier. To determine the spectral interference between all individual subcarriers, the error vector needs to be detected for a large variation of transmitted data symbols, which implies an increase of the measurement time.

In a **second approach, the propagation channel is experimentally characterized and included into an OFDM simulator or analytical framework** (e.g., using delay-domain weighting functions) to compute the interference due to insufficient CP. Several channel characterization techniques have been reported, classified into narrowband and wideband channel sounding depending on the bandwidth of the transmit signal [52].

Narrowband channel sounding is a frequency-domain characterization method. From the frequency response, the complex envelope of the channel impulse reponse (CIR) can be obtained by e.g. windowing and inverse discrete Fourier transformation (IDFT). Narrowband channel sounding is often performed by a vector network analyzer (VNA) [53]. In [54], the setup consists of a signal generator and a digitizer with frequency synchronization based on Global Positioning System (GPS) and the channel response is obtained by FFT processing. The major disadvantage of narrowband channel sounding (versus wideband) is the larger measurement time, which limits this technique to static channels [53]. Using a VNA, another disadvantage is the need for a phase-stable cable between VNA and remote antenna [53], which may become problematic for higher frequencies or a large Tx-Rx separation. An advantage is the low implementation effort, espe-

cially using a VNA, and the possibility to cover a large bandwidth [53].

For **wideband channel sounding**, several time-domain (i.e., delay-domain) characterization methods are reported. In earlier systems, the sounding signal was a periodic short time pulse, where the major disadvantage is the limited dynamic range as a result of the high peak-to-average power ratio [52, 53]. The dynamic range refers to the power ratio between the highest time-domain channel component and the weakest component that can be detected by the channel sounder system [52]. Most recent systems use a pulse compression technique [53], where the sounding signal is a pseudo-random time-domain sequence. The complex envelope of the channel impulse reponse is then obtained by cross-correlation between the received signal and the delay-shifted sounding signal [52]. A widely used sequence is the maximum-length pseudo-random sequence (*m*-sequence) [53] having excellent autocorrelation properties [52]. In [55], the preamble and header code is used as a pseudo-random sequence to implement channel sounding into IEEE 802.11b, which is based on direct-sequence spread-spectrum modulation. While some channel sounders use an analog-to-digital (A/D) convertor sampling at the Nyquist rate [53, 56], others are based on a sliding correlator [57]. In the latter, the (periodic) sequence at the receiver is generated at a slightly different rate, so that correlation processing yields the different time-domain channel components over subsequent sequence periods. As this technique requires a lower sampling rate, it allows a larger bandwidth, but at the cost of a larger measurement time [58]. Another issue is the time and frequency synchronization between transmitter and receiver [2], which requires a coaxial or fibre-optic cable connection [53], a line-of-sight connection to GPS satellites (outdoors) [2] or stable oscillator references [59]. The major limitation of wideband channel sounding is the bandwidth, imposing high-speed requirements on hardware such as the A/D convertor or sliding correlator [53]. To cover a higher bandwidth, a procedure for concatenation of the channel response over different frequency bands was applied in [53]. Moreover, using a pseudo-random binary sequence, the dynamic range is limited by the sequence length [52] and a larger sequence length (i.e., chip size) implies higher hardware requirements and a larger measurement time.

Wideband channel sounding techniques based on frequency-domain characterization are reported as well. As sounding signal, a periodic multi-frequency signal is used and after A/D sampling of the received signal, correlation processing yields the channel's frequency response [60, 61]. In [56], an OFDM-based channel sounder was proposed, where the channel response is detected from the FFT output at the receiver. The time-domain channel components are finally determined from the frequency response just as for narrowband channel sounding.

1.3.2.2 Studies on experimental characterization of the interference power due to insufficient CP

Although a channel impulse response longer than the CP length may severely degrade the channel capacity, only a few studies in literature report on the experimental characterization of the performance loss for specific channels. In [15], the interference due to insufficient CP was estimated for a 60 GHz channel in a hospital for IEEE 802.15.3c and IEEE 802.11ad OFDM. The channel response was measured over a 4 GHz bandwidth using a VNA and the signal-to-interference ratio (SIR) was analytically estimated from the CIR. For 802.15.3c and 802.11ad, 10th percentile SIR values as low as 4.9 dB and 14.2 dB, resp., were reported. In [18], the interference due to insufficient CP was investigated for mobile OFDM-based fourth-generation (4G) cellular communication systems. A multiple-antenna channel at 3.7 GHz in suburban and urban environments was measured over a 20 MHz bandwidth using an OFDM-based frequency-domain characterisation method. Using a frequency-domain channel estimator, the CIR was determined to estimate analytically the signal-to-interference-plus-noise ratio (SINR). It was shown that the CP length has a strong influence on the robustness against a timing offset of the FFT positioning. In [21,62], time-reversed channel shortening was investigated for underwater OFDM channels. The CIR was detected by correlation-based time-domain channel sounding using a linear frequency modulated transmit signal (i.e., chirp sounder) over a frequency band of the order of kHz. Including the CIR into an OFDM simulator, the performance was evaluated in terms of the bit error rate (BER), showing strong dependence on the CP length.

1.3.2.3 Comparison with the thesis' approach

In this dissertation, the approach followed is based on **frequency-domain channel characterization** and the time-domain channel components are obtained by windowing and an **IDFT**. Based on a general OFDM signal model, the interference power due to insufficient CP is computed based on an analytical framework involving the channel impulse response and time-domain weighting functions. This approach can be motivated as follows:

- the measurement is not specific for OFDM parameters such as the CP length and the FFT period, contrary to EVM measurements
- for most IEEE 802.11 indoor static channels, a low-cost implementation using a VNA is possible. In this work, measurements will be performed using a VNA, though the data processing methods presented are directly applicable to any frequency-domain channel sounding technique
- a high dynamic range is required for the determination of the interference due to insufficient CP. While for frequency-domain channel sounding, this

is in principle a matter of proper windowing, this is for time-domain channel characterization limited by the sequence length (i.e., the chip size) as used in the measurement [59].

1.4 Novelties of the dissertation

The substantial novelties obtained in this dissertation can be summarized as follows:

- CIR-based weighting functions for the interference coefficient due to insufficient CP for *general* OFDM parameters
- methodology for experimental detection of the interference coefficient from frequency-domain channel sounding:
  - novel windowing method based on a generalized representation of the interference coefficient
  - accuracy-aware selection criteria for measurement settings (frequency resolution, window width and number of acquisitions)
- concept of an effective noise factor describing the interference due to insufficient CP; closed-form expression as a function of the reverberation time
- analytical description of the spectral interference profile as a function of reverberation time
- experimental values for the loss factor caused by interference due to insufficient CP for large indoor environments and IEEE 802.11 OFDM
- path loss model (including shadowing) for the specific environment of a large conference room and IEEE 802.11; influence of humans during a meeting

1.5 Outline of the dissertation

The remainder of the dissertation is organized as follows.

Chapter 2 centres on the channel-based analysis of the interference coefficient due to insufficient CP. After a detailed description of the OFDM signal model, the CIR-based weighting functions for the interference coefficient are derived. Furthermore, a generalized representation of the interference coefficient is introduced.

Chapter 3 presents the theoretical background for the experimental detection of the interference coefficient from frequency-domain channel sounding. Various conventional and novel windowing methods are defined and a complete error analysis on the interference coefficient is provided. Further, APDP-based weighting functions for the interference power are determined. In addition, the required time window is determined based on room electromagnetics. Finally, an analysis of the error on the interference coefficient due to time resolution and due to leakage is carried out.

In **Chapter 4**, a performance analysis of the windowing methods is carried out with respect to the required measurement range and the performance is related to different window-related error types. This is based on a channel measurement in a large indoor environment for IEEE 802.11 OFDM. In addition, various measured interference characteristics are presented.

In **Chapter 5**, the limitations on the windowing methods caused by a time resolution and leakage are investigated. The implications on the measurement setting requirements (i.e., window width and frequency resolution) are discussed. The limitation through leakage is further discussed in terms of a maximum measurable signal-to-interference ratio (SIR).

In **Chapter 6**, the performance of the windowing methods is evaluated with respect to the processing time and the sensitivity to measurement noise. In addition, the error power reduction by averaging and the required number of sweeps (acquisitions) is investigated.

In **Chapter 7**, the concept of an effective noise factor is theoretically carried out for describing the interference due to insufficient CP for a slowly fading channel. Further, the spectral and the total interference power is analyzed in terms of the reverberation time based on the room electromagnetics theory. Experimental validation is performed based on channel measurements in large conference rooms and for typical IEEE 802.11 OFDM parameters.

In **Chapter 8**, path loss and shadowing is modeled based on channel measurements in large conference rooms for IEEE 802.11. The influence of the presence of humans is investigated. Based on this path loss model, the effect of typical IEEE 802.11n features (including frequency, bandwidth and MIMO configuration) on the required number of access points, total power consumption (due to radiation) and maximum (physical) throughput is investigated.

In **Chapter 9**, the dissertation's most important conclusions are highlighted and potential applications and future work are discussed.

1.6 Publications

1.6.1 A1

(publications in journals listed in the ISI Web of Science)

1. F. Heereman, W. Joseph, E. Tanghe, D. Plets, L. Verloock, and L. Martens, "Path loss model and prediction of range, power and throughput for 802.11n in large conference rooms," *AEÜ-International Journal of Electronics and Communications*, vol. 66, no. 7, pp. 561-568, Jul. 2012.

2. F. Heereman, W. Joseph, E. Tanghe, L. Verloock, and L. Martens, "Performance degradation due to multipath noise for narrowband OFDM systems: channel-based analysis and experimental determination," *IEEE Transactions on Wireless Communications*, vol. 14, no. 3, pp. 1396-1405, Mar. 2015.

3. F. Heereman, W. Joseph, E. Tanghe, and L. Martens, "Frequency-domain windowing methods for channel-based interference detection in CP-OFDM systems over time-dispersive channels," *IEEE Transactions on Communications*, *submitted.*

1.6.2 P1

(articles in conference proceedings listed in the ISI Web of Science)

1. F. Heereman, W. Joseph, E. Tanghe, D. Plets, and L. Martens, "Prediction of range, power consumption and throughput for IEEE 802.11n in large conference rooms," in *European Conference on Antennas and Propagation (EuCAP)*, Rome, Italy, Apr. 2011, pp. 692 - 696.

2. F. Heereman, W. Joseph, E. Tanghe, D. Plets, and L. Martens, "Development of path loss model for 802.11n in large conference rooms," in *IEEE International Symposium on Antennas and Propagation (APSURSI)*, Spokane, Washington, USA, Jul. 2011, pp. 2785 - 2788.

3. F. Heereman, W. Joseph, E. Tanghe, D. Plets, and L. Martens, "Small-scale fading and delay in conference room with 802.11 coverage problems", in *European Conference on Antennas and Propagation (EuCAP)*, Prague, Czech Republic, Mar. 2012, pp. 2021 - 2024.

4. F. Heereman, W. Joseph, E. Tanghe, D. Plets, A. Bamba, L. Verloock and L. Martens, "Performance loss due to multipath propagation for IEEE 802.11

systems," in *European Conference on Antennas and Propagation (EuCAP)*, Gothenburg, Sweden, Apr. 2013, pp. 2610-2613.

5. F. Heereman, W. Joseph, and L. Martens, "Analysis of 802.11 OFDM in high multipath environments," in *IEEE Vehicular Technology Conference (VTC Spring)*, Glasgow, Scotland, U.K., May 2015, pp. 1-4.

1.6.3 C3

(other conference contributions)

1. F. Heereman, W. Joseph, and L. Martens, "Performance loss due to diffuse multipath for IEEE 802.11 systems", in *BESTCOM meeting*, Leuven, Belgium, Oct. 2013.

2. F. Heereman, W. Joseph, and L. Martens, "Performance loss due to diffuse multipath for IEEE 802.11 systems", in *UGent - 14th FEA PhD Symposium*, Ghent, Belgium, Dec. 2013.

3. F. Heereman, W. Joseph, and L. Martens, "Analysis of 802.11 OFDM in high multipath environments", in *European Conference on Antennas and Propagation (EuCAP)*, The Hague, The Netherlands, Apr. 2014, pp. 2507-2508.

2

Interference due to insufficient CP: channel-based analysis

In this chapter, an analytical framework is developed to relate the interference due to insufficient CP to the channel. Based on an idealized OFDM system, the constellation error vector due to insufficient CP is analytically determined by means of *interference coefficients*. These interference coefficients describe the interference between individual subcarriers and OFDM symbols and determine the corresponding additive contribution to the constellation error vector. The interference coefficients are analytically related to the channel impulse response (CIR) by delay-domain *weighting functions*, which describe the contribution of each channel component to the interference coefficient. The analytical framework is applicable for a general OFDM technology and specific implications for IEEE 802.11 are discussed in addition.

Further, the weighting functions proposed in this section are compared with another weighting function proposed in [1]. While the weighting function proposed in this dissertation is based on the *CIR* and determines the *interference coefficient*, the weighting function proposed in [1] is based on the *averaged power delay profile* (APDP) and determines directly the *total interference power*. Finally, the signal-to-interference-plus-noise ratio (SINR), which can be considered as a performance metric, is analytically related to the interference coefficient.

This chapter is structured as follows:

- Section 2.1: idealized OFDM system: assumptions and mathematical signal

model

- Section 2.2: analytical framework relating the error vector due to insufficient CP to the channel impulse response
- Section 2.3: error vector due to insufficient CP for IEEE 802.11
- Section 2.4: comparison with APDP-based weighting function for total interference power proposed in [1]
- Section 2.5: SINR including interference due to insufficient CP

2.1 OFDM signal model

This section describes the *idealized* OFDM system, which is used for the channel-based analysis of the interference due to insufficient CP (Section 2.2). In the *idealized* OFDM system, two impairements are considered: white Gaussian noise (AWGN) and interference due to insufficient CP (also referred to as multipath noise). The latter refers to the constellation error vector caused by insufficient CP. For the determination of this error vector, no other hardware-related imperfections are explicitly considered [63] - [65]. At the transmitter, a rectangular transmit pulse and an idealized digital-to-analog convertor (DAC) with an infinitely small resolution are considered. At the receiver side, it is assumed that there are no imperfections such as phase noise, I/Q imbalance or non-linearities. Further, it is assumed that any carrier or clock frequency offset is perfectly compensated by an idealized frequency synchronization. The finite bandwidth of the receiver's channel select filter and thus a non-zero sampling period are taken into account in the OFDM model. Further, all filters and amplifiers are assumed to be flat (over the channel bandwidth). An analog-to-digital converter (ADC) with an infinitely small resolution is considered. This assumption, which implies no discretization of the analog signal, is reasonable, because the I/Q signal is adapted to the input range of the ADC by the variable gain amplifier (VGA) and the constellation error vector is of the same order of the signal when a symbol error occurs. A one-tap frequency-domain equalization (FEQ) without ISI/ICI cancellation is considered. Moreover, a perfect channel estimation is assumed. Concerning the propagation channel, it is assumed that there is no Doppler shift and that the channel is static during each OFDM packet. A mathematical model of the idealized OFDM system is given in Sections 2.1.1 and 2.1.2. In the idealized OFDM system, it is further assumed that the FFT window positioning is near-optimal (Section 2.1.3), approaching the best-case situation of the smallest interference due to insufficient CP. In practice, the interference due to insufficient CP is highly dependent on the FFT window positioning, which may be impaired by the delay spread of the channel [4]. Then, the effect of a timing offset corresponds to an effective decrease of the CP length.

2.1.1 Transmitter and channel

The (normalized) data symbols $\tilde{X}_{m,k,i}$ to be transmitted are modulated as follows [14, 63]. Note that integer m is an index referring to the OFDM packet, integer k is an index referring to the OFDM symbol and integer i is the subcarrier index ($i = -N_{\mathrm{subc}}, -N_{\mathrm{subc}}+1, ..., N_{\mathrm{subc}}$, where N_{subc} is a positive integer). For practical systems, an inverse fast Fourier transform (IFFT) is usually applied, after which the CP is inserted (Fig. 2.1). After digital-to-analog conversion (DAC), the analog signal is typically filtered to achieve orthogonal analog subcarrier signals. In the *idealized* signal model used in the dissertation, it is assumed that perfect

analog harmonic signals are obtained for the different subcarriers, as proposed in [14]. Finally, the signal is upconverted to the carrier frequency of the channel, f_c, and amplified.

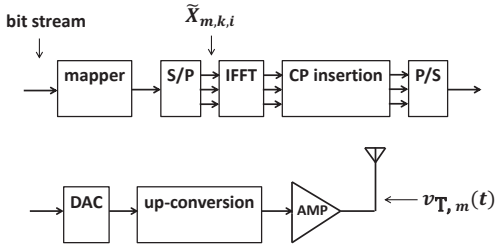

Figure 2.1: Block diagram of the OFDM transmitter.

Mathematically, the transmitted (voltage) signal for OFDM packet m, $v_{\mathrm{T},m}(t)$ [V], as a function of the time t is described by:

$$\begin{aligned} v_{\mathrm{T},m}(t) = g_\mathrm{T} \sum_k \sum_{i=-N_\mathrm{subc}}^{N_\mathrm{subc}} \Re\Bigg[& \tilde{X}_{m,k,i} \exp(j\omega_\mathrm{c} t) \\ & \times \exp\Big(ji\Delta\omega_\mathrm{subc}(t - k(D_\mathrm{FFT} + D_\mathrm{CP}))\Big) \\ & \times \Bigg(\mathrm{U}\Big(t + D_\mathrm{CP} - k(D_\mathrm{FFT} + D_\mathrm{CP})\Big) \\ & - \mathrm{U}\Big(t - D_\mathrm{FFT} - k(D_\mathrm{FFT} + D_\mathrm{CP})\Big)\Bigg)\Bigg], \end{aligned} \tag{2.1}$$

where $\Re[\,\cdot\,]$ indicates the real part of a complex number, j is the imaginary unit, $\omega_\mathrm{c} = 2\pi f_\mathrm{c}$, U$(\,\cdot\,)$ is the unit step function, D_FFT is the FFT duration or integration time, D_CP is the CP length, and $\Delta\omega_\mathrm{subc}$ is the subcarrier spacing in the (angular) frequency domain: $\Delta\omega_\mathrm{subc} = 2\pi/D_\mathrm{FFT}$. g_T [V] is a factor taking into account the amplification in the transmitter circuit and is related to the transmit power per subcarrier.

The channel is assumed to be static during one OFDM packet. For each OFDM packet m, the channel is described by the frequency response $C_m(\omega)$. The corresponding received signal is then determined by

$$v_{\mathrm{R},m}(t) = \int_{-\infty}^{\infty} c_{\mathrm{tot},m}(\tau)\, v_{\mathrm{T},m}(t-\tau)\,\mathrm{d}\tau, \tag{2.2}$$

where $c_{\mathrm{tot},m}(\tau)$ is the total impulse reponse, including the channel and the channel select filter of the receiver. $c_{\mathrm{tot},m}(\tau)$ is the inverse continuous Fourier transform of

the channel response, $C_m(\omega)$, multiplied by the frequency response of the channel select filter centered around the carrier frequency, i.e., $H_{\rm filt}(\omega - \omega_{\rm c})$.

2.1.2 Receiver

The signal processing of the receiver is schematically shown in Fig. 2.2 [14,63,66]. The received signal passes through a band-select filter and a low-noise amplifier (LNA). After down-conversion to baseband, the I/Q signals pass through a channel select-filter and a variable gain amplifier (VGA), which is controlled by the automatic gain control (AGC). The resulting signal, with complex representation $v_{\rm R,I/Q,}{}_m(t)$, is sampled by an analog-to-digital converter (ADC). After removing the CP and a serial-to-parallel conversion (S/P), a fast Fourier transform (FFT) is applied. It is assumed that a one-tap frequency-domain equalization (FEQ) is applied on the FFT output, $Y_{m,k,i}$. After parallel-to-serial conversion (P/S), the resulting equalized symbols, $\tilde{Y}_{m,k,i}$, are demodulated by the OFDM demapper.

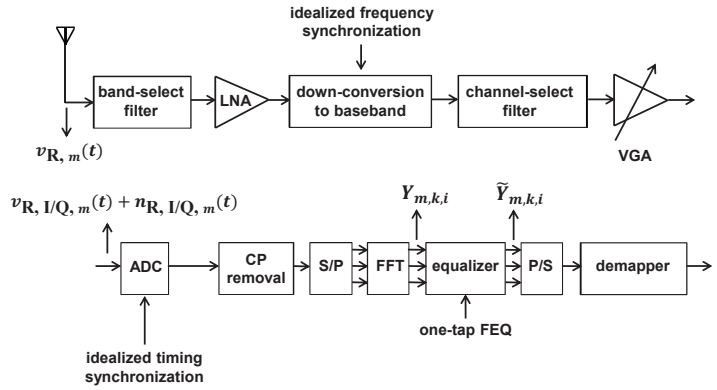

Figure 2.2: Block diagram of the OFDM receiver.

A mathematical model is given as follows. $v_{\rm R,I/Q,}{}_m(t)$ is obtained by amplification and down-conversion to baseband of $v_{\rm R,}{}_m(t)$. The FFT output $Y_{m,k,i}$ is determined by the DFT of the sampled OFDM signal:

$$Y_{m,k,i} = \sum_{l=0}^{N_{\rm sample}-1} \big(v_{\rm R,I/Q,}{}_m(t_{k,l}) + n_{\rm R,I/Q,}{}_m(t_{k,l})\big) \times \exp(-j2\pi i\, l/N_{\rm sample}). \tag{2.3}$$

Here, $t_{k,l} = t_{\rm win,0} + k(D_{\rm FFT} + D_{\rm CP}) + lD_{\rm FFT}\, N_{\rm sample}^{-1}$, where $t_{\rm win,0}$ is the start instant of the FFT window for OFDM symbol $k = 0$ and $N_{\rm sample}$ is the FFT size. The near-optimal $t_{\rm win,0}$ will be determined in the following section. In Eq. 2.3,

$n_{\mathrm{R,I/Q},m}(t)$ is the contribution to the I/Q signal due to the AWGN (not related to the propagation channel) [65], described by a noise factor F_{AWGN} [67].

The equalized FFT output, $\tilde{Y}_{m,k,i}$, is obtained by dividing the FFT output by the channel estimation, $H_{m,k,i}$. Taking into account that the channel estimation is based on training symbols with a large CP length compared to the data OFDM symbols [14], errors on $H_{m,k,i}$ due to an insufficient CP length are completely negligible (i.e., perfect channel estimation). In this case, $H_{m,k,i}$ is easily determined as proportional to the channel response:

$$H_{m,k,i} = g_{\mathrm{T}} N_{\mathrm{sample}} \exp\Big(j2\pi D_{\mathrm{FFT}}^{-1} i \Delta t_{\mathrm{win},0}\Big) C_{\mathrm{tot},m}(\omega_i) \tag{2.4}$$

where $C_{\mathrm{tot},m}(\omega)$ is the frequency response of the total channel (cascade of transmission channel and channel select filter). $\Delta t_{\mathrm{win},0}$ is a time parameter indicating the FFT window positioning and is defined as the start time of the FFT window in reference to the start time of the FFT period of the transmitted OFDM symbol. Finally, the symbol error vector $\Delta\tilde{Y}_{m,k,i}$, as detected by the demapper, is determined by $\Delta\tilde{Y}_{m,k,i} = \tilde{Y}_{m,k,i} - \tilde{X}_{m,k,i}$.

2.1.3 Near-optimal FFT window positioning

In this section, a *near-optimal* FFT window positioning, yielding approximately the smallest interference due to insufficient CP, is proposed. Although the channel-based analysis of the interference due to insufficient CP in Section 2.2 is worked out for a general FFT window positioning, a certain FFT window positioning should still be selected when the interference is being experimentally determined based on a measured channel. In this dissertation, the interest is on the experimental characterization of the interference power assuming an *idealized* FFT window positioning, yielding the smallest interference due to an insufficient CP. As the interference power is dependent on the FFT window positioning and the specific channel, the *exact* optimal positioning should be determined by optimization of the experimental interference power as a function of the window positioning time parameter. However, assuming that the power of the channel impulse response is concentrated at the minimum delay (such as in a line-of-sight condition), a near-optimal FFT window positioning can be determined in a standardized way which only depends on the minimum delay of the channel. This allows a simplified and standardized way of experimental characterization of the interference power.

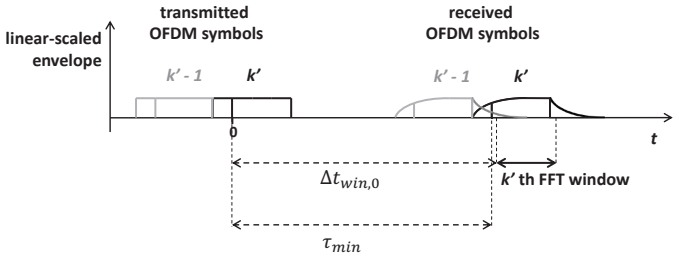

Figure 2.3: Schematical (linear-scaled) envelope of two successive OFDM symbols as transmitted and as received time signals. The near-optimal FFT window positioning proposed is given by $\Delta t_{\mathrm{win},0} = \tau_{\mathrm{min}} + D_{\mathrm{FFT}}\, N_{\mathrm{sample}}^{-1}$.

The FFT window positioning is determined by a time parameter $\Delta t_{\mathrm{win},0}$, defined as the start time of the FFT window in reference to the start time of the FFT period of the transmitted OFDM symbol. This is illustrated in Fig. 2.3. Fig. 2.3 schematically shows two successive OFDM symbols as transmitted and as received. Assuming that the OFDM symbol is not distorted by the channel select filter, a near-optimal FFT window positioning is obtained when

$$\Delta t_{\mathrm{win},0} = \tau_{\mathrm{min}} + D_{\mathrm{FFT}}\, N_{\mathrm{sample}}^{-1} \tag{2.5}$$

where τ_{min} is the minimum delay of the channel impulse response (i.e., the delay of the first arriving propagation path). This means that the last time sample used for the k'th FFT (Eq. 2.3) coincides with the start instant of the received OFDM symbol with index $k' + 1$. In Eq. 2.5, the sampling period, $D_{\mathrm{FFT}}\, N_{\mathrm{sample}}^{-1}$, is added because the last time point of the FFT period is not effectively used for FFT computation (Eq. 2.3).

The proposed near-optimal FFT window positioning can be motivated as follows (see Fig. 2.3). When $\Delta t_{\mathrm{win},0} < \tau_{\mathrm{min}} + D_{\mathrm{FFT}}\, N_{\mathrm{sample}}^{-1}$, the distortion of the OFDM symbol k' (in the beginning of the FFT window) becomes higher compared to the near-optimal positioning (Fig. 2.3), resulting into a higher ICI. Moreover, there would be a higher ISI with the preceding OFDM symbol $(k' - 1)$. On the other hand, when $\Delta t_{\mathrm{win},0} > \tau_{\mathrm{min}} + D_{\mathrm{FFT}}\, N_{\mathrm{sample}}^{-1}$, the received OFDM symbol k' would be highly distorted at the end of the FFT window, causing ICI. Moreover, the following OFDM symbol $(k' + 1)$ would overlap with the FFT window for OFDM symbol k', which causes severe ISI.

The channel select filter causes the received OFDM signal to be smoothed around the end instant of the FFT window, $t = \tau_{\mathrm{min}} + D_{\mathrm{FFT}}$, with a time resolution of the order of the sampling period, $D_{\mathrm{FFT}}\, N_{\mathrm{sample}}^{-1}$ (being the inverse of the bandwidth). Consequently, this will cause ICI and ISI with the following OFDM symbol if $\Delta t_{\mathrm{win},0} = \tau_{\mathrm{min}} + D_{\mathrm{FFT}}\, N_{\mathrm{sample}}^{-1}$. On the other hand, if the FFT window is positioned at $\Delta t_{\mathrm{win},0} = \tau_{\mathrm{min}}$, the interference at the end of the FFT window

will be strongly reduced, but at the beginning of the window, the signal distortion will be higher. However, this effect of the channel select filter is not taken into account in determining a near-optimal FFT window positioning. Consequently, a near-optimal FFT window positioning is given by Eq. 2.5.

2.2 Channel-based analysis of the interference due to insufficient CP

In this section, the error vector due to insufficient CP is analytically derived in terms of the channel impulse response and (delay-domain) weighting functions. Section 2.2.1 presents a summary of the detailed derivation given in Appendix A and provides the results, including the definition of the weighting functions and the interference coefficients and their relation to the error vector due to insufficient CP. In Section 2.2.2, the error vector is approximated by neglecting the aliasing effect.

2.2.1 CIR-based weighting functions for the interference coefficient

The equalized error vector due to insufficient CP, $\Delta\tilde{Y}_{\mathrm{delay},k',i'}$, is analytically determined based on the OFDM signal model described in Section 2.1. The error vector is treated per OFDM packet and the packet index m will be omitted for reasons of clarity. **The detailed derivation given in Appendix A is summarized as follows.** The received signal, $v_{\mathrm{R,I/Q}}(t)$ (Eq. 2.2), is over the FFT window decomposed into a Fourier series to evaluate how initially harmonic subcarrier signals interfere with each other after transmission through the time-dispersive channel. This is the total channel, concerning the cascade of the channel select filter and the transmission channel and is characterized by an impulse reponse $c_{\mathrm{tot}}(\tau)$. However, as a result of the distortion, the received signal has a different value at the start and the end of the FFT integration interval. Therefore, a correction must be made in order that the Fourier series decomposition of the received signal is also valid at the first sample, i.e., at time instant $t_{k',0}$. To counter this issue, the FFT output is divided into two terms: (i) a discrete Fourier transform (DFT) with a symmetrical weighting at the borders of the FFT interval and (ii) a remaining correction term. The first term can then be determined in terms of the Fourier series coefficients of the continuous received signal over the FFT interval. These Fourier coefficients can be easily obtained as the time-domain integration of a harmonic (rectangular-shaped) subcarrier signal partially overlapping the FFT interval. Finally, the FFT output is equalized by an idealized one-tap scheme and the equalized symbol error vector is obtained by subtracting the errorless (equalized) FFT output, $\tilde{X}_{k',i'}$ from the actual equalized FFT output.

Further, the following definitions are made. The ***OFDM symbol separation***, Δk, is defined by $k' - k$ and the ***subcarrier separation***, Δi, by $i' - i$. The Δkth ***interference delay interval*** is defined as the interval involving all delays that contribute to the FFT output through an interference process with an OFDM symbol separation Δk. This is illustrated in Fig. 2.4. The start delay of the interference

delay interval, $\tau_{\mathrm{int},1,\Delta k}$, is determined by

$$\tau_{\mathrm{int},1,\Delta k} = \Delta t_{\mathrm{win},0} - D_{\mathrm{FFT}} + \Delta k(D_{\mathrm{FFT}} + D_{\mathrm{CP}}) \tag{2.6}$$

where $\Delta t_{\mathrm{win},0}$ is a time parameter indicating the FFT window positioning and is defined as the start time of the FFT window in reference to the start time of the FFT period of the transmitted OFDM symbol (Fig. 2.4). The interference delay interval can be divided up into 3 subintervals of type A, B and C, defined by:

$$\begin{cases} \text{(A)} & \tau \in [\tau_{\mathrm{int},1,\Delta k};\, \tau_{\mathrm{int},1,\Delta k} + D_{\mathrm{FFT}}] \\ \text{(B)} & \tau \in [\tau_{\mathrm{int},1,\Delta k} + D_{\mathrm{FFT}};\, \tau_{\mathrm{int},1,\Delta k} + D_{\mathrm{FFT}} + D_{\mathrm{CP}}] \\ \text{(C)} & \tau \in [\tau_{\mathrm{int},1,\Delta k} + D_{\mathrm{FFT}} + D_{\mathrm{CP}};\, \tau_{\mathrm{int},1,\Delta k} + 2D_{\mathrm{FFT}} + D_{\mathrm{CP}}] \end{cases} \tag{2.7}$$

The meaning of these subintervals is illustrated in Fig. 2.4. A delay from subinterval A leads to a *left-hand partial* overlap between the received replica of the transmit signal and the FFT window. A delay from subinterval B results into a *complete* overlap and a delay from subinterval C gives a *right-hand partial* overlap.

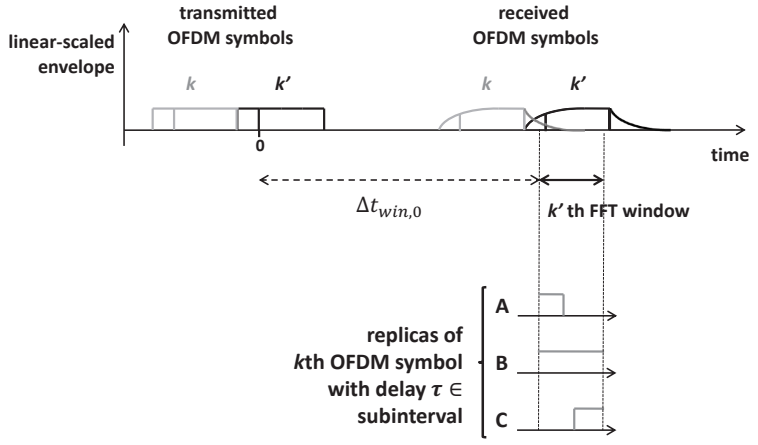

Figure 2.4: Schematical illustration of transmitted and received OFDM symbols. The received signal is a superposition of replicas of the transmit signal with different delays, which are classified into 3 subintervals types depending on the extent of overlap with the FFT window: type A (left-hand partial overlap), type B (complete overlap) and type C (right-hand partial overlap).

From Appendix A, the equalized error vector due to insufficient CP at the k'th

OFDM symbol and the i'th subcarrier, $\Delta\tilde{Y}_{\mathrm{delay},k',i'}$ is determined as follows:

$$\Delta\tilde{Y}_{\mathrm{delay},k',i'} = \frac{1}{C_{\mathrm{tot}}(\omega_{i'})} \sum_{k} \sum_{i} \tilde{X}_{k,i} \exp\Big(j2\pi D_{\mathrm{FFT}}^{-1}(i\tau_{\mathrm{int},1,\Delta k} - i'\tau_{\mathrm{int},1,0})\Big) \times \left(y_{\mathrm{corr},k'-k}(\omega_i) + \sum_{n=-\infty}^{\infty} y_{\mathrm{Four},i'-i+nN_{\mathrm{sample}},k'-k}(\omega_i) \right) \tag{2.8}$$

In Eq. 2.8, the ***Fourier-type interference coefficient***, $y_{\mathrm{Four},\Delta i,\Delta k}(\omega)$, is defined (for general Δi) by means of the weighting function $g_{\mathrm{Four},\Delta i}(\tau)$:

$$\begin{cases} y_{\mathrm{Four},\Delta i,\Delta k}(\omega) = \int\limits_{-\infty}^{\infty} g_{\mathrm{Four},\Delta i}(\tau - \tau_{\mathrm{int},0,\Delta k}) c_{\mathrm{tot}}(\tau) \exp(-j\omega\tau)\, \mathrm{d}\tau \\ \qquad\qquad \big(\text{for } \{\Delta i; \Delta k\} \neq \{0;0\}\big) \\ y_{\mathrm{Four},\Delta i,\Delta k}(\omega) = \int\limits_{-\infty}^{\infty} \big(g_{\mathrm{Four},\Delta i}(\tau - \tau_{\mathrm{int},0,\Delta k}) - 1\big) c_{\mathrm{tot}}(\tau) \exp(-j\omega\tau)\, \mathrm{d}\tau \\ \qquad\qquad \big(\text{for } \Delta i = \Delta k = 0\big) \end{cases} \tag{2.9}$$

In Eq. 2.8, the ***correction-type interference coefficient***, $y_{\mathrm{corr},\Delta k}(\omega)$, is defined by means of the weighting function $g_{\mathrm{corr}}(\tau)$:

$$y_{\mathrm{corr},\Delta k}(\omega) = \int\limits_{-\infty}^{\infty} g_{\mathrm{corr}}(\tau - \tau_{\mathrm{int},0,\Delta k}) c_{\mathrm{tot}}(\tau) \exp(-j\omega\tau)\, \mathrm{d}\tau \tag{2.10}$$

$C_{\mathrm{tot}}(\omega_{i'})$ represents the frequency response of the total channel at the (angular) frequency of the detecting subcarrier i', $\omega_{i'}$, which is defined as $\omega_{\mathrm{c}} + i'\Delta\omega_{\mathrm{subc}}$. ω_i is analogously defined for the source subcarrier. The delay shift parameter $\tau_{\mathrm{int},0,\Delta k}$ is defined by $\tau_{\mathrm{int},1,\Delta k} + D_{\mathrm{FFT}}$. In essence, Eqs. 2.9 and 2.10 mean that **the interference coefficient is determined as the continuous Fourier transform of the channel impulse reponse multiplied by a weighting function evaluated at the source subcarrier frequency.**

The weighting functions $g_{\mathrm{corr}}(\tau)$ and $g_{\mathrm{Four},\Delta i}(\tau)$ are defined in Tables 2.1 and 2.2 and are plotted in Fig. 2.5. The function $g_{0,\Delta i}(\tau)$ is defined for $0 < \tau < D_{\mathrm{FFT}}$ by

$$g_{0,\Delta i}(\tau) = \frac{j}{2\pi\Delta i}\Big(\exp(-j\Delta i\Delta\omega_{\mathrm{subc}}\tau) - 1\Big). \tag{2.11}$$

In the notation of the Fourier-type interference coefficient, $y_{\mathrm{Four},\Delta i,\Delta k}$, "Four" refers to the fact that these coefficients are related to the decomposition of the received signal over the FFT window into a Fourier series. This contribution to

Table 2.1: The weighting function $g_{\mathrm{corr}}(\tau)$ defined per subinterval (1)-(5).

subinterval type	$g_{\mathrm{corr}}(\tau) =$
(1) $\tau < -D_{\mathrm{FFT}}$	0
(2) $-D_{\mathrm{FFT}} \leq \tau \leq 0$ (A)	$1/(2N_{\mathrm{sample}})$
(3) $0 < \tau < D_{\mathrm{CP}}$ (B)	0
(4) $D_{\mathrm{CP}} \leq \tau \leq D_{\mathrm{CP}} + D_{\mathrm{FFT}}$ (C)	$-1/(2N_{\mathrm{sample}})$
(5) $D_{\mathrm{CP}} + D_{\mathrm{FFT}} < \tau$	0

Table 2.2: The weighting function $g_{\mathrm{Four},\Delta i}(\tau)$ defined per subinterval (1)-(5).

	$\Delta i = 0$	$\Delta i \neq 0$
(1)	0	0
(2)	$\tau/D_{\mathrm{FFT}} + 1$	$g_{0,\Delta i}(\tau + D_{\mathrm{FFT}})$
(3)	1	0
(4)	$(D_{\mathrm{CP}} - \tau)/D_{\mathrm{FFT}} + 1$	$-g_{0,\Delta i}(\tau - D_{\mathrm{CP}})$
(5)	0	0

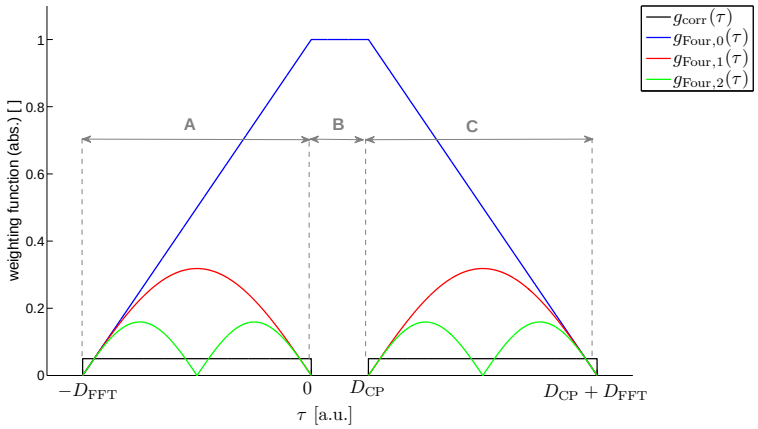

Figure 2.5: Weighting functions (in absolute value) for correction-type and Fourier-type interference coefficient, $g_{\mathrm{corr}}(\tau)$ and $g_{\mathrm{Four},\Delta i}(\tau)$, respectively, for different subcarrier separation Δi. All functions are depicted at scale, except $g_{\mathrm{corr}}(\tau)$. Subintervals (2), (3) and (4) correspond to the subintervals of type A, B and C, resp., of the interference delay interval.

the error vector corresponds to the case of an infinite sample rate. In the notation of correction-type interference coefficient type, $y_{\mathrm{corr},\Delta k}$, "corr" indicates that this is a correction term due to the finite sample rate. In Eq. 2.8, the Fourier-type interference coefficients for $n \neq 0$ are due to the aliasing effect related to the finite FFT size (N_{sample}).

In Eq. 2.8, the error term proportional to data symbol $\tilde{X}_{k',i'}$ ($\Delta k = 0$ and $\Delta i = 0$) originates from the fact that the channel estimation is assumed to be ideal, i.e., detected in the training sequence with an infinitely large CP length, while the FFT output is based on a finite CP length. Error terms proportional to a data symbol $\tilde{X}_{k,i}$ of the current OFDM symbol ($\Delta k = 0$) and any other subcarrier ($\Delta i \neq 0$) are referred to as *intercarrier interference* (ICI). Error terms proportional to a data symbol $\tilde{X}_{k,i}$ of any other OFDM symbol ($\Delta k \neq 0$) are referred to as *intersymbol interference* (ISI).

2.2.2 Generalized representation of Fourier-type interference coefficient - Error vector with neglecting the aliasing effect

In Eq. 2.8, which determines the error vector $\Delta\tilde{Y}_{\mathrm{delay},k',i'}$, a series of aliased Fourier-type interference coefficients appears (aliasing effect):

$$\sum_{n\neq 0} y_{\mathrm{Four},i'-i+nN_{\mathrm{sample}},\Delta k}(\omega_i) \tag{2.12}$$

In this section, an approximation of the error vector is derived neglecting these aliased terms. These aliased Fourier-type interference coefficients are related to a "virtual" detecting subcarrier at a frequency $\omega_{i'+nN_{\mathrm{sample}}}$, which lies *outside* the actual bandwidth of the OFDM system, and a source subcarrier at a frequency ω_i, lying *in* the actual bandwidth. To address this, the Fourier-type interference coefficient for a non-zero Δi is first decomposed into two terms each related to the respective frequency (*generalized representation*) in Section 2.2.2.1. The approximative expression for the error vector is motivated in Section 2.2.2.2 and the expression is given as a conclusion in Section 2.2.2.3.

2.2.2.1 Generalized representation of the Fourier-type interference coefficient

The decomposition of the Fourier-type interference coefficient (for a non-zero Δi) is done for subintervals A and C of the interference delay interval separately. For the subinterval B, there is no contribution to the Fourier-type interference coefficient (for a non-zero Δi), as follows from the definition of the weighting function (Table 2.2).

The contributions to the Fourier-type interference coefficient due to subintervals A and C are denoted by $y_{\mathrm{Four},\Delta i,\Delta k;\mathrm{A}}(\omega_i)$ and $y_{\mathrm{Four},\Delta i,\Delta k;\mathrm{C}}(\omega_i)$, respectively. E.g. for $y_{\mathrm{Four},\Delta i,\Delta k;\mathrm{A}}(\omega_i)$, the decomposition (for a non-zero Δi) is accomplished as follows. From Eq. 2.9, Table 2.2 and Eq. 2.11, it follows that

$$\begin{aligned} y_{\mathrm{Four},\Delta i,\Delta k;\mathrm{A}}(\omega_i) = \frac{j}{2\pi\Delta i} \int_{-\infty}^{\infty} & \Big(\mathrm{U}(\tau-\tau_{\mathrm{int},1,\Delta k}) - \mathrm{U}(\tau-\tau_{\mathrm{int},1,\Delta k}-D_{\mathrm{FFT}})\Big) \\ & \times \Big(\exp\big(-j2\pi\Delta i D_{\mathrm{FFT}}^{-1}(\tau-\tau_{\mathrm{int},1,\Delta k})\big)-1\Big) \\ & \times c_{\mathrm{tot}}(\tau)\exp(-j\omega_i\tau)\,\mathrm{d}\tau \end{aligned} \tag{2.13}$$

$$\begin{aligned} = K_{\mathrm{Four},\Delta i;\mathrm{A}} \Bigg[& \int_{-\infty}^{\infty} g_{\mathrm{un}}(\tau-\tau_{\mathrm{int},0,\Delta k}) c_{\mathrm{tot}}(\tau)\exp(-j\omega_i\tau)\,\mathrm{d}\tau \\ - \delta_{\mathrm{Four},\Delta i,\Delta k;\mathrm{A}} & \int_{-\infty}^{\infty} g_{\mathrm{un}}(\tau-\tau_{\mathrm{int},0,\Delta k}) c_{\mathrm{tot}}(\tau)\exp(-j\omega_{i'}\tau)\,\mathrm{d}\tau \Bigg] \end{aligned} \tag{2.14}$$

where

$$K_{\mathrm{Four},\Delta i;\mathrm{A}} = (j2\pi\Delta i)^{-1} \tag{2.15a}$$

$$\delta_{\mathrm{Four},\Delta i,\Delta k;\mathrm{A}} = \exp(j2\pi\Delta i\tau_{\mathrm{int},1,\Delta k}/D_{\mathrm{FFT}}) \tag{2.15b}$$

The weighting function $g_{\mathrm{un}}(\tau)$ is defined by

$$g_{\mathrm{un}}(\tau) = \mathrm{U}(\tau+D_{\mathrm{FFT}}) - \mathrm{U}(\tau), \tag{2.16}$$

where $\mathrm{U}(\,\cdot\,)$ is unit step function. For subinterval C, the decomposition is similar.

Conclusion:

As a conclusion, the generalized representation of $y_{\mathrm{Four},\Delta i,\Delta k;\mathrm{A}}(\omega_i)$ and $y_{\mathrm{Four},\Delta i,\Delta k;\mathrm{C}}(\omega_i)$ is given by:

$$y_{\mathrm{Four},\Delta i,\Delta k;\mathrm{A}}(\omega_{\mathrm{s}}) = K_{\mathrm{Four},\Delta i;\mathrm{A}}\big(\tilde{y}_{\Delta k}(\omega_{\mathrm{s}}) - \delta_{\mathrm{Four},\Delta i,\Delta k;\mathrm{A}}\ \tilde{y}_{\Delta k}(\omega_{\mathrm{d}})\big) \tag{2.17a}$$

$$y_{\mathrm{Four},\Delta i,\Delta k;\mathrm{C}}(\omega_{\mathrm{s}}) = K_{\mathrm{Four},\Delta i;\mathrm{C}}\big(\tilde{y}_{\Delta k+1}(\omega_{\mathrm{s}}) - \delta_{\mathrm{Four},\Delta i,\Delta k;\mathrm{C}}\ \tilde{y}_{\Delta k+1}(\omega_{\mathrm{d}})\big) \tag{2.17b}$$

where ω_{s} and ω_{d} denote the (angular) source and detecting subcarrier frequency, resp.: $\omega_{\mathrm{d}} = \omega_{\mathrm{s}} + 2\pi\Delta i D_{\mathrm{FFT}}^{-1}$. The *generalized interference coefficient*, $\tilde{y}_{\Delta k}(\omega)$, is defined on the basis of a rectangular weighting function, $g_{\mathrm{un}}(\tau)$:

$$\tilde{y}_{\Delta k}(\omega) = \int_{-\infty}^{\infty} g_{\mathrm{un}}(\tau-\tau_{\mathrm{int},0,\Delta k}) c_{\mathrm{tot}}(\tau)\exp(-j\omega\tau)\,\mathrm{d}\tau, \tag{2.18}$$

The coefficients appearing in Eqs. 2.17a and 2.17b are resp. defined by Eqs. 2.15a–2.15b and by

$$K_{\mathrm{Four},\Delta i;\mathrm{C}} = -(j2\pi\Delta i)^{-1} \tag{2.19a}$$

$$\delta_{\mathrm{Four},\Delta i,\Delta k;\mathrm{C}} = \exp(j2\pi\Delta i(\tau_{\mathrm{int},1,\Delta k} + D_{\mathrm{CP}})/D_{\mathrm{FFT}}) \tag{2.19b}$$

2.2.2.2 Neglecting of aliased Fourier-type interference coefficients

From Eq. 2.18 and considering the rectangular profile of the weighting function, it follows that $\tilde{y}_{\Delta k}(\omega)$ is approximately only related to the channel frequency reponse ($C_{\mathrm{tot}}(\omega)$) *around* ω. It is assumed that the corresponding frequency width is much smaller than the bandwidth of the OFDM system. Assuming also an *idealized* channel select filter, with a frequency-flat response over the bandwidth and a zero response outside the bandwidth, this implies that the terms $\tilde{y}_{\Delta k}(\omega_{\mathrm{d}})$ corresponding to "virtual" subcarriers outside the actual bandwidth of the OFDM system can be neglected. Substituting Eq. 2.17a into Eq. 2.12 (concerning subinterval A), one obtains

$$\sum_{n\neq 0} y_{\mathrm{Four},i'-i+nN_{\mathrm{sample}},\Delta k;\mathrm{A}}(\omega_i) \approx \sum_{n\neq 0} K_{\mathrm{Four},i'-i+nN_{\mathrm{sample}};\mathrm{A}} \tilde{y}_{\Delta k}(\omega_{\mathrm{s}}) \tag{2.20}$$

$$\approx \frac{-j}{\pi N_{\mathrm{sample}}} \sum_{n>0} \frac{x}{x^2-n^2} \tilde{y}_{\Delta k}(\omega_{\mathrm{s}}) \tag{2.21}$$

where $x = \Delta i/N_{\mathrm{sample}}$ and Eq. 2.15a is substituted into Eq. 2.20 to obtain Eq. 2.21. An expression analogous to Eq. 2.21 for subinterval C can be obtained. The expressions for subintervals A and C can be joined to:

$$\sum_{n\neq 0} y_{\mathrm{Four},i'-i+nN_{\mathrm{sample}},\Delta k}(\omega_i) \approx \underbrace{\frac{-2j}{\pi} \sum_{n>0} \frac{x}{x^2-n^2}}_{\ll 1 \text{ if } |x|\ll 1} y_{\mathrm{corr},\Delta k}(\omega_i) \tag{2.22}$$

Eq. 2.22 states that the series of aliased Fourier-type interference coefficients is approximately proportional to the correction-type interference coefficient. Note that $|x|$ is always smaller than 1 due to the guard band. From a numerical analysis, this proportionality factor is smaller than unity for $|x|$ up to 0.65. The proportionality factor is less than -10 dB (in power) for $|x|$ up to 0.29. The proportionality factor becomes higher as $|x|$ increases, reaching a ratio of 5.0 dB and 10.7 dB for an $|x|$ of 0.8 and 0.9, respectively. Thus, the proportionality factor due to the aliasing effect becomes dominant if the detecting and the source subcarrier are both located near the opposite outer parts of the channel bandwidth. Consequently, the aliasing effect can be neglected for subcarriers that are rather centrally located in the bandwidth, which is the further focus of the dissertation. The aliasing effect is not further explicitly studied in this dissertation and is neglected unless otherwise

mentioned. However, considering the potential importance of the correction-type interference coefficient, the Fourier-type and correction-type interference coefficient will both be treated in this dissertation.

2.2.2.3 Approximative expression for error vector

After neglecting the aliased Fourier-type interference coefficients in the error vector (Eq. 2.8), the remaining interference coefficients are (i) $y_{\mathrm{corr},\Delta k}(\omega_i)$ and (ii) $y_{\mathrm{Four},\Delta i,\Delta k}(\omega_i)$. First, considering the rectangular profile of the weighting function for the correction-type interference coefficient (Table 2.1), $y_{\mathrm{corr},\Delta k}(\omega_i)$ is approximately only related to the channel frequency response ($C_{\mathrm{tot}}(\omega)$) around ω_i. Second, considering the decomposition in Eqs. 2.17a and 2.17b, $y_{\mathrm{Four},\Delta i,\Delta k}(\omega_i)$ is approximately only related to the channel frequency response around ω_i and $\omega_{i'}$. Assuming that the concerning frequency ranges around ω_i and $\omega_{i'}$ fall in the bandwidth of the OFDM system, which is realistic for subcarriers that are rather centrally located in the bandwidth, the channel select filter can be considered as frequency-flat. Consequently, the channel select filter falls out of the expression for the equalized error vector (Eq. 2.8).

Conclusion:

As a conclusion, the error vector $\Delta\tilde{Y}_{\mathrm{delay},k',i'}$ is approximately determined by

$$\Delta\tilde{Y}_{\mathrm{delay},k',i'} \approx \frac{1}{C(\omega_{i'})} \sum_i \sum_k \tilde{X}_{k,i} \exp\Big(j2\pi D_{\mathrm{FFT}}^{-1}(i\tau_{\mathrm{int},1,\Delta k} - i'\tau_{\mathrm{int},1,0})\Big) \times \left(y_{\mathrm{corr},k'-k}(\omega_i) + y_{\mathrm{Four},i'-i,k'-k}(\omega_i) \right) \tag{2.23}$$

where $C(\omega_{i'})$ is the frequency response of the *transmission channel* and the interference coefficients $y_{\mathrm{corr},\Delta k}(\omega)$ and $y_{\mathrm{Four},\Delta i,\Delta k}(\omega)$ are similarly defined as in Eqs. 2.9 and 2.10, but now based on the impulse response of the *transmission channel* ($c(\tau)$).

The *total interference coefficient* is defined as the sum of the correction- and the Fourier-type coefficient:

$$y_{\mathrm{tot},\Delta i,\Delta k}(\omega) = y_{\mathrm{corr},\Delta k}(\omega) + y_{\mathrm{Four},\Delta i,\Delta k}(\omega) \tag{2.24}$$

The correction-type, the Fourier-type and the total coefficient will be referred to as the interference coefficient of type y_{corr}, y_{Four} and y_{tot}, respectively. Analogously to the y_{corr} and y_{Four} type coefficient, $y_{\mathrm{tot},\Delta i,\Delta k}$ is related to the channel impulse

response by the sum of the weighting functions for the correction- and the Fourier-type coefficient:

$$g_{\mathrm{tot},\Delta i}(\tau) = g_{\mathrm{corr}}(\tau) + g_{\mathrm{Four},\Delta i}(\tau) \tag{2.25}$$

2.3 Interference coefficients for IEEE 802.11 OFDM

For IEEE 802.11 OFDM, where $D_{\mathrm{FFT}} = 3.2$ µs, only OFDM symbols with $\Delta k = 0$ and $\Delta k = 1$ are relevant with respect to the interference, as even a high reverberation time (τ_{r}) of 200 ns is still much smaller than D_{FFT}. More specifically, for $\Delta k = 0$ only subinterval C is relevant, which corresponds to the type A subinterval for $\Delta k = 1$. Thus, the relevant delay interval is $[\tau_{\mathrm{int},1,1}, \tau_{\mathrm{int},1,1} + D_{\mathrm{FFT}}]$. Assuming that the propagation paths with a delay higher than $\tau_{\mathrm{int},1,1} + D_{\mathrm{FFT}} + D_{\mathrm{CP}}$ can be neglected, $\Delta\tilde{Y}_{\mathrm{delay},k',i'}$ is obtained in good approximation as follows:

$$\begin{aligned}\Delta\tilde{Y}_{\mathrm{delay},k',i'} \approx \frac{1}{C(\omega_{i'})} \sum_{i=-N_{\mathrm{subc}}}^{N_{\mathrm{subc}}} \Big(-\tilde{X}_{k',i} + \tilde{X}_{k'-1,i} \exp(ji\Delta\omega_{\mathrm{subc}} D_{\mathrm{CP}})\Big) \\ \times \exp\Big(-j(i'-i)\Delta\omega_{\mathrm{subc}}\Delta t_{\mathrm{win},0}\Big)\Big) \\ \times \Big(y_{\mathrm{corr},1}(\omega_i) + y_{\mathrm{Four},i'-i,1}(\omega_i)\Big)\end{aligned} \tag{2.26}$$

Here, the interference coefficients are based on the weighting functions corresponding to $\Delta k = 1$, i.e., $g_{\mathrm{corr}}(\tau - \tau_{\mathrm{int},0,1})$ and $g_{\mathrm{Four},\Delta i}(\tau - \tau_{\mathrm{int},0,1})$ (Eqs. 2.9 and 2.10). Assuming that, based on the room electromagnetics theory [5], the averaged power-delay profile of the channel decays exponentially for delays higher than $\tau_{\mathrm{int},1,1}$, this approximation holds with a deviation of the (frequency-averaged) power less than 0.5 dB for $\tau_{\mathrm{r}} < 0.2 D_{\mathrm{FFT}}$. This assumption is realistic in an indoor environment for IEEE 802.11, where the CP length and thus $\tau_{\mathrm{int},1,1}$ is at least 400 ns.

The terms in Eq. 2.26 proportional to $\tilde{X}_{k'-1,i}$ (for $-N_{\mathrm{subc}} \le i \le N_{\mathrm{subc}}$) are due to ISI, while the terms proportional to $\tilde{X}_{k',i}$ for which $i \neq i'$ are due to ICI. The term proportional to $\tilde{X}_{k',i'}$ is due to the fact that the ideal channel equalization coefficient, $H_{k',i'}$, does not compensate for the distortion of the received signal over the FFT integration interval, due to a larger CP in the training sequence. Note also that **ISI and ICI terms have the same power**. For the near-optimal FFT window positioning (Section 2.1.3), i.e., yielding approximately the smallest interference due to insufficient CP, it is considered that $\Delta t_{\mathrm{win},0} = \tau_{\min} + D_{\mathrm{FFT}} N_{\mathrm{sample}}^{-1}$ (Section 2.1.3). As for IEEE 802.11, only the interference coefficient corresponding to the preceding OFDM symbol is relevant (i.e., $\Delta k = 1$), the index Δk is further omitted (unless otherwise mentioned) in the coefficient's notation, like $y_{\mathrm{corr}}(\omega)$ and $y_{\mathrm{Four},i'-i}(\omega)$.

2.4 Comparison with APDP-based weighting function for total interference power proposed in [1]

In this section, the weighting functions derived in this dissertation (Section 2.2.1) are compared with the weighting function proposed in [1]. In the case of a slowly fading channel, where there is no Doppler shift, [1] determines the time-averaged *total* interference power, $I_{\mathrm{TOT},\Delta k}$, originating from *all* subcarriers and corresponding to a certain OFDM symbol separation Δk, by means of the following power-related weighting function:

$$I_{\mathrm{TOT},\Delta k} = \sum_{k=-\infty}^{\infty} g_{\mathrm{Four},0}(\tau - \tau_{\mathrm{int},0,\Delta k})|c_{\mathrm{APDP}}(k)|^2 \tag{2.27}$$

In Eq. 2.27, $|c_{\mathrm{APDP}}(k)|^2$ represents the coefficients of the time-averaged power delay profile (APDP) per delay tap index k. This is derived based on a delay-discrete channel model following the wide-sense stationary uncorrelated scattering (WSSUS) model. According to the WSSUS model [45], the components of a tapped delay line channel are not correlated in the delay domain and the time-domain correlation properties are time-invariant. As a result, the (time-averaged) interference power from a certain source subcarrier to all detecting subcarriers jointly, is then proportional to the extent of overlap between the OFDM signal's replica and the FFT integration interval. E.g., for a channel component with a delay τ_k in subinterval A (of the interference delay interval) (Fig. 2.5), the power-related weighting function is then proportional to $\tau_k - \tau_{\mathrm{int},1,\Delta k}$, where $\tau_{\mathrm{int},1,\Delta k}$ is the start of the Δkth interference delay interval. This corresponds to the weighting function $g_{\mathrm{Four},0}(\tau)$ (Fig. 2.5).

Analogously to Eq. 2.27, the weighting functions derived in this dissertation (Section 2.2.1) allow to determine the *spectral* interference power, $I_{\Delta i,\Delta k}$, corresponding to an OFDM symbol separation Δk and a subcarrier separation Δi:

$$I_{\Delta i,\Delta k} = \sum_{k=-\infty}^{\infty} |g_{\mathrm{tot},\Delta i}(\tau - \tau_{\mathrm{int},0,\Delta k})|^2|c_{\mathrm{APDP}}(k)|^2 \tag{2.28}$$

When adding up the spectral interference power terms, $I_{\Delta i,\Delta k}$, over all Δi, this should equal the total interference power given by Eq. 2.27. It can be shown that, for an infinite number of subcarriers, this applies. For an infinite FFT size, the correction-type interference coefficient disappears (Table 2.1). Comparing Eq. 2.27 with Eq. 2.28, the equality to be shown is given by:

$$\sum_{\Delta i=-\infty}^{\infty} |g_{\mathrm{Four},\Delta i}(\tau)|^2 = g_{\mathrm{Four},0}(\tau) \tag{2.29}$$

From Table 2.2, Eq. 2.29 obviously holds for $0 < \tau < D_{\mathrm{CP}}$. Due to the symmetry of the weighting function's magnitude between (i) subinterval $-D_{\mathrm{FFT}} < \tau < 0$ and (ii) subinterval $D_{\mathrm{CP}} < \tau < D_{\mathrm{CP}} + D_{\mathrm{FFT}}$, as follows from Table 2.2 and is illustrated in Fig. 2.5, the proof of Eq. 2.29 can be reduced to subinterval $-D_{\mathrm{FFT}} < \tau < 0$. Bringing the weighting function's definitions (Table 2.2) into Eq. 2.29, the equivalent equality to be proven is given by

$$\underbrace{\frac{1}{(2\pi)^2} \sum_{\Delta i \in \mathbb{Z}_0} \frac{1}{\Delta i^2} |1 - \exp(-j2\pi\Delta i x)|^2 + x^2}_{z(x)} = x \qquad (0 < x < 1) \tag{2.30}$$

where the function $z(x)$ denotes the left-hand side of Eq. 2.30.

Proof:

First, it follows from Eq. 2.30 that $z(0) = 0$ and $z(1) = 1$. Second, the second derivative of $z(x)$ yields

$$\frac{\mathrm{d}z(x)}{\mathrm{d}x} = \frac{1}{\pi} \sum_{\Delta i \in \mathbb{Z}_0} \frac{1}{\Delta i} \sin(2\pi\Delta i x) + 2x \tag{2.31}$$

$$\frac{\mathrm{d}^2 z(x)}{\mathrm{d}x^2} = 2 \sum_{\Delta i \in \mathbb{Z}} \cos(2\pi\Delta i x) \tag{2.32a}$$

$$= 0 \qquad (0 < x < 1) \tag{2.32b}$$

Eq. 2.32b follows from Fourier series decomposition of the Dirac delta function:

$$\delta(x') = \frac{1}{2\pi} \sum_{k=-\infty}^{\infty} \exp(jkx') \qquad (-2\pi < x' < 2\pi) \tag{2.33}$$

From Eq. 2.32b and considering that $z(0) = 0$ and $z(1) = 1$, it follows that $z(x) = x$, which is to be proven.

2.5 SINR due to insufficient CP

In this section, the *instantaneous* signal-to-interference-plus-noise ratio (SINR) is presented as a performance metric per OFDM packet. Therefore, the packet index m is not explicitly included in the notation. The *instantaneous* SINR detected at subcarrier i' is defined as the ratio between (i) the (errorless) signal power at the demapper (of the receiver), averaged over all constellation points and (ii) the averaged error power at the demapper:

$$\mathrm{SINR}_{\mathrm{inst},i'} = \frac{\langle |\tilde{X}_{k',i'}|^2 \rangle_{k'}}{\langle |\Delta\tilde{Y}_{k',i'}|^2 \rangle_{k'}}. \tag{2.34}$$

Here, $\langle \cdot \rangle_{k'}$ indicates an averaging over all OFDM symbols k'. $\mathrm{SINR}_{\mathrm{inst}}$ is called *instantaneous* because it is based on one channel realization (per mth OFDM packet).

Assuming that the data symbols $\tilde{X}_{k,i}$ are uncorrelated, it follows from Eq. 2.34 and Eq. 2.8 that

$$\mathrm{SINR}_{\mathrm{inst},i'} = \frac{P_{\mathrm{T,subc}}|C(\omega_{i'})|^2}{F_{\mathrm{AWGN}}k_{\mathrm{B}}T/D_{\mathrm{FFT}} + P_{\mathrm{T,subc}}I_{i'}} \tag{2.35}$$

where $P_{\mathrm{T,subc}}$ is the (linear-scaled) transmit power per subcarrier, k_{B} is the Boltzmann constant and T is the room temperature, being 290 K according to the IEEE Standard [67]. $I_{i'}$ is the sum of the interference power terms over all source subcarriers i and all OFDM symbol separations Δk:

$$I_{i'} = \sum_{\Delta k} \sum_{i=-N_{\mathrm{subc}}}^{N_{\mathrm{subc}}} |y_{\mathrm{tot},i'-i,\Delta k}(\omega_i)|^2 \tag{2.36}$$

If the frequency width of the spectral interference (i.e., the interference power as a function of Δi) is much smaller than the bandwidth, $I_{i'}$ is not much influenced by the subcarrier index i' and is mainly determined by the detecting subcarrier frequency. Hence, it can be considered that i' is systematically zero. Assuming that i' is systematically zero, the total interference power (as well as the instantaneous SINR) are only a function of the detecting subcarrier frequency, which is denoted by $I(\omega_{\mathrm{d}})$.

For IEEE 802.11, only interference from the same OFDM symbol ($\Delta k = 0$) and the preceding one ($\Delta k = 1$) are practically relevant. Based on Eq. 2.26, it follows that

$$I(\omega_{\mathrm{d}}) = 2 \sum_{\Delta i=-N_{\mathrm{subc}}}^{N_{\mathrm{subc}}} |y_{\mathrm{tot},\Delta i,1}(\omega_{\mathrm{d}} - 2\pi\Delta i/D_{\mathrm{FFT}})|^2 \tag{2.37}$$

2.6 Conclusions

In this chapter, an analytical framework is developed to relate the interference due to insufficient CP to the transmission channel. Based on an idealized OFDM system, the constellation error vector due to insufficient CP is analytically determined by means of *interference coefficients*. These interference coefficients characterize the elementary interference processes (between individual subcarriers and OFDM symbols) and determine the corresponding additive contribution to the constellation error vector. The interference coefficient is analytically related to the channel impulse response (CIR) by delay-domain *weighting functions*, which describe the contribution of each channel component to the interference coefficient.

Two types of interference coefficients are proposed: a Fourier-type coefficient and a correction-type coefficient. The Fourier-type coefficient represents the interference coefficient in the case of an infinitely small sampling period. The correction-type coefficient is an additional correction as a result of the non-zero sampling period. The proportionality factor of the correction-type coefficient may become more important for subcarriers which are outerly located in the bandwidth of the OFDM system (due to aliasing effect), which is not further studied in this dissertation. While the Fourier-type coefficient is related to the channel frequency response around the source as well as the detecting subcarrier, the correction-type coefficient is only related to the channel frequency response around the source subcarrier.

The weighting functions proposed in this chapter are compared with another weighting function proposed in [1]. While the former is based on the *CIR* and determines the *interference coefficient*, the latter is based on the *averaged power delay profile* (APDP) and determines directly the *total interference power*. It is found that, for an infinitely small sampling period, the averaged total interference power obtained from the weighting functions proposed in this chapter is identical to the one obtained by the weighting function proposed in [1].

For IEEE 802.11 indoors, it is found that the spectral intercarrier and intersymbol interference power are typically identical. Further, the signal-to-interference-plus-noise ratio (SINR), which can be considered as a performance metric, is described in terms of the interference coefficient.

3

Determination of the interference coefficient from frequency-domain channel sounding: theory

3.1 Introduction and overview of the chapter

The interference coefficient, describing the interference due to insufficient CP from a *source subcarrier* at frequency $\omega_{\rm s}$, to a *detecting subcarrier* at frequency $\omega_{\rm d}$, is related with the channel impulse response (CIR) as follows (Section 2.2):

$$y_\alpha(\omega_{\rm s}) = \int_{-\infty}^{\infty} g_\alpha(\tau - \tau_{{\rm int},0}) c(\tau) \exp(-j\omega_{\rm s}\tau)\, {\rm d}\tau, \tag{3.1}$$

In the notation of the interference coefficient, $y_\alpha(\omega_{\rm s})$, α indicates (i) the coefficient type and (ii) the subcarrier separation, Δi, if applicable: $y_{\rm corr}$, $y_{{\rm Four},\Delta i}$ or $y_{{\rm tot},\Delta i}$. $g_\alpha(\tau)$ is the weighting function for the corresponding coefficient type and Δi, i.e., $g_{\rm corr}(\tau)$, $g_{{\rm Four},\Delta i}(\tau)$ or $g_{{\rm tot},\Delta i}(\tau)$. $\tau_{{\rm int},0}$ and $\tau_{{\rm int},1}$ correspond to $\tau_{{\rm int},0,\Delta k}$ and $\tau_{{\rm int},1,\Delta k}$, resp., as defined in Section 2.2. In this chapter, the OFDM symbol separation, Δk, is omitted in the notation (unless otherwise mentioned) for reasons of clarity, as the focus in this chapter is on a fixed Δk.

The major question addressed in this chapter is how to determine accurately the interference coefficient (Eq. 3.1) from frequency-domain channel sounding, where the channel frequency response is measured over a limited frequency range, referred to as the ***measurement range*** ($\Delta f_{\rm meas}$), and with a non-zero frequency spacing, referred to as the ***frequency resolution***. The computation procedure consists in essence of two steps:

- a delay-discrete CIR representation is obtained by an inverse discrete Fourier transform (IDFT) of the measured channel response samples
- the delay-discrete CIR representation is included in a delay-discrete form of the delay-domain integral (Eq. 3.1)

However, the following particular **issues** arise (see Fig. 1.6):

- a finite ***time window***: the time window of the delay-discrete CIR is limited by the non-zero frequency resolution ($\Delta f_{\rm res}$): only channel components with a delay up to $\Delta f_{\rm res}^{-1}$ can be experimentally detected. Due to the non-zero frequency resolution, the channel impulse response is converted into an aliased form, which is periodic over a delay width of $\Delta f_{\rm res}^{-1}$ (aliasing effect). However, to determine interference due to insufficient CP, the time window should be certainly larger than the CP length, as relevant delays (causing interference) are higher than the CP length.
- a non-zero ***time resolution***: The *time resolution* is the delay spacing of the delay-discrete channel components and equals the inverse of the frequency width over which the IDFT is applied (IDFT frequency interval, $\Delta f_{\rm win}$). To determine the interference coefficient (Eq. 3.1), the channel components

should be resolved with a sufficiently small time resolution in relation to the variability of the weighting function.

- a limited ***dynamic range***: The *dynamic range* is defined by the ratio in power between the strongest channel component and the weakest measurable one. Besides measurement noise, the dynamic range is limited by the finite IDFT frequency interval (due to the finite measurement range). This limitation on the dynamic range is related to the discontinuous behaviour of the channel response near the edges of the IDFT frequency interval (non-identical channel response comparing the two opposite edges). The finite IDFT frequency interval implies in fact a rectangular frequency-domain window. Hence, the limitation on the dynamic range is mathematically related to leakage via the sidelobes of the window in the delay-domain.

Approach to the issues of time window, time resolution and dynamic range

To determine the interference coefficient (Eq. 3.1), the **time window** should cover the whole interference delay interval (where the weighting function is not trivially zero). This delay interval starts at $\tau_{\mathrm{int},1}$ and has a duration of $2D_{\mathrm{FFT}} + D_{\mathrm{CP}}$, which may result into a quite large required time window, e.g., for IEEE 802.11, where $D_{\mathrm{FFT}} = 3.2$ µs. However, based on the theory of room electromagnetics [5], the most relevant part of the interference delay interval has a duration of the order of the reverberation time (τ_{r}), as the channel impulse response decays roughly exponentially with τ_{r} as a time constant. In practice, the **interference delay interval will be cut off** to $[\tau_{\mathrm{int},1}, \tau_{\mathrm{int},2}]$, where $\tau_{\mathrm{int},2} - \tau_{\mathrm{int},1}$ is of the order of τ_{r} and $\tau_{\mathrm{int},2}$ is referred to as the *cut-off delay*. The weighting function is then set to zero in Eq. 3.1 for a delay τ higher than the cut-off delay. The duration of the modified interference delay interval (after a cut-off) is denoted by $\Delta\tau_{\mathrm{CO}}$.

The **time resolution and the dynamic range** can both be improved by extending the IDFT frequency interval, which implies an extended measurement range. However, a larger measurement range may be problematic, as it increases the frequency range where the measurement equipment (e.g., antennas, network analyzer and amplifier) needs to operate. Moreover, the channel measurement may be disturbed by external sources outside the frequency band of interest and the measurement time will increase. For these reasons, the measurement range should be limited as much as possible. Another approach to improve the time resolution and the dynamic range concerns *windowing* of the measured channel response prior to IDFT computation. Especially, the dynamic range can be substantially improved if the windowed channel response has a "smooth" transition to zero near the edges of the IDFT frequency interval. On the other hand, if the channel response is weighted non-uniformly, this may also involve an adverse effect on the accuracy of the interference coefficient, depending on the relative position of the source and

detecting subcarrier with respect to the window. Depending on the window profile and the positioning of the window, different ***windowing methods*** can be proposed.

Some definitions of different frequency ranges

In practice, the aim is to determine the interference coefficient accurately for a given *set* of detecting subcarriers. The corresponding frequency range, determined by the detecting subcarriers of interest, is referred to as the ***calculation range*** (Δf_{calc}). To determine the interference coefficient, the channel response around both the source and the detecting subcarrier are relevant (Section 2.2.2.1), so that the measurement range should certainly cover all source and detecting subcarriers of interest (see Fig. 1.7). This frequency range, determined by all source and detecting subcarriers of interest, is referred to as the ***zero-excess measurement range*** ($\Delta f_{\mathrm{meas},0}$). To achieve sufficient time resolution and dynamic range, the required measurement range could be larger than the zero-excess measurement range. The deviation between the measurement range and the zero-excess measurement range is referred to as the ***excess measurement range*** ($\Delta f_{\mathrm{meas,exc}}$).

Overview of this chapter

In the remainder of this chapter, the following matters are worked out:

- **Interference coefficient in relation with the channel frequency response** (Section 3.2):
  The definition of the interference coefficient (Eq. 3.1) is expressed in the frequency-domain. This provides insight on the question in which the part of the frequency-domain, the channel response is relevant with respect to the interference coefficient.

- **General computation procedure of the interference coefficient** (Section 3.3):
  The general computation procedure of the interference coefficient is mathematically worked out. This procedure consists of (frequency-domain) windowing of the measured channel response and a discrete delay-domain expression for the interference coefficient. The delay-discrete channel representation is obtained by an IDFT of the (windowed) channel response samples.

- **Definition of different windowing methods** (Section 3.4):
  Different windowing methods are defined in order to improve the time resolution and the dynamic range. A novel windowing method is introduced based the generalized representation of the Fourier-type interference coefficient.

- **Error analysis of the interference coefficient** (Section 3.5):
  A mathematical framework for the overall error on the interference coefficient is provided and different error types are defined. Based on this error analysis, important knowledge will be obtained (in the remainder of the dissertation) on which measurement settings and which windowing method are to be used to suppress the error power (on the interference coefficient).

- **Relative error power versus dB-scaled deviation** (Section 3.6):
  As a tractable accuracy metric, the *relative error power* will be used, defined as the ratio between the frequency-averaged error power (on the interference coefficient) and the frequency-averaged interference power. In Section 3.6, it is investigated which relative error power is needed to obtain a given dB-scaled deviation of the interference power. For practical interference characterization, the *dB-scaled deviation* is preset and should be expressed in terms of a threshold level of the *relative error power*, from which the measurement settings can be properly selected.

- **APDP-based expression for the frequency-averaged interference power** (Section 3.7):
  The interference coefficient is defined by means of a *CIR*-based weighting function (Eq. 3.1). However, to apply the room electromagnetics theory, which involves the *averaged power delay profile* (APDP), an APDP-based expression for the interference power should first be determined. In Section 3.7, an APDP-based expression for the frequency-averaged interference power is proposed.

- **Time-domain cut-off requirement: relation between the required time window and the reverberation time** (Section 3.8):
  Based on the theory of room electromagnetics, it is analytically investigated at which delay the weighting function may be cut off to have the resulting relative error power below a given accuracy level. This cut-off requirement has important implications on which time window or frequency resolution is required for the channel measurement.

- **Error power due to a non-zero time resolution and leakage** (Section 3.9):
  For the performance analysis of the different windowing methods with respect to the required measurement range (Chapter 4), the error powers due to a non-zero time resolution and leakage need to be determined for a measured channel. This is important to find out which error type is the restricting factor with respect to the measurement range requirement. Because exact calculations of these error powers, based on a channel impulse response with a much smaller time resolution, are demanding a computational capacity of a higher order, theoretical estimations of a lower numerical complexity are

proposed in Section 3.9. For the error due to the non-zero time resolution, this is based on the theory of room electromagnetics.

3.2 Interference coefficient in relation with the channel frequency response

The interference coefficient is defined based on the channel impulse reponse (Eq. 3.1). In this section, the interference coefficient is related to the channel frequency response. As the interference coefficient, $y_\alpha(\omega_\mathrm{s})$, is determined by the Fourier transform of the channel impulse reponse multiplied by a delay-domain weighting function (Eq. 3.1), one obtains

$$y_\alpha(\omega_\mathrm{s}) = \Big[\mathcal{F}\big[g_\alpha(\tau-\tau_{\mathrm{int},0})\big](\omega) * C(\omega)\Big](\omega_\mathrm{s}) \tag{3.2}$$

$$= \int_{-\infty}^{\infty} C(\omega_\mathrm{s}-\omega)G(\omega)\,\mathrm{d}\omega \tag{3.3}$$

where $\mathcal{F}\big[\,\cdot\,\big](\omega)$ represents the (continuous) Fourier transform and $*$ denotes a convolution operator. $G(\omega)$ is defined by the Fourier transform of the weighting function:

$$G(\omega) = \mathcal{F}\big[g_\alpha(\tau-\tau_{\mathrm{int},0})\big](\omega) \tag{3.4}$$

$$= \exp(-j\omega\tau_{\mathrm{int},0})\mathcal{F}\big[g_\alpha(\tau)\big](\omega) \tag{3.5}$$

Physically, $G(\omega)$ indicates which part of the frequency-domain needs to be measured in order to accurately determine the interference coefficient.

In particular, the *generalized* interference coefficient (Section 2.2.2.1) is determined by a *rectangular* weighting function over a delay interval $[\tau_{\mathrm{int},1}, \tau_{\mathrm{int},2}]$:

$$g_\alpha(\tau-\tau_{\mathrm{int},0}) = \mathrm{U}(\tau-\tau_{\mathrm{int},1}) - \mathrm{U}(\tau-\tau_{\mathrm{int},2}) \tag{3.6}$$

The Fourier transform of this rectangular weighting function, $\tilde{G}(\omega)$, is related to a $\mathrm{sinc}(\,\cdot\,)$ function:

$$\tilde{G}(\omega) = \Delta\tau_\mathrm{CO}\exp\Big(-j\omega\frac{\tau_{\mathrm{int},1}+\tau_{\mathrm{int},2}}{2}\Big)\mathrm{sinc}\Big(\frac{\Delta\tau_\mathrm{CO}\omega}{2}\Big) \tag{3.7}$$

where $\Delta\tau_\mathrm{CO}$ represents the duration of the delay interval:

$$\Delta\tau_\mathrm{CO} = \tau_{\mathrm{int},2} - \tau_{\mathrm{int},1} \tag{3.8}$$

Consequently, $\tilde{G}(\omega)$ has a frequency width of the order of $\Delta\tau_\mathrm{CO}^{-1}$. In essence, this means that the generalized interference coefficient, $\tilde{y}(\omega)$, is mainly related to the channel frequency response around ω over a width of the order of $\Delta\tau_\mathrm{CO}^{-1}$.

From the generalized representation of the interference coefficient (Section 2.2.2.1), the Fourier-type interference coefficient for a non-zero subcarrier separation is related to the generalized interference coefficient, $\tilde{y}(\omega)$, at the

source subcarrier frequency, ω_{s}, and at the detecting subcarrier frequency, ω_{d}. The correction-type interference coefficient is related to the generalized interference coefficient at the source subcarrier frequency only. Consequently, the part of the frequency-domain that is physically relevant to accurately determine the interference coefficient is located around the source and the detecting subcarrier frequency, each over a frequency width of the order of $\Delta\tau_{\mathrm{CO}}^{-1}$. This is illustrated in Fig. 3.1.

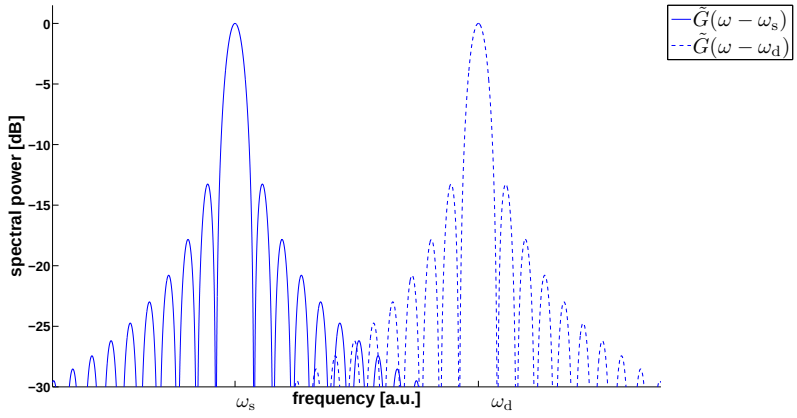

Figure 3.1: The part of the frequency-domain that is physically relevant to accurately determine the interference coefficient is concentrated around the source subcarrier frequency (ω_{s}) and the detecting subcarrier frequency (ω_{d}). The frequency width is related to the inverse duration of the interference delay interval.

For the determination of the interference coefficient, a frequency-discrete form of Eq. 3.3 could be considered. However, due to the presence of a fast-varying exponential harmonic (such as in Eq. 3.5 and Eq. 3.7), a very small frequency resolution would be required. Therefore, the approach followed in this dissertation for computation of the interference coefficient is based on the delay-domain.

3.3 General computation procedure of the interference coefficient

In this section, the general computation procedure of the interference coefficient (Eq. 3.1) is mathematically worked out using (frequency-domain) windowing. The measured channel response samples are multiplied by a *window function* prior to computation of the inverse discrete Fourier transform (IDFT). The width of the IDFT frequency interval is also referred to as the *window width* (Δf_{win}). The window width is assumed to be an *even* multiple of the frequency resolution. The resulting IDFT coefficients are used as a delay-domain channel representation in the discrete baseband form of Eq. 3.1.

To obtain this baseband form, the channel response is shifted in the frequency domain, bringing the window centre frequency to zero:

$$y_\alpha(\omega_{\mathrm{win}} + \Delta\omega_{\mathrm{s}}) = \int_{-\infty}^{\infty} g_\alpha(\tau - \tau_{\mathrm{int},0}) c_{\mathrm{B}}(\tau) \exp(-j\Delta\omega_{\mathrm{s}}\tau)\,\mathrm{d}\tau, \tag{3.9}$$

where ω_{win} is the (angular) window centre frequency and $\Delta\omega_{\mathrm{s}}$ is defined by $\omega_{\mathrm{s}} - \omega_{\mathrm{win}}$. $c_{\mathrm{B}}(\tau)$ is the inverse continuous Fourier transform of the shifted channel response:

$$c_{\mathrm{B}}(\tau) = \exp(-j\omega_{\mathrm{win}}\tau) c(\tau). \tag{3.10}$$

Then, Eq. 3.9 is converted into a discrete form as follows. First, the windowed channel response is decomposed as a Fourier series over the IDFT frequency interval. In this way, an exact discretization of the delay-domain integral (Eq. 3.1) can be obtained. For $|\Delta\omega_{\mathrm{s}}| < \pi\Delta f_{\mathrm{win}}$, we obtain

$$\begin{aligned} W(\Delta\omega_{\mathrm{s}}) y_\alpha(\omega_{\mathrm{win}} + \Delta\omega_{\mathrm{s}}) = \Delta f_{\mathrm{win}}^{-1} \sum_{k=-\infty}^{\infty} \Big[w(\tau) * \Big(g_\alpha(\tau - \tau_{\mathrm{int},0}) c_{\mathrm{B}}(\tau) \Big) \Big] (\tau_k) \\ \times \exp(-j\tau_k \Delta\omega_{\mathrm{s}}), \end{aligned} \tag{3.11}$$

where $W(\omega)$ is the window function, centered at zero and with a width of $2\pi\Delta f_{\mathrm{win}}$. By definition, $W(0)$ equals 1. τ_k is defined by $k\Delta f_{\mathrm{win}}^{-1}$, where k is an integer. $w(\tau)$ is the inverse Fourier transform of $W(\omega)$ and $\big[\,\cdot * \cdot\,\big](\tau)$ denotes a convolution of two functions, evaluated at τ. If the pulse width of $w(\tau)$, i.e., of the order of the inverse of Δf_{win}, is sufficiently small, the weighting function commutes in good approximation with the convolution operator:

$$w(\tau) * \Big(g_\alpha(\tau - \tau_{\mathrm{int},0}) c_{\mathrm{B}}(\tau) \Big) \approx g_\alpha(\tau - \tau_{\mathrm{int},0}) \Big(w(\tau) * c_{\mathrm{B}}(\tau) \Big) \tag{3.12}$$

If the time window, i.e., $\Delta f_{\mathrm{res}}^{-1}$, is sufficiently large, the coefficients $\big[w(\tau) * c_{\mathrm{B}}(\tau)\big](\tau_k)$ $(k = 0, ..., N-1)$ are in good approximation connected with the IDFT coefficients of the windowed channel response, denoted as $c_{\mathrm{IDFT}}(k)$ $(k = 0, ..., N-1)$:

$$\Big[w(\tau) * c_{\mathrm{B}}(\tau)\Big](\tau_k) \approx \Delta f_{\mathrm{win}} \;\; c_{\mathrm{IDFT}}(k), \tag{3.13}$$

where

$$\begin{aligned} c_{\mathrm{IDFT}}(k) =& \frac{1}{N} \sum_{m=1}^{N-1} W\big(\Delta\omega_{\mathrm{s}}(m)\big)\; C\big(\omega_{\mathrm{win}} + \Delta\omega_{\mathrm{s}}(m)\big)\; \exp\big(j\tau_k \Delta\omega_{\mathrm{s}}(m)\big) \\ &+ \frac{1}{2N}\Bigg(\lim_{\epsilon\to 0^+} W\big(\Delta\omega_{\mathrm{s}}(0) + \epsilon\big)\; C\big(\omega_{\mathrm{win}} + \Delta\omega_{\mathrm{s}}(0)\big)\; \exp\big(j\tau_k \Delta\omega_{\mathrm{s}}(0)\big) \\ &+ \lim_{\epsilon\to 0^+} W\big(\Delta\omega_{\mathrm{s}}(N) - \epsilon\big)\; C\big(\omega_{\mathrm{win}} + \Delta\omega_{\mathrm{s}}(N)\big)\; \exp\big(j\tau_k \Delta\omega_{\mathrm{s}}(N)\big)\Bigg). \end{aligned} \tag{3.14}$$

Here, N is the ratio between Δf_{win} and Δf_{res}. $\Delta\omega_{\mathrm{s}}(m)$ is defined by $-\pi\Delta f_{\mathrm{win}} + 2\pi\Delta f_{\mathrm{res}} m$ and $C(\omega)$ is the channel response (as a function of the angular frequency). The limits of the window function at both edges ($m = 0$ and $m = N$) is relevant for a discontinuous window, e.g., a rectangular window. Finally, assuming that the time window is large enough, the terms of a higher delay ($\tau_k \geq \Delta f_{\mathrm{res}}^{-1}$) can be neglected in Eq. 3.11. Substituting Eqs. 3.12 and 3.13 into Eq. 3.11, the interference coefficient is obtained in good approximation as

$$y_\alpha(\omega_{\mathrm{win}} + \Delta\omega) \approx \frac{1}{W(\Delta\omega)} \sum_{k=0}^{N-1} g_\alpha(\tau_k - \tau_{\mathrm{int},0}) c_{\mathrm{IDFT}}(k) \exp(-j\tau_k \Delta\omega), \tag{3.15}$$

where $\Delta\omega$ is more generally the difference between the frequency evaluated and the window centre frequency. Thus, in this case, $\Delta\omega = \Delta\omega_{\mathrm{s}}$. **Eq. 3.15 represents the discrete baseband form of the definition of the interference coefficient (Eq. 3.1)**.

The discrete baseband form (Eq. 3.15) holds on condition that (i) the time window is sufficiently large and (ii) the window width (IDFT frequency interval) is sufficiently large. The latter condition is necessary to Eq. 3.12, where the weighting function is brought out of the convolution with $w(\tau)$. However, $w(\tau)$ has a pulse width of the order of inverse window width, which causes the **non-zero time resolution** of the experimental (delay-discrete) channel impulse reponse. In addition, the sidelobes of $w(\tau)$ may cause **leakage** from high-intensity channel

components outside the interference delay interval, which result into the limitation of the dynamic range of the experimental (delay-discrete) channel impulse reponse.

3.4 Definition of different windowing methods

In Sections 3.4.1–3.4.3, the following windowing methods are presented (Fig. 3.2), classified depending on the window positioning and the profile. Methods of type I and II are based on a fixed and moving window, resp., and on a conventional weighting function, which is dependent on the subcarrier separation for the Fourier-type interference coefficient. For method types I and II, a Hann window (method *I-Hann* and *II-Hann*, resp.) and a rectangular window are considered (method *I-rect* and *II-rect*, resp.). In addition, a Hann window with window correction is studied (method *I-HC* and *II-HC*, resp.). Method type III, which is introduced in this dissertation, is based on the decomposition of the Fourier-type interference coefficient in terms of a generalized (frequency-dependent) interference coefficient, which is evaluated at the source and detecting subcarrier separately. For method type III, a Hann and a rectangular window are considered (*III-Hann* and *III-rect*, resp.).

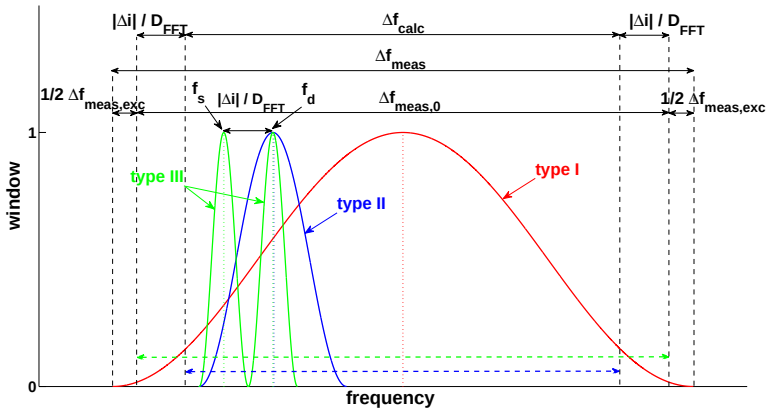

Figure 3.2: To determine the interference for a subcarrier separation $\pm|\Delta i|$ over a given calculation range (Δf_{calc}), 3 windowing method types can be used. Type I applies a fixed window centered over the measurement range (Δf_{meas}). Type II uses a moving window centered around the detecting subcarrier (f_{d}). Type III applies a moving window to determine the generalized interference coefficient centered around both source and detecting subcarrier frequency (f_{s} and f_{d}). The window centre ranges over Δf_{calc} for type II and over the zero-excess measurement range ($\Delta f_{\mathrm{meas},0}$) for type III. Finally, the excess measurement range ($\Delta f_{\mathrm{meas,exc}}$) is indicated.

3.4.1 Type I method

In method type I, a **fixed window** is centered over the calculation range (Fig. 3.2). An IDFT of the (windowed) channel response samples is calculated using Eq. 3.14 and the interference coefficient is computed using Eq. 3.15, where the evaluation frequency corresponds to the source subcarrier. If the window is sufficiently large, the window function can be approximated by unity in Eq. 3.15. Under this assumption, two window profiles are investigated: a Hann window (method *I-Hann*) and a rectangular window (method *I-rect*). To achieve that the window function approximately equals unity over the whole zero-excess measurement range, method I-Hann requires that $\Delta f_{\mathrm{win}} \gg \Delta f_{\mathrm{meas},0}$, implying a substantial measurement range excess. Method I-rect only requires that the window covers the zero-excess measurement range ($\Delta f_{\mathrm{win}} > \Delta f_{\mathrm{meas},0}$). Further, non-uniform window profiles can be compensated by *window correction*, where the window function in Eq. 3.15 is effectively taken into account. In theory, this is possible when $\Delta f_{\mathrm{win}} > \Delta f_{\mathrm{meas},0}$. This will be investigated for the type I method using a Hann window (method *I-HC*).

3.4.2 Type II method

In method type II, a **moving window is applied centered around the detecting subcarrier** frequency, f_{d} (Fig. 3.2). For a Hann window without window correction (method *II-Hann*), this approach requires a window width that is considerably larger than twice the subcarrier frequency separation. Consequently, the required measurement range excess is of the order of twice the subcarrier frequency separation and is disconnected from the calculation range, contrary to method I-Hann. Using a rectangular window (method *II-rect*) or a Hann window with window correction (method *II-HC*), a window width strictly larger than twice the subcarrier frequency separation is required.

The calculation procedure for method type II is a straightforward extension of method type I. An IDFT of the (windowed) channel response samples is calculated using Eq. 3.14, where the window centre frequency varies over all measured frequency points covering the whole calculation range. The interference coefficient is calculated using Eq. 3.15, where $c_{\mathrm{IDFT}}(l)$ are the IDFT coefficients corresponding to the centre frequency that is nearest to the detecting subcarrier frequency (ω_{d}).

3.4.3 Type III method

All methods proposed so far require that the window systematically covers both the source and the detecting subcarrier frequency. In fact, the problem is that the Fourier-type coefficient is physically related to the channel at the source as well as the detecting subcarrier. Method type III tackles this problem by decomposing the

Fourier-type interference coefficient for a non-zero subcarrier separation in terms of a generalized (frequency-dependent) interference coefficient, which is evaluated at the **source and detecting subcarrier separately**. This generalized interference coefficient can be determined from a measured channel response by applying a moving window around the evaluation frequency.

The Fourier-type and the correction-type interference coefficient are divided up into a component corresponding to delays in subinterval type A and C (of the Δkth interference delay interval), resp. denoted by $y_{\alpha,\Delta k;\mathrm{A}}(\omega_\mathrm{s})$ and $y_{\alpha,\Delta k;\mathrm{C}}(\omega_\mathrm{s})$. In this section, the OFDM symbol index separation, Δk, is explicitly included in the notation. From Section 2.2.2.1, the Fourier-type coefficient for a non-zero subcarrier separation can be represented in terms of the generalized interference coefficient, $\tilde{y}_{\Delta k}(\omega)$:

$$y_{\alpha,\Delta k;\mathrm{A}}(\omega_\mathrm{s}) = K_{\alpha;\mathrm{A}}\big(\tilde{y}_{\Delta k}(\omega_\mathrm{s}) - \delta_{\alpha,\Delta k;\mathrm{A}}\ \tilde{y}_{\Delta k}(\omega_\mathrm{d})\big) \tag{3.16a}$$

$$y_{\alpha,\Delta k;\mathrm{C}}(\omega_\mathrm{s}) = K_{\alpha;\mathrm{C}}\big(\tilde{y}_{\Delta k+1}(\omega_\mathrm{s}) - \delta_{\alpha,\Delta k;\mathrm{C}}\ \tilde{y}_{\Delta k+1}(\omega_\mathrm{d})\big) \tag{3.16b}$$

Considering the rectangular weighting function for the correction-type interference coefficient (Table 2.1), the representation of Eq. 3.16 is also applicable to the correction-type interference coefficient. The parameters $K_{\alpha;\mathrm{A}}$, $\delta_{\alpha,\Delta k;\mathrm{A}}$, $K_{\alpha;\mathrm{C}}$ and $\delta_{\alpha,\Delta k;\mathrm{C}}$ are given in Table 3.1.

Table 3.1: Parameters for the generalized representation of the Fourier-type interference coefficient for $\Delta i \neq 0$ and the correction-type interference coefficient.

	α	
parameter	"Four, Δi" ($\Delta i \neq 0$)	"corr"
$K_{\alpha;\mathrm{A}}$	$1/(j2\pi\Delta i)$	$1/(2N_\mathrm{sample})$
$\delta_{\alpha,\Delta k;\mathrm{A}}$	$\exp(j2\pi\Delta i\tau_{\mathrm{int},1,\Delta k}/D_\mathrm{FFT})$	0
$K_{\alpha;\mathrm{C}}$	$-1/(j2\pi\Delta i)$	$-1/(2N_\mathrm{sample})$
$\delta_{\alpha,\Delta k;\mathrm{C}}$	$\exp(j2\pi\Delta i(\tau_{\mathrm{int},1,\Delta k} + D_\mathrm{CP})/D_\mathrm{FFT})$	0

The calculation method for method type III is as follows.

1. Firstly, $\tilde{y}_{\Delta k}(\omega)$, $\tilde{y}_{\Delta k+1}(\omega)$ and $y_{\mathrm{Four},0,\Delta k}(\omega)$ are determined from the measured channel response by applying a moving window centered around ω. An IDFT of the (windowed) channel response is computed using Eq. 3.14 for a set of centre frequencies with a resolution of a multiple of Δf_res and covering the whole zero-excess measurement range. The coefficients $\tilde{y}_{\Delta k}(\omega)$ ($\tilde{y}_{\Delta k+1}(\omega)$) and $y_{\mathrm{Four},0,\Delta k}(\omega)$ are computed using Eq. 3.15 and their corresponding weighting function, where $c_\mathrm{IDFT}(k)$ are the IDFT coefficients corresponding to the window centre frequency that is nearest to the

evaluation frequency (ω). In Eq. 3.15, ω_{win} represents the window centre frequency corresponding to the source and detecting subcarrier term, $\omega_{\mathrm{win,s}}$ and $\omega_{\mathrm{win,d}}$, respectively. In Eq. 3.15, $\Delta\omega$ represents $\Delta\omega_{\mathrm{s}}$ and $\Delta\omega_{\mathrm{d}}$, resp., defined as:

$$\Delta\omega_{\mathrm{s}} = \omega_{\mathrm{s}} - \omega_{\mathrm{win,s}} \tag{3.17}$$

$$\Delta\omega_{\mathrm{d}} = \omega_{\mathrm{d}} - \omega_{\mathrm{win,d}} \tag{3.18}$$

If the resolution of the window centre frequency is small compared to the window width, the window function in Eq. 3.15 equals unity in good approximation. The calculation of $\tilde{y}_{\Delta k}(\omega)$ ($\tilde{y}_{\Delta k+1}(\omega)$) and $y_{\mathrm{Four},0,\Delta k}(\omega)$ is performed for ω ranging over the zero-excess measurement range and the calculation range, respectively. Further, the resolution of the frequency points for which $\tilde{y}_{\Delta k}(\omega)$ ($\tilde{y}_{\Delta k+1}(\omega)$) and $y_{\mathrm{Four},0,\Delta k}(\omega)$ are calculated must fit a multiple times into the minimum subcarrier frequency separation (D_{FFT}^{-1}).

2. Secondly, $y_{\mathrm{Four},\Delta i,\Delta k;\mathrm{A}}(\omega)$ and $y_{\mathrm{Four},\Delta i,\Delta k;\mathrm{C}}(\omega)$ for a non-zero Δi as well as $y_{\mathrm{corr},\Delta k;\mathrm{A}}(\omega)$ and $y_{\mathrm{corr},\Delta k;\mathrm{C}}(\omega)$ are calculated from Eq. 3.16.

For method type III, a Hann window (method *III-Hann*) and a rectangular window (method *III-rect*) are investigated. In these methods, the resolution of the window centre frequency is set to Δf_{res} and no window correction is applied. As Δf_{res} is typically much smaller than the window width, window correction would not give any profit with respect to limiting the measurement range and is not investigated.

3.5 Error analysis

In Section 3.4, different windowing methods were proposed to calculate the interference coefficient ($y_\alpha(\omega_\mathrm{s})$) over a given calculation range (Δf_calc) from a measured channel response. The error between the calculated and the exact value, $\Delta y_\alpha(\omega_\mathrm{s})$, is analyzed in this section, which will give important knowledge on which measurement settings and which windowing method are to be used to achieve a given accuracy. From this section, the OFDM symbol index separation, Δk, is not explicitly included in the notation for reasons of clarity.

3.5.1 Error due to a time-domain cut-off and due to measurement noise

In the case that the interference delay interval is cut off, the following ***cut-off error*** is introduced:

$$\Delta y_{\alpha,\mathrm{CO}}(\omega_\mathrm{s}) = -\int_{\tau_{\mathrm{int},2}}^{\infty} g_\alpha(\tau-\tau_{\mathrm{int},0})c(\tau)\exp(-j\omega_\mathrm{s}\tau)\,\mathrm{d}\tau, \tag{3.19}$$

where $\tau_{\mathrm{int},2}$ is the cut-off delay. This error is a result of the non-zero frequency resolution (Δf_res).

A second error is referred to as the ***measurement noise***: the channel response is measured with an error, $\Delta C_\mathrm{MN}(\omega_m)$, at the frequency points ω_m. Via the channel response samples, this error will also be processed by an IDFT (Eq. 3.14) and a weighted time-domain integration (Eq. 3.15), resulting into a certain error on the interference coefficient, $\Delta y_{\alpha,\mathrm{MN}}(\omega_\mathrm{s})$. The influence of the windowing methods on the error power due to measurement noise will be investigated in Section 6.2. The measurement noise can be suppressed by averaging the measured channel response samples over a number of sweeps.

3.5.2 Error analysis of the remaining error

Apart from the error due to the cut-off (if applied) and the measurement noise, the remaining error is mathematically analyzed into different error types for all methods, based on the interference coefficient representation introduced for method type III (Eq. 3.16). This representation is also used for the error analysis for method types I and II, because it turned out that otherwise different error types are correlated and may add up to a much smaller total error. The representation of the interference coefficient used in the error analysis is expressed as follows:

$$y_\alpha(\omega_\mathrm{s}) = K_\alpha\big(\tilde{y}(\omega_\mathrm{s}) - \delta_\alpha\ \tilde{y}(\omega_\mathrm{d})\big) \tag{3.20}$$

where $\tilde{y}(\omega)$ is determined by a general weighting function $\tilde{g}_\alpha(\tau-\tau_{\mathrm{int},0})$ (similarly to Eq. 3.1). The parameters K_α and δ_α and $\tilde{g}_\alpha(\tau)$ are determined as follows:

- for $y_{\mathrm{Four},\Delta i}$ ($\Delta i \neq 0$) and y_{corr}: the representation is as determined in Section 3.4.3: dividing the interference coefficient up into terms from subintervals A and C (of the interference delay interval) and using a rectangular weighting function, $\tilde{g}_\alpha(\tau) = g_{\mathrm{un}}(\tau)$ for subinterval A and $\tilde{g}_\alpha(\tau) = g_{\mathrm{un}}(\tau - D_{\mathrm{FFT}} - D_{\mathrm{CP}})$ for subinterval C.

- for $y_{\mathrm{Four},\Delta i}$ ($\Delta i = 0$): the representation is only formally written into the form of Eq. 3.20 without dividing up into subintervals. This simply means that $K_\alpha = 1$, $\delta_\alpha = 0$ and that $\tilde{g}_\alpha(\tau) = g_{\mathrm{Four},0}(\tau)$.

For method type III, the source subcarrier term at frequency ω_{s} in Eq. 3.16 makes use of the (moving) window with a centre frequency $\omega_{\mathrm{win,s}}$ that is nearest to ω_{s} and analogously, the detecting subcarrier term (ω_{d}) uses the nearest window with centre frequency $\omega_{\mathrm{win,d}}$. The representation for method type III can easily be used for calculation method types I and II. For method type II, the only difference is that $\omega_{\mathrm{win,s}}$ equals $\omega_{\mathrm{win,d}}$, as there is one moving window centered around the detecting subcarrier frequency. For method type I, the only difference is that $\omega_{\mathrm{win,s}}$ and $\omega_{\mathrm{win,d}}$ equal ω_{win}, i.e., the centre frequency of the fixed window. Note that the definitions of $\Delta\omega_{\mathrm{d}}$ and $\Delta\omega_{\mathrm{s}}$ (Eqs. 3.17 and 3.18) remain applicable for all methods types. Analogously to Eq. 3.10, the inverse continuous Fourier transform of the channel response shifted to baseband, i.e., $C(\omega - \omega_{\mathrm{win,s}})$ and $C(\omega - \omega_{\mathrm{win,d}})$, are resp. determined by

$$c_{\mathrm{B,s}}(\tau) = \exp(-j\omega_{\mathrm{win,s}}\tau)c(\tau) \tag{3.21}$$

$$c_{\mathrm{B,d}}(\tau) = \exp(-j\omega_{\mathrm{win,d}}\tau)c(\tau) \tag{3.22}$$

From this error analysis, the remaining error can be divided into 3 different error types, referred to as

- $\Delta y_{\alpha,\mathrm{NU}}(\omega_{\mathrm{s}})$, the ***error due to non-uniform windowing***

- $\Delta y_{\alpha,\mathrm{CM}}(\omega_{\mathrm{s}})$, the ***error due to commutation*** (of the weighting function and the convolution with $w(\tau)$)

- $\Delta y_{\alpha,\mathrm{AL}}(\omega_{\mathrm{s}})$, the ***error due to aliasing***,

where $w(\tau)$ the inverse continuous Fourier transform of the window function, $W(\omega)$. As the error types due to non-uniform windowing and due to commutation are strongly dependent on the windowing method and will disappear for a sufficiently large window width, these error types are referred to as **window-related error types**. The error due to aliasing is essentially due to the non-zero frequency resolution.

3.5.2.1 Error due to non-uniform windowing

The *error due to non-uniform windowing* ($\Delta y_{\alpha,\mathrm{NU}}$) is caused by the non-uniform profile of the window and depends on the value of the window function at the source and the detecting subcarrier. For methods without window correction, this error equals

$$\begin{aligned}\Delta y_{\alpha,\mathrm{NU}}(\omega_\mathrm{s}) = K_\alpha\Big(&\big(1 - W(\Delta\omega_\mathrm{s})\big)\tilde{y}(\omega_{\mathrm{win,s}} + \Delta\omega_\mathrm{s}) \\ &- \delta_\alpha\big(1 - W(\Delta\omega_\mathrm{d})\big)\tilde{y}(\omega_{\mathrm{win,d}} + \Delta\omega_\mathrm{d})\Big)\end{aligned} \tag{3.23}$$

This error is negligible compared to the interference coefficient (Eq. 3.16) if the window function is approximately 1 at both the source and the detecting subcarrier frequency. If the detecting subcarrier term is not involved (i.e., δ_α equals zero), the requirement is only on the source subcarrier. For methods using window correction, the error equals

$$\Delta y_{\alpha,\mathrm{NU}}(\omega_\mathrm{s}) = K_\alpha\delta_\alpha\left(1 - \frac{W(\Delta\omega_\mathrm{d})}{W(\Delta\omega_\mathrm{s})}\right)\tilde{y}(\omega_{\mathrm{win,d}} + \Delta\omega_\mathrm{d}) \tag{3.24}$$

This shows that the error becomes negligible when the window function has approximately the same value at both the source and the detecting subcarrier and may be smaller than 1. If the detecting subcarrier term is not involved, the error disappears.

3.5.2.2 Error due to commutation

From the error analysis, the *error due to commutation* is determined for methods without window correction by:

$$\begin{aligned}\Delta y_{\alpha,\mathrm{CM}}(\omega_\mathrm{s}) = K_\alpha\Delta f_\mathrm{win}^{-1}\int_{-\infty}^{\infty}\Bigg[&\hat{c}_{\mathrm{B,s}}(\tau)\sum_{k=-\infty}^{\infty}\Big(\tilde{g}_\alpha(\tau_k - \tau_{\mathrm{int},0}) - \tilde{g}_\alpha(\tau - \tau_{\mathrm{int},0})\Big) \\ &\times w(\tau - \tau_k)\exp\big(-j\tau_k\Delta\omega_\mathrm{s}\big)\Bigg]\,\mathrm{d}\tau \\ - K_\alpha\delta_\alpha\Delta f_\mathrm{win}^{-1}\int_{-\infty}^{\infty}\Bigg[&\hat{c}_{\mathrm{B,d}}(\tau)\sum_{k=-\infty}^{\infty}\Big(\tilde{g}_\alpha(\tau_k - \tau_{\mathrm{int},0}) - \tilde{g}_\alpha(\tau - \tau_{\mathrm{int},0})\Big) \\ &\times w(\tau - \tau_k)\exp\big(-j\tau_k\Delta\omega_\mathrm{d}\big)\Bigg]\,\mathrm{d}\tau\end{aligned} \tag{3.25}$$

The channel appears in Eq. 3.25 under an aliased form. At a delay component τ, the sum of all physical channel components with a delay of $\tau + l\Delta f_\mathrm{res}^{-1}$, where l is

an integer, is detected:

$$\hat{c}_{\mathrm{B,s}}(\tau) = \sum_{l=-\infty}^{\infty} c_{\mathrm{B,s}}(\tau - l\Delta f_{\mathrm{res}}^{-1}) \tag{3.26}$$

and analogously for $\hat{c}_{\mathrm{B,d}}(\tau)$. Assuming that the real channel impulse response is negligible outside the time window, this aliased form means approximately that the real channel impulse response over the time window, $[0, \Delta f_{\mathrm{res}}^{-1}]$, is periodically extended. In fact, the first term in Eq. 3.25, due to the source subcarrier term (Eq. 3.16), is physically similar to the second term, due to the detecting subcarrier term. Each channel component (τ) of the channel impulse response in aliased form causes an error detected at any other delay point τ_k (Eq. 3.25), if the weighting function differs as evaluated at τ and τ_k. This error is then proportional to $w(\tau - \tau_k)$. Thus, $\Delta y_{\alpha,\mathrm{CM}}(\omega_{\mathrm{s}})$ is the error due to the commutation of the weighting function and the convolution with $w(\tau)$.

The implications of the commutation error are carried out in more detail. First note that, apart from $\tilde{g}_{\mathrm{Four},0}(\tau - \tau_{\mathrm{int},0})$, the weighting function has a rectangular profile with a start ($\tau_{\mathrm{int},1}$) that is typically located at least the CP length after the first arriving path (Section 2.2). Without losing generality, we assume that the weighting functions are cut off at a delay $\tau_{\mathrm{int},2}$, as is typically done for IEEE 802.11. Consequently, the interference delay interval is restricted to $[\tau_{\mathrm{int},1}, \tau_{\mathrm{int},2}]$, where $\tilde{g}_{\mathrm{Four},0}(\tau - \tau_{\mathrm{int},0})$ has just a linear profile ($\propto (\tau - \tau_{\mathrm{int},1})$) and the other weighting functions are uniform (Fig. 3.3). Two implications can be drawn:

- A *first implication* is that, for the rectangular weighting function, the channel components τ in a region of the order of $\Delta f_{\mathrm{win}}^{-1}$ around $\tau_{\mathrm{int},1}$ and $\tau_{\mathrm{int},2}$ will cause an error as detected by delay points τ_k in the respective regions (Fig. 3.3). This is mainly due to the mainlobe of $w(\tau)$, i.e., the resolution error, but also the first few sidelobes may contribute in the same order. The latter is referred to as *near leakage*. For the linear profile, the error around $\tau_{\mathrm{int},1}$ is strongly reduced, but there is a comparable error over the whole interference delay interval. Around $\tau_{\mathrm{int},2}$, where the weighting function is cut off, the error is similar to a rectangular profile. As all these errors are due to a convolution distance, $\tau - \tau_k$, of the order of $\Delta f_{\mathrm{win}}^{-1}$, this error type is referred to as the error due to a non-zero time resolution or ***resolution error***.

- A *second implication* is that strong channel components outside the interference delay interval may cause an error as detected inside the interval, even when these channel components are located many times the sidelobe width, i.e., $\Delta f_{\mathrm{win}}^{-1}$, from the interference delay interval, implying a very small $w(\tau - \tau_k)$. This type of leakage error is referred to as ***far leakage***. The first arriving (strongest) paths, which form the signal, lie typically out of the interference delay interval. This set of strongest channel components

is periodically extended in the aliased channel form, resulting in two main sources of far leakage: (i) the physical (non-extended) set of channel components, referred to as ***direct leakage***, and (ii) its replica appearing at a delay of $\Delta f_{\mathrm{res}}^{-1}$ higher, referred to as ***aliased leakage*** (Fig. 3.3). Note that aliased leakage is essentially due to a finite window width and a non-zero frequency resolution jointly.

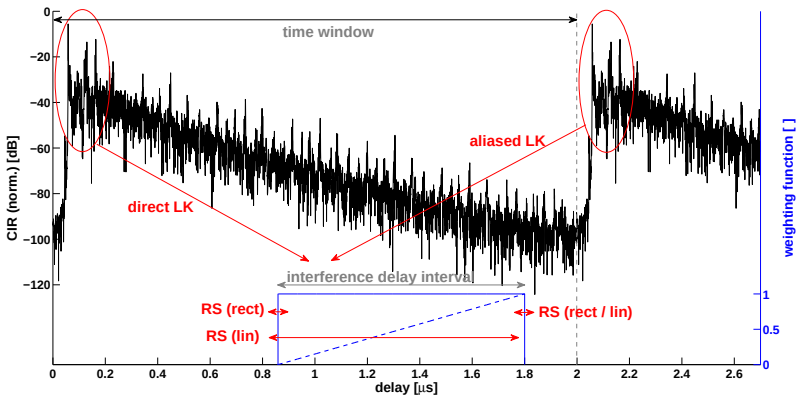

Figure 3.3: Channel impulse response (CIR) in aliased form, measured over a time window of 2 µs*. The CIR is normalized to the total power. Weighting functions with a rectangular ("rect", solid) and a linear ("lin", dash) profile are shown for an interference delay interval for* 800 ns *CP. Different error types due to a non-zero time resolution and leakage ("LK") are indicated: (i) direct leakage, (ii) aliased leakage, (iii) resolution error ("RS") (including near leakage) for both weighting function profiles.*

In a strict sense, the commutation error can be divided into a term (in Eq. 3.25) due to the mainlobe part of $w(\tau)$ and a term due to the sidelobe part. The former term is then strictly due to the non-zero time resolution and the latter due to leakage. However, it is more physical to join the near leakage with the resolution error. Therefore, the joint error will simply referred to as "resolution": $\Delta y_{\alpha,\mathrm{RS}}(\omega_{\mathrm{s}})$. The error due to direct and aliased leakage are denoted as $\Delta y_{\alpha,\mathrm{LK},\,\mathrm{dir}}(\omega_{\mathrm{s}})$ and $\Delta y_{\alpha,\mathrm{LK},\,\mathrm{al}}(\omega_{\mathrm{s}})$, respectively.

3.5.2.3 Error due to aliasing

For windowing methods without window correction, the *error due to aliasing*, $\Delta y_{\alpha,\mathrm{AL}}(\omega_\mathrm{s})$, is determined from the error analysis as

$$\begin{aligned}\Delta y_{\alpha,\mathrm{AL}}(\omega_\mathrm{s}) = \\ K_\alpha \Delta f_\mathrm{win}^{-1} \sum_{k=-\infty}^{\infty} \left[w(\tau) * \left(\tilde{g}_\alpha(\tau - \tau_{\mathrm{int},0}) \Big(\hat{c}_{\mathrm{B,s}}(\tau) - c_{\mathrm{B,s}}(\tau) \Big) \right) \right] (\tau_k) \\ \times \exp\big(-j\tau_k \Delta\omega_\mathrm{s}\big) \\ - K_\alpha \delta_\alpha \Delta f_\mathrm{win}^{-1} \sum_{k=-\infty}^{\infty} \left[w(\tau) * \left(\tilde{g}_\alpha(\tau - \tau_{\mathrm{int},0}) \Big(\hat{c}_{\mathrm{B,d}}(\tau) - c_{\mathrm{B,d}}(\tau) \Big) \right) \right] (\tau_k) \\ \times \exp\big(-j\tau_k \Delta\omega_\mathrm{d}\big)\end{aligned} \tag{3.27}$$

This error corresponds to the interference coefficient that would be obtained based on the **non-physical contributions in the aliased form of the channel impulse response**, $\hat{c}_{\mathrm{B,s}}(\tau)$ and $\hat{c}_{\mathrm{B,d}}(\tau)$. Indeed, in the interference delay interval, this aliased form contains contributions of real channel components that are shifted over a multiple of $\Delta f_\mathrm{res}^{-1}$. If the time window is large enough, these non-physical contributions are negligible to the real channel component in the interference delay interval, resulting into an error that is negligible compared to the interference coefficient. Assuming that the channel impulse response decays roughly exponentially with τ_r as a time constant, the relative error power is of the order of $\exp(-1/(\Delta f_\mathrm{res}\tau_\mathrm{r}))$. Note that, if the interference delay interval is cut off, the corresponding error $\Delta y_{\alpha,\mathrm{CO}}(\omega_\mathrm{s})$ is typically larger than $\Delta y_{\alpha,\mathrm{AL}}(\omega_\mathrm{s})$, as the former is based on real channel components with a lower delay, starting already from $\tau_{\mathrm{int},2}$.

3.5.2.4 Error due to commutation and aliasing for methods using window correction

For methods using window correction, $\Delta y_{\alpha,\mathrm{CM}}(\omega_\mathrm{s})$ and $\Delta y_{\alpha,\mathrm{AL}}(\omega_\mathrm{s})$ are defined in the same way as for methods without window correction (Eqs. 3.26 and 3.27), but these are subsequently divided by the window function evaluated at the source subcarrier frequency, $W(\Delta\omega_\mathrm{s})$. Obviously, this also applies to the error terms related to $\Delta y_{\alpha,\mathrm{CM}}(\omega_\mathrm{s})$, i.e., $\Delta y_{\alpha,\mathrm{RS}}(\omega_\mathrm{s})$, $\Delta y_{\alpha,\mathrm{LK,\,dir}}(\omega_\mathrm{s})$ and $\Delta y_{\alpha,\mathrm{LK,\,al}}(\omega_\mathrm{s})$.

3.5.3 Overall error

As a conclusion, the total error equals

$$\begin{aligned}\Delta y_\alpha = \Delta y_{\alpha,\mathrm{CO}} + \Delta y_{\alpha,\mathrm{MN}} + \Delta y_{\alpha,\mathrm{NU}} + \Delta y_{\alpha,\mathrm{RS}} \\ + \Delta y_{\alpha,\mathrm{LK,\,dir}} + \Delta y_{\alpha,\mathrm{LK,\,al}} + \Delta y_{\alpha,\mathrm{AL}}\end{aligned} \tag{3.28}$$

where the argument (ω_{s}) is omitted to shorten the notation.

3.6 Relative error power versus dB-scaled deviation

If the interference coefficient, $y_\alpha(\omega_\mathrm{s})$, is measured with an error $\Delta y_\alpha(\omega_\mathrm{s})$ over a certain calculation range, the question is still how to quantify the accuracy. First, the interference coefficient is subject to fading-like fluctuations as a function of the source subcarrier frequency (ω_s), as it originates from a set of channel (time-domain) components with a delay separation of the order of the reverberation time. E.g., for a τ_r of $100\ \mathrm{ns}$, the coherence frequency width is of the order of $10\ \mathrm{MHz}$. The deviation in dB of the interference coefficient may become large as ω_s approaches a fade. Second, the error may be correlated with the interference coefficient over the calculation range, resulting into a raised deviation in dB. The error due to non-uniform windowing is expected to be correlated, as follows directly from Eqs. 3.23 and 3.24. The measurement noise may also be correlated to the interference coefficient if it is dominated by multiplicative noise.

3.6.1 Spectral interference power

The different error types, defined in Section 3.5, are in preference physically analyzed in terms of the error power averaged over the calculation range. For the *spectral interference*, the absolute error power, $E_{\alpha'}$, is defined as:

$$E_{\alpha'} = \langle |\Delta y_\alpha(\omega_\mathrm{s})|^2 \rangle_{\omega_\mathrm{s}}, \tag{3.29}$$

where $\langle \cdot \rangle_{\omega_\mathrm{s}}$ indicates that the (linear-scaled) average is taken over the source subcarrier frequency range of interest. Note that α indicates the interference coefficient's index "corr", "$\mathrm{Four}, \Delta i$" or "$\mathrm{tot}, \Delta i$". α' is an extended index, indicating (i) the coefficient type (y_corr / y_Four / y_tot) and (ii) the subcarrier separation (Δi) when determining the spectral interference. Note that also for the y_corr type coefficient, $E_{\alpha'}$ is theoretically dependent on Δi. Indeed, the actual source subcarrier frequency range is Δi dependent, as the detecting subcarrier frequency range is assumed to be fixed. The relative error power, $\tilde{E}_{\alpha'}$, is defined by the ratio between $E_{\alpha'}$ and the frequency-averaged power of the corresponding interference coefficient, $I_{\alpha',\mathrm{av}}$:

$$\tilde{E}_{\alpha'} = \frac{E_{\alpha'}}{I_{\alpha',\mathrm{av}}}, \tag{3.30}$$

where

$$I_{\alpha',\mathrm{av}} = \langle |y_\alpha(\omega_\mathrm{s})|^2 \rangle_{\omega_\mathrm{s}} \tag{3.31}$$

The relative error power will be used as a tractable and physically meaningful accuracy metric, but does not tell directly at which deviation in dB the interference coefficient is obtained. This depends on whether the interest is in the frequency-averaged or frequency-dependent interference power and on the degree of correlation with the error.

3.6.1.1 Frequency-dependent interference power

If the aim is to determine the interference coefficient (or power) as a function of the frequency, the interest is rather in the range of the order of the root-mean-square (rms) level than in the fades. Therefore, the deviation in dB is formally quantified with respect to the rms level. The dB-scaled deviation is defined as function of the detecting subcarrier frequency (ω_{d}):

$$\Delta I_{\alpha'}(\omega_{\mathrm{d}}) = 20\log\Big(\Big|\frac{y_{\alpha}(\omega_{\mathrm{s}}) + \Delta y_{\alpha}(\omega_{\mathrm{s}})}{y_{\alpha}(\omega_{\mathrm{s}})}\Big|\Big) \tag{3.32}$$

where $\omega_{\mathrm{d}} = \omega_{\mathrm{s}} + \Delta i \Delta\omega_{\mathrm{subc}}$. Assuming that the local rms level is relatively constant over the calculation range, the overall rms level, $y_{\alpha',\mathrm{rms}}$, is used as reference to determine the dB-scaled deviation:

$$\Delta I_{\alpha'}(\omega_{\mathrm{d}}) = 20\log\Big(\Big|\frac{y_{\alpha',\mathrm{rms}} + \Delta y_{\alpha}(\omega_{\mathrm{s}})}{y_{\alpha',\mathrm{rms}}}\Big|\Big) \tag{3.33}$$

$$\approx 20\log(\mathrm{e})\frac{\Re[\Delta y_{\alpha}(\omega_{\mathrm{s}})]}{y_{\alpha',\mathrm{rms}}} \tag{3.34}$$

where $y_{\alpha',\mathrm{rms}} = I_{\alpha',\mathrm{av}}^{1/2}$ and e is Euler's number and $\Re[\,\cdot\,]$ represents the real part of a complex number. In Eq. 3.34, it is assumed that the error is much smaller than the rms level. Assuming that the phase of the error is uniformly distributed over the calculation range (i.e., no correlation between error and coefficient at rms level), it follows from Eq. 3.34 that the standard deviation of $\Delta I_{\alpha'}(\omega_{\mathrm{d}})$ over the detecting subcarrier frequency range of interest is related to the relative error power as follows:

$$\Big(\langle|\Delta I_{\alpha'}(\omega_{\mathrm{d}})|^2\rangle_{\omega_{\mathrm{d}}}\Big)^{1/2} \approx 6.14\ \tilde{E}_{\alpha'}^{1/2} \tag{3.35}$$

Note that $\tilde{E}_{\alpha'}$ is in linear scale. Thus, for a dB-scaled deviation (at rms level) with a standard deviation of $1\ \mathrm{dB}$, a relative error power of maximum $-15.8\ \mathrm{dB}$ is required. Assuming that the error is distributed as a complex Gaussian variable, the averaged absolute value of the dB-scaled deviation is a factor $(2/\pi)^{0.5}$ lower than the standard deviation:

$$\langle|\Delta I_{\alpha'}(\omega_{\mathrm{d}})|\rangle_{\omega_{\mathrm{d}}} \approx 4.90\ \tilde{E}_{\alpha'}^{1/2} \tag{3.36}$$

Thus, for a dB-scaled deviation with an averaged absolute value of $1\ \mathrm{dB}$, a relative error power of maximum $-13.8\ \mathrm{dB}$ is required. If the error is assumed to be *completely* correlated with the interference coefficient at rms level, the factor in the right-hand side of Eqs. 3.35 and 3.36 is a factor $\sqrt{2}$ higher. The case of a *complete* correlation refers to a linear relationship of the error: $\Delta y_{\alpha}(\omega_{\mathrm{s}}) = \epsilon y_{\alpha}(\omega_{\mathrm{s}})$, where ϵ is a constant for all ω_{s}.

3.6.1.2 Frequency-averaged interference power

If the aim is to determine the frequency-averaged spectral interference power, the dB-scaled deviation is determined by

$$\Delta I_{\alpha',\mathrm{av}} = 10\log\left(\frac{\langle\left|y_\alpha(\omega_\mathrm{s})+\Delta y_\alpha(\omega_\mathrm{s})\right|^2\rangle_{\omega_\mathrm{s}}}{\langle\left|y_\alpha(\omega_\mathrm{s})\right|^2\rangle_{\omega_\mathrm{s}}}\right) \tag{3.37}$$

This can be generally related to the relative error power, $\tilde{E}_{\alpha'}$, based on the Cauchy-Schwarz inequality:

$$20\log\left(1-\tilde{E}_{\alpha'}^{1/2}\right) \le \Delta I_{\alpha',\mathrm{av}} \le 20\log\left(1+\tilde{E}_{\alpha'}^{1/2}\right) \tag{3.38}$$

If $\tilde{E}_{\alpha'}$ is much smaller than 1, Eq. 3.38 is in good approximation equivalent to

$$|\Delta I_{\alpha',\mathrm{av}}| \le 8.69\ \tilde{E}_{\alpha'}^{1/2} \tag{3.39}$$

For a dB-scaled deviation with an absolute value of maximum 1 dB, it follows from Eq. 3.38 that a relative error power of maximum -19.3 dB is required. If the error is not correlated with the interference coefficient, the first order error is cancelled out by the frequency averaging:

$$\langle\left|y_\alpha(\omega_\mathrm{s})+\Delta y_\alpha(\omega_\mathrm{s})\right|^2\rangle_{\omega_\mathrm{s}} \approx \langle\left|y_\alpha(\omega_\mathrm{s})\right|^2\rangle_{\omega_\mathrm{s}} + \langle\left|\Delta y_\alpha(\omega_\mathrm{s})\right|^2\rangle_{\omega_\mathrm{s}} \tag{3.40}$$

Consequently, the dB-scaled deviation equals

$$\Delta I_{\alpha',\mathrm{av}} \approx 10\log(1+\tilde{E}_{\alpha'}) \tag{3.41}$$

$$\approx 4.34\ \tilde{E}_{\alpha'} \tag{3.42}$$

where in Eq. 3.42, $\tilde{E}_{\alpha'}$ is assumed to be much smaller than 1. From Eq. 3.41, it follows that a relative error power of maximum -5.9 dB is required for an interference power deviation of 1 dB.

3.6.2 Total interference power

When determining the total interference, α' indicates (i) the coefficient type and (ii) the subcarrier separation range over which all spectral terms are added up. The absolute error power, $E_{\alpha'}$, is then obtained by summing up the frequency-averaged spectral error terms:

$$E_{\alpha'} = \sum_{\Delta i}\langle|\Delta y_{\alpha(\Delta i)}(\omega_\mathrm{s})|^2\rangle_{\omega_\mathrm{s}}, \tag{3.43}$$

where $\alpha(\Delta i)$ denotes that α varies with Δi. The relative error power, $\tilde{E}_{\alpha'}$, remains defined by Eq. 3.30, where the frequency-averaged total interference power is obtained by summing up the frequency-averaged spectral interference terms:

$$I_{\alpha',\mathrm{av}} = \sum_{\Delta i}\langle|y_{\alpha(\Delta i)}(\omega_\mathrm{s})|^2\rangle_{\omega_\mathrm{s}} \tag{3.44}$$

The dB-scaled deviation on the *frequency-dependent* total interference power is determined similarly to the spectral interference (Eq. 3.32):

$$\Delta I_{\alpha'}(\omega_{\mathrm{d}}) = 10\log\left(\frac{\sum_{\Delta i}\left|y_{\alpha(\Delta i)}(\omega_{\mathrm{d}}-\Delta i\Delta\omega_{\mathrm{subc}})+\Delta y_{\alpha(\Delta i)}(\omega_{\mathrm{d}}-\Delta i\Delta\omega_{\mathrm{subc}})\right|^2}{\sum_{\Delta i}\left|y_{\alpha(\Delta i)}(\omega_{\mathrm{d}}-\Delta i\Delta\omega_{\mathrm{subc}})\right|^2}\right) \tag{3.45}$$

where the spectral interference power terms are added up as a function of the detecting subcarrier frequency (ω_{d}). The dB-scaled deviation on the *frequency-averaged* total interference is also determined similarly to the spectral interference (Eq. 3.37):

$$\Delta I_{\alpha',\mathrm{av}} = 10\log\left(\frac{\sum_{\Delta i}\langle\left|y_{\alpha(\Delta i)}(\omega_{\mathrm{s}})+\Delta y_{\alpha(\Delta i)}(\omega_{\mathrm{s}})\right|^2\rangle_{\omega_{\mathrm{s}}}}{\sum_{\Delta i}\langle\left|y_{\alpha(\Delta i)}(\omega_{\mathrm{s}})\right|^2\rangle_{\omega_{\mathrm{s}}}}\right) \tag{3.46}$$

The dB-scaled deviation of the total interference is related to the total relative error power in the same way as for the spectral interference. Thus, for the frequency-dependent total interference power, Eqs. 3.35 and 3.36 are still applicable and Eqs. 3.38, 3.39, 3.41 and 3.42 for the frequency-averaged total interference power.

3.6.3 Conclusion

In practice, the required relative error power is determined from the required dB-scaled deviation depending on (i) whether the frequency-dependent or frequency-averaged interference is to be determined and (ii) whether correlation between the interference coefficient and the error is taken into account. From the resulting required relative error power, $\tilde{E}_{\mathrm{thresh}}$, the required measurement settings are determined. Unless otherwise mentioned, a $\tilde{E}_{\mathrm{thresh}}$ requirement of -14 dB will be further considered, based on an average absolute dB-scaled deviation of 1 dB of the frequency-dependent interference power at rms level, assuming no correlation (Eq. 3.36).

3.7 APDP-based expression for the frequency-averaged interference power

In this section, an APDP-based estimation method is presented for the frequency-averaged interference power, $I_{\alpha',\mathrm{av}}$, defined in Section 3.6. Based on the room electromagnetics theory, this estimation method allows to investigate analytically the error power due to a time-domain cut-off (Section 3.8) and the interference power (Chapter 7) as a function of the reverberation time.

The estimation method is obtained by considering two cases. The first case refers to (i) the y_{corr} coefficient or to (ii) $y_{\mathrm{Four},\Delta i}$ with a small subcarrier frequency separation compared to the window width (i.e., $|\Delta i|/D_{\mathrm{FFT}} \ll \Delta f_{\mathrm{win}}$). The second case considers the $y_{\mathrm{Four},\Delta i}$ coefficient with a subcarrier frequency separation of the order of the window width or larger.

In the first case, the estimation method is based on Eqs. 3.11 and 3.12. The interference coefficient, $y_\alpha(\omega_\mathrm{s})$, is obtained as a time-domain summation using the composed weighting function, $g_\alpha(\tau)$, and a discrete time-domain channel representation, $c_{\mathrm{IDFT},\infty}(k)$, obtained with an infinitely small frequency resolution and baseband with respect to the window centre frequency ($\omega_{\mathrm{win,d}}$) corresponding to the detecting subcarrier:

$$W(\omega_\mathrm{s}-\omega_{\mathrm{win,d}})y_\alpha(\omega_\mathrm{s}) \approx \sum_{k=-\infty}^{\infty} g_\alpha(\tau_k-\tau_{\mathrm{int},0})\; c_{\mathrm{IDFT},\infty}(k)\; \exp(-j\tau_k(\omega_\mathrm{s}-\omega_{\mathrm{win,d}})), \tag{3.47}$$

where

$$c_{\mathrm{IDFT},\infty}(k) = \Delta f_{\mathrm{win}}^{-1}\big[w(\tau) * c_{\mathrm{B,d}}(\tau)\big](\tau_k) \tag{3.48}$$

Note that Eq. 3.47 only applies if the windowing method used performs properly, i.e., if the window width (or the measurement range) is sufficiently large. Assuming that in addition to the actual source subcarrier frequency (ω_s) of interest, Eq. 3.47 largely holds over the whole window, i.e., $|\omega_\mathrm{s}-\omega_{\mathrm{win,d}}| < \pi\Delta f_{\mathrm{win}}$, Parseval's theorem can be applied to estimate the frequency-averaged spectral interference power (i.e., squared magnitude of the interference coefficient):

$$I_{\alpha',\mathrm{av}} \approx R_{\mathrm{win}}^{-1} \sum_{k=-\infty}^{\infty} |g_\alpha(\tau_k-\tau_{\mathrm{int},0})|^2 \langle |c_{\mathrm{IDFT},\infty}(k)|^2\rangle_{\omega_{\mathrm{win,d}}} \tag{3.49}$$

where $\langle\,\cdot\,\rangle_{\omega_{\mathrm{win,d}}}$ denotes that the average is taken over all window centre frequencies ($\omega_{\mathrm{win,d}}$) in the case of a moving window (method types II and III) and repre-

sents then an APDP. R_{win} is the normalized energy of the window function:

$$R_{\mathrm{win}} = 2\pi\Delta f_{\mathrm{win}}^{-1} \int_{-\pi\Delta f_{\mathrm{win}}}^{\pi\Delta f_{\mathrm{win}}} |W(\omega)|^2 \,\mathrm{d}\omega \tag{3.50}$$

R_{win} equals $3/8$ and 1 for a Hann and a rectangular window, respectively. Due to Parseval's theorem, implying a frequency-domain integration over the *full* window, the frequency-averaged interference power as estimated by Eq. 3.49 is actually based on the whole measurement range, while the interest is only in the calculation range. Therefore, Eq. 3.49 is applicable on assumption that the effect of this frequency range mismatch is negligible. In particular, this is the case if the locally frequency-averaged interference power is constant over the whole measurement range, i.e., the interference power is not essentially frequency-dependent (apart from fading-like variations).

In the second case, where the subcarrier frequency separation is no longer much smaller than the window width, Eq. 3.47 cannot hold over the whole window. However, assuming that the window width is much larger than τ_{r}^{-1} to suppress the resolution error (Section 3.9), the subcarrier frequency separation is much larger than τ_{r}^{-1}. The latter is of the order of the frequency coherence width of the generalized interference coefficient, which is then uncorrelated between source and detecting subcarrier frequency. Based on the representation in terms of the generalized interference coefficient (Eq. 3.16) and a derivation analogous to the first case (in terms of the generalized weighting function), it is found that Eq. 3.49 is still an estimation of the frequency-averaged interference power.

3.8 Error power due to a time-domain cut-off

In theory, the duration of the interference delay interval for ISI and ICI is twice the FFT integration time (D_{FFT}) plus the CP length (D_{CP}) (Section 2.2). For IEEE 802.11, where the reverberation time (τ_{r}) of an indoor channel is typically much smaller than the FFT integration time (i.e., 3.2 µs), the interval duration can be shortened by cutting off the weighting function, resulting into a smaller required time window. In this section, it is analytically investigated at which delay the weighting function may be cut off to have the resulting relative error power below a given accuracy level. This is important to determine in practice which time window or frequency resolution is required for the channel measurement. It is expected that the interval duration after a cut-off, $\Delta\tau_{\mathrm{CO}}$, should be of the order of the reverberation time, though a detailed analysis is needed because of the effect of the weighting function's profile.

The analysis is based on the APDP-based estimation of the interference power (Eq. 3.49). By definition (Section 3.5), the absolute error power due to a cut-off corresponds to the interference power caused by channel components with a delay higher than the cut-off delay, $\tau_{\mathrm{int},2}$. Therefore, the absolute error power is estimated using Eq. 3.49, where the summation is restricted to delay taps τ_k higher than $\tau_{\mathrm{int},2}$. The interference power is estimated based on Eq. 3.49 without cut-off. Based on the theory of room electromagnetics, the APDP in Eq. 3.49 decays exponentially with τ_{r} as a time constant, allowing to analyze the relative error power due a cut-off in terms of the reverberation time.

In the analysis, the following parameters are considered: a reverberation time ranging over $[10, 400]$ ns, a CP length of 400 ns or 800 ns and an FFT size (N_{sample}) of 64 or 512 (IEEE 802.11n [26] and 11ac [27], resp.). The relative error power is determined as a function of the cut-off interval duration, $\Delta\tau_{\mathrm{CO}}$, ranging from zero to D_{FFT}. This is carried out for all subcarrier separations (Δi) and different coefficient types (y_{corr}, $y_{\mathrm{Four},\Delta i}$ and $y_{\mathrm{tot},\Delta i}$). For all parameter values, it is found that the relative error power is the largest for $y_{\mathrm{Four},0}$ (at a zero Δi), which is typically the most important interference coefficient. This can be explained by the weighting function's profile in subinterval A, considering that subintervals B and C of the interference delay interval can be neglected due to the reverberation time being considerably smaller than D_{FFT}. For $y_{\mathrm{Four},0}$, where the profile is linear, the profile's centre is located at a higher delay, whereas otherwise the profile is more uniformly distributed (Fig. 2.5).

As a second part of the analysis, the required interval duration ($\Delta\tau_{\mathrm{CO}}$) to achieve a relative error power of -14 dB is then determined based on the coefficient $y_{\mathrm{Four},0}$. Over all parameters values, the ratio between the required $\Delta\tau_{\mathrm{CO}}$ and τ_{r} ranges between 6.5 and 6.6, showing a limited variation. Indeed, since this required interval duration is at least once the reverberation time smaller than

D_{FFT}, there is a good agreement with the case of an infinite D_{FFT}. In this case, providing an upper limit estimation, the relative error power due to a cut-off ($\tilde{E}_{\mathrm{CO}}$) can be analytically determined by the following simple expression:

$$\tilde{E}_{\mathrm{CO}} \approx \frac{\int_{\Delta\tau_{\mathrm{CO}}}^{\infty} \left(\frac{\Delta\tau}{D_{\mathrm{FFT}}}\right)^2 \exp(-\Delta\tau/\tau_{\mathrm{r}})\,\mathrm{d}\Delta\tau}{\int_{0}^{\infty} \left(\frac{\Delta\tau}{D_{\mathrm{FFT}}}\right)^2 \exp(-\Delta\tau/\tau_{\mathrm{r}})\,\mathrm{d}\Delta\tau} \tag{3.51}$$

$$\approx \exp(-x)(1 + x + 0.5x^2), \tag{3.52}$$

where x is the ratio between $\Delta\tau_{\mathrm{CO}}$ and τ_{r}. From Eq. 3.52, it follows that, to achieve a -14 dB relative error power, the ratio between the interval duration and τ_{r} should be 6.6.

The main conclusion is that, to suppress the relative error power due to a cut-off below -14 dB, the cut-off must be applied at a delay exceeding the start of the interference delay interval by at least 6.6 times the reverberation time. This requirement is most critically determined by the spectral interference at a zero subcarrier separation. Experimental validation will be provided in Section 6.3.

3.9 Error power due to a non-zero time resolution and leakage

In this section, theoretical estimation methods of the relative error power due to resolution (including near leakage), direct and aliased leakage are presented. These estimations are used to determine the restricting error type with respect to the measurement range requirement for different windowing methods (Chapters 5), giving important insight into the method's performance and the measurement range requirement. To calculate the real type-specific error powers corresponding to a certain window width (Δf_{win}), the channel impulse response needs to be measured with a much larger window width (i.e., a much smaller time resolution). This may require a much larger measurement range than the one corresponding to Δf_{win}, especially for method type I. Moreover, the computational capacity required is of a higher order (compared to the calculation of the interference). Therefore, a theoretical estimation of the error power is introduced. For the error power due to resolution, a theoretical estimation for the y_{corr} coefficient type is proposed in terms of the window width and the reverberation time. For the $y_{\mathrm{Four},\Delta i}$ coefficient, the resolution error power is related to the theoretical estimation derived for y_{corr}. For the error power due to direct and aliased leakage, the theoretical estimation proposed is based on a one-tap representation of the set of time-domain channel components causing direct and aliased leakage, respectively. The calculation method of the real error power is described in Section 3.9.1, while the theoretical estimation of the error power due to resolution and leakage is presented in Sections 3.9.2 and 3.9.3, respectively. The theoretical estimation methods are experimentally validated in Section 5.1.

3.9.1 Calculation method of the error power due to resolution and leakage

The calculation method of the real error power due to resolution and leakage is based on the error due to commutation (Eq. 3.25). Both terms in Eq. 3.25, corresponding to the source and detecting subcarrier, resp., are similarly calculated. E.g., the first term is rewritten as a DFT-like transformation:

$$\Delta y_{\alpha,\mathrm{CM}}(\omega_{\mathrm{s}}) = K_{\alpha}\Delta f_{\mathrm{win}}^{-1}\sum_{k=-\infty}^{\infty} c_{\mathrm{CM}}(k)\exp\bigl(-j\tau_k\Delta\omega_{\mathrm{s}}\bigr) \;+\; \text{2nd term} \quad (3.53)$$

where the time-domain coefficients $c_{\mathrm{CM}}(k)$ are determined as

$$\begin{aligned} c_{\mathrm{CM}}(k) = &\Bigl[\tilde{g}_{\alpha}(\tau-\tau_{\mathrm{int},0})\Bigl(w(\tau)*\hat{c}_{\mathrm{B,s}}(\tau)\Bigr)\Bigr](\tau_k) \\ &-\Bigl[w(\tau)*\Bigl(\tilde{g}_{\alpha}(\tau-\tau_{\mathrm{int},0})\hat{c}_{\mathrm{B,s}}(\tau)\Bigr)\Bigr](\tau_k) \end{aligned} \quad (3.54)$$

Remind that $\hat{c}_{\mathrm{B,s}}(\tau)$ is the (baseband) channel impulse response in aliased form and that $\tau_{\mathrm{int},0}$ is defined as $\tau_{\mathrm{int},1} + D_{\mathrm{FFT}}$, where $\tau_{\mathrm{int},1}$ is the start delay of the interference delay interval (for ISI/ICI). τ_k are the discrete delay taps (i.e., $k\Delta f_{\mathrm{win}}^{-1}$, where k is an integer) and $w(\tau)$ is the (continuous) inverse Fourier transform of the window function. Remind also that $\Delta\omega_{\mathrm{s}}$ is the excess of the source subcarrier frequency (ω_{s}) with respect to the window centre frequency. The coefficients $c_{\mathrm{CM}}(k)$ are to be determined for τ_k in a delay range exceeding the interference delay interval, so that the near leakage at the interval's edges is captured. Outside this delay range, $c_{\mathrm{CM}}(k)$ is negligible.

The determination of $c_{\mathrm{CM}}(k)$ is carried out by convolution of the τ-dependent function in the right-hand side of Eq. 3.54 with a test pulse, $w_{\mathrm{test}}(\tau)$, being the (continuous) inverse Fourier transform of a Hann window with a frequency width, $\Delta f_{\mathrm{win,test}}$, much larger than the actual window width (Δf_{win}) for which the error power is calculated. In this way, it follows mathematically from Eq. 3.54 that the coefficients $c_{\mathrm{CM}}(k)$ can be calculated based on a (discretized) convolution between $w(\tau)$ and a time-domain channel with the fine time resolution ($\Delta f_{\mathrm{win,test}}^{-1}$). This channel is determined in terms of the IDFT of the large-windowed channel response (Eq. 3.14). The contribution in the commutation error due to resolution (including near leakage), direct and aliased leakage is then obtained by restricting the delay range of the time-domain channel (with the fine time resolution) to the channel components causing the respective error type (Fig. 3.3). For the resolution error power, this is a delay range exceeding the interference delay interval, so that the near leakage at the interval's edges is captured. For the direct and the aliased leakage, the delay range is restricted to the corresponding set of strongest channel components (outside the interference delay interval).

3.9.2 Theoretical estimation of the error power due to resolution: analysis in terms of the reverberation time

In this section, the relative error power due to resolution is related to the reverberation time (τ_{r}) and the window width (Δf_{win}). The main idea is as follows. According to the theory of room electromagnetics [5], the APDP decays exponentially with τ_{r} as a time constant. Assuming that this theory is applicable from a delay $\tau_{\mathrm{int},1}$, the start of the interference delay interval (Fig. 3.3), the interference power is proportional to (i) the average power of the channel component at a delay $\tau_{\mathrm{int},1}$ and to (ii) τ_{r}. For the y_{corr} coefficient, where the weighting function has a rectangular profile, the absolute error power due to resolution mainly originates from channel components centered around $\tau_{\mathrm{int},1}$ with a certain time width, $\Delta\tau_{\mathrm{RS}}$. If the sidelobes of the window's Fourier transform can be neglected, $\Delta\tau_{\mathrm{RS}}$ is of the order of $\Delta f_{\mathrm{win}}^{-1}$. Since the absolute error power is then proportional to (i) the average power of the channel component at a delay $\tau_{\mathrm{int},1}$ and to (ii) $\Delta f_{\mathrm{win}}^{-1}$, it follows

that the relative error power is inversely proportional to $\Delta f_{\mathrm{win}} \times \tau_{\mathrm{r}}$.

For the $y_{\mathrm{Four},\Delta i}$ coefficient with a high subcarrier separation ($|\Delta i|$) the situation is comparable, as the weighting function ($g_{\mathrm{Four},\Delta i}(\tau)$) is quasi-uniform (Fig. 2.5). For a smaller subcarrier separation, the weighting function's profile becomes linear (Section 2.2), resulting into two opposite effects. *First*, if $|\Delta i| \ll D_{\mathrm{FFT}}\Delta f_{\mathrm{win}}/2$, the weighting function takes a linear profile around $\tau_{\mathrm{int},1}$ over a delay width of the time resolution, $\Delta f_{\mathrm{win}}^{-1}$. Consequently, the absolute error power that originates from channel components with a delay around $\tau_{\mathrm{int},1}$, is lowered compared to the case of y_{corr}. This is referred to as *cancellation effect*. Note that, although the resolution error is determined in terms of a rectangular weighting function ($\tilde{g}_\alpha(\tau)$) (Eq. 3.25), the two terms in Eq. 3.25, corresponding to the source and detecting subcarrier frequency, resp., can both be combined to one term using the composed weighting function, $g_{\mathrm{Four},\Delta i}(\tau)$. A *second* effect is that, if $|\Delta i|$ further decreases to $|\Delta i| \ll D_{\mathrm{FFT}}\Delta\tau_{\mathrm{CO}}^{-1}/2$, the weighting function's centre is located at a higher delay due to the linear profile. This has an additional adverse effect on the relative error power, contrary to y_{corr}, where the weighting function has a rectangular profile. Based on Eq. 3.49 and a linear weighting function profile, the additional adverse effect implies an 8.6 dB increase of the relative error power. The total effect yields a lowering of the relative error power, as experimentally shown in Section 5.1. In the remainder of this section, the relative error power due to resolution is analyically related to the reverberation time for the y_{corr} coefficient.

For the y_{corr} coefficient, the error power due to resolution originates from channel components with a delay around the edges of the interference delay interval, $[\tau_{\mathrm{int},1}, \tau_{\mathrm{int},2}]$ (Fig. 3.3). The error power due to the right-hand edge can be typically neglected due to the exponential APDP decay. Considering only the left-hand edge, the resolution error is determined as the part of the commutation error (Eq. 3.25) caused by channel components with a delay around $\tau_{\mathrm{int},1}$:

$$\Delta y_{\alpha,\mathrm{RS}}(\omega_{\mathrm{s}}) = K_\alpha \Delta f_{\mathrm{win}}^{-1} \int_{\tau_{\mathrm{int},1}-\Delta\tau_{\mathrm{int},1}}^{\tau_{\mathrm{int},1}+\Delta\tau_{\mathrm{int},1}} \hat{c}_{\mathrm{B,s}}(\tau) g_{\mathrm{CM}}(\tau)\,\mathrm{d}\tau \tag{3.55}$$

where the integration interval, $[\tau_{\mathrm{int},1} - \Delta\tau_{\mathrm{int},1}, \tau_{\mathrm{int},1} + \Delta\tau_{\mathrm{int},1}]$, is sufficiently wide to capture all resolution error power, including near leakage. Note that δ_α (Eq. 3.25) is zero because of the y_{corr} coefficient type. $g_{\mathrm{CM}}(\tau)$ denotes the time-domain function taken over from Eq. 3.25 and describes the contribution of a channel component with a delay τ to the commutation error:

$$g_{\mathrm{CM}}(\tau) = \sum_{k=-\infty}^{\infty} \Big(\tilde{g}_\alpha(\tau_k - \tau_{\mathrm{int},0}) - \tilde{g}_\alpha(\tau - \tau_{\mathrm{int},0})\Big) w(\tau - \tau_k) \exp\big(-j\tau_k \Delta\omega_{\mathrm{s}}\big) \tag{3.56}$$

From Eq. 3.56, $g_{\mathrm{CM}}(\tau)$ is centered around $\tau_{\mathrm{int},1}$ with a certain time width, $\Delta\tau_{\mathrm{RS}}$. If the sidelobes of $w(\tau)$ are neglected, $\Delta\tau_{\mathrm{RS}}$ is of the order of $\Delta f_{\mathrm{win}}^{-1}$. However, the sidelobes may have an essential effect on the width, especially for a rectangular window.

The resolution error is related to the discrete channel component, $c_{\mathrm{IDFT}}(k_1)$, where k_1 is the index of the discrete delay tap (τ_k) nearest to $\tau_{\mathrm{int},1}$. Indeed, the coefficients $c_{\mathrm{IDFT}}(k)$, determined from Eq. 3.14, correspond exactly to the convolution of the channel impulse response (in aliased form) with the time-domain pulse of $w(\tau)$. Assuming that the time-domain channel is composed of a dense set of uncorrelated components around a delay $\tau_{\mathrm{int},1}$ and that $\Delta\tau_{\mathrm{RS}}$ is much smaller than τ_{r}, it follows from Eq. 3.55 that the resolution error can be estimated as follows:

$$|\Delta y_{\alpha,\mathrm{RS}}(\omega_{\mathrm{s}})|^2 \approx \frac{R(\beta,\gamma)}{R_{\mathrm{win}}}|K_\alpha|^2|c_{\mathrm{IDFT}}(k_1)|^2, \tag{3.57}$$

where $R(\beta,\gamma)$ is the normalized energy of the time-domain pulse $g_{\mathrm{CM}}(\tau)$ around $\tau_{\mathrm{int},1}$:

$$R(\beta,\gamma) = \Delta f_{\mathrm{win}}^{-1} \int_{\tau_{\mathrm{int},1}-\Delta\tau_{\mathrm{int},1}}^{\tau_{\mathrm{int},1}+\Delta\tau_{\mathrm{int},1}} |g_{\mathrm{CM}}|^2(\tau)\,\mathrm{d}\tau \tag{3.58}$$

The normalized energy can be written in good approximation as a function of β and γ, defined as follows

$$\beta = \mathrm{ceil}(\tau_{\mathrm{int},1}\Delta f_{\mathrm{win}}) - \tau_{\mathrm{int},1}\Delta f_{\mathrm{win}} \tag{3.59}$$

$$\gamma = 4\pi\frac{\Delta\omega_{\mathrm{s}}}{\Delta f_{\mathrm{win}}} \tag{3.60}$$

γ is a parameter describing the relative position of the source subcarrier frequency (ω_{s}), i.e., the evaluation frequency (as shown in Eq. 3.53), with respect to the window. γ varies from zero (i.e., ω_{s} located in the middle of the window) to 1 (i.e., ω_{s} located at the window's edge). β is a parameter describing the relative mismatch between $\tau_{\mathrm{int},1}$ and the discrete delay taps, τ_k. β also falls in the range of $[0,1[$. Note that β varies fast with the window width. Assuming a limited dependency on β, the normalized energy is further considered in terms of the mean:

$$R_{\mathrm{M}}(\gamma) = \langle R(\beta,\gamma)\rangle_\beta \tag{3.61}$$

where $\langle\,\cdot\,\rangle_\beta$ indicates that the (linear-scaled) average is taken over the β range of $[0,1[$.

Based on the room electromagnetics theory, the APDP decays exponentially in the interference delay interval with τ_{r} as a time constant. Thus, the interference

power can be analytically determined from Eq. 3.49 as proportional to τ_r. Based on this estimation of the interference power and averaging the resolution error from Eq. 3.57 over the whole calculation range, the relative error power due to resolution (including near leakage) is estimated as follows:

$$\tilde{E}_{\alpha',\mathrm{RS}} \approx \frac{\langle R_\mathrm{M}(\gamma)\rangle_{\omega_\mathrm{s}}}{\Delta f_\mathrm{win}\,\tau_\mathrm{r}} \tag{3.62}$$

Note that for method type I, $R_\mathrm{M}(\gamma)$ is implicitly dependent on the source subcarrier frequency (ω_s) via γ, which has been defined by Eq. 3.60. For method types II and III, γ is fixed over the calculation range. Note also that no window correction (of the windowing method) is considered.

A numerical analysis of the (normalized) energy, $R(\beta,\gamma)$, is carried out for a Hann and a rectangular window. For a γ varying from 0 to 0.999, the mean, minimum and maximum of $R(\beta,\gamma)$ is determined over the whole β range (Table 3.2). The time width, $\Delta\tau_\mathrm{RS}$, which covers by definition 90% of the energy of the time-domain pulse $g_\mathrm{CM}(\tau)$ around $\tau_{\mathrm{int},1}$, is also determined. This time width is normalized to $\Delta f_\mathrm{win}^{-1}$. The mean of $R(\beta,\gamma)$ ($R_\mathrm{M}(\gamma)$) and the normalized time width (i.e., $\Delta\tau_\mathrm{RS}\times\Delta f_\mathrm{win}$) are also shown in Fig. 3.4 for both window profiles. For a γ equal to zero, R_M is almost the same for a Hann and a rectangular window, i.e., -6.5 dB and -6.7 dB, respectively. If γ increases towards unity, R_M even decreases slightly towards -9.0 dB for a Hann window, while for a rectangular window, R_M rises strongly, reaching 18.6 dB at a γ of 0.999. Compared to a γ equal to zero, R_M (for a rectangular window) increases already by 1 dB and 3 dB from a γ of 0.44 and 0.71, respectively. Further, the deviation of $R(\beta,\gamma)$ with respect to the mean is not higher than 1.4 dB and 2.7 dB for a Hann and a rectangular window, resp., for a zero γ (Table 3.2). For a higher γ, this deviation is even smaller. For a Hann window, the normalized time width is almost independent on γ, ranging between 1.1 and 1.3. For a rectangular window, the normalized width increases strongly as γ approaches unity, from 2.6 at a zero γ to already 10.8 at a γ of 0.9 and higher than 50 from a γ of 0.99.

The increase of R_M as γ approaches unity, observed for a rectangular window, is mainly caused by the increased width. The latter is a result of constructive interference from the summation over the sidelobes in Eq. 3.56, appearing if γ approaches unity. For a Hann window, this effect is very limited, as the proportion of the sidelobes energy is much smaller (i.e., -32.9 dB versus -10.1 dB for a rectangular window). Interestingly, the rising trend of the width and the energy for a rectangular window tends to be roughly inversely proportional to $1-\gamma$ (Fig. 3.4). From a γ of 0.8, the energy follows well the inversely proportional trend:

$$R_\mathrm{M}(\gamma) \approx d_\mathrm{rect} R_\mathrm{M}(0)(1-\gamma)^{-1} \tag{3.63}$$

with a correction factor d_rect ranging in $[-4.7,-2.7]$ dB with a (dB-scaled) mean of -3.4 dB. This is a slight deviation considering the energy's variation over more

Table 3.2: Parameters of the time-domain resolution error at the edge of a rectangular weighting function: (i) the mean (M), minimum (MIN) and maximum (MAX) of the normalized energy, $R(\beta, \gamma)$, and (ii) the normalized time width. This is given for a Hann and a rectangular window and as a function of γ, indicating the position of the evaluation frequency with respect to the window.

γ	Hann				rectangular			
	energy (norm.) [dB]			width	energy (norm.) [dB]			width
	M	MIN	MAX	(norm.) [ ]	M	MIN	MAX	(norm.) [ ]
0	-6.5	-7.5	-5.1	1.1	-6.7	-9.4	-4.1	2.6
0.25	-6.8	-7.7	-5.5	1.1	-6.4	-9.0	-3.9	2.8
0.5	-7.4	-8.0	-6.4	1.1	-5.5	-7.7	-3.3	3.3
0.9	-8.8	-8.9	-8.7	1.2	0.3	-0.4	1.2	10.8
0.99	-9.0	-9.0	-9.0	1.3	9.9	9.8	10.1	> 50
0.999	-9.0	-9.0	-9.0	1.3	18.6	18.6	18.6	> 50

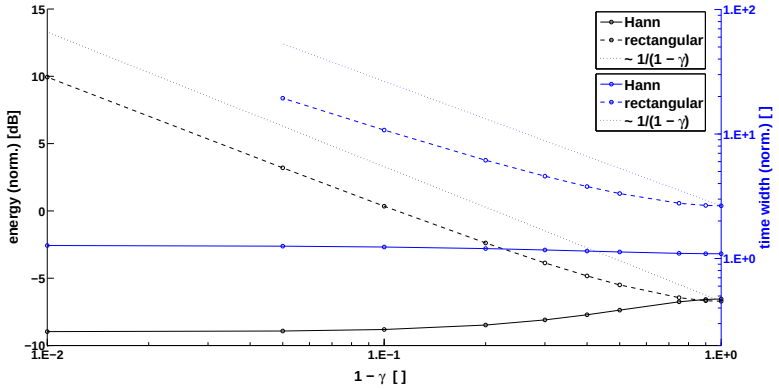

Figure 3.4: The mean (normalized) energy ($R_{\mathrm{M}}(\gamma)$) and the (normalized) time width ($\Delta\tau_{\mathrm{RS}} \times \Delta f_{\mathrm{win}}$) are analytically determined as a function of $1-\gamma$ for a Hann and a rectangular window. The trend proportional to $(1-\gamma)^{-1}$ is added for comparison.

than two orders of magnitude. Physically, this trend means that the resolution error power is rather determined by the *excess* of the window with respect to the evaluation frequency (ω_{s}), than to the window width itself. Consequently, for methods I-rect and II-rect, where ω_{s} may be located outerly with respect to the window (i.e., γ approaching unity), there is still a certain excess required to suppress the resolution error, even when the window width is large. This excess corresponds to a measurement range excess ($\Delta f_{\mathrm{meas,\,exc}}$).

The **main conclusion** is that for methods using a Hann window (without win-

dow correction), the relative error power due to resolution for the y_{corr} interference coefficient is estimated as inversely proportional to the reverberation time and the window width (Eq. 3.62). This is based on the room electromagnetics theory. For method III-Hann, the proportionality factor for the relative error power (Eq. 3.62), R_{M}, is -6.5 dB. For method III-rect, where γ is about zero, the same relation is found with a proportionality factor of -6.7 dB. However, for methods I-rect and II-rect, where γ may approach unity, the resolution error power is rather determined by the excess of the window with respect to the evaluation frequency, than to the window width itself. Compared to y_{corr}, the error power for $y_{\mathrm{Four},\Delta i}$ is expected to be lowered for a small subcarrier separation (i.e., $|\Delta i| \ll D_{\mathrm{FFT}} \Delta f_{\mathrm{win}}/2$) (i.e., cancellation effect). Finally, as the error power estimation shows, the window width required to suppress the resolution error becomes smaller when the reverberation time is larger, i.e., when the interference becomes more significant.

3.9.3 Theoretical estimation method of the error power due to direct and aliased leakage

The theoretical estimation method of the error power due to direct and aliased leakage is based on a one-tap representation of the set of the time-domain channel components, causing direct and aliased leakage, respectively (Fig. 3.3). This set lies outside the interference delay interval and is typically dominated by the strongest time-domain channel components. The one-tap power is determined as the total power of the set of real channel components involved. Assuming a LOS scenario, the tap is set at the delay of first arriving path (τ_{p}), determined by maximizing the APDP measured with a sufficiently small time resolution. In addition, τ_{p} is shifted to the nearest delay falling just between two subsequent discrete delay taps, τ_k (i.e., $k\Delta f_{\mathrm{win}}^{-1}$). Indeed, if τ_{p} approaches a discrete delay tap, the error power estimation due to direct and aliased leakage falls to zero, since all discrete delay taps coincide with the sidelobes' nulls of $w(\tau)$. Note that the sidelobes' time width equals $\Delta f_{\mathrm{win}}^{-1}$. Consequently, adjusting τ_{p} in this way, it is expected that the theoretical estimation behaves as an upper envelope above the real error power as a function of the window width.

From Eq. 3.25, it follows mathematically that the error due to far leakage caused by a one-tap channel impulse reponse, $\delta(\tau - \tau_{\mathrm{p}})$ (where $\delta(\,\cdot\,)$ is the Dirac delta function), is determined by:

$$\Delta y_{\alpha,\mathrm{LK}}(\omega_{\mathrm{s}}) = \exp\bigl(-j\tau_{\mathrm{p}}\,\omega_{\mathrm{win,s}}\bigr)\Delta f_{\mathrm{win}}^{-1} \times \sum_{k=-\infty}^{\infty} g_{\alpha}(\tau_k - \tau_{\mathrm{int},0}) w\bigl(\tau_k - \tau_{\mathrm{p}} - l\Delta f_{\mathrm{res}}^{-1}\bigr) \exp\bigl(-j\tau_k \Delta\omega_{\mathrm{s}}\bigr) \tag{3.64}$$

Remind that $\omega_{\mathrm{win,s}}$ is the window centre frequency corresponding to the source subcarrier frequency (ω_{s}). In Eq. 3.64, l is an integer indicating that the delay of actual tap (of the channel under aliased form) causing leakage is $\tau_{\mathrm{p}} + l\Delta f_{\mathrm{res}}^{-1}$. To determine the error due to direct and aliased leakage, l is set at zero and 1, respectively. In Eq. 3.64, it is obviously assumed that τ_{p} falls outside the interference delay interval. Note that in Eq. 3.64, the composed weighting function, $g_{\alpha}(\tau)$, is used instead of the generalized weighting function, $\tilde{g}_{\alpha}(\tau)$, used in the two-term representation of the error (Eq. 3.25). Note also that the summation in Eq. 3.64 is restricted to delay taps in the interference delay interval, since the weighting function is zero outside this interval. This estimation method is obviously of a lower computational complexity compared to the exact calculation method (Section 3.9.1), where the time-domain coefficients need to be determined by a convolution.

4

Performance analysis of different windowing methods: required measurement range

In this chapter, a performance analysis of the windowing methods defined in Section 3.4 is carried out with the focus on the required *measurement range*. The measurement range refers to the frequency range over which the channel response is measured. To determine the interference due to insufficient CP at a given accuracy, this measurement range must be sufficiently large as a result of the window width requirement to achieve sufficient time resolution and dynamic range. Consequently, the required measurement range may exceed the *zero-excess measurement range*, which is the frequency range determined by all subcarriers of interest. However, the measurement range is preferably limited as much as possible, as a larger measurement range imposes higher requirements on the measurement equipment and involves possibly additional external sources disturbing the channel measurement. In this chapter, the required measurement range is evaluated for different windowing methods based on a channel measurement in a large exposition hall and for typical IEEE 802.11ac OFDM parameters.

This chapter is organized as follows:

- **Section 4.1** describes the experimental setup and the channel measurement in a large exposition hall
- **Section 4.2** reports on the convergence analysis of the interference coeffi-

cient as a function of the window width. This convergence analysis is carried out to determine the measurement range required to achieve a given accuracy level of the interference coefficient.

- In **Section 4.3**, the required measurement range is extensively discussed for the different windowing methods and the performance is related to the different types of window-related errors.
- **Section 4.4** presents some practically relevant interference characteristics of the measured channel.

4.1 Experimental setup and measurements

To measure the channel response, the following measurement setup is used (Fig. 4.1). The Tx and Rx antennas are connected to a Rohde & Schwarz ZNB vector network analyzer (VNA), which measures the scattering parameter S_{21} as a function of the frequency. Broadband omnidirectional, vertically polarized Cobham antennas are used of type XPO2V-0.8-6.0-GF/1441 with a gain of 2 dBi. The VNA output signal is transferred over the Tx-Rx separation using a 20 m coaxial cable and amplified before being transmitted by Tx. A broadband Nextec-RF amplifier is used of type NB00453 with a gain of 28 dB. The Rx antenna is connected with the VNA input by a short coaxial cable. The amplifier is placed before the Tx antenna to avoid a measurement error due to linearity imperfections of the amplifier. To obtain the channel response, a calibration is performed at the Tx and Rx terminal by a through standard (i.e., transmission normalization). The measured channel response is averaged over a number of sweeps in order that the relative error power due to measurement noise is not higher than the required accuracy level ($\tilde{E}_{\mathrm{thresh}}$).

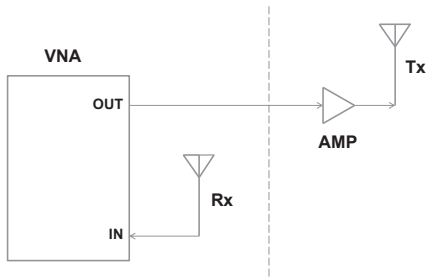

Figure 4.1: Block scheme of the measurement setup. At the Rx side: network analyzer (VNA) and Rx antenna, at the Tx side (remote): amplifier ("AMP") and Tx antenna.

The channel reponse is measured over a frequency range of $[2.5, 5.1]$ GHz. The transmit power of the VNA is set at -10 dBm to ensure that the amplifier input is below the 1 dB compression point. The resolution bandwidth used is 10 kHz and the sweep time is 0.46 s. Based on an interference delay interval cut off at a width of 6.6 times the reverberation time (τ_{r}) to achieve a relative error power of -14 dB, a time window of 2 µs is required for a CP length up to 800 ns and for a τ_{r} up to 160 ns. Hence, the frequency resolution is set at 500 kHz. The number of sweeps is 1000 to cancel out the measurement noise as much as possible for the performance analysis of the windowing methods. The number of sweeps required to obtain a relative error power due to measurement noise of -14 dB (after averaging) is investigated in Section 6.2.

The measurement is performed in the International Convention Center (ICC)

in Ghent in room "Minneplein" (Figs. 4.2 and 4.3). The Tx and Rx antenna are positioned with a separation of 15.8 m at a height of 1.9 m and 1.4 m, respectively. The "Minneplein" room is used for expositions, receptions and congresses. The area has a maximum length of 46 m, a maximum width of 43 m and a height of 3.9 m. About 98 m of the area is surrounded by exterior glass walls. At both sides of the "Minneplein" room, located at the first floor, there is a stair well leading to an exposition hall on the ground floor, "Arteveldeforum", with an area of about 1600 m^2. The area of the two stair wells has dimensions of about 14×18 m and 31×6 m, respectively. The "Arteveldeforum" room is surrounded by exterior glass walls over about 66 m and is connected with the "Pedro de Gante" exposition room over a length of 23 m by a glass wall. The height of the "Arteveldeforum" and the "Pedro de Gante" room is 3.2 m and 4.5 m, resp., and the "Pedro de Gante" room has an area of about 1600 m^2.

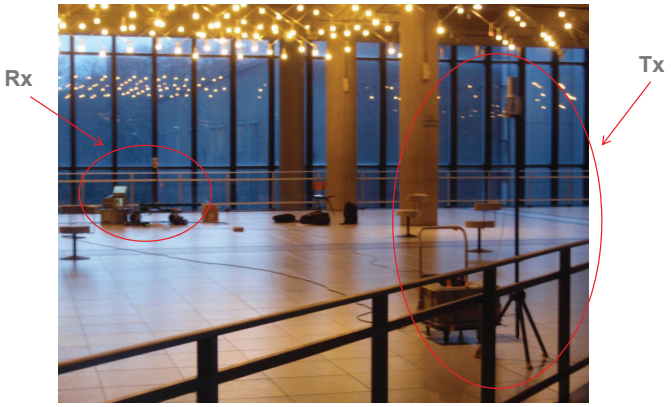

Figure 4.2: "Minneplein" room in International Convention Center (ICC, Ghent) with measurement setup.

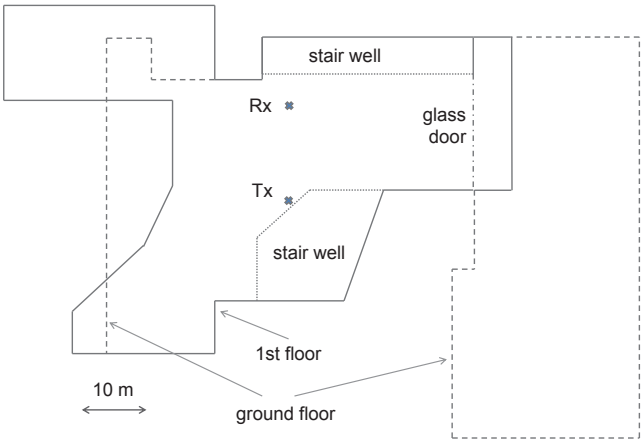

Figure 4.3: Floor plan (to scale) of "Minneplein" room (first floor). There are two stair wells leading to the "Arteveldeforum" (ground floor), which is separated from the "Pedro de Gante" room by glass doors (dash-dot line). The walls of the first and the ground floor are depicted in solid and dash line, respectively. The Tx and Rx positions of the channel measurement are indicated.

4.2 Convergence analysis method

To evaluate the performance of the windowing methods concerning the required measurement frequency range (Δf_{meas}), a convergence analysis of the interference coefficient as a function of the *measurement range* is carried out based on a measured channel (Section 4.1) and using typical IEEE 802.11 parameters. In this analysis, the relative error power due to non-uniform windowing and due to commutation (Section 3.5) is determined as a function of the measurement range (Δf_{meas}), resulting into the required Δf_{meas} to achieve a given relative error power ($\tilde{E}_{\mathrm{thresh}}$). For the performance analysis of the windowing methods, the interest is only in the relevant window-related error types, i.e., the error due to non-uniform windowing ($\Delta y_{\alpha,\mathrm{NU}}$) and due to commutation ($\Delta y_{\alpha,\mathrm{CM}}$), which comprises the error due to a non-zero time resolution and direct and aliased leakage. Indeed, the error due to a cut-off of the interference delay interval is not dependent on the windowing method used (Eq. 3.19). The error due to aliasing, $\Delta y_{\alpha,\mathrm{AL}}$, is negligible, as for a time window of 2 µs, the corresponding relative error power is of the order of -58 dB or smaller for a reverberation time (τ_{r}) up to 150 ns. The relative error power due to measurement noise is reduced to $\tilde{E}_{\mathrm{thresh}}$ or lower by averaging the measured channel response over a number of sweeps, N_{sweeps}. However, in the Δf_{meas} range of convergence, where the relative error power due to non-uniform windowing and due to commutation falls below the accuracy level ($\tilde{E}_{\mathrm{thresh}}$), it is assumed that the relative error power due to measurement noise is approximately independent on the windowing method used, nor on Δf_{meas}. This will be experimentally verified in Section 6.2. Therefore, the measurement noise is not relevant in the performance analysis of the windowing methods.

Calculation method for the window-related error power

The absolute error power due to non-uniform windowing and due to commutation is calculated as follows. The spectral interference coefficient, $y_{\alpha}(\omega_{\mathrm{s}})$, as calculated from a measurement range Δf_{meas} and based on the nth set of N_{sweeps} sweeps, is denoted as $y_{\alpha,n}(\omega_{\mathrm{s}}, \Delta f_{\mathrm{meas}})$. The error due to non-uniform windowing and due to commutation is determined in good approximation by the difference between the interference coefficient as calculated for the actual measurement range, Δf_{meas}, and the one calculated for the maximum measurement range, $\Delta f_{\mathrm{meas,max}}$. In addition, this is averaged over all measurement repetitions to cancel out the measurement noise as much as possible. Thus, the calculation method for the absolute error power due to non-uniform windowing and commutation is determined as follows (left-hand side):

$$\left\langle \left| \left\langle y_{\alpha,n}(\omega_\mathrm{s}, \Delta f_\mathrm{meas}) - y_{\alpha,n}(\omega_\mathrm{s}, \Delta f_\mathrm{meas,max}) \right\rangle_n \right|^2 \right\rangle_{\omega_\mathrm{s}} \approx \left\langle \left| \Delta y_{\alpha,\mathrm{NU}}(\omega_\mathrm{s}, \Delta f_\mathrm{meas}) + \Delta y_{\alpha,\mathrm{CM}}(\omega_\mathrm{s}, \Delta f_\mathrm{meas}) \right|^2 \right\rangle_{\omega_\mathrm{s}} + \left\langle \left| \Delta y_{\alpha,\mathrm{NU}}(\omega_\mathrm{s}, \Delta f_\mathrm{meas,max}) + \Delta y_{\alpha,\mathrm{CM}}(\omega_\mathrm{s}, \Delta f_\mathrm{meas,max}) \right|^2 \right\rangle_{\omega_\mathrm{s}} \tag{4.1}$$

In Eq. 4.1, $\langle \cdot \rangle_n$ indicates that the average is taken over all measurement repetitions n, each consisting of N_sweeps sweeps. In the right-hand side, the errors due to non-uniform windowing and commutation (Section 3.5) are dependent on Δf_meas and independent on n. If $\Delta f_\mathrm{meas,max}$ is sufficiently large, the second term in the right-hand side of Eq. 4.1 becomes negligible, as it concerns window-related errors. In this case, the left-hand side provides a good approximation of the absolute error power due to non-uniform windowing and commutation (first term of right-hand side). In any case, it provides an order estimation, considering that the error power corresponding to $\Delta f_\mathrm{meas,max}$ is smaller or of the same order than the one corresponding to Δf_meas. Eq. 4.1 applies if the time resolution corresponding to $\Delta f_\mathrm{meas,max}$ is considerably smaller than the one corresponding to Δf_meas. Otherwise, the error due to non-uniform windowing and commutation would be approximately equal for both measurement ranges and the left-hand side of Eq. 4.1 would be much smaller than the absolute error power. Practically, it is assumed that this requirement of uncorrelated errors is fulfilled if the time resolution corresponding to $\Delta f_\mathrm{meas,max}$ is smaller than half the time resolution corresponding to Δf_meas. This is certainly the case for all windowing methods if $\Delta f_\mathrm{meas} < \Delta f_\mathrm{meas,max}/2$.

Eq. 4.1 is obtained based on Eq. 3.28, where the error due to aliasing is neglected as the corresponding relative error power is typically several orders of magnitude smaller than $\tilde{E}_\mathrm{thresh}$ and there is an additional cancellation in the Δf_meas range of convergence (of the interference coefficient). The measurement noise is neglected based on two effects: (i) the averaging over different measurement repetitions and (ii) the cancellation of the measurement error in the range of convergence. The second effect is caused by the fact that in the Δf_meas range where the interference coefficient calculation converges, the error due to measurement noise converges too (Section 6.2). Hence, the measurement error obtained at Δf_meas is in good approximation equal to the one obtained at $\Delta f_\mathrm{meas,max}$, and the resulting measurement error contribution to the left-hand side of Eq. 4.1 is negligible.

The measurement range required to achieve an accuracy level ($\tilde{E}_\mathrm{thresh}$) of -14 dB is determined as follows. Note that the value of -14 dB is based on Section 3.6. The relative error power is determined by dividing the estimation of the

absolute error power due to non-uniform windowing and commutation (left-hand side of Eq. 4.1 for the spectral interference) by the frequency-averaged interference power, $I_{\alpha',\mathrm{av}}$. The latter, defined in Section 3.6, is determined using method III-Hann from the maximum measurement range ($\Delta f_{\mathrm{meas,max}}$) and including averaging of the interference coefficient over all measurement repetitions. Note that for the total interference, the spectral error power terms need to be added up over all subcarrier separations, as described in Section 3.6. Further, the relative error power, determined as a function of a set of Δf_{meas} points, is interpolated and the required measurement range is found as the smallest Δf_{meas} value from which the relative error power remains consistently below $\tilde{E}_{\mathrm{thresh}}$.

Parameter values used for the convergence analysis

The interference coefficient is calculated over a detecting subcarrier frequency range with a width of 241 MHz and centered at 3.8 GHz. The calculation is done for a subcarrier separation (Δi) ranging from -255 to 255, corresponding to a maximum frequency separation of 79.7 MHz for IEEE 802.11. This is based on a central detecting subcarrier for a 160 MHz bandwidth (IEEE 802.11ac [27]). In Section 6.2, it is found that for a -14 dB accuracy level, the required number of sweeps (N_{sweeps}) is 80. As the total number of sweeps is 1000, the available number of measurement repetitions (N_{rep}) is 12. The resolution of the detecting subcarrier frequency (Δf_{d}) for which the interference coefficient is calculated is set at $(5D_{\mathrm{FFT}})^{-1}$, i.e., 62.5 kHz. The measurement range is centered at 3.8 GHz and Δf_{meas} ranges from 200 MHz to 2600 MHz. As the relative error power is found to fluctuate fast as a function of Δf_{meas}, a dense set of Δf_{meas} points needs to be selected for the calculation of the relative error power, especially near the accuracy level. A 1 MHz step is chosen for the Δf_{meas} range of $[200, 650]$ MHz, a 10 MHz step for the range of $[650, 1100]$ MHz and a 100 MHz step for the range of $[1200, 2600]$ MHz. Note that 1 MHz is the smallest possible step for a 500 kHz frequency resolution (Δf_{res}). The 8 windowing methods proposed in Section 3.4 are applied over this Δf_{meas} set. For method type III, the set of the window width that is actually applied is systematically 400 MHz lower than the Δf_{meas} set mentioned (Fig. 3.2). Note that the type II method without window correction is only applicable from a Δf_{meas} of 242 MHz, where the window width is 1 MHz (Fig. 3.2). For methods I-HC and II-HC, the Δf_{meas} set starts at the zero-excess measurement range, ranging between 241 MHz and 400 MHz (depending on $|\Delta i|$), because the window function must be non-zero at the source subcarrier to apply window correction. Moreover, for the convergence analysis for a calculation range lower than 241 MHz (Section 4.3.1.1), an additional Δf_{meas} set is included of $[2, 199]$ MHz with a 1 MHz step.

An optimal FFT window positioning is considered (Section 2.1.3), resulting into an interference delay interval starting at a delay ($\tau_{\mathrm{int},1}$) of 459 ns and 859 ns

for 400 ns and 800 ns CP, resp., assuming 512 FFT points (N_{sample}). The interference delay interval is cut off at a delay $\tau_{\mathrm{int},2}$ being 1324 ns and 1800 ns for 400 ns and 800 ns CP, respectively. The interval duration, $\tau_{\mathrm{int},2} - \tau_{\mathrm{int},1}$, is minimum 6.6 τ_{r}, to achieve a relative error power due to cut-off of maximum -14 dB (Section 3.8). Based on this interference delay interval, a τ_{r} of 131 ± 2 ns and 138 ± 1 ns is found for 400 ns and 800 ns CP, respectively.

Verification of neglecting the influence of measurement noise on the convergence analysis

The assumption that the contribution of the measurement noise to the estimation of the absolute error power due to non-uniform windowing and commutation (Eq. 4.1) is negligible, is validated based on a limited set of Δf_{meas} points. A step of 20 MHz is taken for the Δf_{meas} range of $[160, 340]$ MHz, a 10 MHz step for the range of $[340, 400]$ MHz and a 100 MHz step for the range of $[400, 2600]$ MHz. A finer step is taken where method types II and III start to be applicable (i.e., with a small window width). A smaller step of 5 MHz is taken in the range of $[240, 260]$ MHz. In the range of $[400, 500]$ MHz, an additional Δf_{meas} subset is included, being $\{405, 410, 425, 450, 475\}$ MHz. The absolute error power due to measurement noise appearing in the left-hand side of Eq. 4.1 is determined in good approximation by:

$$\left\langle \left| \langle \Delta z_{\mathrm{MN},n}(\omega_{\mathrm{s}}) \rangle_n \right|^2 \right\rangle_{\omega_{\mathrm{s}}} \approx \frac{1}{N_{\mathrm{rep}}} \left(\left\langle \left| z_n(\omega_{\mathrm{s}}) \right|^2 \right\rangle_{n,\omega_{\mathrm{s}}} - \left\langle \left| \langle z_n(\omega_{\mathrm{s}}) \rangle_n \right|^2 \right\rangle_{\omega_{\mathrm{s}}} \right) \tag{4.2}$$

where $z_n(\omega_{\mathrm{s}})$ is a short notation for

$$z_n(\omega_{\mathrm{s}}) = y_{\alpha,n}(\omega_{\mathrm{s}}, \Delta f_{\mathrm{meas}}) - y_{\alpha,n}(\omega_{\mathrm{s}}, \Delta f_{\mathrm{meas,max}}) \tag{4.3}$$

and $\Delta z_{\mathrm{MN},n}(\omega_{\mathrm{s}})$ is the error on $z_n(\omega_{\mathrm{s}})$ due to measurement noise. In Eq. 4.2, it is assumed that (i) $z_n(\omega_{\mathrm{s}})$ and $\Delta z_{\mathrm{MN},n}(\omega_{\mathrm{s}})$ are uncorrelated over different measurement repetitions n, (ii) the error has a centrally symmetric distribution in the complex plane, and (iii) the number of measurement repetitions is sufficiently large. The relative error power ($\tilde{E}_{\mathrm{z}}$) due to measurement noise on the absolute error power due to non-uniform windowing and commutation is then calculated as

$$\tilde{E}_{\mathrm{z}} = \frac{\left\langle \left| \langle \Delta z_{\mathrm{MN},n}(\omega_{\mathrm{s}}) \rangle_n \right|^2 \right\rangle_{\omega_{\mathrm{s}}}}{\left\langle \left| \langle z_n(\omega_{\mathrm{s}}) \rangle_n \right|^2 \right\rangle_{\omega_{\mathrm{s}}}} \tag{4.4}$$

Based on the measured channel, including 12 measurement repetitions, and using Eqs. 4.4 and 4.3, $\tilde{E}_{\mathrm{z}}$ is calculated over the limited Δf_{meas} set for all 8 windowing methods and all subcarrier separations (i.e., $|\Delta i| \leq 255$). For 400 ns CP, $\tilde{E}_{\mathrm{z}}$

ranges between -54.4 dB and -26.5 dB for the y_{corr} type coefficient and between -56.6 dB and -15.6 dB for the y_{Four} type coefficient. For 800 ns CP, $\tilde{E}_{\mathrm{z}}$ ranges between -56.2 dB and -24.5 dB for y_{corr} and between -57.7 dB and -9.1 dB for y_{Four}. This shows that the measurement noise appearing in the left-hand side of Eq. 4.1 can indeed be neglected and that this provides a good approximation of the absolute error power due to non-uniform windowing and commutation.

4.3 Measured frequency range requirement

In this section, the performance of the different windowing methods (Section 3.4) is evaluated with respect to the required the frequency range (Δf_{meas}) over which the channel needs to be measured to determine the interference due to insufficient CP. The required Δf_{meas} has been determined in the convergence analysis described in Section 4.2. The detecting subcarrier varies over a fixed calculation range (Δf_{calc}), centered at 3.8 GHz and with a width of 241 MHz. Consequently, the zero-excess measurement range, i.e., the frequency range of interest defined by all source and detecting subcarriers involved, has a width ($\Delta f_{\mathrm{meas},\,0}$) of $\Delta f_{\mathrm{calc}} + 2|\Delta i|/D_{\mathrm{FFT}}$, when determining the spectral interference for $\pm|\Delta i|$ (Fig. 3.2). As the interference is related to the channel at the source as well as the detecting subcarrier, it is expected that the required measurement range (Δf_{meas}) is always larger than $\Delta f_{\mathrm{meas},\,0}$. Therefore, the interest is in fact in the excess measurement range ($\Delta f_{\mathrm{meas,\,exc}}$), defined by the difference between Δf_{meas} and $\Delta f_{\mathrm{meas},\,0}$.

The required Δf_{meas} is determined based on the channel measurement presented in Section 4.1 for 400 ns and 800 ns CP, which is essentially different for some windowing methods. The analysis is carried out separately for the interference coefficient terms of type y_{corr} and y_{Four}. A first reason is that the proportionality factor of the y_{corr} term, i.e., $(2N_{\mathrm{sample}})^{-1}$, may increase due to the aliasing effect, especially for detecting subcarriers in the outer parts of the channel bandwidth (Section 2.2). The y_{corr} term may then become dominant with respect to the composed interference coefficient (of type y_{tot}). A second reason is that the y_{corr} analysis will provide useful information concerning the y_{Four} type coefficient. Generally, the required Δf_{meas} for y_{tot} is then determined by the requirement of the most dominant term.

The required Δf_{meas} is determined for 8 different windowing methods (Section 3.4). For type I, a fixed window is applied over the measurement range (Δf_{meas}), while for types II and III, a moving window is applied. While for types I and II, the conventional (time-domain) weighting function is applied, type III is based on a generalized weighting function. First, the methods using a Hann window (i.e., methods I-, II- and III-Hann) are discussed (Section 4.3.1) and secondly, the methods using a rectangular window (i.e., methods I-, II- and III-rect) (Section 4.3.2). Finally, the methods using a Hann window correction (i.e., methods I- and II-HC) are discussed in Section 4.3.3. To follow Sections 4.3.1 – 4.3.3 more easily, it is useful to keep Fig. 3.2, illustrating the different windowing methods, in mind.

The determination of the spectral interference may be useful for e.g., channel equalization design. However, for the determination of the channel's performance, the interest is rather in the *total* interference. This is the spectral interference

power at a certain detecting subcarrier, summed over all source subcarriers. Consequently, the required Δf_{meas} may be smaller for the determination of the total interference. In Section 4.3.4, the Δf_{meas} requirement will be discussed for the total interference and compared to the requirement for the spectral interference. This section provides a good summary of the effect of the windowing method on the required Δf_{meas}.

4.3.1 Methods using a Hann window

The results of the convergence analysis are given here for all methods jointly enabling a better comparison, but are discussed per window type (Sections 4.3.1-4.3.3). To follow this discussion, it is useful to keep Fig. 3.2 (i.e., schematical presentation of the windowing methods) in mind. For 400 ns CP, the required Δf_{meas} is shown in Fig. 4.4 for coefficient types y_{corr} and y_{Four} and in Fig. 4.5 for 800 ns CP. In the latter, the methods using a rectangular window are not included for reasons of clarity. In Fig. 4.7 (Section 4.3.2), these results for 800 ns CP and y_{Four} will be shown for method types I, II, and III separately. Finally, the *overall* required Δf_{meas}, i.e., to determine the spectral interference for the whole Δi range of $[-255, 255]$, is presented in Table 4.1. Note that the overall zero-excess measurement range is equal to 400 MHz.

From Figs. 4.4 and 4.5, it is observed that the required measurement range is largely, though not completely symmetrical with respect to a zero subcarrier separation, $\Delta i = 0$. However, considering the symmetrical design of the windowing methods (Fig. 3.2) and the reciprocal character of the interference, a symmetrical required measurement range would be expected. The reciprocal character of the interference refers to the fact that the Fourier-type coefficient remains unchanged in magnitude when converting the role of the source and detecting subcarrier (see Section 2.2.2.1). The deviation from a perfectly symmetrical required measurement range can be explained by the frequency-selective nature of the channel. The interference coefficient, which is dependent on the source subcarrier frequency, is detected in a *deterministic* way over a certain set of source subcarriers. However, for an opposite Δi, a different set of source subcarriers is concerned, as the detecting subcarriers are assumed to be fixed for all Δi.

4.3.1.1 Method I-Hann

For method I-Hann, the required measurement range (Δf_{meas}) is considerably larger than the zero-excess measurement range ($\Delta f_{\mathrm{meas},\,0}$). This is observed for both coefficient types, y_{corr} and y_{Four}, for 400 ns CP (Figs. 4.4(a) and 4.4(b)), as well for 800 ns CP (Figs. 4.5(a) and 4.5(b)). For a zero subcarrier separation ($\Delta i = 0$), the following excess measurement range ($\Delta f_{\mathrm{meas,\,exc}}$) is required in addition to a zero-excess range $\Delta f_{\mathrm{meas},\,0}$ of 241 MHz: 300 / 314 MHz for

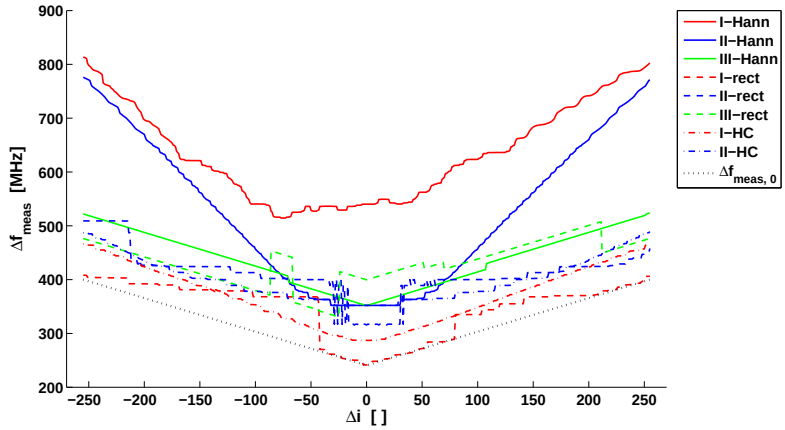

(a) y_{corr}

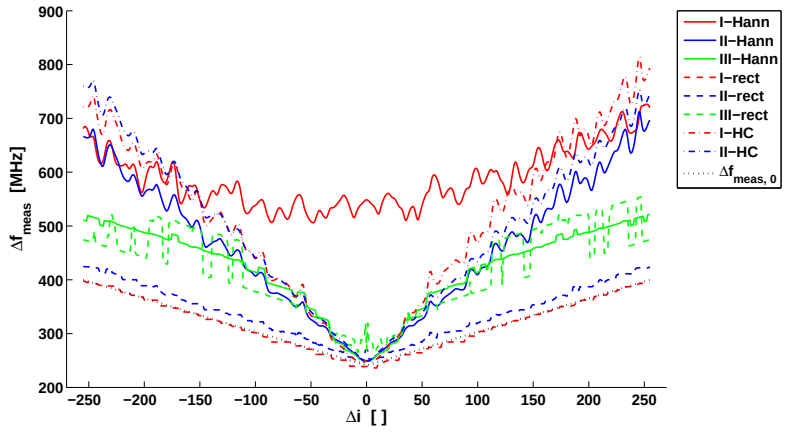

(b) y_{Four}

*Figure 4.4: Required measurement range (Δf_{meas}) for **400 ns CP** as a function of the subcarrier separation (Δi) for different windowing methods. This is based on a* 241 MHz *calculation range and a relative error power of* -14 dB*. The requirement is given for both interference coefficient types, (a) y_{corr} and (b) y_{Four}. The zero-excess measurement range ($\Delta f_{\mathrm{meas},0}$) is added for comparison.*

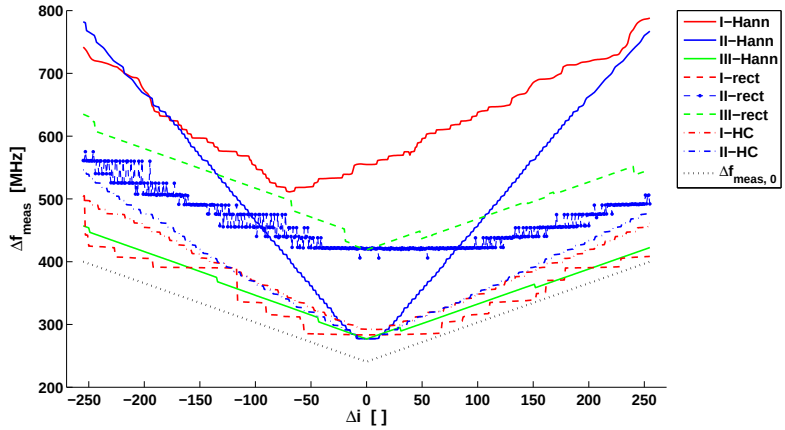

(a) y_{corr}

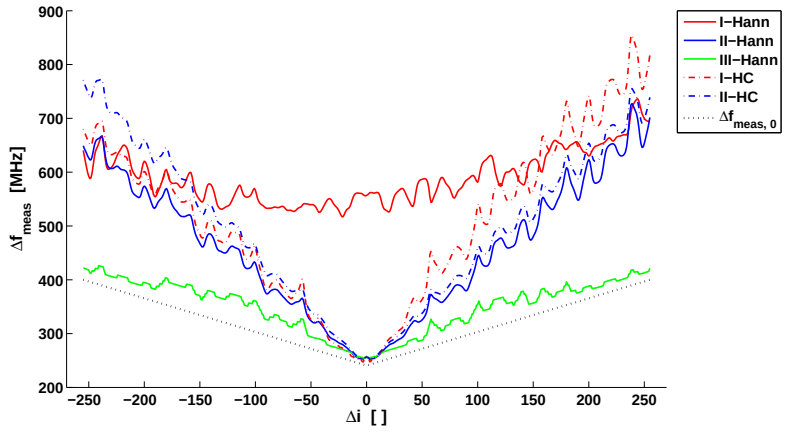

(b) y_{Four}

*Figure 4.5: Required measurement range (Δf_{meas}) for **800 ns CP** as a function of the subcarrier separation (Δi) for different windowing methods. This is based on a* 241 MHz *calculation range and a relative error power of* -14 dB*. The requirement is given for both interference coefficient types, (a) y_{corr} and (b) y_{Four}. The zero-excess measurement range ($\Delta f_{\mathrm{meas},0}$) is added for comparison.*

Table 4.1: Overall required measurement range (Δf_{meas} [MHz]) to determine the spectral interference for all subcarrier separations ($|\Delta i| \leq 255$) using different windowing methods. This is based on a 241 MHz calculation range, a maximum subcarrier frequency separation of 80 MHz and a relative error power of -14 dB. The requirement is given for interference coefficient types y_{corr} and y_{Four}, as well as for the composed type y_{tot}.

method	400 ns CP			800 ns CP		
	y_{corr}	y_{Four}	y_{tot}	y_{corr}	y_{Four}	y_{tot}
I-Hann	814	726	781	788	736	769
II-Hann	776	712	750	782	728	764
III-Hann	524	535	535	457	457	464
I-rect	408	397	406	505	902	902
II-rect	509	424	451	575	970	970
III-rect	559	572	561	635	1082	1082
I-HC	466	813	698	504	855	728
II-HC	489	771	701	546	773	719

400 / 800 ns CP, resp., for the y_{corr} coefficient type and 308 / 316 MHz for y_{Four}. For a higher subcarrier separation, the required excess measurement range even increases. For a $|\Delta i|$ of 255, the average excess $\Delta f_{\mathrm{meas,\,exc}}$ required in addition to a $\Delta f_{\mathrm{meas},\,0}$ of 400 MHz is 408 / 365 MHz for 400 / 800 ns CP for y_{corr} and 300 / 267 MHz for y_{Four}. Here, the average is taken over Δi being ± 255. Finally, the overall required Δf_{meas} is 814 / 788 MHz for 400 / 800 ns CP, resp., for y_{corr} and 726 / 736 MHz, resp., for y_{Four} (Table 4.1). For the composed coefficient type, y_{tot}, the overall required Δf_{meas} is 781 / 769 MHz, resp., which is between the requirement for y_{corr} and y_{Four}. All these requirements are caused by the error due to non-uniform windowing (Section 3.5). To suppress this error, it is required for method I-Hann that the applied window is approximately equal to 1 over the zero-excess measurement range, which requires that Δf_{meas} is considerably larger than $\Delta f_{\mathrm{meas},\,0}$. Therefore, the required *excess* $\Delta f_{\mathrm{meas,\,exc}}$ is related to and at least of the order of the calculation range, Δf_{calc}, as well twice the subcarrier frequency separation, i.e., $2|\Delta i|/D_{\mathrm{FFT}}$.

For method I-Hann, the required measurement range is completely determined by the error due to non-uniform windowing. This can be motivated as follows. For method III-Hann, this error is negligible compared to the accuracy level of -14 dB (Section 4.3.1.3). Since at a certain Δf_{meas}, the applied window for method I-Hann (fixed window) is always larger than for method III-Hann (moving window), the error due to resolution and leakage (Section 3.5) for method I-Hann is expected to be lower than the accuracy level at the Δf_{meas} that is required for

method III-Hann, and a priori for higher values of Δf_{meas}. From Figs. 4.4(a)–4.5(b), it follows that, for method I-Hann, the required measurement range can only be determined by the error due to non-uniform windowing.

To investigate the influence of the calculation range (CR), Δf_{calc}, on the required Δf_{meas}, a convergence analysis is also performed for a set of Δf_{calc} values lower than 241 MHz (CR1): 171 MHz (CR2), 101 MHz (CR3) and 31 MHz (CR4). The required $\Delta f_{\mathrm{meas,\,exc}}$ obtained for 800 ns CP is shown in Fig. 4.6. Especially for a small subcarrier separation, a larger $\Delta f_{\mathrm{meas,\,exc}}$ is required if Δf_{calc} increases. Indeed, the applied window is forced to extend its central part, i.e., where the window function is approximately unity, over the whole zero-excess measurement range, including the outer parts. The effect of Δf_{calc} on the required $\Delta f_{\mathrm{meas,\,exc}}$ is strongest for low $|\Delta i|$. For $\Delta i = 0$, the required $\Delta f_{\mathrm{meas,\,exc}}$ over the set CR4 to CR1 is 56 MHz, 134 MHz, 227 MHz and 314 MHz, resp., for y_{corr} and 34 MHz, 115 MHz, 202 MHz and 316 MHz, resp., for y_{Four}. For 400 ns CP, very similar results are obtained.

From these findings and based on Section 3.5, it is reasonable to express the required $\Delta f_{\mathrm{meas,\,exc}}$ to suppress the error due to non-uniform windowing as proportional to $\Delta f_{\mathrm{meas,\,0}}$:

$$\Delta f_{\mathrm{meas,\,exc}} = a_{\mathrm{I-Hann}} \Delta f_{\mathrm{meas,\,0}}, \tag{4.5}$$

where $a_{\mathrm{I-Hann}}$ is a dimensionless factor with an inferior dependency on Δf_{calc} and Δi. Remind that $\Delta f_{\mathrm{meas,\,0}}$ is determined by $\Delta f_{\mathrm{calc}} + 2|\Delta i|/D_{\mathrm{FFT}}$. For a -14 dB accuracy level, experimental $a_{\mathrm{I-Hann}}$ values are determined from the convergence analysis, based on CR1 – CR4 and $-255 \leq \Delta i \leq 255$ (Table 4.2). There is no significant difference between 400 ns and 800 ns CP. Based on both CP lengths, $a_{\mathrm{I-Hann}}$ values of 1.23 ± 0.35 and 0.88 ± 0.23 are found for y_{corr} and y_{Four}, respectively. For y_{corr}, the channel is evaluated around the source subcarrier only, whereas for y_{Four}, around both the source and detecting subcarrier. The detecting subcarrier is less critically located with respect to the window, which explains the little lower $a_{\mathrm{I-Hann}}$ value for y_{Four}. From Table 4.2, $a_{\mathrm{I-Hann}}$ ranges between 0.55 and 2.70 for y_{corr} and 0.24 and 1.85 for y_{Four}. This variation is caused by the varying ratio between the calculation range (Δf_{calc}) and the frequency subcarrier separation ($\Delta i/D_{\mathrm{FFT}}$) (Fig. 3.2). However, it is shown that $a_{\mathrm{I-Hann}}$ is on average approximately equal to 1, i.e., a measurement range is required of on average 2 times the zero-excess measurement range.

In practice, this means that, to determine the interference over a certain frequency band, the channel needs to be measured over a frequency range being about twice the frequency band. This may be problematic, especially for high (e.g., GHz) bandwidth channels. Moreover, for method I-Hann, the error power due to non-uniform windowing is clearly concentrated near the outer parts of the calculation range, where the actual accuracy will be worse than the overall level of

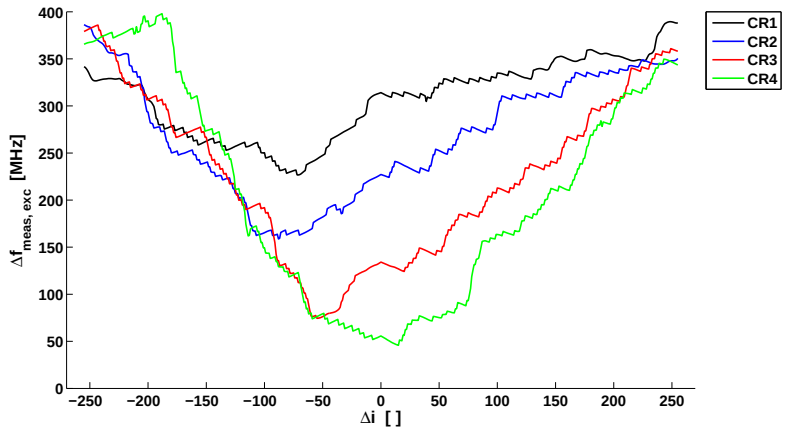

(a) y_{corr}

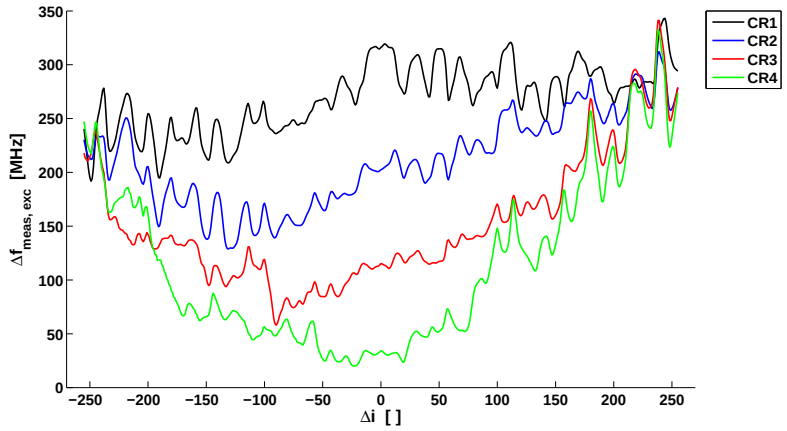

(b) y_{Four}

Figure 4.6: From a convergence analysis for 800 ns *CP, the required excess measurement range for a varying calculation range (CR1 – CR4) is determined for both coefficient types.*

-14 dB.

4.3.1.2 Method II-Hann

Method II-Hann applies a moving window centered at the detection subcarrier frequency, which varies over the calculation range. In this way, the window is only forced to extend its central part over the subcarrier frequency separation (Fig. 3.2). For small separations (i.e., $2|\Delta i|/D_{\mathrm{FFT}} \ll \Delta f_{\mathrm{calc}}$), this yields a considerable reduction of the required measurement range. This is observed for both coeffi-

Table 4.2: Experimental $a_{\mathrm{I-Hann}}$ values (dimensionless) are determined based on calculation range CR1 – CR4 and $-255 \leq \Delta i \leq 255$. Mean (M), standard deviation (SD), minimum (MIN) and maximum (MAX) are given for different CP lengths and both coefficient types (y_{corr} and y_{Four}).

CP [ns]	type	M	SD	MIN	MAX
400	y_{corr}	1.20	0.29	0.77	2.07
	y_{Four}	0.88	0.21	0.24	1.65
800	y_{corr}	1.26	0.40	0.55	2.70
	y_{Four}	0.88	0.25	0.37	1.85
400/800	y_{corr}	1.23	0.35	0.55	2.70
	y_{Four}	0.88	0.23	0.24	1.85

cient types, y_{corr} and y_{Four}, for 400 ns CP (Figs. 4.4(a) and 4.4(b)) as well as for 800 ns CP (Figs. 4.5(a) and 4.5(b)). For a zero subcarrier separation, the following $\Delta f_{\mathrm{meas,\,exc}}$ is required in addition to a $\Delta f_{\mathrm{meas},\,0}$ of 241 MHz: 111 / 37 MHz for 400 / 800 ns CP resp., for the y_{corr} coefficient type and 9 / 15 MHz for y_{Four}. For a higher $|\Delta i|$, the required $\Delta f_{\mathrm{meas,\,exc}}$ increases approximately proportionally to $|\Delta i|$. For a $|\Delta i|$ of 255, the average excess $\Delta f_{\mathrm{meas,\,exc}}$ required in addition to a $\Delta f_{\mathrm{meas},\,0}$ of 400 MHz is 374 / 365 MHz for 400 / 800 ns CP for y_{corr} and 281 / 275 MHz for y_{Four}. Finally, the overall required Δf_{meas} is 776 / 782 MHz for 400 / 800 ns CP, resp., for y_{corr} and 712 / 728 MHz, resp., for y_{Four} (Table 4.1).

Based on Section 3.5, the requirement to suppress the error due to non-uniform windowing can be expressed as follows for method II-Hann:

$$\Delta f_{\mathrm{meas,\,exc}} = 2a_{\mathrm{II-Hann}}|\Delta i|/D_{\mathrm{FFT}}, \tag{4.6}$$

where $a_{\mathrm{II-Hann}}$ is a (dimensionless) proportionality factor. Experimental values of $a_{\mathrm{II-Hann}}$ are obtained from the convergence analysis based on higher $|\Delta i|$, where the convergence of method II-Hann is restricted by the error due to non-uniform windowing. As explained in Section 4.3.1.1, this is certainly the case where the required Δf_{meas} for method II-Hann exceeds the one for method III-Hann. From Figs. 4.4(a) – 4.5(b), these Δi ranges are $|\Delta i| \geq 79$ / 17 for 400 / 800 ns CP, resp., for y_{corr} and $|\Delta i| \geq 112$ / 14 for y_{Four}. The following $a_{\mathrm{II-Hann}}$ values are obtained: 2.50 ± 0.20 for y_{corr} and 1.79 ± 0.19 for y_{Four} (Table 4.3). There is no significant difference between 400 ns and 800 ns CP. For the same reason as for method I-Hann (Section 4.3.1.1), $a_{\mathrm{II-Hann}}$ is somewhat larger for the y_{corr} coefficient type. $a_{\mathrm{II-Hann}}$ is substantially larger than $a_{\mathrm{I-Hann}}$. Indeed, for method I-Hann, the inner part of the calculation range is properly covered by the central part of the fixed Hann window, while for method II-Hann, the relative positions

of source and detecting subcarrier remain the same with respect to the moving Hann window. From Table 4.2, $a_{\mathrm{II-Hann}}$ ranges between 2.30 and 3.84 for y_{corr} and 1.37 and 2.65 for y_{Four}. This variation is smaller compared to $a_{\mathrm{I-Hann}}$ (Table 4.2), because the required excess measurement range is no longer connected to the calculation range due to the moving window (Fig. 3.2).

The conclusion is that, compared to method I-Hann, method II-Hann requires a substantially smaller Δf_{meas} for small subcarrier separations (i.e., $2|\Delta i|/D_{\mathrm{FFT}} \ll \Delta f_{\mathrm{calc}}$). The important improvement of method II-Hann is that the required Δf_{meas} is disconnected from the calculation range. An additional advantage for method II-Hann is that the error is, besides fading, uniformly distributed over the calculation range, whereas for method I-Hann, the error power due to non-uniform windowing is concentrated near the outer parts. The major drawback of method II-Hann is that the channel still needs to be measured over an additional frequency range ($\Delta f_{\mathrm{meas,\,exc}}$) of 3.6 to 5 times (i.e., 2 $a_{\mathrm{II-Hann}}$) the subcarrier frequency separation. This may still be problematic for large bandwidth (e.g., GHz) channels.

Table 4.3: Experimental $a_{\mathrm{II-Hann}}$ values (dimensionless) are determined based on higher $|\Delta i|$ values, where the convergence of method II-Hann is restricted by non-uniform windowing. Mean (M), standard deviation (SD), minimum (MIN) and maximum (MAX) are given for different CP lengths and both coefficient types (y_{corr} and y_{Four}).

CP [ns]	type	range:	M	SD	MIN	MAX
400	y_{corr}	$|\Delta i| \geq$79	2.42	0.05	2.31	2.54
	y_{Four}	$|\Delta i| \geq$112	1.77	0.15	1.43	2.13
800	y_{corr}	$|\Delta i| \geq$17	2.56	0.25	2.30	3.84
	y_{Four}	$|\Delta i| \geq$14	1.80	0.21	1.37	2.65
400 / 800	y_{corr}	combined	2.50	0.20	2.30	3.84
	y_{Four}	combined	1.79	0.19	1.37	2.65

4.3.1.3 Method III-Hann

For methods I- and II-Hann, it has been shown that both the source and detecting subcarrier frequency are required to be covered by the central part of the applied Hann window (Sections 4.3.1.1 and 4.3.1.2), causing an increase of the required excess measurement range for a higher subcarrier separation. In fact, the problem is that the y_{Four} type coefficient is physically related to the channel around the source as well as the detecting subcarrier. Method III-Hann tackles this problem by decomposing the coefficient ($y_{\mathrm{Four},\Delta i}$) for a non-zero subcarrier separation in terms of a generalized, Δi-independent interference coefficient, which is evaluated

at the source and detecting subcarrier separately. This generalized interference coefficient can then be determined from a measured channel response by applying a moving Hann window.

For a higher $|\Delta i|$, where method II-Hann is limited by the non-uniform windowing (Table 4.3), the required Δf_{meas} drops considerably when comparing method III-Hann to II-Hann (Figs. 4.4(a) – 4.5(b)). For a $|\Delta i|$ of 255, the average required $\Delta f_{\mathrm{meas,\,exc}}$ is reduced from 374 / 365 MHz to 123 / 40 MHz for 400 / 800 ns CP, resp., for y_{corr} and from 281 / 275 MHz to 117 / 22 MHz for 400 / 800 ns CP, resp., for y_{Four}. For a smaller $|\Delta i|$, the required Δf_{meas} for method III-Hann is the same or even a little bit higher than for method II-Hann, especially for 400 ns CP. Indeed, for a smaller $|\Delta i|$, method II-Hann is no longer restricted by the error due to non-uniform windowing and benefits from a larger applied window compared to method III-Hann. However, this is rather secondary to the improvement that method III-Hann shows for a higher $|\Delta i|$. At zero Δi, methods II- and III-Hann are mathematically identical, in agreement with the same required Δf_{meas} as obtained from the convergence analysis. The corresponding required $\Delta f_{\mathrm{meas,\,exc}}$ is 111 / 36 MHz for 400 / 800 ns CP, resp., for y_{corr} and 8 / 15 MHz for y_{Four}. Contrary to y_{corr}, the required $\Delta f_{\mathrm{meas,\,exc}}$ for y_{Four} is considerably smaller at zero Δi compared to a $|\Delta i|$ of 255, especially for 400 ns CP. This is a result of the cancellation effect of the error due to a non-zero time resolution (Section 3.9). Finally, comparing method III-Hann to II-Hann, the overall required Δf_{meas} is reduced from 776 / 782 MHz to 524 / 457 ns for 400 / 800 ns CP, resp., for y_{corr} and from 712 / 728 MHz to 535 / 457 MHz, resp., for y_{Four} (Table 4.1).

For method III-Hann, the error due to non-uniform windowing is no longer a restricting factor as regards to the required Δf_{meas}. Indeed, this error is suppressed as the frequency resolution of the measured channel, Δf_{res}, is much smaller than the window width, which corresponds to $\Delta f_{\mathrm{meas,\,exc}}$ for method III (Section 3.4). To satisfy this requirement, a sufficiently small Δf_{res} of 0.5 MHz was chosen for measuring the channel. Exact calculations of the relative error power due to non-uniform windowing ($\tilde{E}_{\mathrm{NU}}$) confirm that this error is negligible for method III-Hann (i.e., $\tilde{E}_{\mathrm{NU}} \ll -14$ dB). Note that the relative error power, which is defined in Section 3.6, is further denoted more shortly by omitting the index α'. For 800 ns CP, the maximum $\tilde{E}_{\mathrm{NU}}$ (over $-255 \leq \Delta i \leq 255$) is -38.8 dB and -28.8 dB for y_{corr} and y_{Four}, resp., at a $\Delta f_{\mathrm{meas,\,exc}}$ of 5 MHz. At a higher $\Delta f_{\mathrm{meas,\,exc}}$, $\tilde{E}_{\mathrm{NU}}$ is negligible a fortiori. At a $\Delta f_{\mathrm{meas,\,exc}}$ of 25 MHz, the maximum $\tilde{E}_{\mathrm{NU}}$ is respectively -66.7 dB and -56.7 dB for y_{corr} and y_{Four}.

To determine whether the required Δf_{meas} is determined by the error due to resolution or leakage, the (relative) error power due to direct and aliased leakage ($\tilde{E}_{\mathrm{LK,\,dir}}$ and $\tilde{E}_{\mathrm{LK,\,al}}$, resp.) is calculated theoretically, i.e., by replacing the corresponding time-resolved components of the real channel by one tap (Section 3.9).

For a window width (or thus $\Delta f_{\mathrm{meas,\,exc}}$) of 25 MHz, the maximum $\tilde{E}_{\mathrm{LK,\,dir}}$ (over $-255 \leq \Delta i \leq 255$) is -56.9 / -62.3 dB, resp., for 400 / 800 ns CP for y_{corr} and -51.4 / -53.1 dB for y_{Four} (Table 4.4). The maximum $\tilde{E}_{\mathrm{LK,\,al}}$ is respectively -72.6 / -30.6 dB for y_{corr} and -61.2 / -19.4 dB for y_{Four}. For a larger window width, $\tilde{E}_{\mathrm{LK,\,al}}$ decreases fast. Since this theoretical calculation method provides an upper limit for the real $\tilde{E}_{\mathrm{LK,\,dir}}$ and $\tilde{E}_{\mathrm{LK,\,al}}$, it turns out that, at least from a $\Delta f_{\mathrm{meas,\,exc}}$ of 25 MHz, the error power due to direct and aliased leakage is negligible compared to the -14 dB accuracy level. The maximum required $\Delta f_{\mathrm{meas,\,exc}}$ (over $-255 \leq \Delta i \leq 255$) is 124 / 57 MHz for 400 / 800 ns CP, resp., for y_{corr} and 135 / 57 MHz for y_{Four}, showing that for method III-Hann, the main restricting factor of the required Δf_{meas} is the error due to a non-zero time resolution.

Table 4.4: Theoretical estimations of the maximum relative error power due to direct and aliased leakage ($\tilde{E}_{\mathrm{LK,\,dir}}$ and $\tilde{E}_{\mathrm{LK,\,dir}}$, resp.) for method III-Hann. This is given for a window width ranging from 25 MHz to 75 MHz and for both coefficient types (y_{corr} and y_{Four}).

CP [ns]	type	$\tilde{E}_{\mathrm{LK,\,dir}}$ (MAX) [dB]			$\tilde{E}_{\mathrm{LK,\,al}}$ (MAX) [dB]		
		25 MHz	50 MHz	75 MHz	25 MHz	50 MHz	75 MHz
400	y_{corr}	-56.9	-75.0	-85.2	-72.6	-90.7	-100.5
	y_{Four}	-51.4	-69.3	-79.3	-61.2	-79.3	-89.8
800	y_{corr}	-62.3	-80.4	-89.9	-30.6	-48.6	-60.4
	y_{Four}	-53.1	-71.1	-80.3	-19.4	-37.5	-49.3

4.3.2 Methods using a rectangular window

In Section 4.3.1.3, method III-Hann has been proposed to tackle the major problem of the more conventional methods I- and II-Hann, being a higher $\Delta f_{\mathrm{meas,\,exc}}$ requirement for a higher $|\Delta i|$ (type I and II) as well as for a higher Δf_{calc} (type I), as a result of non-uniform windowing. Another approach is to use a fixed rectangular window (method I-rect) or a moving rectangular window (method II-rect). Indeed, the error due to non-uniform windowing equals zero if the source and detecting subcarrier frequency is systematically covered by a rectangular window (Section 3.5). This is achieved when $\Delta f_{\mathrm{meas,\,exc}}$ is positive. As for method III-Hann, the restricting factor is the error due to a non-zero time resolution, the effect of applying a rectangular window (method III-rect) instead of a Hann window is also investigated. The effect of a rectangular window instead of a Hann window differs essentially for 400 ns and 800 ns CP and is discussed separately.

4.3.2.1 Results for 400 ns CP

For 400 ns CP, the required Δf_{meas} for method I-rect is considerably smaller than for method I-Hann. This is observed for both coefficient types and over the whole subcarrier separation range (Figs. 4.4(a) – 4.4(b)). Where method I-Hann requires a $\Delta f_{\mathrm{meas,\,exc}}$ in the range of $[224, 414]$ MHz for the y_{corr} coefficient type and $[195, 329]$ MHz for the y_{Four} type, the $\Delta f_{\mathrm{meas,\,exc}}$ required by method I-rect lies only in the range $[-2, 100]$ MHz and $[-11, 6]$ MHz, respectively. Applying a rectangular window results into a reduction of the overall required Δf_{meas} (taking into account all subcarrier separations) from 814 MHz and 726 MHz for y_{corr} and y_{Four}, resp., to 408 MHz and 397 MHz (Table 4.1), which is approximately equal to the overall zero-excess measurement range of 400 MHz.

For the type II method at 400 ns CP, a rectangular window instead of a Hann window yields a considerable reduction of $\Delta f_{\mathrm{meas,\,exc}}$ for a higher $|\Delta i|$, i.e., where method II-Hann is restricted by the error due to non-uniform windowing. For a $|\Delta i|$ of 255, the average required $\Delta f_{\mathrm{meas,\,exc}}$ drops from 374 MHz and 281 MHz for y_{corr} and y_{Four}, resp., to 84 MHz and 24 MHz. For y_{Four}, the required $\Delta f_{\mathrm{meas,\,exc}}$ does not vary much over Δi, ranging from 6 MHz to 38 MHz. The overall required Δf_{meas} (over all subcarrier separations) is reduced from 776 MHz and 712 MHz for y_{corr} and y_{Four}, resp., to 509 MHz and 424 MHz (Table 4.1).

For the type III method at 400 ns CP, no substantial effect is found from applying a rectangular window instead of a Hann window. For method III-Hann, a $\Delta f_{\mathrm{meas,\,exc}}$ is required in the range $[111, 124]$ MHz for y_{corr} and $[8, 135]$ MHz for y_{Four}, while for method III-rect, a required $\Delta f_{\mathrm{meas,\,exc}}$ is found in the range $[74, 159]$ MHz and $[20, 172]$ MHz, respectively. For method III-Hann, the overall required Δf_{meas} is 524 MHz and 535 MHz for y_{corr} and y_{Four}, resp., and 559 MHz and 572 MHz for method III-rect (Table 4.1).

4.3.2.2 Results for 800 ns CP

For 800 ns CP (Figs. 4.5(a) and 4.7), the effect of rectangular windowing is essentially different from 400 ns CP, in particular for y_{Four} around zero Δi. For method type I, the required Δf_{meas} is still significantly reduced over all subcarrier separations for y_{corr}, but not for y_{Four}. For y_{corr}, a required $\Delta f_{\mathrm{meas,\,exc}}$ in the range $[227, 389]$ MHz for method I-Hann is reduced to $[4, 106]$ MHz for method I-rect. This results into an overall required Δf_{meas} decreasing from 788 MHz to 505 MHz (Table 4.1). For y_{Four}, the required $\Delta f_{\mathrm{meas,\,exc}}$ shows a peak for $|\Delta i| \leq 2$ up to 661 MHz, exceeding the required $\Delta f_{\mathrm{meas,\,exc}}$ of 316 MHz for method I-Hann (Fig. 4.7(a)). Apart from this peak, the required $\Delta f_{\mathrm{meas,\,exc}}$ for method I-rect is generally smaller than for method I-Hann, but considerably higher than for 400 ns CP (Fig. 4.4(b)). In contrast to 400 ns CP, the required Δf_{meas} is

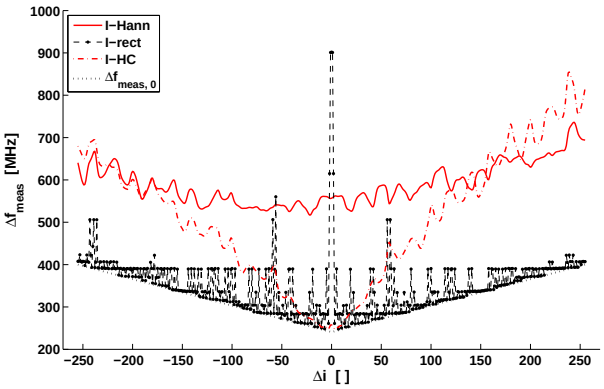

(a) type I methods

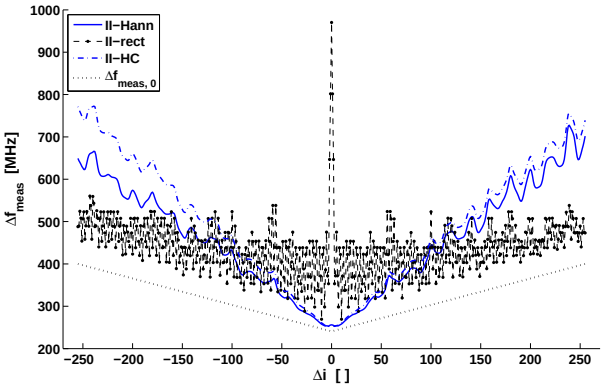

(b) type II methods

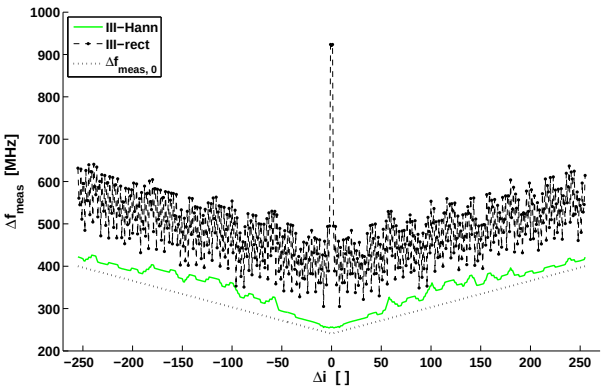

(c) type III methods

Figure 4.7: Required measurement range (Δf_{meas}) for 800 ns *CP as a function of the subcarrier separation (Δi) for different windowing methods. This is based on a* 241 MHz *calculation range and a* -14 dB *error ratio. The requirement is given for interference coefficient type* y_{Four}*. The zero-excess measurement range ($\Delta f_{\mathrm{meas},\,0}$) is added for comparison.*

strongly fluctuating with Δi between the zero-excess measurement range and a certain Δf_{meas} value of about 390 ± 1 MHz.

For method II-rect, the required Δf_{meas} for y_{corr} is, compared to method II-Hann, no longer smaller over the whole Δi range (Fig. 4.5(a)). This is the case in a Δi range of $[-104, 83]$. At zero Δi, method II-rect requires a $\Delta f_{\mathrm{meas,\,exc}}$ of 181 MHz, while only a $\Delta f_{\mathrm{meas,\,exc}}$ of 37 MHz is needed for method II-Hann. Over a Δi range of $[-40, 104]$, method II-rect requires a constant Δf_{meas} value of about 421 ± 1 MHz. For a higher $|\Delta i|$, the Δf_{meas} required by method II-rect is smaller than for method II-Hann. At a $|\Delta i|$ of 255, the average required $\Delta f_{\mathrm{meas,\,exc}}$ is reduced from 375 MHz (II-Hann) to 127 MHz (II-rect). As a result, the overall required Δf_{meas} for y_{corr} decreases from 782 MHz for method II-Hann to 575 MHz for method II-rect (Table 4.1). For y_{Four}, the effect of rectangular windowing is similar to method I-rect (Fig. 4.7(b)). The required $\Delta f_{\mathrm{meas,\,exc}}$ peaks for $|\Delta i| \leq 2$, up to 730 MHz. The required Δf_{meas} is strongly fluctuating with Δi with an upper envelope that follows rather a constant Δf_{meas} value than a constant excess $\Delta f_{\mathrm{meas,\,exc}}$, as observed for 400 ns CP (Fig. 4.4(a)). For a $|\Delta i|$ smaller than 55, this Δf_{meas} value lies about in the range $[439, 453]$ MHz. Compared to method II-Hann, method II-rect requires a larger Δf_{meas} over a Δi range of $[-162, 125]$. For a higher $|\Delta i|$, method II-rect performs better. However, the required Δf_{meas} peaking around zero Δi causes the overall required Δf_{meas} to increase from 728 MHz for method II-Hann to 970 MHz for method II-rect (Table 4.1).

For the type III method, the effect of a rectangular window is, compared to a Hann window, adverse for 800 ns CP. For y_{corr}, the $\Delta f_{\mathrm{meas,\,exc}}$ required by method III-rect ranges over $[147, 235]$ MHz with an average of 187 MHz, which is much larger than for method III-Hann, requiring an average $\Delta f_{\mathrm{meas,\,exc}}$ of 40 MHz (Fig. 4.5(a)). The overall required Δf_{meas} increases severely from 457 MHz (III-Hann) to 635 MHz (III-rect) (Table 4.1). For y_{Four}, the required $\Delta f_{\mathrm{meas,\,exc}}$ for method III-rect peaks over $|\Delta i| \leq 1$, up to 681 MHz, exceeding highly the required $\Delta f_{\mathrm{meas,\,exc}}$ of 15 MHz for method III-Hann (Fig. 4.7(c)). For a higher $|\Delta i|$, the required $\Delta f_{\mathrm{meas,\,exc}}$ is strongly fluctuating with an upper envelope varying over about $[214, 250]$ MHz. This is much larger than the $\Delta f_{\mathrm{meas,\,exc}}$ required for method III-Hann, with a maximum of 57 MHz. Again, the overall required Δf_{meas} dramatically rises from 457 MHz (III-Hann) to 1082 MHz (III-rect) (Table 4.1).

4.3.2.3 Conclusion

Based on this discussion, the effect on the required measurement range (Δf_{meas}) resulting from a rectangular window instead of a Hann window can be summarized as follows. For 400 ns CP, the effect is beneficial for the methods of type I and II for both coefficient types. No significant effect is found for the type III

method. For 800 ns CP, the required Δf_{meas} increases severely for y_{Four} around a zero Δi, which is observed for method types I, II and III. This is dramatic as, for the most important interference coefficient (zero Δi), an excess measurement range between 661 MHz and 730 MHz is needed in addition of a calculation range of only 241 MHz. Apart from this peak, method I-rect performs better for both coefficient types, while method II-rect performs only better for a high $|\Delta i|$ (i.e., higher than about 80 to 160) and method III-rect performs worse over the whole Δi range. The detrimental effect for 800 ns CP is caused by the error due to aliased leakage, which is generally more severe for a rectangular window than for a Hann window. For 400 ns CP, the relative error power due to aliased leakage is much smaller, which results in a smaller Δf_{meas} requirement. The effect of leakage will be discussed in detail in Chapter 5.

4.3.3 Methods using Hann window correction

In methods I- and II-HC, the non-uniform windowing is compensated by dividing the interference coefficient obtained via method I- or II-Hann by the window function, $W(\Delta\omega_{\mathrm{s}})$, as evaluated at the source subcarrier frequency, ω_{s}. This Hann window correction yields that for the y_{corr} type coefficient, the error due to non-uniform windowing disappears and that for the y_{Four} type, this error power becomes negligible compared to the interference power if the Hann window function is approximately equal at the source and detection subcarrier (Section 3.5). The latter is achieved for both method type I and II on condition that the excess measurement range ($\Delta f_{\mathrm{meas,\,exc}}$) is of the order of the subcarrier frequency separation. Whereas window correction suppresses the error due to non-uniform windowing, other error types are divided by $W(\Delta\omega_{\mathrm{s}})$ and may consequently increase (at a given Δf_{meas}). The performance of methods I- and II-HC is essentially different for coefficient types y_{corr} and y_{Four}.

4.3.3.1 Results for y_{corr}

For y_{corr}, the required $\Delta f_{\mathrm{meas,\,exc}}$ is considerably smaller for methods I-HC and II-HC compared to methods I-Hann and II-Hann, resp., where the restricting factor is non-uniform windowing (Figs. 4.4(a) and 4.5(a)). For the type I method, the improvement is over the whole Δi range. By Hann window correction, the required $\Delta f_{\mathrm{meas,\,exc}}$ is reduced from 300 / 314 MHz for 400 / 800 ns CP, resp., to 46 / 52 MHz at zero Δi, and (averaged) from 408 / 365 MHz to 65 / 83 MHz at a $|\Delta i|$ of 255. Methods II-Hann and II-HC are mathematically identical at zero Δi, with a required $\Delta f_{\mathrm{meas,\,exc}}$ of 111 / 37 MHz for 400 / 800 ns CP, respectively. At a higher $|\Delta i|$, there is a substantial improvement due to Hann window correction. At a $|\Delta i|$ of 255, the required $\Delta f_{\mathrm{meas,\,exc}}$ is reduced from (averaged) 374 / 375 MHz for 400 / 800 ns CP, resp., to 88 / 112 MHz. For methods

I-HC and II-HC, the required $\Delta f_{\mathrm{meas,\,exc}}$ increases only slightly with $|\Delta i|$. Finally, the overall required Δf_{meas} (i.e., for the determination of the spectral interference over the whole Δi range) is reduced by Hann window correction from 814 / 788 MHz to 466 / 504 MHz for the type I method and from 776 / 782 MHz to 489 / 546 MHz for type II (Table 4.1).

For the y_{corr} coefficient type, the restricting factor for methods I-HC and II-HC is the error due to the non-zero time resolution, considering the small relative error power due to leakage for method III-Hann (Table 4.4). These values may be even smaller for methods II- and III-Hann due to the larger window width. Although these error powers are increased by $-20\log(W(\Delta\omega_{\mathrm{s}}))$ in dB-scale by the Hann window correction, the resulting error power due to leakage is still negligible compared to the -14 dB accuracy threshold. Indeed, based on a $\Delta f_{\mathrm{meas,\,exc}}$ of 50 MHz and even in the worst case of a high $|\Delta i|$ of 255, the increase is estimated as 17.4 dB for method II-HC and (averaged) 16.8 dB for method I-HC. Based on a window width of at least 50 MHz (Table 4.4), this means that the relative error power due to direct or aliased leakage falls below -31.2 dB.

4.3.3.2 Results for y_{Four}

For y_{Four} (Figs. 4.4(b) and 4.5(b)), the Hann window correction for method type I causes a reduction of the required $\Delta f_{\mathrm{meas,\,exc}}$ over a Δi range of about $[-148, 127]$ and $[-173, 119]$ for 400 ns and 800 ns CP, respectively. At zero Δi, the required $\Delta f_{\mathrm{meas,\,exc}}$ drops from 308 / 316 MHz for 400 / 800 ns CP, resp., to 9 / 17 MHz. For a higher $|\Delta i|$, the required $\Delta f_{\mathrm{meas,\,exc}}$ appears to be somewhat larger for method I-HC. At a $|\Delta i|$ of 255, the required $\Delta f_{\mathrm{meas,\,exc}}$ increases from (averaged) 300 / 267 MHz for 400 / 800 ns CP, resp., to 357 / 349 MHz. For a higher $|\Delta i|$, the required $\Delta f_{\mathrm{meas,\,exc}}$ is approximately proportional to $|\Delta i|$. Indeed, to suppress the error due to non-uniform windowing, a $\Delta f_{\mathrm{meas,\,exc}}$ is required of the order of the subcarrier frequency separation, i.e.,

$$\Delta f_{\mathrm{meas,\,exc}} = 2a_{\mathrm{I-HC}}|\Delta i|/D_{\mathrm{FFT}}. \tag{4.7}$$

Based on $|\Delta i| > 10$, the following $a_{\mathrm{I-HC}}$ values are obtained: 2.4 ± 0.5 for 400 ns CP and 2.4 ± 0.7 for 800 ns CP.

For the type II method, the required $\Delta f_{\mathrm{meas,\,exc}}$ increases slightly over the whole Δi range when applying Hann window correction. The proportional relation between the required $\Delta f_{\mathrm{meas,\,exc}}$ and $|\Delta i|$ for method II-Hann largely remains unchanged. Indeed, as for the type II method, the moving Hann window is systematically centered at the detection subcarrier frequency, the source subcarrier frequency has to be covered by the central part of the window. This requires an excess $\Delta f_{\mathrm{meas,\,exc}}$ being proportional to the subcarrier frequency separation. Based on $|\Delta i| > 10$, the ratio factor $a_{\mathrm{II-HC}}$, defined as in Eq. 4.7, is found to be 2.3 ± 0.1

for 400 ns CP and 2.3 $\pm$ 0.2 for 800 ns CP. Finally, the overall required Δf_{meas} increases by Hann window correction from 726 / 736 MHz for 400 ns and 800 ns CP, resp., to 813 / 855 MHz for the type I method and from 712 / 728 MHz to 771 / 773 MHz for type II (Table 4.1).

4.3.3.3 Conclusion

The main conclusion is that Hann window correction yields a considerable reduction of the required Δf_{meas} for the y_{corr} type coefficient for both the methods of type I and II. For the y_{Four} type, methods I-HC and II-HC do not perform better than method II-Hann: the Δf_{meas} requirement is still dominated by non-uniform windowing, resulting into a required excess $\Delta f_{\mathrm{meas,\,exc}}$ of more than 4 times the subcarrier frequency separation. Indeed, y_{corr} is an interference coefficient that is physically based on evaluating the channel around the source subcarrier only, while for y_{Four}, the evaluation is around both the source and the detecting subcarrier. Hence, Hann window correction is only effective for method type I and for a sufficiently small subcarrier separation, so that the window function has approximately equal values at the source and detection subcarrier.

4.3.4 Required measurement range for the determination of the total interference

In Sections 4.3.1 to 4.3.3, it has been discussed which measurement frequency range, Δf_{meas}, is required for the determination of the *spectral* interference with a given accuracy. This may be useful for e.g., equalization design. For the determination of the channel's performance, the interest is rather in the *total* interference. This is the spectral interference power at a certain detecting subcarrier, summed over all source subcarriers. Consequently, the required measurement range (Δf_{meas}) may be smaller for the determination of the total interference. In this section, the required measurement range for the total interference is investigated for different windowing methods and compared to the requirement for the spectral interference.

In Sections 4.3.1 to 4.3.3, the convergence analysis of the interference is based on a *fixed calculation range* for all subcarrier separations, i.e., the detecting subcarrier frequency ranges over a fixed frequency range (Δf_{calc}). Consequently, the zero-excess measurement range, i.e., the frequency range of interest defined by all source and detecting subcarriers involved, has a width ($\Delta f_{\mathrm{meas},\,0}$) of $\Delta f_{\mathrm{calc}} + 2|\Delta i|/D_{\mathrm{FFT}}$, when determining the spectral interference for $\pm|\Delta i|$ (Fig. 3.2). The variation of $\Delta f_{\mathrm{meas},\,0}$ with $|\Delta i|$ is useful for the convergence analysis to show the effect on the required Δf_{meas}. In the more practical case where the aim is to determine the interference due to insufficient CP for a given set of channels or a frequency band, the interest is only in the spectral interference

terms for which both the source and detecting subcarrier fall in this frequency band. Thus, in this case, there is a *fixed zero-excess measurement range*, corresponding to the frequency band of interest. The frequency band width will also be denoted by Δf_{calc}, as it is the calculation range corresponding to $\pm|\Delta i|$ jointly. In Fig. 4.8, the windowing methods are schematically illustrated in the case of a fixed zero-excess measurement range. The difference with the case of a fixed calculation range (Fig. 3.2) is that for method type II, the window centre frequency has to move over the whole zero-excess measurement range when determining the spectral interference for $\pm|\Delta i|$. In this section, a convergence analysis of the interference is presented based on the same frequency range as in Sections 4.3.1 to 4.3.3 (i.e., with a 241 MHz width and centered at 3.8 GHz), but now considered as a frequency band (i.e., the case of a fixed zero-excess measurement range). The analysis includes both the spectral and the total interference and provides a good summary of all windowing methods as regards to the Δf_{meas} requirement.

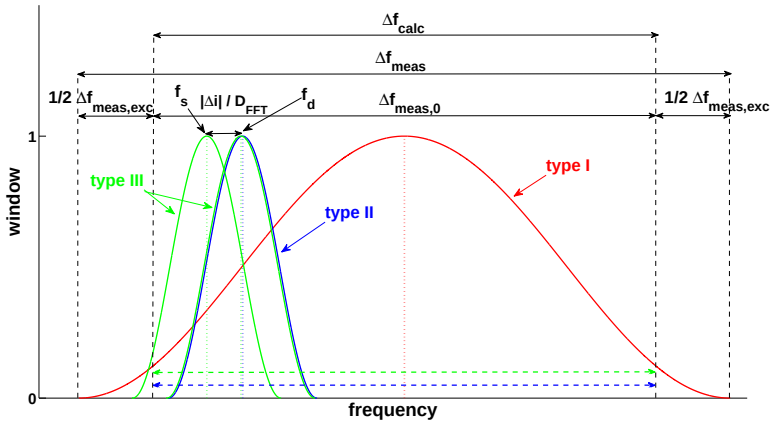

Figure 4.8: Schematical illustration of the windowing methods in the case of a fixed zero-excess measurement range ($\Delta f_{\mathrm{meas},0}$). For all source and detecting subcarrier frequencies (f_{s} and f_{d}, resp.) lying both in this frequency band, the interference due to insufficient CP is determined. In this case, the calculation range (Δf_{calc}) falls together with the zero-excess measurement range. The measurement range (Δf_{meas}) and the excess measurement range ($\Delta f_{\mathrm{meas,exc}}$) are indicated as well.

For the determination of the total interference power over the frequency band, it is assumed that the detecting subcarrier is always in the centre of the channel bandwidth, i.e., the detecting subcarrier index i' (Section 2.2) is zero. The total interference as a function of the detecting subcarrier frequency is obtained by adding up all spectral power terms over a Δi range of $[-255, 255]$ (i.e., a 160 MHz bandwidth), as far as the corresponding source subcarriers fall within the frequency

band. If the (frequency) width of the spectral (frequency-averaged) interference power is much smaller than the bandwidth, the total interference power as determined is also representative for other detecting subcarriers located in the central part of the channel bandwidth. This condition is realistic, as explained as follows. The spectral interference width, $|\Delta i_{\mathrm{w}}|$, is defined as twice the smallest $|\Delta i|$ for which at least 90% of the total interference power originates from the range $[-|\Delta i|, |\Delta i|]$. Based on the measured channel, $|\Delta i_{\mathrm{w}}|$ is found to be 36 / 38 for 400 ns and 800 ns CP, respectively. The corresponding frequency width (Δf_{w}), i.e., $|\Delta i_{\mathrm{w}}|/D_{\mathrm{FFT}}$, then equals 11.2 / 11.8 MHz, resp., which is indeed much smaller than a 160 MHz channel bandwidth. This also shows that the effect of not including the spectral interference terms originating from (source) subcarriers outside the frequency band, is only limited to the edges of the frequency band.

From a convergence analysis analogous to Section 4.2, the required measurement range, Δf_{meas}, is determined for a relative error power of -14 dB. This is expressed in terms of the excess measurement range, $\Delta f_{\mathrm{meas,\,exc}}$, which is still defined as the difference between Δf_{meas} and $\Delta f_{\mathrm{meas},\,0}$. Note that, in this convergence analysis, $\Delta f_{\mathrm{meas},\,0}$ always equals 241 MHz. Note also that for method types II and III, $\Delta f_{\mathrm{meas,\,exc}}$ corresponds to the window width (Δf_{win}) (Fig. 4.8). The required $\Delta f_{\mathrm{meas,\,exc}}$ for the total interference is compared with the maximum $\Delta f_{\mathrm{meas,\,exc}}$ (i.e., over a Δi range of $[-255, 255]$) required for the spectral interference (Table 4.5). The requirement for the total interference is dominated by the one for the most important spectral interference terms. For the channel under study, the total (frequency-averaged) interference power due to the y_{corr} coefficient is 20.6 / 20.3 dB smaller for 400 / 800 ns CP, resp., than the one based on the y_{tot} coefficient type. Reminding that $|\Delta i_{\mathrm{w}}|$ is 36 / 38 for 400 / 800 ns CP, resp., it follows that the $\Delta f_{\mathrm{meas,\,exc}}$ requirement for the total interference will be dominated by the spectral terms of type y_{Four} for $|\Delta i| \leq 18$ / 19.

4.3.4.1 Results for methods using a Hann window

For method I-Hann, the required excess measurement range ($\Delta f_{\mathrm{meas,\,exc}}$) for the total interference is not substantially reduced compared to the spectral interference (Table 4.5). For the spectral interference, the restricting factor over the whole Δi range and for both coefficient types is the error due to non-uniform windowing, resulting into a required $\Delta f_{\mathrm{meas,\,exc}}$ of the order of $\Delta f_{\mathrm{meas},\,0}$ (Section 4.3.1.1). Consequently, this requirement also applies for the total interference. The ratio ($a_{\mathrm{I-Hann}}$) between the required $\Delta f_{\mathrm{meas,\,exc}}$ and $\Delta f_{\mathrm{meas},\,0}$ is $1.2 - 1.3$. Compared to the value of 0.9 ± 0.2 obtained for y_{Four} in Section 4.3.1.1, the former value is somewhat higher, because the error due to non-uniform windowing is now critical at both outer sides of the zero-excess measurement range (instead of one side).

Using method II-Hann for the spectral interference, a $\Delta f_{\mathrm{meas,\,exc}}$ larger than four times the subcarrier frequency separation is required to suppress the error due

Table 4.5: This table presents the excess measurement range ($\Delta f_{\mathrm{meas,\,exc}}$) [MHz] required to determine the spectral and the total interference over a 241 MHz *frequency band for a* 160 MHz *bandwidth. The relative error power is* -14 dB. *For the spectral interference, the requirement is also given specifically for the y_{corr} and y_{Four} type interference terms forming the composed type, y_{tot}.*

	400 ns CP				800 ns CP			
method	spectral			total	spectral			total
	y_{corr}	y_{Four}	y_{tot}	y_{tot}	y_{corr}	y_{Four}	y_{tot}	y_{tot}
I-Hann	300	313	313	298	314	318	328	311
II-Hann	531	469	511	33	542	488	522	32
III-Hann	122	135	124	15	57	57	64	14
I-rect	127	1	1	-3	71	661	661	321
II-rect	268	184	210	45	320	730	729	368
III-rect	159	161	172	46	229	682	682	351
I-HC	46	325	262	36	72	337	271	37
II-HC	258	531	466	195	292	543	496	196

to non-uniform windowing (Section 4.3.1.2). Note that the maximum of twice the subcarrier frequency separation corresponds to the channel bandwidth (B), i.e., 160 MHz. The ratio between the maximum required $\Delta f_{\mathrm{meas,\,exc}}$ (Table 4.5) and B yields $3.3 - 3.4$ for y_{corr} and $2.9 - 3.1$ for y_{Four}. This ratio corresponds essentially to $a_{\mathrm{II-Hann}}$ as defined in Section 4.3.1.2, where a value of 2.5 ± 0.2 and 1.8 ± 0.2 is obtained for y_{corr} and y_{Four}, respectively. The difference is about 1, which shows in fact an agreement. Indeed, for all type II methods, the $\Delta f_{\mathrm{meas,\,exc}}$ required for spectral interference is systematically twice the subcarrier frequency separation larger than in the case of a fixed calculation range. This is because the window centre has to move now over the whole (fixed) zero-excess measurement range. Consequently, the ratio between the required $\Delta f_{\mathrm{meas,\,exc}}$ and twice the subcarrier frequency separation is now systematically 1 higher. For the total interference, the required $\Delta f_{\mathrm{meas,\,exc}}$ is significantly reduced from $469 - 542$ MHz to $32 - 33$ MHz. Indeed, as only subcarrier separations within the spectral interference width are relevant, it is sufficient that $\Delta f_{\mathrm{meas,\,exc}}$ is of the order of Δf_{w} instead of B. The ratio between the $\Delta f_{\mathrm{meas,\,exc}}$ required for the total interference and Δf_{w} is found to be $2.7 - 2.9$, agreeing well with the ratio value for y_{Four} just mentioned.

For method III-Hann, the $\Delta f_{\mathrm{meas,\,exc}}$ required for the spectral interference is in good approximation the same as obtained based on a fixed calculation range (Section 4.3.1.3), reaching values of maximum 135 / 64 MHz for 400 / 800 ns

CP, respectively. The restricting factor is the error due to a non-zero time resolution. For the total interference, the required $\Delta f_{\mathrm{meas,\,exc}}$ is considerably reduced to $14 - 15$ MHz. This is caused by the cancellation effect of the error due to a non-zero time resolution (Section 3.9), which occurs for the y_{Four} coefficient type at a small $|\Delta i|$.

4.3.4.2 Results for methods using a rectangular window

For the methods using a rectangular window, the excess measurement range ($\Delta f_{\mathrm{meas,\,exc}}$) required for the spectral interference is found peaking around zero Δi for y_{Four} at 800 ns CP (Section 4.3.2). This is caused by the error due to leakage, as shown in Section 5.2. An extremely large $\Delta f_{\mathrm{meas,\,exc}}$ is required, ranging from 661 MHz (method I-rect) to 730 MHz (method II-rect) (Table 4.5). For the total interference, the required $\Delta f_{\mathrm{meas,\,exc}}$ is about halved and ranges from 321 MHz (method I-rect) to 368 MHz (method II-rect). However, this still means a very large $\Delta f_{\mathrm{meas,\,exc}}$ requirement compared to the frequency band. The reduced $\Delta f_{\mathrm{meas,\,exc}}$ requirement for the total interference can be explained by the fact that the $\Delta f_{\mathrm{meas,\,exc}}$ peak width just mentioned, i.e., $|\Delta i| \leq 2$, is smaller than the spectral interference width.

For the methods using a rectangular window and at 400 ns CP, the required $\Delta f_{\mathrm{meas,\,exc}}$ is generally smaller. For method I-rect, an excess measurement range of about zero is required for y_{Four} (spectral interference) as well as for the total interference. However, for type I methods, the error power is, apart from fluctuations through fading, not uniformly distributed over the calculation range and may be concentrated near the outer parts of the frequency band. Note that a small negative excess requirement is possible because the error power is averaged over the calculation range. For method II-rect, a (maximum) $\Delta f_{\mathrm{meas,\,exc}}$ of $184 - 268$ MHz is required for the spectral interference (Table 4.5), which is larger than for method I-rect. Indeed, since for type II methods, the window centre moves over the whole zero-excess measurement range, the (maximum) $\Delta f_{\mathrm{meas,\,exc}}$ required for the spectral interference must be larger than B. For the total interference, the required $\Delta f_{\mathrm{meas,\,exc}}$ is reduced to 45 MHz, because the relevant subcarrier separations are limited to the spectral interference width. For method III-rect, the required $\Delta f_{\mathrm{meas,\,exc}}$ is reduced from $159 - 172$ MHz for the spectral interference to 46 MHz for the total interference. Indeed, the $\Delta f_{\mathrm{meas,\,exc}}$ required for spectral interference is strongly reduced for y_{Four} and a small $|\Delta i|$ at 400 ns CP, just as for method III-Hann (Fig. 4.4(b)).

4.3.4.3 Results for methods using Hann window correction

For method I-HC, an excess measurement range ($\Delta f_{\mathrm{meas,\,exc}}$) of only $46 - 72$ MHz is required for y_{corr} (spectral interference), which is much smaller

compared to method I-Hann (Table 4.5). The restricting factor is the resolution error (due to a non-zero time resolution) (Section 4.3.3). For y_{Four}, the (maximum) required $\Delta f_{\mathrm{meas,\,exc}}$ ranges from 325 MHz to 337 MHz. Indeed, to suppress the error due to non-uniform windowing, the (maximum) $\Delta f_{\mathrm{meas,\,exc}}$ required for the spectral interference must be larger than B (Section 4.3.3). The ratio between the maximum required $\Delta f_{\mathrm{meas,\,exc}}$ and B is found to be $2.0 - 2.1$, which agrees fairly with the $a_{\mathrm{I-HC}}$ value of 2.4 ($\pm$ 0.5 or $\pm$ 0.7) obtained in Section 4.3.3. For the total interference, the required $\Delta f_{\mathrm{meas,\,exc}}$ is much smaller than for y_{Four} (spectral interference). Indeed, $\Delta f_{\mathrm{meas,\,exc}}$ needs only to be larger than Δf_{w}, since only subcarrier separations within the spectral interference width are relevant. The ratio between the required $\Delta f_{\mathrm{meas,\,exc}}$ and Δf_{w} equals $3.1 - 3.2$.

For method II-HC, the required $\Delta f_{\mathrm{meas,\,exc}}$ for the spectral interference must be larger than B, just as for other type II methods. For y_{corr}, the Hann window correction is effective, reducing the required $\Delta f_{\mathrm{meas,\,exc}}$ from $531 - 542$ MHz for method II-Hann to $258 - 292$ MHz for method II-HC (Table 4.5). For y_{Four}, the Hann window correction is slightly adverse and a $\Delta f_{\mathrm{meas,\,exc}}$ is required of $3.3 - 3.4$ times B. For the total interference, the required $\Delta f_{\mathrm{meas,\,exc}}$ is $195 - 196$ MHz, which is still much larger than Δf_{w}. Contrary to method II-Hann, the required $\Delta f_{\mathrm{meas,\,exc}}$ is not reduced to the order of Δf_{w}. Indeed, for method II-HC, the $\Delta f_{\mathrm{meas,\,exc}}$ required for the total interference must be larger than B, as otherwise the Hann window correction implies that the interference coefficient may be divided by a window function value of nearly zero.

4.3.4.4 Requirement for the composed interference coefficient (type y_{tot})

For the composed interference coefficient, i.e., of type y_{tot}, the Δf_{meas} required for the spectral interference lies somewhere between the requirement of the y_{corr} type and the y_{Four} type coefficient, if these are of the same order. If the y_{Four} term is dominant, the requirement for y_{tot} is approximately the same as for y_{Four}. At a zero Δi, the spectral interference power due to y_{Four} is typically much larger than the one due to y_{corr}. For a subcarrier frequency separation of the order of half the bandwidth, the spectral interference power due to y_{Four} becomes typically of the same order of the one due to y_{corr}. This follows from the weighting functions (Section 2.2) and is experimentally confirmed. Based on the measured channel, the ratio between the y_{corr} interference power and the y_{tot} interference power at zero Δi is -37 dB for both 400 ns and 800 ns CP. This ratio reaches -10 dB for a $|\Delta i|$ higher than 55. For a $|\Delta i|$ higher than 150, this ratio ranges between -6.8 dB and -0.9 dB.

The maximum $\Delta f_{\mathrm{meas,\,exc}}$ required for the spectral interference due to y_{tot} lies largely between the requirements for y_{corr} and y_{Four} (Table 4.5). However, for methods I-, II- and III-rect, the required $\Delta f_{\mathrm{meas,\,exc}}$ for y_{tot} is mainly determined by y_{Four}, as this requirement originates from a zero Δi, where y_{Four} is dominant.

For method I-rect at 400 ns CP, the y_{tot} requirement is apparently not influenced by the y_{corr} requirement. However, this is caused by the error power fluctuations as a function of the window width, resulting into an exceptional deviation of the convergence analysis. The main conclusions drawn also apply for the maximum required Δf_{meas} based on a fixed calculation range (Table 4.1).

4.4 Measured interference power

In this section, some important measurement results of the interference due to insufficient CP are presented. For the measured channel (Section 4.1), the interference is determined over a frequency band centered at 3.8 GHz and with a 241 MHz width. Method III-Hann is applied using a window width of 150 MHz. As the zero-excess measurement range has a width of 241 MHz and the window width always equals the excess measurement range for method type III (Section 3.4.3), this corresponds to a measurement range (Δf_{meas}) of 391 MHz. Consequently, based on Table 4.5, the relative error power due to window-related errors (i.e., non-uniform windowing, resolution and leakage) is smaller than -14 dB. The relative error power due to a cut-off is limited by -14 dB (Section 4.2). The number of sweeps used for averaging is 960, ensuring that the relative error power due to measurement noise is much smaller than -14 dB (Section 6.2).

Fig. 4.9 shows the measured spectral interference profile. This is the frequency-averaged interference power as a function of the subcarrier separation, which has already been defined in Section 3.6 as $I_{\mathrm{tot},\Delta i,\mathrm{av}}$ (Eq.3.31). The index "tot" indicates that the composed interference coefficient type, y_{tot}, is considered. From Fig. 4.9, the ratio between the spectral interference for 400 ns and 800 ns CP is 12.3 ± 1.0 dB and ranges over $[9.5, 15.1]$ dB. The spectral interference width, $|\Delta i_{\mathrm{w}}|$, has been defined as twice the smallest $|\Delta i|$ for which at least 90% of the total interference power originates from the range $[-|\Delta i|, |\Delta i|]$. It is found that $|\Delta i_{\mathrm{w}}|$ is 36 / 38 for 400 / 800 ns CP, respectively.

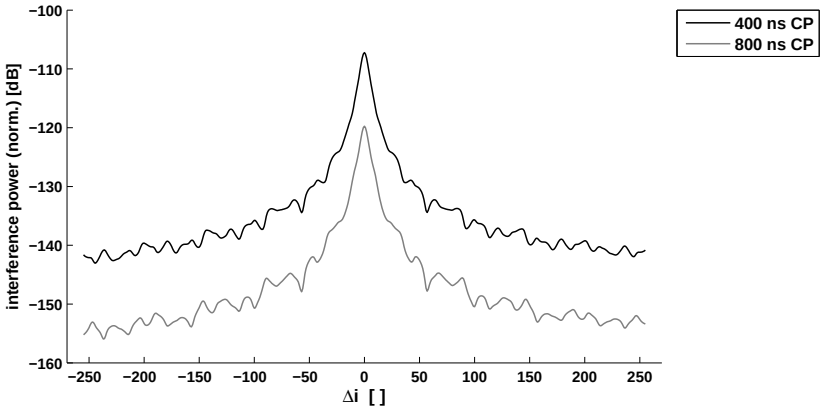

Figure 4.9: For a frequency band centered at 3.8 GHz *and with a* 241 MHz *width, the (normalized) spectral interference power is determined as a function of the subcarrier separation* (Δi) *from a measured channel for* 400 ns *and* 800 ns *CP.*

Fig. 4.10 shows the total interference power as a function of the detecting sub-

carrier frequency. This comprises interference from all source subcarriers and from any OFDM symbol (including ISI and ICI). This has been defined in Section 2.5 as $I(\omega_\mathrm{d})$. The frequency-dependent signal, i.e., $|C(\omega_\mathrm{d})|^2$, is determined at the same frequency resolution (Δf_d) as for the interference, i.e., 62.5 kHz, applying a moving Hann window with a width of 150 MHz over the channel response and a time-domain integration with a weighting function being unity (Section 2.2). Note that the interference and the signal are defined as normalized to the transmit power per subcarrier, $P_{\mathrm{T,subc}}$. The (normalized) thermal noise level is thus given by $k_\mathrm{B}T/(D_\mathrm{FFT}P_{\mathrm{T,subc}})$. For a transmit power of 30 dBm over a 160 MHz bandwidth, the thermal noise level is then -121.9 dB. The frequency-averaged total interference power is -93.6 dB and -106.0 dB for 400 ns and 800 ns CP, resp., and the frequency-averaged signal power is -59.8 dB. The signal-to-interference ratio is then 33.8 dB and 46.2 dB for 400 ns and 800 ns CP, respectively. Assuming a noise factor F_AWGN of 10 dB, the corresponding signal-to-interference-plus-noise ratio (SINR) is degraded from 52.1 dB in the case of no interference due to insufficient CP (i.e., the hypothetical case of an infinite CP length) to 33.7 dB and 45.2 dB for 400 ns and 800 ns CP, respectively.

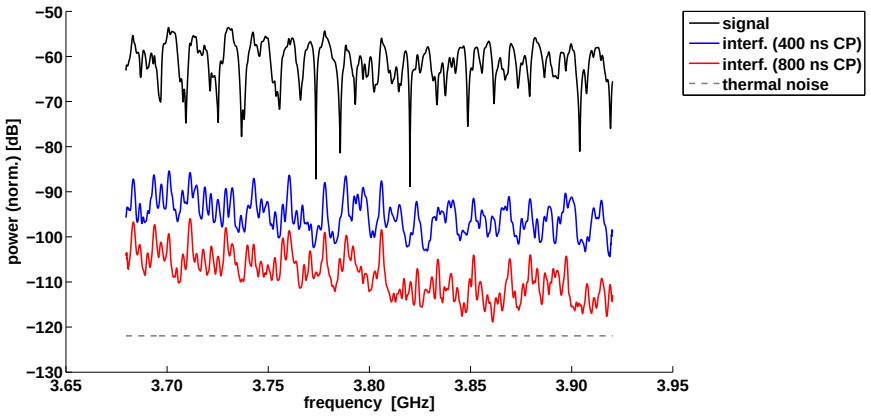

Figure 4.10: The (normalized) total interference power as a function of the detecting subcarrier frequency is determined from a measured channel for 400 ns *and* 800 ns *CP. The (normalized) signal and thermal noise level are added. The latter refers to a transmit power of* 30 dBm *at a* 160 MHz *bandwidth.*

4.5 Conclusions

In this chapter, the performance of various windowing methods with respect to the time resolution and the dynamic range is experimentally evaluated. The performance evaluation is performed at a fixed accuracy level of the interference coefficient (at a relative error power of -14 dB). To determine accurately the interference coefficient over a given subcarrier frequency range, a certain measurement range is needed as a result of the window width requirement to achieve sufficient time resolution and dynamic range. As experimentally shown in this chapter, the required measurement range may exceed the zero-excess measurement range, which is the frequency range determined by all subcarriers of interest. The required measurement range excess is evaluated for different windowing methods based on a channel measurement in a large exposition hall and for typical IEEE 802.11ac OFDM parameters.

The overall conclusion of this evaluation can be formulated as follows. To determine the **spectral interference** (the interference coefficient), method III-Hann is most appealing, especially for a higher bandwidth (subcarrier separation). Other Hann window-based methods require a measurement range excess of the order of the bandwidth (methods II-Hann, I-HC, II-HC) or even the zero-excess measurement range (method I-Hann). Methods using a rectangular window suffer from leakage for a higher CP.

To determine the **total interference power**, method III-Hann is found to be also very attractive. Methods II-Hann and I-HC are very useful too, requiring a measurement range excess of the order of the spectral interference width. However, method I-HC is less attractive to determine the interference as a function of the frequency because of a non-uniformly distributed error. Other Hann window-based methods still require a measurement range excess of the order of the bandwidth (method II-HC) or the zero-excess measurement range (method I-Hann). Methods using a rectangular window may again suffer from leakage, especially at a higher CP.

Finally, some practically relevant interference characteristics of the measured channel are reported. The signal-to-interference ratio is found 33.8 dB and 46.2 dB for 400 ns and 800 ns CP, respectively. Assuming a noise factor F_{AWGN} of 10 dB, the corresponding signal-to-interference-plus-noise ratio (SINR) is degraded from 52.1 dB in the case of no interference due to insufficient CP to 33.7 dB and 45.2 dB for 400 ns and 800 ns CP, respectively. The spectral interference width, capturing 90% of the total interference power, is found to be extended over a subcarrier separation of 36 / 38 for 400 / 800 ns CP, respectively.

5

Limitations for windowing methods due to time resolution and leakage

To determine the interference due to insufficient CP at a given accuracy level, the required measurement frequency range for different windowing methods has been discussed in Chapter 4. For methods I-Hann, II-Hann, I-HC and II-HC, non-uniform windowing has found to be the limiting error type, yielding a window width requirement related to the calculation range and/or the bandwidth. In this chapter, the limitations caused by a non-zero time resolution and (direct and aliased) leakage are investigated with the focus on methods III-Hann and I-rect, serving as reference for other methods. This is performed by inspection of the type-specific error power. Just as for the analysis of the required measurement range (Chapter 4), this is carried out based on the channel measurement described in Section 4.1 and for typical IEEE 802.11 parameters (Section 4.2).

In Section 5.1, the theoretical estimations methods for the error power due to resolution and (direct and aliased) leakage, introduced in Section 3.9, are experimentally validated. Using these estimations methods, the limiting error type with respect to the required measurement range is determined in Section 5.2 and the implications on the windowing method's limitations and the measurement setting requirements (i.e., window width and frequency resolution) are discussed. In Section 5.3, the limitation through leakage is further discussed in terms of a maximum measurable signal-to-interference ratio (SIR).

5.1 Validation of the theoretical estimation of the error power due to resolution and leakage

In this section, the *theoretical* estimation method of the relative error power due to a non-zero time resolution (including near leakage) (Section 3.9.2) and direct and aliased leakage (Section 3.9.3) is experimentally validated. For the calculation of the *real* type-specific error power (Section 3.9.1) at a given window width, the channel impulse reponse must be detected with a much higher window width (i.e., a much smaller time resolution). Moreover, this demands a higher order of computational capacity. Therefore, theoretical estimations of the type-specific error power have been introduced (Section 3.9). For the relative error power due to resolution ($\tilde{E}_{\mathrm{RS}}$), a theoretical estimation for the y_{corr} coefficient type was proposed in terms of the window width and the reverberation time. This theoretical error power serves as a reference for the $y_{\mathrm{Four},\Delta i}$ coefficient, where the (real) resolution error power is typically strongly reduced for a small subcarrier separation (i.e., cancellation effect) and becomes of the same order as for y_{corr} for a higher subcarrier separation. For the relative error power due to direct and aliased leakage ($\tilde{E}_{\mathrm{LK,dir}}$ and $\tilde{E}_{\mathrm{LK,al}}$, resp.), the proposed theoretical estimation is based on a one-tap representation of the set of time-domain channel components causing direct and aliased leakage, respectively. These theoretical estimations of the error power will be used to reveal the limiting error types with respect to the measurement range requirement (Section 5.2) and the general limitations through leakage (Section 5.3).

Based on the channel measurement described in Section 4.1, the real relative error power due to resolution, direct and aliased leakage and their theoretical estimations are calculated for method III-Hann for $800\ \mathrm{ns}$ CP. Considering the required excess measurement range varying between $14\ \mathrm{MHz}$ and $135\ \mathrm{MHz}$ (Sections 4.3.1.3 and 4.3.4.1), the computation is executed for the following set of window widths (Δf_{win}): $\{25, 50, 75, 100, 200, 300\}$ MHz.

The exact calculations (Section 3.9.1) are based on a window width of $2200\ \mathrm{MHz}$, i.e., corresponding to the maximum available measurement range of $2600\ \mathrm{MHz}$. The real error powers due to direct leakage, resolution and aliased leakage are calculated based on the channel components with a delay in the range of $[0, 250]$ ns, $[250, 2000]$ ns, and $[2000, 2250]$ ns (i.e., aliased channel form), resp. (Fig. 3.3). Note that the time window's width is $2000\ \mathrm{ns}$. It has been verified that the delay range of $[250, 2000]$ ns includes no far leakage, i.e., the error power due to commutation is centred over or near the delay interference interval.

For the theoretical estimation of the error power due to resolution (Eq. 3.62 in Section 3.9.2), a reverberation time of $138\ \mathrm{ns}$ is considered (from Section 4.2). For the theoretical estimation of the error power due to direct and aliased leakage (Section 3.9.3), a one-tap channel with a (frequency-domain) response of $-60.0\ \mathrm{dB}$

was used, determined from the real channel's components with a delay in the range of $[0, 250]$ ns. The one-tap channel is set at a delay of 58.2 ns and 2058.2 ns for direct and aliased leakage, respectively. The first arriving path, at a 58.2 ns delay, is determined from maximizing the APDP measured at a window width of 2200 MHz.

The type-specific error powers are determined for the spectral interference for a subcarrier separation $|\Delta i|$ up to 255. Other calculation parameters are as mentioned in Section 4.2. In Fig. 5.1, the real relative error power due to resolution, direct and aliased leakage and the corresponding theoretical estimations are shown for a window width of 75 MHz and a Δi range of $[0, 100]$, allowing a more detailed view. All error powers are essentially found symmetric with respect to a zero Δi. Further, the (real) relative error power due to all window-related error types, as determined in Section 4.2, is added for comparison. This error power includes the error due to non-uniform windowing and due to commutation. The latter consists of the error due to resolution and direct and aliased leakage. Note that, from Fig. 5.1, there is an excellent agreement between the real error power due to all window-related error types and due to resolution (i.e., a maximum deviation of 1.0 dB). This indicates already that the limiting error type for method III-Hann is resolution, which is discussed in more detail in Section 5.2.

5.1.1 Results for error power due to resolution

The deviation of the theoretical versus the real error power due to resolution varies over all subcarrier separations in the range of $[2.1, 4.2]$ dB for coefficient type y_{corr} and in the range of $[2.3, 27.9]$ dB for type y_{Four} (Fig. 5.1). While for y_{corr}, the real and the theoretical error power are of the same order for all subcarrier separations, this is for y_{Four} only the case for a higher subcarrier separation. This is due to the cancellation effect (Section 3.9.2), i.e., the cancellation of the resolution error for a $|\Delta i|$ much smaller than $D_{\mathrm{FFT}}\Delta f_{\mathrm{win}}/2$, i.e., 120 for a 75 MHz window width. For a $|\Delta i|$ higher than 120, the deviation of the theoretical versus the real error power ranges over $[2.3, 7.5]$ dB. For other window widths, largely similar findings are obtained. Over all window widths and subcarrier separations, the deviation ranges over $[-2.2, 5.5]$ dB for y_{corr} and $[-3.5, 37.2]$ dB for y_{Four} (Table 5.1).

The deviation between the theoretical estimation and the real error power due to resolution for the y_{corr} coefficient can be explained as follows. As mentioned in Section 3.9.2, the theoretical estimation is mainly based on two assumptions. First, for the estimation of the absolute error power, it is assumed that with respect to the time resolution, the time-domain channel consists of a *dense* set of components around the start delay ($\tau_{\mathrm{int},1}$) of the interference delay interval. Second, to relate the interference power to the reverberation time, it is assumed that the APDP decays exponentially over the interference delay interval. Note that

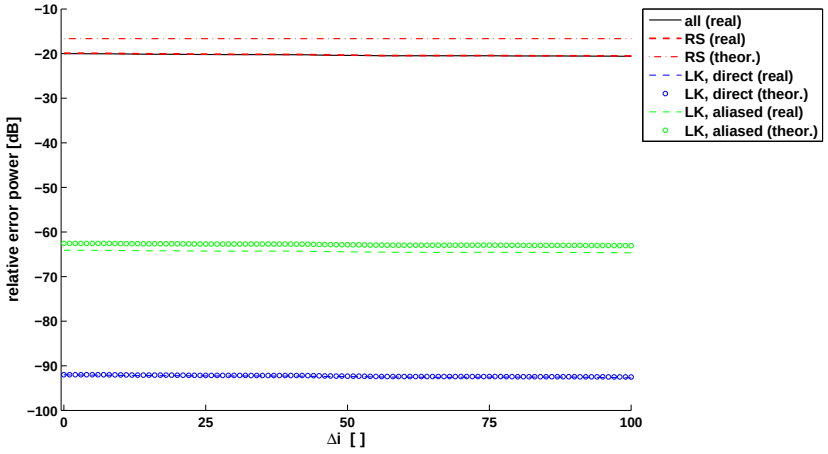

(a) y_{corr}

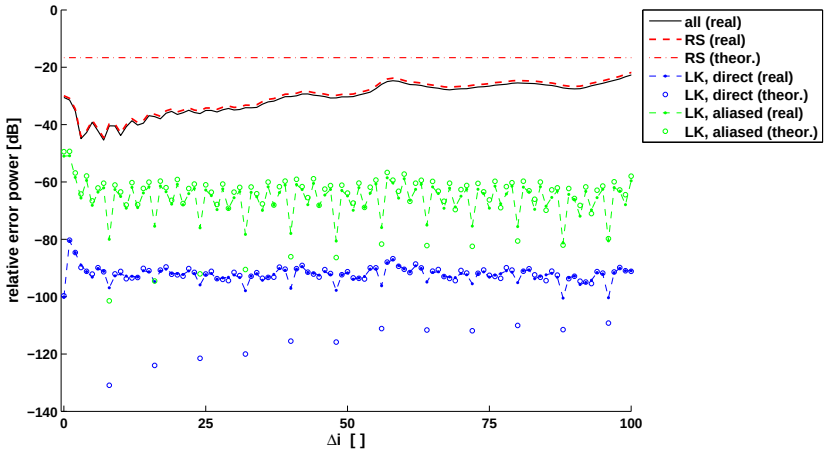

(b) y_{Four}

Figure 5.1: The theoretical estimation of the relative error powers due to resolution ("RS"), direct and aliased leakage ("LK"), are compared with the real error power. This is determined as a function of the subcarrier separation, Δi, based on method III-Hann, 800 ns *CP and a* 75 MHz *window width. The real relative error power due to all window-related error types ("all") is added too. Both coefficient types, y_{corr} (a) and y_{Four} (b), are considered.*

Table 5.1: The minimum ("MIN") and maximum ("MAX") deviation [dB] of the theoretical versus the real error power are determined over all subcarrier separations (Δi) and over different window widths. Both coefficient types, y_{corr} and y_{Four}, are considered. This table confirms the validity of the theoretical error power estimations as (i) an order estimation for the resolution error power, apart from the cancellation effect for y_{Four} (at a small Δi) and as (ii) an upper envelope for the error power types due to leakage.

error type	y_{corr}		y_{Four}	
	MIN	MAX	MIN	MAX
resolution	-2.2	5.5	-3.5	37.2
direct leakage	-1.1	3.6	-1.8	4.7
aliased leakage	-0.1	11.9	-0.4	12.9

these assumptions refer to the window width required for accurate performance of the windowing method. If with respect to the corresponding time resolution, the channel is rather dominated by specular components over the interference delay interval, both assumptions are no longer realistic, resulting into a deviation of the theoretical estimation. Especially, strong specular components around $\tau_{\mathrm{int},1}$ may cause deviations from the theoretical estimation. This behaviour can be observed in Fig. 6.3, showing an APDP at a window width of 200 MHz.

The conclusion for the resolution error is that the theoretical (relative) error power is a good order estimation for the y_{corr} coefficient type. For y_{Four}, this is only the case at a high subcarrier separation, as the resolution error power is reduced for a small subcarrier separation (i.e, $|\Delta i| \ll D_{\mathrm{FFT}} \Delta f_{\mathrm{win}}/2$). Hence, the theoretical estimation serves as a reference for the y_{Four} type coefficient.

5.1.2 Results for error power due to direct and aliased leakage

Concerning the direct and aliased leakage at a 75 MHz window width, the theoretical and the real error power agree well for both coefficient types (Fig. 5.1), apart from the strong error power drops observed for the y_{Four} type at certain subcarrier separations. This is caused by destructive interference in the time-domain summation involving the Δi dependent weighting function and the sidelobes of the window function's Fourier transform (Eq. 3.64 in Section 3.9.3). These error power drops are more pronounced for the theoretical error power, which originates from one time-domain channel component. As the interest is rather in the error power at rms level, the strong drops are cancelled out by local averaging of the (linear-scaled) error power over every 3 subsequent subcarriers separations, Δi. Therefore, the deviation between the theoretical and the real error power is determined based on their local average.

At a 75 MHz window width, the deviation of the theoretical versus the real (lo-

cally averaged) error power due to direct leakage varies over all subcarrier separations in the range of $[-0.0, 0.5]$ dB for the y_{corr} type coefficient and $[-0.7, 0.8]$ dB for the y_{Four} type (Fig. 5.1). For the error power due to aliased leakage, the deviation varies in the range of $[1.5, 2.4]$ dB for y_{corr} and $[1.2, 2.3]$ dB for y_{Four}. This shows that, apart from the strong error power drops, the theoretical estimation is in good approximation an upper limit for the real error power.

Although at a $75\ \mathrm{MHz}$ window width, the theoretical estimation is a fairly good approximation for the real error power, the latter is found to fluctuate as a function of the window width below the theoretical estimation as an upper envelope, especially for the aliased leakage. E.g., at a $50\ \mathrm{MHz}$ window width, the deviation of the theoretical versus the real error power due to aliased leakage varies in the range of $[10.6, 11.9]$ dB for y_{corr} and $[10.4, 12.9]$ dB for y_{Four}. The real error power fluctuating as a function of the window width can be explained by the fact that the window time-domain sidelobes, having a width of $\Delta f_{\mathrm{win}}^{-1}$, are evaluated at discrete delay taps with a resolution of $\Delta f_{\mathrm{win}}^{-1}$ (Eq. 3.64 in Section 3.9.3). Hence, at certain window widths, the sidelobe nulls coincide systematically with the delay taps, resulting in a fall of the error power. By definition, this effect is filtered out for the theoretical estimation (Section 3.9.3). Over all window widths and subcarrier separations, the deviation of the theoretical versus the real error power lies in the range of $[-1.8, 4.7]$ dB and $[-0.4, 12.9]$ dB for direct and aliased leakage, resp. (Table 5.1).

The conclusion for direct and aliased leakage is that the theoretical error power estimation can be considered in good approximation as an upper envelope above the real error power, which may fluctuate as a function of the window width.

5.2 Limiting error types for methods III-Hann and I-rect: time resolution and leakage

In Chapter 4, the required measurement range was discussed for different windowing methods for the channel measurement described in Section 4.1. This section aims to determine the critical error type with respect to the measurement range requirement, which is important for optimizing the measurement settings and understanding the windowing method's limitations. To identify the critical error type, the relative error power due to a non-zero time resolution (including near leakage), $\tilde{E}_{\mathrm{RS}}$, and direct and aliased leakage, $\tilde{E}_{\mathrm{LK,\,dir}}$ and $\tilde{E}_{\mathrm{LK,\,al}}$, resp., are compared with the error power due to all relevant window-related error types, $\tilde{E}$. The latter has been experimentally determined in the convergence analysis described in Section 4.2 and is more specifically due to non-uniform windowing, resolution and (direct and aliased) leakage. Note that the error due to non-uniform windowing is negligible for method III-Hann (Section 4.3.1.3). The type-specific error powers are determined by the theoretical estimation methods (Sections 3.9.2 and 3.9.3). For the resolution error power, a reverberation time of $131\ \mathrm{ns}$ and $138\ \mathrm{ns}$ is considered for $400\ \mathrm{ns}$ and $800\ \mathrm{ns}$ CP, resp. (from Section 4.2). For the direct and aliased leakage, a one-tap channel with a power of $-60.0\ \mathrm{dB}$ was used, set at a delay of $58.2\ \mathrm{ns}$ and $2058.2\ \mathrm{ns}$, resp. (from Section 5.1).

The focus is on methods III-Hann and I-rect, which act as a reference for other methods. The error power types mentioned are shown in Figs. 5.2 and 5.3 for method III-Hann and I-rect, resp., for a window width (Δf_{win}) of $50\ \mathrm{MHz}$ and $450\ \mathrm{MHz}$, respectively. Considering a calculation range of $241\ \mathrm{MHz}$ and a subcarrier separation ($|\Delta i|$) up to 255, this corresponds to a (maximum) measurement range (Δf_{meas}) of $450\ \mathrm{MHz}$ for both methods (Section 3.4). In Section 5.2.1, the error power due to direct and aliased leakage is discussed in detail. This will be useful to Section 5.2.2, where the most critical error type will be determined.

5.2.1 Error power due to direct and aliased leakage

For the y_{Four} interference coefficient type, $\tilde{E}_{\mathrm{LK,\,dir}}$ and $\tilde{E}_{\mathrm{LK,\,al}}$ differ in two main aspects from the coefficient type y_{corr} (Figs. 5.2 and 5.3). First, $\tilde{E}_{\mathrm{LK,\,dir}}$ and $\tilde{E}_{\mathrm{LK,\,al}}$ are strongly fluctuating as a function of Δi. This is caused by destructive interference in the time-domain summation involving the Δi-dependent weighting function ($g_{\mathrm{Four},\Delta i}(\tau)$) and the window function's sidelobes (Eq. 3.64 in Section 3.9.3). Second, $\tilde{E}_{\mathrm{LK,\,dir}}$ and $\tilde{E}_{\mathrm{LK,\,al}}$ are peaking around zero Δi, typically exceeding the relative error for y_{corr}. This is due to the transition from a quasi-uniform to a linear profile of the weighting function, shifting the profile's centre towards a higher delay. From Section 2.2, the profile of $g_{\mathrm{Four},\Delta i}(\tau)$ gets linear when half the weighting function's period is considerably larger than the interference

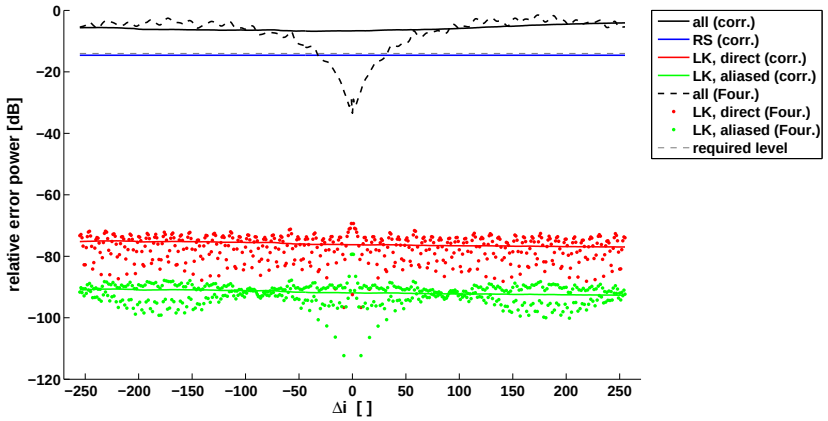

(a) 400 ns CP

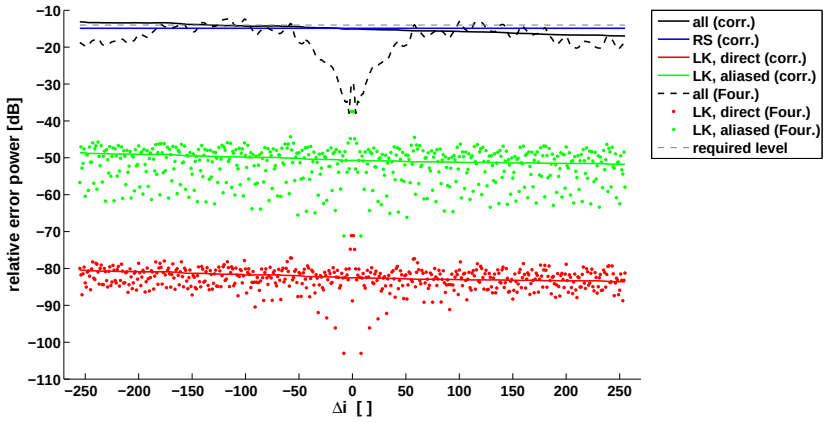

(b) 800 ns CP

Figure 5.2: Relative error ratio as a function of the subcarrier separation for ***method III-Hann*** *for a measurement range of* 450 MHz *(i.e., a* 50 MHz *window width). The (estimated) error powers due to resolution ("RS"), direct and aliased leakage ("LK") are shown. The (real) error power due to all window-related errors ("all") is added for comparison. Both interference coefficient types are considered,* y_{corr} *("corr.") and* y_{Four} *("Four."). The required accuracy level is set at* -14 dB*. Both* 400 ns *CP (a) and* 800 ns *CP (b) are considered.*

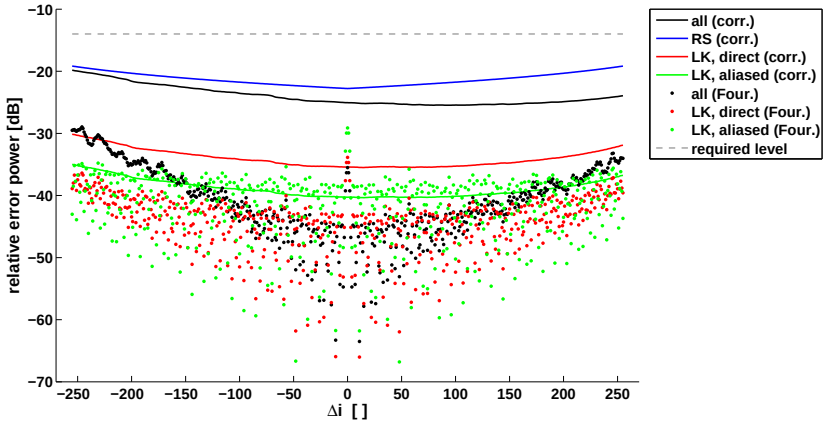

(a) 400 ns CP

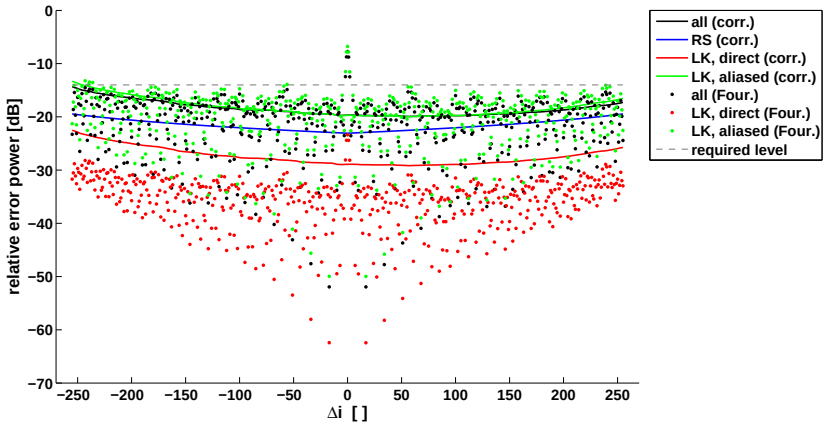

(b) 800 ns CP

Figure 5.3: Relative error ratio as a function of the subcarrier separation for ***method I-rect*** *for a measurement range of* 450 MHz *(i.e., a* 450 MHz *window width). The (estimated) error powers due to resolution ("RS"), direct and aliased leakage ("LK") are shown. The (real) error power due to all window-related errors ("all") is added for comparison. Both interference coefficient types are considered,* y_{corr} *("corr.") and* y_{Four} *("Four."). The required accuracy level is set at* -14 dB*. Both* 400 ns *CP (a) and* 800 ns *CP (b) are considered.*

delay interval duration (after a cut-off if applied), i.e., when $0.5D_{\mathrm{FFT}}/|\Delta i| \gg \tau_{\mathrm{int},2} - \tau_{\mathrm{int},1}$. This corresponds to a threshold $|\Delta i|$ of 1.8 and 1.7 for the 400 ns and 800 ns CP channel, resp., which agrees well with the $|\Delta i|$ peak width of 2 as observed in Figs. 5.2 and 5.3. Thus, based on a weighting function that is normalized over the interference delay interval, the corresponding (normalized) interference power decreases severely due to the APDP decay when the profile becomes linear. On the other hand, the corresponding absolute error power (with normalized weighting function) decreases for direct leakage and increases for aliased leakage, but this effect is inferior. It is found that the total effect on the relative error power is always that it peaks around zero Δi (Table 5.2). For a Δf_{meas} of 450 MHz, the peak exceeds the out-of-peak (linear-scaled) mean level (i.e., $|\Delta i| > 2$) by 7 dB to 13 dB. An extra phenomenon that is observed only for method III-Hann and the direct leakage, is that the relative error power drops strongly specifically at zero Δi, in addition to the peak around (Fig. 5.2). Finally, it is also found that the out-of-peak mean of $\tilde{E}_{\mathrm{LK,\,dir}}$ as well as $\tilde{E}_{\mathrm{LK,\,al}}$ are generally of the same order for both coefficient types (Figs. 5.2 and 5.3). The largest deviation is found for method I-rect and direct leakage, where, at a Δf_{meas} of 450 MHz, the (out-of-peak) mean is $7 - 9$ dB lower for y_{Four} (Table 5.2).

Table 5.2: The relative error power due to direct and aliased leakage ($\tilde{E}_{\mathrm{LK,\,dir}}$ and $\tilde{E}_{\mathrm{LK,\,al}}$, resp.) for method III-Hann and I-rect is given in terms of the mean (M) [dB] for coefficient type y_{corr} and in terms of the out-of-peak mean (M) [dB] and the peak maximum (MAX) [dB] for the y_{Four} type. Values are given for a measurement range (Δf_{meas}) of 450 MHz *and* 800 MHz.

			450 MHz (Δf_{meas})			800 MHz (Δf_{meas})		
CP [ns]	leakage type	method	y_{corr}	y_{Four}		y_{corr}	y_{Four}	
			M	M	MAX	M	M	MAX
400	direct	III-Hann	-76	-76	-69	-130	-130	-123
		I-rect	-34	-43	-34	-41	-51	-40
	aliased	III-Hann	-92	-92	-79	-145	-145	-133
		I-rect	-39	-40	-29	-46	-47	-35
800	direct	III-Hann	-82	-82	-71	-135	-135	-124
		I-rect	-27	-34	-23	-34	-42	-29
	aliased	III-Hann	-50	-50	-37	-106	-106	-93
		I-rect	-18	-19	-7	-25	-25	-13

Although for a Δf_{meas} of 450 MHz, the window width applied is only 50 MHz for method III-Hann versus 450 MHz for method I-rect, $\tilde{E}_{\mathrm{LK,\,dir}}$ and $\tilde{E}_{\mathrm{LK,\,al}}$ are several orders of magnitude larger for method I-rect (Table 5.2). Comparing

method I-rect to III-Hann at a Δf_{meas} of 450 MHz, the (out-of-peak) mean of the error power is between 33.1 dB and 55.1 dB larger for direct leakage and between 31.5 dB and 53.1 dB larger for aliased leakage. For method I-rect and 800 ns CP, $\tilde{E}_{\mathrm{LK,\,al}}$ peaks up to -7 dB, exceeding the -14 dB accuracy level required.

For a higher Δf_{meas}, $\tilde{E}_{\mathrm{LK,\,dir}}$ and $\tilde{E}_{\mathrm{LK,\,al}}$ decrease only moderately for method I-rect, in contrast to method III-Hann. Comparing a Δf_{meas} of 800 MHz to 450 MHz (Table 5.2), method I-rect yields an error power decrease by only $6-8$ dB and $6-7$ dB for direct and aliased leakage, respectively. For a Δf_{meas} of 800 MHz, $\tilde{E}_{\mathrm{LK,\,al}}$ still reaches -13 dB. Note that a Δf_{meas} of 800 MHz corresponds to a window width of 800 MHz and 400 MHz for method I-rect and III-Hann, respectively. For method III-Hann, the error power decreases by $53-54$ dB and $53-56$ dB for direct and aliased leakage, resp., comparing a Δf_{meas} of 800 MHz to 450 MHz. Although this implies a window width increasing by a factor 8 for method III-Hann (while about a doubling for method I-rect), the error power decrease for method III-Hann is relatively stronger than for method I-rect.

Comparing 800 ns to 400 ns CP, the frequency-averaged interference power decreases on average with 12 dB (Section 4.4) due to the APDP decay. The absolute error power due to aliased leakage increases, as the interference delay interval moves towards the aliased LOS channel component. Consequently, the relative error power, $\tilde{E}_{\mathrm{LK,\,al}}$, always increases for a higher CP (Figs. 5.2 and 5.3). However, as the absolute error power due to direct leakage decreases for a higher CP, $\tilde{E}_{\mathrm{LK,\,dir}}$ increases more slightly or may even decrease. Comparing 800 ns to 400 ns CP at a Δf_{meas} of 450 MHz, the (out-of-peak) mean of $\tilde{E}_{\mathrm{LK,\,al}}$ increases by 41 dB and 21 dB for method III-Hann and I-rect, resp., while for $\tilde{E}_{\mathrm{LK,\,dir}}$, there is a decrease with 6 dB for method III-Hann and an increase of $7-9$ dB for method I-rect (Table 5.2).

5.2.2 Limiting error type for measurement range requirement

5.2.2.1 Results for method III-Hann

Fig. 5.2 shows that, for method III-Hann and a Δf_{win} of 50 MHz, the relative error power due to direct and aliased leakage, $\tilde{E}_{\mathrm{LK,\,dir}}$ and $\tilde{E}_{\mathrm{LK,\,al}}$, resp., are much smaller than the total relative error power, $\tilde{E}$ (i.e., due to all window-related errors). For 400 ns CP (Fig. 5.2(a)), the $\tilde{E}_{\mathrm{LK,\,dir}}$ falls at least 68.9 dB and 39.9 dB below $\tilde{E}$ for the y_{corr} type and y_{Four} type coefficient, resp., and $\tilde{E}_{\mathrm{LK,\,al}}$ at least 84.6 dB and 45.9 dB. For 800 ns CP (Fig. 5.2(b)), $\tilde{E}_{\mathrm{LK,\,dir}}$ is found to be at least 66.6 dB and 41.2 dB lower than $\tilde{E}$ for y_{corr} and y_{Four}, resp., and $\tilde{E}_{\mathrm{LK,\,al}}$ at least 34.8 dB and 7.6 dB. Out of the Δi range of $[-57, 56]$, where $\tilde{E}$ is reduced compared to a higher $|\Delta i|$, $\tilde{E}_{\mathrm{LK,\,al}}$ lies at least 27.8 dB below $\tilde{E}$. This shows that, at a Δf_{win} of 50 MHz, the error power ($\tilde{E}$) is mainly due to a non-zero time resolution.

Note that, for 800 ns CP and y_{Four}, the peak of $\tilde{E}$ around zero Δi is, just as for the leakage error, caused by a change of the weighting function profile, i.e., its centre being moved towards a higher delay. For $y_{\mathrm{Four},0}$ (at zero Δi), *exact* calculations (Section 5.1) yield (i) an $\tilde{E}_{\mathrm{RS}}$ of -28.8 dB, which agrees well with the $\tilde{E}$ value of -29.6 dB, and (ii) an $\tilde{E}_{\mathrm{LK,\,al}}$ of -49.4 dB, which is indeed not higher than the theoretical $\tilde{E}_{\mathrm{LK,\,al}}$ estimation of -37.5 dB. This confirms that, also around zero Δi, the error power is mainly caused by a non-zero resolution (for 800 ns CP and the y_{Four} type). For a Δf_{win} larger than 50 MHz, $\tilde{E}_{\mathrm{LK,\,dir}}$ and $\tilde{E}_{\mathrm{LK,\,al}}$ are found to be even more negligible compared to $\tilde{E}$, resulting into the same conclusion.

5.2.2.2 Results for method I-rect

Fig. 5.3 shows that, for method I-rect and a Δf_{win} of 450 MHz, the error power due to leakage is not systematically negligible compared to $\tilde{E}$. For 400 ns CP (Fig. 5.3(a)), the (theoretically estimated) $\tilde{E}_{\mathrm{LK,\,dir}}$ and $\tilde{E}_{\mathrm{LK,\,al}}$ for y_{corr} are respectively at least 8.0 dB and 12.8 dB lower than $\tilde{E}$. The deviation $\tilde{E} - \tilde{E}_{\mathrm{RS}}$ varies between -4.8 dB and -0.7 dB with a mean deviation of -2.7 dB. Considering that the theoretically estimated $\tilde{E}_{\mathrm{LK,\,dir}}$ and $\tilde{E}_{\mathrm{LK,\,al}}$ behave as an upper limit (Section 5.1), this shows that for y_{corr}, the error power ($\tilde{E}$) is still mainly caused by a non-zero time resolution. For the y_{Four} coefficient type, it appears that $\tilde{E}$ may be determined by both resolution and leakage. For $\Delta i < -179$ and $\Delta i > 224$, $\tilde{E}$ exceeds $\tilde{E}_{\mathrm{LK,\,dir}}$ and $\tilde{E}_{\mathrm{LK,\,al}}$, indicating that $\tilde{E}$ is still dominated by resolution. For $|\Delta i| \leq 150$, the deviation $\tilde{E} - \tilde{E}_{\mathrm{LK,\,dir}}$ ranges over $[-1.6, 10.1]$ dB and the deviation $\tilde{E} - \tilde{E}_{\mathrm{LK,\,al}}$ over $[-6.4, 14.9]$ dB, which demonstrates that the error due to leakage may contribute to $\tilde{E}$ as well. Note that, for $|\Delta i| \leq 100$, the deviation $\tilde{E} - \tilde{E}_{\mathrm{LK,\,dir}}$ has a mean of 0.8 dB and a standard deviation of 2.9 dB, which is rather small compared to the fluctuations of $\tilde{E}$ over more than one order of magnitude. For a higher Δf_{win}, the same conclusion can be drawn in general for both coefficient types.

For 800 ns CP and a Δf_{win} of 450 MHz (Fig. 5.3(b)), the deviation $\tilde{E} - \tilde{E}_{\mathrm{RS}}$ for y_{corr} varies over $[1.9, 5.1]$ dB, the deviation $\tilde{E} - \tilde{E}_{\mathrm{LK,\,dir}}$ over $[8.1, 9.3]$ dB and $\tilde{E} - \tilde{E}_{\mathrm{LK,\,al}}$ over $[-1.0, 0.1]$ dB. This shows that $\tilde{E}$ may be determined by both the error due to resolution and aliased leakage. For y_{Four}, the deviation $\tilde{E} - \tilde{E}_{\mathrm{RS}}$ (using the $\tilde{E}_{\mathrm{RS}}$ estimation for y_{corr} as reference) is 15.3 dB at zero Δi, where $\tilde{E}$ is peaking. Outside this peak (i.e., $|\Delta i| > 2$), the deviation varies over $[-29.0, 7.7]$ dB. The deviations $\tilde{E} - \tilde{E}_{\mathrm{LK,\,dir}}$ and $\tilde{E} - \tilde{E}_{\mathrm{LK,\,al}}$ range over $[7.0, 15.7]$ dB and $[-2.2, -0.7]$ dB, respectively. These findings prove that around zero Δi (i.e., $|\Delta i| \leq 2$), $\tilde{E}$ is mainly determined by aliased leakage. Considering the strong fluctuations of $\tilde{E}$ over more than one order of magnitude, the agreement between $\tilde{E}$ and the theoretical estimation of $\tilde{E}_{\mathrm{LK,\,al}}$ is strikingly excellent. For $|\Delta i| > 2$, $\tilde{E}_{\mathrm{LK,\,dir}}$ is certainly negligible compared to $\tilde{E}$. Since for y_{Four}, the actual $\tilde{E}_{\mathrm{RS}}$ may be much smaller than for y_{corr} (i.e., cancellation effect), it is

not obvious for $|\Delta i| > 2$ whether the resolution error is negligible. However, the strong fluctuation of $\tilde{E}$ observed over the whole Δi range (Fig. 5.3(b)), indicates that for y_{Four}, the error is completely dominated by aliased leakage. Indeed, it is not expected that there is a strong fluctuation of the (actual) $\tilde{E}_{\mathrm{RS}}$ as a function of Δi, in contrast with $\tilde{E}_{\mathrm{LK,\,dir}}$ and $\tilde{E}_{\mathrm{LK,\,al}}$. For a higher Δf_{win}, essentially the same results are found. However, as Δf_{win} increases, $\tilde{E}$ will fluctuate below the theoretical $\tilde{E}_{\mathrm{LK,\,al}}$ estimation, which is followed as an upper envelope.

5.2.2.3 Conclusions and implications

For method III-Hann, the overall error power (i.e., due to all relevant window-related error types), $\tilde{E}$, is determined by a non-zero time resolution for both 400 ns and 800 ns CP, certainly for a Δf_{win} larger than 50 MHz. Note that for method III-Hann, the excess measurement range ($\Delta f_{\mathrm{meas,\,exc}}$) corresponds to the window width. Keeping in mind that the overall required $\Delta f_{\mathrm{meas,\,exc}}$ is 124 / 57 MHz for 400 / 800 ns CP, resp., for the y_{corr} coefficient type and 135 / 57 MHz for the y_{Four} type (Table 4.1), it follows that the measurement range requirement is determined by the resolution error.

For method I-rect, the situation differs essentially for 400 ns and 800 ns CP. For 800 ns CP, the error power due to direct leakage and in particular aliased leakage is much larger. It has been shown that for y_{Four} and 800 ns CP, the error power is dominated by aliased leakage, certainly for a Δf_{win} (or Δf_{meas}) larger than 450 MHz. Whereas the overall required Δf_{meas} for 400 ns CP is 408 MHz and 397 MHz for y_{corr} and y_{Four}, resp., this is 505 MHz and 902 MHz for 800 ns CP (Table 4.1). Thus, for y_{Four} and 800 ns CP, the measurement range requirement is certainly determined by aliased leakage. This requirement is critical around zero Δi (Fig. 4.7 in Section 4.3.2), where the interference term is typically most important.

Since for type II methods, the window width (Δf_{win}) is, at a given Δf_{meas}, always smaller than for type I methods, the error power due to resolution and leakage is larger. This applies a fortiori for type III methods, which always have a smaller (or equal) window width than type II methods. Consequently, methods II-rect and III-rect suffer a fortiori from aliased leakage, which is confirmed by the corresponding required Δf_{meas} (Fig. 4.7 in Section 4.3.2). Conversely, the leakage error for methods II-Hann and I-Hann is smaller compared to the one for III-Hann.

Besides applying a larger window width, a possible way-out to suppress the aliased leakage is to increase the time window, i.e., the inverse of the frequency resolution, Δf_{res}, at which the channel is measured. However, to reduce the error power due aliased leakage to the level of direct leakage, this requires a considerably smaller Δf_{res}. For a rectangular weighting function (as used for y_{corr}), the

required Δf_{res} equals

$$\Delta f_{\mathrm{res}} = (2D_{\mathrm{CP}} + 2D_{\mathrm{FFT}}/N_{\mathrm{sample}} + \tau_{\mathrm{int},2} - \tau_{\mathrm{int},1})^{-1}, \tag{5.1}$$

where the duration of the interference delay interval, $\tau_{\mathrm{int},2} - \tau_{\mathrm{int},1}$, has been set to 6.6 times τ_{r} due to a cut-off (Section 3.8). For 800 ns CP, this corresponds to a Δf_{res} of 392 kHz instead of 500 kHz as set in the channel measurement (Section 4.1). However, for the critical spectral term, namely for $y_{\mathrm{Four},0}$ (at zero Δi), the weighting function has a linear profile, which means that the time window must be further enlarged to limit the error power due to aliased leakage to the level of direct leakage. The resulting smaller Δf_{res} required is a drawback because of the higher sweep time and processing time (Section 6.1).

In contrast with aliased leakage, the error due to direct leakage can only be reduced by increasing Δf_{win}. However, for a rectangular window, the error power due to (direct and aliased) leakage decreases only moderately with Δf_{win}, in contrast to a Hann window (Section 5.2.1). This may result into a very large measurement range requirement using a rectangular window. For methods I-rect, II-rect and III-rect, a Δf_{meas} is required between 902 MHz and 1082 MHz for $y_{\mathrm{Four},0}$ (at zero Δi) for 800 ns CP (Table 4.1), whereas the zero-excess measurement range is only 241 MHz at zero Δi.

The relative error power due to resolution is physically only related to time-domain channel components over or near the interference delay interval, which involve propagation paths with a delay higher than the CP length. This also appears from Section 3.9.2, where the resolution error power has been related to the window width and the reverberation time. In contrast, the absolute error power due to direct and aliased leakage is related to the set of strongest components, which are typically the first few arriving paths. These channel components form the received signal of the OFDM system. Therefore, the relative error power, $\tilde{E}_{\mathrm{LK,\,dir}}$ and $\tilde{E}_{\mathrm{LK,\,al}}$, is connected with the signal. If these channel components increase in power, $\tilde{E}_{\mathrm{LK,\,dir}}$ and $\tilde{E}_{\mathrm{LK,\,al}}$ will increase proportionally. This is e.g. the case at a smaller Tx-Rx separation, where the LOS component has a larger power, while the interference power remains constant, as it typically originates from reflected paths. Although for method I-rect at a Δf_{meas} of 450 MHz, $\tilde{E}_{\mathrm{LK,\,dir}}$ is smaller than the required level of -14 dB for both 400 ns and 800 ns CP and both coefficient types (Table 5.2), the direct leakage may become critical for channels with a higher signal-to-interference ratio (SIR). In Section 5.3, the limitations through leakage will be discussed in terms of a maximum measurable SIR for methods III-Hann and I-rect.

5.3 SIR limitations due to leakage

If the time-domain channel components with a delay that is considerably smaller than the CP length increase in power, the relative error power due to direct and aliased leakage ($\tilde{E}_{\mathrm{LK,\,dir}}$ and $\tilde{E}_{\mathrm{LK,\,al}}$, resp.) will increase proportionally (Fig. 3.3). Considering that these channel components form the signal power as received by the OFDM system, the signal power must be smaller than a maximum value, $S_{\max}$, to ensure that $\tilde{E}_{\mathrm{LK,\,dir}}$ and $\tilde{E}_{\mathrm{LK,\,al}}$ are each below the required accuracy threshold level ($\tilde{E}_{\mathrm{thresh}}$). This limitation is expressed in terms of a maximum signal-to-interference ratio (SIR), $\mathrm{SIR}_{\max}$:

$$\mathrm{SIR}_{\max} = S_{\max} - I \;\; [\mathrm{dB}], \tag{5.2}$$

where I is the (frequency-averaged) total interference power originating from any OFDM symbol (i.e., including ISI and ICI). A $\mathrm{SIR}_{\max}$ value can be determined for (i) the spectral interference, ensuring that the accuracy requirement is met for the spectral interference power for all subcarrier separations of interest, or for (ii) the total interference, where the spectral terms are added up over all subcarrier separations.

Once the interference power I exceeds the thermal noise level of the OFDM system, the performance may be substantially degraded. To measure an interference power I as low as the thermal noise level, $\mathrm{SIR}_{\max}$ must not be smaller than the signal-to-noise ratio (SNR) that is actually present at the OFDM receiver. E.g., for an equivalent isotropically radiated power (EIRP) of $10\ \mathrm{mW/MHz}$ for the $2.4\ \mathrm{GHz}$ ISM band [68], a receiver gain of $2\ \mathrm{dBi}$ and a Tx-Rx separation of $4\ \mathrm{m}$, an SNR of already $74\ \mathrm{dB}$ is achieved, assuming a free-space path loss. Therefore, it should be possible to measure SIR values up to about $80\ \mathrm{dB}$ (i.e., $\mathrm{SIR}_{\max} \geq 80\ \mathrm{dB}$) or even higher.

The SIR limitation, $\mathrm{SIR}_{\max}$, is determined for method III-Hann and I-rect based on the channel measurement described in (Section 4.1) and using the theoretical estimation method for the error power due to direct and aliased leakage (Section 3.9.3). The measurement range is varied over a wide range of $[425, 2600]$ MHz. Considering a calculation range of $241\ \mathrm{MHz}$ and a subcarrier separation ($|\Delta i|$) up to 255, the window width applied (Δf_{win}) is systematically $400\ \mathrm{MHz}$ smaller than Δf_{meas} for method III-Hann and varies over $[25, 2200]$ MHz. For method I-rect, Δf_{meas} corresponds to Δf_{win}. The CP lengths considered are $400\ \mathrm{ns}$ and $800\ \mathrm{ns}$.

5.3.1 SIR limitations for determination of spectral interference

In Fig. 5.4, showing $\mathrm{SIR}_{\max}$ as a function of Δf_{meas} for methods III-Hann and I-rect, $\mathrm{SIR}_{\max}$ is determined for the spectral interference and considering both coefficient types, y_{corr} and y_{Four}. Reminding that $\tilde{E}_{\mathrm{LK,\,dir}}$ and $\tilde{E}_{\mathrm{LK,\,al}}$ are in general largest for y_{Four} around zero Δi (Figs. 5.2 and 5.3), it is clear that $\mathrm{SIR}_{\max}$ for

y_{corr} is higher (less critical) than for y_{Four} (Fig. 5.4). Concerning aliased leakage, $\mathrm{SIR}_{\mathrm{max}}$ is between 3.6 dB and 11.4 dB larger comparing y_{corr} to y_{Four}. Concerning direct leakage and for method III-Hann, $\mathrm{SIR}_{\mathrm{max}}$ is between 5.5 dB and 9.6 dB larger for y_{corr}. Concerning direct leakage and for method I-rect, $\mathrm{SIR}_{\mathrm{max}}$ may be somewhat smaller for y_{corr}. This is especially the case for a measurement range not much larger than the (maximum) zero-excess measurement range of 400 MHz (Fig. 5.4). Indeed, in this case, $\tilde{E}_{\mathrm{LK,\,dir}}$ gets larger for y_{corr} at a higher $|\Delta i|$ (Fig. 5.3). However, for a Δf_{meas} larger than 600 MHz, $\mathrm{SIR}_{\mathrm{max}}$ is only maximum 0.7 dB smaller for y_{corr} (Fig. 5.4).

For a Δf_{win} of 50 MHz, method III-Hann reaches already an $\mathrm{SIR}_{\mathrm{max}}$ concerning direct and aliased leakage of 89 dB and 99 dB, resp., for 400 ns CP (Fig. 5.4(a)) and 103 dB and 69 dB, resp., for 800 ns CP (Fig. 5.4(b)). To reach a 100 dB $\mathrm{SIR}_{\mathrm{max}}$, method III-Hann requires for 400 ns CP a Δf_{win} of 79 MHz and 53 MHz for direct and aliased leakage, resp., and 46 MHz and 162 MHz for 800 ns CP. The aliased leakage for 800 ns CP could be further reduced by only a small increase of the time window, considering the strong sensitivity of the leakage on the Hann window width. Although at a Δf_{meas} of 450 MHz, the window width applied is 9 times larger for method I-rect than for III-Hann (i.e., 450 MHz and 50 MHz, resp.), the performance of method I-rect is dramatically poor. Concerning direct and aliased leakage, $\mathrm{SIR}_{\mathrm{max}}$ is only 53 dB and 49 dB, resp., for 400 ns CP (Fig. 5.4(a)) and 55 dB and 39 dB, resp., for 800 ns CP (Fig. 5.4(b)). In contrast with method III-Hann, the improvement through increasing Δf_{win} is slight for method I-rect. Even at an extremely high Δf_{win} of 2500 MHz, $\mathrm{SIR}_{\mathrm{max}}$ concerning direct and aliased leakage increases only up to 69 dB and 65 dB, resp., for 400 ns CP (Fig. 5.4(a)) and 71 dB and 55 dB, resp., for 800 ns CP (Fig. 5.4(b)).

For a higher CP length, the absolute error power due to direct leakage ($E_{\mathrm{LK,\,dir}}$) decreases and the absolute error power due to aliased leakage ($E_{\mathrm{LK,\,al}}$) increases. Consequently, $\mathrm{SIR}_{\mathrm{max}}$ will increase for direct leakage and decrease for aliased leakage, assuming that the spectral profile (i.e., as a function of Δi) of the interference power and the leakage error power remain unchanged. This assumption is realistic, as the spectral interference profile is largely related to the reverberation time (Section 7) and the error power profile remains more or less unchanged (Figs 5.2 and 5.3). The influence of the CP length on $\mathrm{SIR}_{\mathrm{max}}$ is found as just described for both coefficient types, over the whole Δf_{meas} range and for both methods (Fig. 5.4). However, the influence is stronger for method III-Hann. Comparing 800 ns to 400 ns CP, $\mathrm{SIR}_{\mathrm{max}}$ for method III-Hann is found to increase by 13 dB to 18 dB for direct leakage and to decrease by 27 dB to 30 dB for aliased leakage. For method I-rect, $\mathrm{SIR}_{\mathrm{max}}$ increases by 2 dB to 5 dB for direct leakage and decreases by 9 dB to 10 dB for aliased leakage. Especially for method III-Hann, this means that, as regards to $\mathrm{SIR}_{\mathrm{max}}$, the aliased leakage becomes more critical for 800 ns CP, whereas for 400 ns CP, direct leakage is more critical (Fig. 5.4).

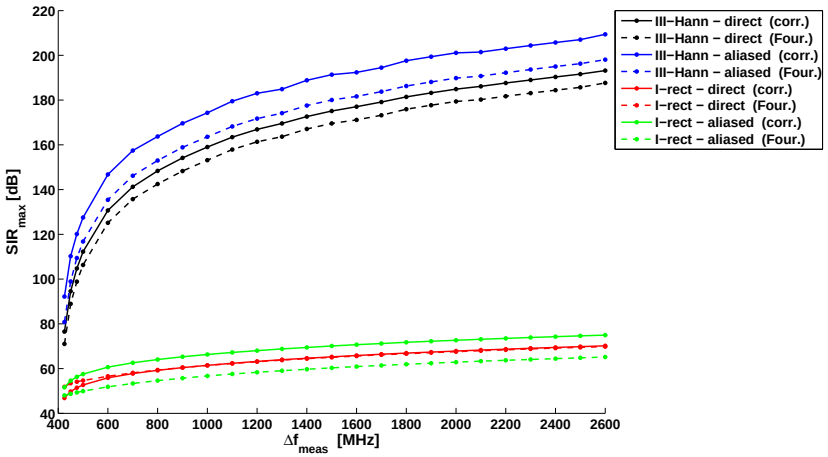

(a) 400 ns CP

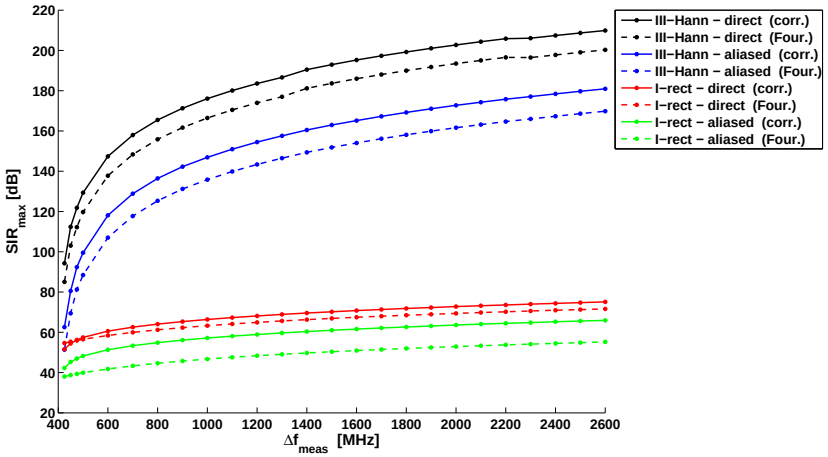

(b) 800 ns CP

Figure 5.4: SIR limitation ($\mathrm{SIR}_{\max}$ [dB]) due to direct and aliased leakage as a function of the measurement range (Δf_{meas}) for methods III-Hann and I-rect. These values refer to a relative error power threshold of -14 dB and apply to the determination of the spectral interference. $\mathrm{SIR}_{\max}$ values are given for 400 ns CP (a) and 800 ns CP (b) and for both coefficient types, y_{corr} ("corr.") and y_{Four} ("Four.").

An important conclusion is also that for method I-rect, there is no substantial improvement (i.e, increase of $\mathrm{SIR}_{\max}$) for direct leakage at a larger CP.

5.3.2 SIR limitations for determination of total interference

If the interest is not in the *spectral* but in the *total* interference power (i.e., the spectral terms summed over all subcarriers separations), it is the *total* absolute error power (Section 3.6) that has to be taken into account to determine the maximum signal power ($S_{\max}$) and the corresponding SIR ($\mathrm{SIR}_{\max}$). If the spectral profile of the interference power has a similar form as the absolute error power (due direct and aliased leakage), $\mathrm{SIR}_{\max}$ will be the same for the total interference power. In the other case, $\mathrm{SIR}_{\max}$ will be larger (i.e., less critical) for the total interference power, because spectral terms with a lower relative error power are involved too.

It is found that $\mathrm{SIR}_{\max}$ values for the total interference are larger (i.e., less critical) but of the same order compared to values for the spectral interference. For the y_{corr} coefficient type, the deviation varies between $1\ \mathrm{dB}$ and $6\ \mathrm{dB}$ for both direct and aliased leakage. Indeed, for y_{corr}, the interference power profile has a form that is quite similar to the absolute error power, as the relative error power ($\tilde{E}_{\mathrm{LK,\,dir}}$ and $\tilde{E}_{\mathrm{LK,\,al}}$) is approximately constant over the whole Δi range (Figs. 5.2 and 5.3).

For the coefficient type y_{Four}, Table 5.3 presents $\mathrm{SIR}_{\max}$ values determined for both the spectral and the total interference. For the total interference, $\mathrm{SIR}_{\max}$ values exceed the one for the spectral interference by $3\ \mathrm{dB}$ to $6\ \mathrm{dB}$ for direct leakage and systematically by $5\ \mathrm{dB}$ for aliased leakage (Table 5.3). Indeed, for y_{Four}, $\mathrm{SIR}_{\max}$ for the spectral interference is mainly determined by the peak of the relative error power around zero Δi (Figs. 5.2 and 5.3). As these subcarrier separations are dominating the total interference power, $\mathrm{SIR}_{\max}$ values for the total interference are of the same order as for the spectral interference.

The important conclusion is that for determining the total interference, $\mathrm{SIR}_{\max}$ is larger (i.e., less critical) but of the same order than SIR limitation values for the spectral interference. Moreover, the conclusions drawn for the spectral interference (Section 5.3.1) concerning the influence of the CP length on $\mathrm{SIR}_{\max}$ are found to apply as well for the total interference.

5.3.3 Implications on measurement range requirement

This analysis of $\mathrm{SIR}_{\max}$ versus the window width gives an idea of which window width (Δf_{win}), or measurement range (Δf_{meas}), is required to suppress the relative error power due to direct and aliased leakage below the required accuracy level ($\tilde{E}_{\mathrm{thresh}}$). Since the real channel's SIR is $33.8\ \mathrm{dB}$ and $46.2\ \mathrm{dB}$ at $400\ \mathrm{ns}$ and $800\ \mathrm{ns}$ CP (Section 4.4), resp., it follows for method III-Hann that the relative error power due to direct and aliased leakage error are both below a $-14\ \mathrm{dB}$ accuracy level from a Δf_{win} larger than $25\ \mathrm{MHz}$ (Table 5.3). For method I-rect,

Table 5.3: SIR limitations ($\mathrm{SIR}_{\max}$ [dB]) due to direct and aliased leakage over a wide range of the applied window width (Δf_{win}) for methods III-Hann and I-rect. These values refer to the y_{Four} type coefficient and to a relative error power threshold of -14 dB. $\mathrm{SIR}_{\max}$ values are given based on the spectral ("S") as well as the total ("T") interference.

method III-Hann								
CP [ns]	leakage type	spectral (S) / total (T)	Δf_{win} [MHz]					
			25	50	100	200	400	1100	2100
400	direct	S	71	89	106	125	142	170	186
		T	74	92	110	128	146	173	189
	aliased	S	81	99	117	135	153	180	196
		T	86	104	122	141	158	185	201
800	direct	S	85	103	120	138	156	184	199
		T	91	109	126	144	162	189	205
	aliased	S	51	69	88	107	125	152	169
		T	57	75	94	112	131	157	174

method I-rect								
CP [ns]	leakage type	spectral (S) / total (T)	Δf_{win} [MHz]					
			425	450	500	600	800	1500	2500
400	direct	S	52	53	55	57	59	65	69
		T	58	58	60	61	64	70	74
	aliased	S	48	49	50	52	55	60	65
		T	53	54	55	57	60	65	70
800	direct	S	55	55	57	58	61	67	71
		T	60	61	62	64	67	72	77
	aliased	S	38	39	40	42	45	50	55
		T	43	44	45	47	50	56	60

this is also the case for 400 ns CP, but not for 800 ns CP. Table 5.3 shows that for method I-rect and a 800 ns CP, a Δf_{win} larger than 500 MHz and 800 MHz is needed for the total and the spectral interference, respectively. As found from linear interpolation (Fig. 5.4(b)), a Δf_{meas} of about 543 MHz is required for the total interference and 947 MHz for the spectral interference. The latter agrees approximately with the required Δf_{meas} from the convergence analysis (Table 4.1), where a measurement range requirement of 902 MHz was found.

The $\mathrm{SIR}_{\max}$ values presented in Table 5.3 are expected to be not strongly dependent on the specific channel. This is especially the case for $\mathrm{SIR}_{\max}$ values for the total interference, where the spectral profile of the interference power is not relevant. Then, $\mathrm{SIR}_{\max}$ values are mainly determined by the window width and the following time-domain parameters: the CP length, the duration of the inter-

ference delay interval (after cut-off) and the time window. More specifically for direct leakage, the CP length and the window width are the most important factors. Hence, $\mathrm{SIR}_{\max}$ values of the same order are expected for other channels. Moreover, the $\mathrm{SIR}_{\max}$ values presented refer to a -14 dB accuracy level. However, the $\mathrm{SIR}_{\max}$ values are systematically proportional to $\tilde{E}_{\mathrm{thresh}}$. E.g., a 3 dB stricter accuracy requirement implies a SIR limitation decreasing by 3 dB.

6

Processing time and measurement noise for different windowing methods - Time-domain cut-off requirement

To determine the interference due to insufficient CP, different windowing methods have been evaluated on the required measurement range (Chapter 4) and on the limitations from a non-zero time resolution and leakage (Chapter 5). In fact, both chapters are focused on window-related error types (Section 3.5). In this chapter, the focus is on the processing time and the other error types, i.e., due to measurement noise and a time-domain cut-off. This is carried out based on the channel measurement described in Section 4.1 and for typical IEEE 802.11 parameters (Section 4.2).

In Section 6.1, the performance of the windowing methods is evaluated in terms of the processing time. In Section 6.2, the influence of the windowing methods on the error power due to measurement noise is investigated, as well as the error power reduction by averaging and the required number of sweeps. In Section 6.3, experimental validation is provided for the cut-off requirement, which is theoretically introduced in Section 3.8. This requirement is essential with respect to the frequency resolution of the channel measurement.

6.1 Processing time

In this section, the performance of the windowing methods is investigated with respect to the processing time, which is done both experimentally and theoretically.

6.1.1 Experimental processing time

The experimental processing time is determined based on the calculations performed in the convergence analysis from Section 4.2. The interference coefficient of type y_{corr} and y_{Four} is calculated for a detecting subcarrier frequency range centered at 3.8 GHz and with a width (Δf_{calc}) of 241 MHz and for a subcarrier separation Δi, ranging from -255 to 255. This calculation is executed for a measurement frequency range (Δf_{meas}) varying from 160 MHz to 2600 MHz. For each calculation, the processing time is measured for the two processing parts: (i) the calculation of the channel impulse reponse and (ii) the calculation of the interference coefficient. The computations are subsequently performed on a PC featuring an Intel processor of type Core i5-2400 (with 4 CPUs that have a base frequency of 3.1 GHz) and 8 GB RAM using Matlab version 7.12.0.635 (64-bit).

The processing time is measured for a limited set of Δf_{meas} points. A step of 20 MHz is taken for the Δf_{meas} range of $[160, 340]$ MHz, a 10 MHz step for the range of $[340, 400]$ MHz and a 100 MHz step for the range of $[400, 2600]$ MHz. A finer step is taken where windowing method types II and III start to be applicable (i.e., with a small window width). A smaller step of 5 MHz is taken in the range of $[240, 260]$ MHz. In the range of $[400, 500]$ MHz, an additional Δf_{meas} subset is included, being $\{405, 410, 425, 450, 475\}$ MHz.

The processing time is only measured for methods I-, II- and III-Hann and for 800 ns CP. The processing time does not depend on the window profile. For methods I-HC and II-HC, the additional processing time needed for window correction is normally negligible compared to the one needed for the time-domain integration (Eq. 3.15). The processing time for 400 ns CP is very comparable to the one for 800 ns CP, as the interference delay interval over which the time-domain intregration is calculated has approximately the same duration.

The experimental processing time as a function of Δf_{meas} is shown in Fig. 6.1. By the method definition, method type II is applicable for a Δf_{meas} larger than Δf_{calc}, i.e., 241 MHz. Method type III is applicable for a Δf_{meas} larger than the maximum zero-excess measurement range, i.e., 400 MHz. The processing time measured by Matlab is rounded to seconds. Note that samples with a zero processing time are missing in Fig. 6.1 due to the log-scale.

6.1.2 Theoretical analysis of the processing time

6.1.2.1 Computation of the channel impulse reponse

For the calculation of the channel impulse reponse, the processing time is dominated by the IDFT (Eq. 3.14). For method type I, the processing time for the

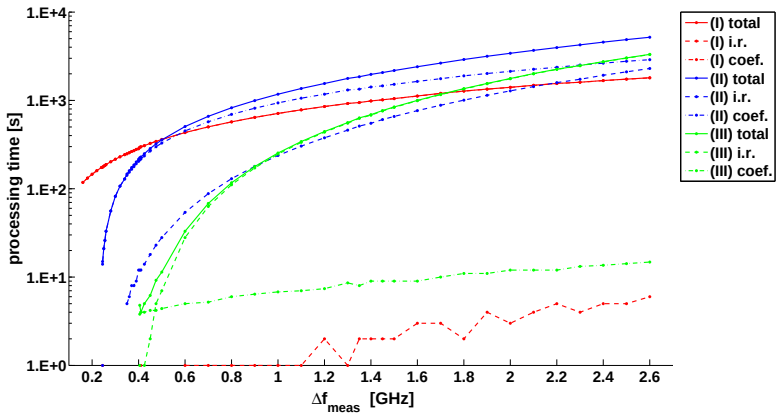

Figure 6.1: Experimental processing time as a function of the measurement range (Δf_{meas}) for the calculation of the channel impulse response ("i.r.") and the interference coefficient ("coef."). The total processing time is also added. This is given for windowing method types I, II and III.

calculation of the channel impulse response, $T_{\mathrm{I,ir}}$, is in good approximation just proportional to the square of the IDFT size:

$$T_{\mathrm{I,ir}} \approx b_{\mathrm{I,ir}} \left(\frac{\Delta f_{\mathrm{meas}}}{\Delta f_{\mathrm{res}}} \right)^2, \tag{6.1}$$

where the frequency resolution of the measured channel response, Δf_{res}, is assumed to be much smaller than Δf_{meas} and $b_{\mathrm{I,ir}}$ is a proportionality factor ([s]). For method type II, the window moves over the calculation range (Δf_{calc}) and has a reduced width of $\Delta f_{\mathrm{meas}} - \Delta f_{\mathrm{calc}}$ (Fig. 3.2), resulting into the following type II processing time

$$T_{\mathrm{II,ir}} \approx b_{\mathrm{II,ir}} \frac{\Delta f_{\mathrm{calc}}}{\Delta f_{\mathrm{res}}} \left(\frac{\Delta f_{\mathrm{meas}} - \Delta f_{\mathrm{calc}}}{\Delta f_{\mathrm{res}}} \right)^2. \tag{6.2}$$

For method type III, the window moves over the maximum zero-excess measurement range, which is $\Delta f_{\mathrm{calc}} + B$, where B is the bandwidth representing twice the maximum subcarrier frequency separation. In this case, B equals 159 MHz and the maximum zero-excess measurement range has a width of 400 MHz. The window width is reduced to $\Delta f_{\mathrm{meas}} - \Delta f_{\mathrm{calc}} - B$. Therefore, the type III processing time is as follows:

$$T_{\mathrm{III,ir}} \approx b_{\mathrm{III,ir}} \frac{\Delta f_{\mathrm{calc}} + B}{\Delta f_{\mathrm{res}}} \left(\frac{\Delta f_{\mathrm{meas}} - \Delta f_{\mathrm{calc}} - B}{\Delta f_{\mathrm{res}}} \right)^2. \tag{6.3}$$

6.1.2.2 Computation of the interference coefficient

For the calculation of the interference coefficient, the processing time is dominated by the coefficient type y_{Four}, because this depends on both the source and the detecting subcarrier frequency, while the y_{corr} coefficient type depends only on the source subcarrier frequency. For method types I and II, the processing time is dominated by the time-domain integration (Eq. 3.15). In general, the summation size is the interference delay interval duration (after cut-off if applied), i.e., $\tau_{\mathrm{int},2} - \tau_{\mathrm{int},1}$, divided by the time resolution, i.e., the inverse of the window width. The time-domain integration is calculated for a number of detecting subcarrier frequency points, proportional to Δf_{calc}, and for a number of subcarrier separations, i.e., $2N_{\mathrm{subc}} + 1$. Here, N_{subc} is the highest subcarrier index, being 255 in this case. Consequently, the type I processing time for the calculation of the interference coefficient, $T_{\mathrm{I,coef}}$, is as follows:

$$T_{\mathrm{I,coef}} \approx b_{\mathrm{I,coef}} X_0 \frac{\Delta f_{\mathrm{calc}}}{\Delta f_{\mathrm{res}}} (2N_{\mathrm{subc}} + 1)\Big((\tau_{\mathrm{int},2} - \tau_{\mathrm{int},1})\Delta f_{\mathrm{meas}}\Big), \tag{6.4}$$

where X_0 is defined as the ratio between Δf_{res} and Δf_{d}, i.e., the frequency resolution at which the interference is calculated (Section 3.4.2). In this case, X_0 equals 8. Analogously, the type II processing time is as follows:

$$T_{\mathrm{II,coef}} \approx b_{\mathrm{II,coef}} X_0 \frac{\Delta f_{\mathrm{calc}}}{\Delta f_{\mathrm{res}}} (2N_{\mathrm{subc}} + 1)\Big((\tau_{\mathrm{int},2} - \tau_{\mathrm{int},1})\big(\Delta f_{\mathrm{meas}} - \Delta f_{\mathrm{calc}}\big)\Big). \tag{6.5}$$

For the type III method, the generalized interference coefficient is first calculated over the maximum zero-excess measurement range by the time-domain integration (Eq. 3.15). Then, the coefficient $y_{\mathrm{Four},\Delta i}$ is calculated (for a non-zero subcarrier separation) as a linear combination of the generalized interference coefficient at the source and the detecting subcarrier (Eq. 3.16). Consequently, the type III processing time consists of the two following terms:

$$\begin{aligned} T_{\mathrm{III,coef}} \approx b_{\mathrm{III,coef}} \Bigg(& X_0 \frac{\Delta f_{\mathrm{calc}} + B}{\Delta f_{\mathrm{res}}} \Big((\tau_{\mathrm{int},2} - \tau_{\mathrm{int},1})\big(\Delta f_{\mathrm{meas}} - \Delta f_{\mathrm{calc}} - B\big)\Big) \\ & + 2X_0 \frac{\Delta f_{\mathrm{calc}}}{\Delta f_{\mathrm{res}}} (2N_{\mathrm{subc}} + 1) \Bigg). \end{aligned} \tag{6.6}$$

Note that all the proportionality factors ($b_{\mathrm{I,ir}}$, $b_{\mathrm{I,coef}}$, ...) ([s]) are expected to be of the same order and may depend on the programming code and the PC's computational capacity. Note also that for each fraction in Eqs. 6.1-6.6 where Δf_{res} appears as denominator, Δf_{res} is assumed to be much smaller than the numerator. This is normally the case for a realistic Δf_{meas}.

6.1.3 Experimental validation

The dependency of the processing time on Δf_{meas} as theoretically described in Section 6.1.2 by Eqs. 6.1-6.6 is validated based on the experimental processing time. The proportionality factors are determined as a function of Δf_{meas} and are found to be generally constant in good approximation. However, for a processing time below 10 s, some deviation is observed due to the rounding error of the processing time or the appearance of other computation steps of a lower order. Therefore, the mean and standard deviation of the proportionality factor is determined based on a Δf_{meas} range starting at a higher Δf_{meas} in some cases (Table 6.1). A standard deviation much smaller than the mean is found, indicating a good agreement between the theoretical and experimental processing time. The minimum and maximum are determined based on the whole Δf_{meas} range to show all deviations. For the channel impulse reponse calculation, the minimum is zero due to an experimental zero processing time (i.e., rounding error). Further, the minimum and maximum values are of the same order as the mean, showing that the theoretical processing time is at least a good order estimation.

Table 6.1: Experimental values of the proportionality factor (b) in Eqs. 6.1-6.6 (i.e., $b_{\mathrm{I,ir}}$,...), for the processing time needed for the calculation of the channel impulse response ("i.r.") and the interference coefficient ("coef."). The mean (M) and standard deviation (SD) are only determined based on a measurement range higher than Δf_{meas}.

method type	i.r. / coef.	b [1.E-7 s] M	SD	MIN	MAX	Δf_{meas} [MHz]
I	i.r.	2.3	0.5	0.0	14.9	1100
	coef.	3.9	0.1	3.7	4.0	160
II	i.r.	2.1	0.0	0.0	2.5	410
	coef.	6.7	0.2	6.5	12.1	350
III	i.r.	2.2	0.0	0.0	5.0	500
	coef.	8.9	0.6	8.1	10.0	405

6.1.4 Discussion of the processing time for different windowing method types

Compared to method type I, the processing time for the impulse response calculation is typically much higher for method types II and III, due to the additional factor related to the moving window (Eqs. 6.2 and 6.3). The beneficial effect of the smaller IDFT size for method types II and III is rather inferior. Fig. 6.1 shows that the type I processing time is at least one order of magnitude smaller than for type II and III. For type III, the processing time is strongly reduced for a Δf_{meas} smaller than 500 MHz (i.e., a window width smaller than 100 MHz).

The processing time for the interference coefficient calculation can be considered as composed of 3 factors for type I and II and of 2 factors for type III (Eqs. 6.4-6.6). Considering that each factor is much larger than 1 and roughly of the same order, the processing time is typically much smaller for type III compared to type I or II. Fig. 6.1 shows that $T_{\mathrm{III,coef}}$ is at least one order of magnitude smaller than for type I and II. $T_{\mathrm{I,coef}}$ and $T_{\mathrm{II,coef}}$ are of the same order unless the window width for type II becomes very small (e.g., < 10 MHz).

From Fig. 6.1, the total processing time for type III is lower than for method I and II up to a Δf_{meas} of 1700 MHz. For a Δf_{meas} of 450 MHz, corresponding to an excess measurement range of 50 MHz, the total processing time for type III is 6 s, while 326 s and 286 s for types I and II, respectively. For a Δf_{meas} of 600 MHz, corresponding to a higher excess measurement range of 200 MHz, the total processing time for type III is 33 s, while 432 s and 506 s for types I and II, respectively. For an extremely high Δf_{meas} of 1400 MHz, the processing time for type III is 689 s and becomes comparable to the processing time for type I and II, i.e., 984 s and 1970 s, respectively. The considerably smaller total processing time of type III for a realistic excess measurement range can be explained by comparing $T_{\mathrm{III,ir}}$ (Eq. 6.3) with $T_{\mathrm{I,coef}}$ (Eq. 6.4) or $T_{\mathrm{II,coef}}$ (Eq. 6.5). Where $T_{\mathrm{III,ir}}$ features the square of the window width, $T_{\mathrm{I,coef}}$ and $T_{\mathrm{II,coef}}$ feature (i) the number of subcarrier separations and (ii) a larger window width, exceeding the type III window width by $\Delta f_{\mathrm{calc}} + B$ for type I and by B for type II. Note that $\tau_{\mathrm{int},2} - \tau_{\mathrm{int},1}$ is of the order of $\Delta f_{\mathrm{res}}^{-1}$. The conclusion is that especially for channels with a high bandwidth, the total processing time for method type III is much lower than for type I and II at a given (realistic) measurement range. In any case, the type III processing time remains practically feasible, as it is dominated by the square of the required window width, which is mainly related to the channel's reverberation time (Section 3.9).

So far, the processing time has been compared for different method types at the *same* measurement range. The actual processing time is determined at the *required* measurement range, which depends on the method used. Based on the maximum required measurement range (over all Δi) for the interference coefficient $y_{\mathrm{tot},\Delta i}$ and a -14 dB relative error power, the corresponding processing time required is determined by linear interpolation of the experimental processing time (Table 6.2). The total processing time of method III-Hann is only 19 / 8 s for 400 / 800 ns CP, respectively. This is much lower than for method types I and II, where the processing time ranges between 266 s and 1121 s. Even when the required measurement range is lower, such as for methods I- and II-rect for 400 ns CP (Table 4.1), method III-Hann takes a considerably lower processing time. This shows that method III-Hann is also efficient from a computational point of view.

Table 6.2: Processing time ([s]) corresponding to the measurement range required to achieve a -14 dB relative error power. This is given for the calculation of the channel impulse response ("i.r.") and the interference coefficient ("coef."). The total processing time is also added.

method	400 ns CP			800 ns CP		
	i.r.	coef.	total	i.r.	coef.	total
I-Hann	1	513	514	1	550	551
II-Hann	109	583	692	115	651	766
III-Hann	14	4	19	4	4	8
I-rect	0	271	272	1	643	644
II-rect	18	247	266	220	901	1121
III-rect	20	4	24	319	7	326
I-HC	1	459	460	1	521	522
II-HC	88	527	615	96	596	691

6.2 Measurement noise

The measurement error on the channel response results into an additional error on the interference coefficient, which is referred to as measurement noise (Section 3.6). The measurement error is caused by imperfections of the measurement setup or external sources and is expected to fluctuate over subsequent sweeps. Systematical imperfections of the measurement setup, e.g., due to connecting the long cable to the remote antenna after transmission calibration, are assumed to be negligible. The relative error power due to measurement noise is aimed to be reduced below a given accuracy level by averaging the measured channel response over a number of sweeps, N_{sweeps}, before applying a windowing method. As the sweep time is of the order of 1 s, small variations of the environment may occur over subsequent sweeps, such as moving people in adjacent rooms. However, it is assumed that the effect on the measured channel response can be neglected.

The absolute error power due to measurement noise is defined analogously to Eq. 3.29 (Section 3.6). This error power varies statistically over different measurement repetitions n, each consisting of N_{sweeps} sweeps, and is denoted by $E_{\alpha',\mathrm{MN},n}$, where α' is the extended index of α (Section 3.6). A statistical upper limit for $E_{\alpha',\mathrm{MN},n}$ is connected with the *average* absolute error power due to measurement noise. This is defined as the (linear-scaled) average of $E_{\alpha',\mathrm{MN},n}$ over an infinite number of measurement repetitions and is denoted by $E_{\alpha',\mathrm{MN-av}}$. Assuming that the measurement error on the interference coefficient is distributed over different measurement repetitions as a complex Gaussian variable, $E_{\alpha',\mathrm{MN},n}$ is expected to be smaller than $1.14 \times E_{\alpha',\mathrm{MN-av}}$ at a confidence level of at least 68%. Considering the statistical behaviour, the measurement noise is investigated in terms of the average absolute error power, $E_{\alpha',\mathrm{MN-av}}$.

First, the influence of the windowing method used on the error power due to measurement noise is investigated (Section 6.2.1). The relative error power due to measurement noise is discussed in more detail in Section 6.2.2. Finally, Section 6.2.3 is focused on the measurement noise reduction by averaging. All results are based on the channel measurement including 1000 sweeps described in Section 4.1.

6.2.1 Influence of the windowing method on the error power due to measurement noise

For the performance analysis of the windowing methods with respect to the required measurement range (Δf_{meas}) (Chapter 4), the convergence analysis is only based on the error power due to non-uniform windowing, resolution and leakage, while the error power due to measurement noise is cancelled out (Section 4.2). This is based on the assumption that the relative error power due to measurement noise is no longer dependent on the windowing method nor Δf_{meas} in the Δf_{meas} range of convergence. This range refers to a Δf_{meas} larger than the Δf_{meas} requirement determined in the convergence analysis. This assumption implies that the measurement noise has no essential effect on the performance of the window-

ing methods as regards to the measurement range requirement. Moreover, it would mean that, to suppress the measurement noise below a given relative error power, the required number of sweeps for averaging can be determined at just one measurement range lying in the range of convergence (Section 6.2.2). In this section, the assumption just mentioned is validated based on the channel measurement described in Section 4.1.

As an extension to the convergence analysis (Section 4.2), the average absolute error power due to measurement noise is determined over the limited set of Δf_{meas} points, ranging from 160 MHz to 2600 MHz. This error power, $E_{\alpha',\mathrm{MN-av}}(\Delta f_{\mathrm{meas}})$, is calculated in good approximation as follows:

$$E_{\alpha',\mathrm{MN-av}}(\Delta f_{\mathrm{meas}}) \approx \left\langle \left| y_{\alpha,n}(\omega_{\mathrm{s}}, \Delta f_{\mathrm{meas}}) - \hat{y}_{\alpha}(\omega_{\mathrm{s}}, \Delta f_{\mathrm{meas}}) \right|^2 \right\rangle_{\omega_{\mathrm{s}},n} \tag{6.7}$$

In Eq. 6.7, $y_{\alpha,n}(\omega_{\mathrm{s}}, \Delta f_{\mathrm{meas}})$ is the interference coefficient ($y_{\alpha}(\omega_{\mathrm{s}})$) as determined by the nth measurement repetition (each based on N_{sweeps} sweeps) and using a measurement range with a width of Δf_{meas}. $\langle \cdot \rangle_{\omega_{\mathrm{s}},n}$ indicates that the average is subsequently taken over the ω_{s} range of interest and the available measurement repetitions. $\hat{y}_{\alpha}(\omega_{\mathrm{s}}, \Delta f_{\mathrm{meas}})$ is an estimate of the noise-free calculation of the interference coefficient:

$$\hat{y}_{\alpha}(\omega_{\mathrm{s}}, \Delta f_{\mathrm{meas}}) = \left\langle y_{\alpha,n}(\omega_{\mathrm{s}}, \Delta f_{\mathrm{meas}}) \right\rangle_{n} \tag{6.8}$$

where the average is taken over the available measurement repetitions. In Eq. 6.7–6.8, it is assumed that (i) the measurement error on the interference coefficient varies uncorrelated over subsequent measurement repetitions, (ii) this error varies over different measurement repetitions in a centrally symmetric way (in the complex plane), and (iii) the number of available measurement repetitions (N_{rep}) is sufficiently large. The number of sweeps (N_{sweeps}) considered is 80 with 12 measurement repetitions.

The actual error power, $E_{\alpha',\mathrm{MN-av}}(\Delta f_{\mathrm{meas}})$, is compared with the error power of the *reference measurement noise*, defined as the measurement noise obtained by method III-Hann at a Δf_{meas} of 2600 MHz. The deviation between the actual and the reference error power is considered over the range of convergence, i.e., for a Δf_{meas} larger than the Δf_{meas} requirement obtained from the convergence analysis (Section 4.2). This deviation is quantified by the maximum absolute value of the dB-scaled error power deviation between (i) the linearly interpolated actual error power and (ii) the reference error power. This deviation parameter, denoted by $\Delta E_{\alpha',\mathrm{MN-av}}$, is determined for the spectral interference over all subcarrier separations (i.e., $|\Delta i| \leq 255$) and the resulting mean, standard deviation, minimum and maximum are in given in Table 6.3.

For methods III-Hann, I-rect, II-rect and III-rect, the maximum $\Delta E_{\alpha',\mathrm{MN-av}}$ is not higher than 0.6 dB for both coefficient types, y_{corr} and y_{Four}, and for 400 ns and 800 ns CP (Table 6.3). This shows that in the range of convergence, the actual error power due to measurement noise is indeed approximately equal to the reference error power.

Table 6.3: The deviation between the actual and the reference error power due to measurement noise is studied over the range of convergence of different windowing methods. The maximum deviation, $\Delta E_{\alpha',\mathrm{MN-av}}$ [dB], is determined for the spectral interference over all subcarrier separations, based on which the mean (M), standard deviation (SD), minimum (MIN) and maximum (MAX) are determined. This is given for both interference coefficient types, y_{corr} and y_{Four}.

CP [ns]	method	y_{corr}				y_{Four}			
		M [dB]	SD [dB]	MIN [dB]	MAX [dB]	M [dB]	SD [dB]	MIN [dB]	MAX [dB]
400	I-Hann	1.3	0.1	1.2	1.5	1.4	0.1	1.1	1.5
	II-Hann	1.7	0.6	0.1	2.1	1.2	0.2	0.2	1.6
	III-Hann	0.0	0.0	0.0	0.1	0.1	0.0	0.0	0.3
	I-rect	0.0	0.0	0.0	0.1	0.0	0.0	0.0	0.1
	II-rect	0.0	0.0	0.0	0.1	0.1	0.1	0.0	0.6
	III-rect	0.0	0.0	0.0	0.0	0.0	0.0	0.0	0.2
	I-HC	0.1	0.0	0.1	0.2	0.9	1.3	0.2	14.5
	II-HC	0.1	0.0	0.0	0.2	1.2	0.2	0.4	1.8
800	I-Hann	1.3	0.1	1.1	1.5	1.3	0.1	1.1	1.5
	II-Hann	1.7	0.4	0.1	2.1	1.2	0.2	0.1	1.6
	III-Hann	0.0	0.0	0.0	0.1	0.1	0.0	0.0	0.1
	I-rect	0.0	0.0	0.0	0.0	0.0	0.0	0.0	0.0
	II-rect	0.0	0.0	0.0	0.0	0.0	0.0	0.0	0.0
	III-rect	0.0	0.0	0.0	0.0	0.0	0.0	0.0	0.1
	I-HC	0.1	0.0	0.0	0.2	0.8	0.6	0.2	6.7
	II-HC	0.1	0.1	0.0	0.2	1.2	0.2	0.0	1.9

For methods I-Hann and II-Hann, the maximum $\Delta E_{\alpha',\mathrm{MN-av}}$ is slightly larger, ranging between 1.5 dB and 2.1 dB and the mean $\Delta E_{\alpha',\mathrm{MN-av}}$ ranges between 1.2 dB and 1.7 dB. However, the deviation between the actual and reference error power decreases fast as Δf_{meas} varies over the range of convergence. For a smaller Δf_{meas}, the actual error power due to measurement noise is typically smaller than the reference error power, due to the non-uniform window introducing a smaller power. For method I- and II-HC, the maximum $\Delta E_{\alpha',\mathrm{MN-av}}$ is not higher than 0.2 dB for y_{corr}. For y_{Four}, there is a substantial deviation between the actual and reference error power for method I-HC, with a maximum $\Delta E_{\alpha',\mathrm{MN-av}}$ up to 14.5 dB for 400 ns CP. A $\Delta E_{\alpha',\mathrm{MN-av}}$ larger than 2 dB is found for a small subcarrier separation (i.e., about $|\Delta i| \leq 10$) with the maximum $\Delta E_{\alpha',\mathrm{MN-av}}$ at a Δi of -6. This can be explained by the small required excess measurement range of 4 MHz in addition to a zero-excess measurement range of 244 MHz, considering that the error power is very sensitive for a small excess range due to the window correction. However, the deviation between the actual and reference error power

decreases fast as Δf_{meas} varies over the range of convergence. For a measurement range of 260 MHz or higher, the deviation is already limited to 0.4 dB. For 800 ns CP, the situation is found very similar. Note that for a Δf_{meas} smaller than the range of convergence, the actual error power due to measurement noise is typically larger than the reference error power, which is due to the window correction.

The **conclusion** is that in the range of convergence, the actual error power due to measurement noise is in general approximately equal to the reference error power. For method I-HC, the actual error power may be substantially larger for a very small measurement excess range, but in the range of convergence, it drops fast towards to the reference error power. These findings can be explained as follows. Due to the linearity of the windowing methods, the measurement error on the interference coefficient can be considered as an interference coefficient corresponding to the measurement error on the channel response. Consequently, in the range of convergence, where the windowing method performs accurately for the undisturbed channel response, the measurement error on the interference coefficient is expected to converge as well. Then, the error power due to measurement noise is the same for all windowing methods. When comparing the actual error power at a Δf_{meas} of 2600 MHz with the reference error power, a deviation of maximum 0.1 dB is found for all windowing methods, for both coefficient types and both CP lengths.

6.2.2 Error power due to measurement noise

For the channel measurement described in Section 4.1, the number of sweeps for averaging (N_{sweeps}), required to suppress the measurement noise below a relative error power of -14 dB, is determined. This is based on method III-Hann at a window width of 200 MHz. This corresponds to a Δf_{meas} of 600 MHz, which falls in the range of convergence (Table 4.1). The relative error power due to measurement noise, $\tilde{E}_{\alpha',\mathrm{MN-av}}$, is determined as a function of N_{sweeps} by dividing the average absolute error power, calculated using Eq. 6.7 for the spectral interference, by the (frequency-averaged) interference power, $I_{\alpha',\mathrm{av}}$ (Section 3.6). For the total interference, the absolute error power is obtained by adding up the spectral absolute error power terms over all subcarrier separations. N_{sweeps} is varied over the following set: $\{1, 10, 20, 40, 80, 160, 240\}$. Up to an N_{sweeps} of 80, the number of measurement repetitions (N_{rep}) considered is 12. For an N_{sweeps} of 160 and 240, N_{rep} is resp. 6 and 4, because the total number of sweeps available is 1000. For the estimate of the noise-free interference coefficient (Eq. 6.8), the average is always taken over 1000 sweeps. Other calculation parameters are the same as for the convergence analysis from Section 4.2.

It is found that $\tilde{E}_{\alpha',\mathrm{MN-av}}$ is less than -14 dB for both 400 ns and 800 ns CP from an N_{sweeps} of 80. The corresponding $\tilde{E}_{\alpha',\mathrm{MN-av}}$ is shown in Fig. 6.2 for both coefficient types, y_{corr} and y_{Four}, and for both CP lengths. For the spectral interference ($|\Delta i| \leq 255$), the maximum $\tilde{E}_{\alpha',\mathrm{MN-av}}$ for y_{Four} is -26.3 dB and -14.7 dB for 400 ns and 800 ns CP, respectively. For y_{corr}, $\tilde{E}_{\alpha',\mathrm{MN-av}}$ is

less critical, with a maximum of -29.3 dB and -20.4 dB for 400 ns and 800 ns CP, respectively. For the total interference based on the composed coefficient type (y_{tot}), $\tilde{E}_{\alpha',\mathrm{MN-av}}$ is -28.4 dB and -18.2 dB for 400 ns and 800 ns CP, respectively.

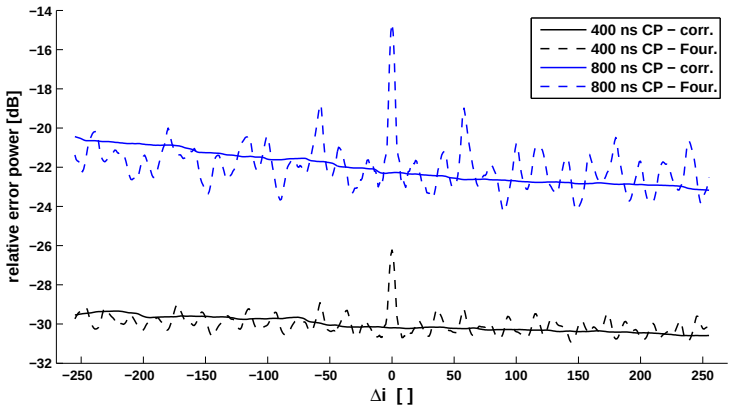

Figure 6.2: The relative error power ($\tilde{E}_{\alpha',\mathrm{MN-av}}$) due to measurement noise after averaging over 80 sweeps is experimentally determined as a function of the subcarrier separation (Δi). This is given for both coefficient types y_{corr} ("corr.") and y_{Four} ("Four.") and for 400 ns and 800 ns CP.

For coefficient type y_{Four}, $\tilde{E}_{\alpha',\mathrm{MN-av}}$ peaks around zero Δi (Fig. 6.2) and becomes comparable to the error power for y_{corr} from a $|\Delta i|$ of 4. Compared to the Δi-averaged level for y_{corr}, being -30.0 / -22.0 dB for 400 / 800 ns CP, resp., the peak height is 3.8 dB and 7.3 dB, respectively. Moreover, it is observed that the error power for 800 ns CP is larger than for 400 ns.

These findings can be explained by the time-domain profile of the weighting functions and the profile of the measurement error power on the channel impulse response (CIR). Fig. 6.3 shows the averaged power delay profile (APDP) and the corresponding error power due to measurement noise after averaging over 80 sweeps. These are based on method III-Hann applied at a window width of 200 MHz. The APDP and the CIR error power are obtained by averaging the time-domain channel components and the corresponding measurement error power, resp., over the range of the moving center frequency, being $[3.6, 4]$ GHz. In addition, the CIR error power is averaged over 12 measurement repetitions. Note that Fig. 6.3 shows the APDP and the measurement error power after normalization to the total APDP power. From Fig. 6.3, the CIR error power consists of a flat component, which is typically caused by an additive noise (on the measured channel response), and a component that follows the APDP approximately proportionally. The latter is typically caused by a multiplicative noise, where the measurement error on the channel reponse is proportional to the channel reponse with a proportionality factor that is only slightly dependent on the frequency. The

flat error power level is determined as -82.0 dB and the ratio between APDP and multiplicative error power is 43.2 dB, based on a delay range of $[57.5, 400]$ ns. For 800 ns CP, the CIR error power is mainly flat in the interference delay interval, starting at a delay of 859 ns. For 400 ns CP, the interference delay interval ranges from 459 ns to 1324 ns (i.e., after cut-off), based on which the ratio between the time-integrated CIR error power and the flat component is 6.1 dB. Thus, for 400 ns CP, the measurement noise is dominated by both the multiplicative and the flat component.

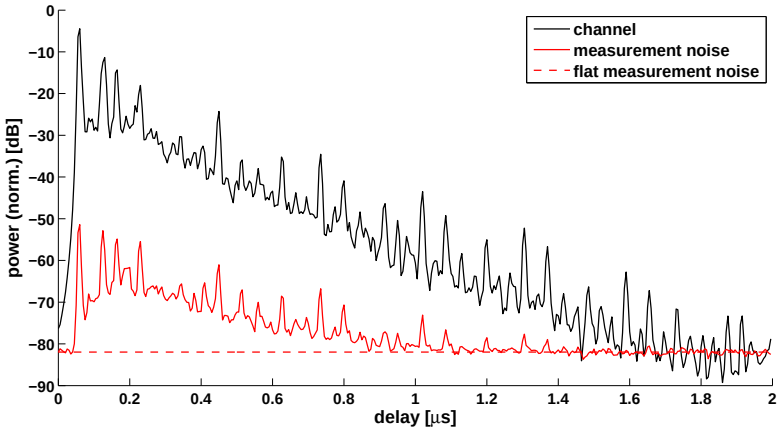

Figure 6.3: Averaged power delay profile (APDP) and the corresponding error power due to measurement noise after averaging over 80 sweeps. The error power consists of a flat and a multiplicative component. All power profiles are normalized to the total APDP power.

The time-domain profile of the CIR error power has the following implications on the relative error power due to measurement noise ($\tilde{E}_{\alpha',\mathrm{MN-av}}$). The latter has been defined as the ratio between the absolute error power and the interference power, which are both obtained based on a weighted time-domain integration of the channel components and the corresponding measurement error, respectively (Eq. 3.15 in Section 3.4.1). Remind that the weighting function for the y_{corr} coefficient type has a uniform profile over the interference delay interval, while for y_{Four}, this profile is linear for a small $|\Delta i|$ and becomes quasi-uniform for a higher $|\Delta i|$ (Section 2.2). If the CIR error power is dominated by the multiplicative component over the interference delay interval, $\tilde{E}_{\alpha',\mathrm{MN-av}}$ corresponds to the ratio between the CIR error power and the APDP, irrespective of the weighting function profile. If the CIR error power is dominated by the flat component over the interference delay interval, $\tilde{E}_{\alpha',\mathrm{MN-av}}$ will be larger for a linear weighting function profile than for a (quasi-)uniform profile, as the linear profile's centre is located at a higher delay. Consequently, for the y_{Four} type coefficient, $\tilde{E}_{\alpha',\mathrm{MN-av}}$ peaks around zero Δi and for a higher $|\Delta i|$, it becomes comparable to the case of y_{corr}. Moreover, in the case of a flat CIR error power, $\tilde{E}_{\alpha',\mathrm{MN-av}}$ is obviously larger for

a higher CP length, while this remains unchanged for a multiplicative error power. All these arguments explain the findings that have been observed from Fig. 6.2.

The **conclusion** is as follows. Especially for a large CP length, where the CIR error power is typically dominated by a (time-domain) flat component, the most critical interference power (to suppress the measurement noise below a given relative error power), is for the $y_{\mathrm{Four},0}$ coefficient (for a zero subcarrier separation). This is typically the most important spectral component. The total interference power, for which the absolute error power is composed of all spectral error power terms, is less critical. Indeed, for the total interference (i.e., $|\Delta i| \leq 255$), $\tilde{E}_{\alpha',\mathrm{MN-av}}$ is -28.4 dB and -18.2 dB for 400 ns and 800 ns CP, which is smaller than $\tilde{E}_{\alpha',\mathrm{MN-av}}$ obtained for $y_{\mathrm{Four},0}$, i.e., -26.3 dB and -14.7 dB, respectively.

6.2.3 Measurement noise reduction by averaging

In this section, it is investigated how efficiently the measurement noise is reduced by averaging the measured channel response over a number of sweeps. Assuming that (i) the measurement error on the interference coefficient based on 1 sweep (i.e., without averaging) varies uncorrelated over subsequent sweeps, and that (ii) this error varies over different sweeps in a centrally symmetric way (in the complex plane), it follows that $\tilde{E}_{\alpha',\mathrm{MN-av}}$ is inversely proportional to N_{sweeps}. As described in Section 6.2.2, $\tilde{E}_{\alpha',\mathrm{MN-av}}$ is determined as a function of N_{sweeps}. This is shown in Fig. 6.4 for the following α' cases: (i) spectral interference of coefficient type y_{corr}, (ii) spectral interference of coefficient type $y_{\mathrm{Four},0}$ (at zero Δi) and (iii) total interference (i.e., $|\Delta i| \leq 255$) using coefficient type y_{tot}. The mentioned theoretical relationship between $\tilde{E}_{\alpha',\mathrm{MN-av}}$ and N_{sweeps} is also extrapolated from the experimental data at 1 sweep. For 800 ns CP, it is found that this theoretical relationship applies well. The deviation between the estimated and the extrapolated $\tilde{E}_{\alpha',\mathrm{MN-av}}$ for the spectral interference is maximum 1.2 dB and 1.6 dB for coefficient types y_{corr} and y_{Four}, respectively. For the total interference, the deviation is maximum 0.4 dB. For 400 ns CP, the deviation is found higher, especially for an N_{sweeps} from 40. The deviation reaches values up to 6.2 dB and 7.1 dB for y_{corr} and y_{Four}, resp., for the spectral interference and 3.7 dB for the total interference. This deviation at 400 ns CP is unlikely to be caused by an unsufficiently large number of measurement repetitions (N_{rep}) to estimate the error power (Eq. 6.7). Indeed, at an N_{sweeps} of 80, where N_{rep} is still 12, there is already a deviation up to 5.6 dB. This indicates that the assumptions for the theoretical relationship between $\tilde{E}_{\alpha',\mathrm{MN-av}}$ and N_{sweeps} are not completely fulfilled. E.g., there may be a certain correlation of the measurement error over subsequent sweeps, which would imply that $\tilde{E}_{\alpha',\mathrm{MN-av}}$ decreases slower than inversely proportional to N_{sweeps}. Note also that, from Fig. 6.4, the deviation becomes larger at a smaller CP length and for a weighting function profile centered at a lower delay, where the measurement noise is relatively more dominated by the multiplicative component.

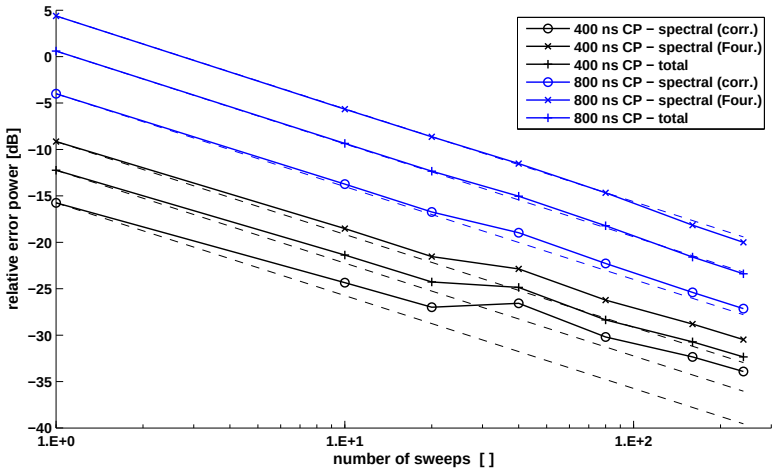

Figure 6.4: The relative error power ($\tilde{E}_{\alpha',\mathrm{MN-av}}$) due to measurement noise is experimentally determined as a function of the number of sweeps (N_{sweeps}) for averaging. This is given for (i) the spectral interference at a zero subcarrier separation for coefficient types y_{corr} ("corr.") and y_{Four} ("Four.") and (ii) for the total interference. From the one-sweep point, the error power is also extrapolated inversely proportionally to N_{sweeps} (dash lines).

These findings have important implications on how to determine in practice the number of sweeps for averaging (N_{sweeps}) required to suppress the measurement noise below a given relative error power, $\tilde{E}_{\mathrm{thresh}}$. In a first approach, $\tilde{E}_{\alpha',\mathrm{MN-av}}$ is estimated as a function of N_{sweeps} using Eq. 6.7, based on a number of repetitions (N_{rep}) of the actual measurement, each consisting of N_{sweeps} sweeps. This approach is most accurate, but the estimation of the measurement error power requires a channel measurement including a total number of sweeps that is much larger than the actual number of sweeps (N_{sweeps}) required for the determination of the interference power itself. In a second approach, $\tilde{E}_{\alpha',\mathrm{MN-av}}$ is extrapolated based on the inversely proportional relationship between $\tilde{E}_{\alpha',\mathrm{MN-av}}$ and N_{sweeps}. Hence, it is sufficient to determine $\tilde{E}_{\alpha',\mathrm{MN-av}}$ only at a small N_{sweeps} using the first approach, saving a lot of measurement time. The theoretical relationship has been validated for 800 ns CP, which is most critical for the measurement noise compared to 400 ns CP.

6.3 Validation of the time-domain cut-off requirement

In this section, the time-domain cut-off requirement proposed in Section 3.8 is experimentally validated. This requirement refers to the situation where the reverberation time (τ_r) of an indoor channel is considerably smaller than the FFT integration time, which is typically the case for IEEE 802.11. According to the requirement, the cut-off must be applied at a delay exceeding the start of the interference delay interval by at least 6.6 times τ_r in order to suppress the relative error power due to a cut-off below -14 dB. The requirement is based on the room electromagnetics theory, i.e., the APDP decays exponentially. However, this assumption is no longer realistic if the time-domain channel is dominated by specular components in the interference delay interval, which is particularly the case if the window width required for the APDP-based estimation method (Section 3.7) becomes larger. Therefore, the cut-off requirement needs to be validated, which is done based on the channel measurement described in Section 4.1 and for IEEE 802.11 parameters. Note that the error due to a cut-off is not dependent on the windowing method used (Section 3.5).

The validation is performed by comparing the interference coefficient determined based on a cut-off interval width ($\Delta\tau_\mathrm{CO}$) of 6.6 times τ_r with the one based on a $\Delta\tau_\mathrm{CO}$ which is several times τ_r larger. Considering a CP length of 400 ns and a τ_r of 131 ns, the interference delay intervals (after cut-off) are $[459, 1324]$ ns (Section 4.2) and $[459, 1800]$ ns, respectively. Over a calculation range centered at 3.8 GHz with a width of 241 MHz, the interference coefficient is determined using method III-Hann with a window width of 2200 MHz and channel response averaging over 960 sweeps to cancel out window-related errors and the measurement noise, respectively. Consequently, the deviation of the interference coefficient as determined from both cut-off intervals corresponds in good approximation to the error due to a cut-off.

In Fig. 6.5, the resulting relative error power due to a cut-off is shown as a function of the subcarrier separation (Δi) for both coefficient types, y_corr and y_Four. The maximum relative error power is -13.7 dB, which agrees excellently with the expected value of -14 dB. Moreover, Fig. 6.5 shows that the most critical error power is obtained for coefficient type y_Four at a zero Δi, as theoretically found in Section 3.8. The excellent agreement of the maximum relative error power can be explained by the fact that the weighting function corresponding to coefficient $y_{\mathrm{Four},0}$ (for zero Δi) is relatively slowly varying with the delay due to its linear profile. Then, if the APDP decays exponentially at least on average, which is realistic, the cut-off requirement is already applicable.

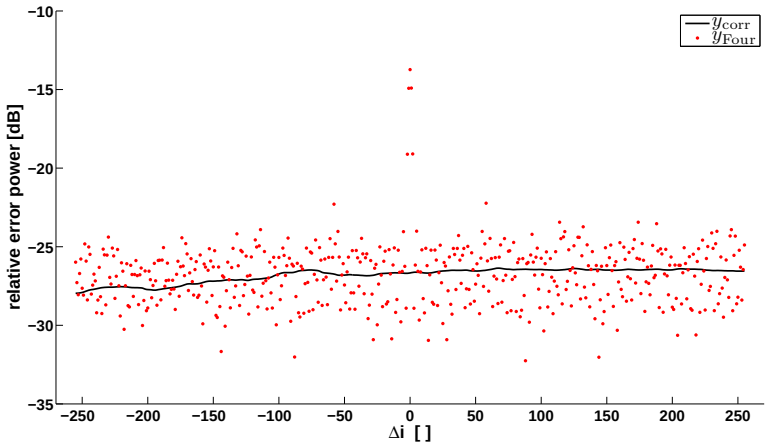

Figure 6.5: The relative error power due to a time-domain cut-off is experimentally determined as a function of the subcarrier separation (Δi) for a cut-off interval duration of 6.6 *times the reverberation time. This is given for both interference coefficient types,* y_{corr} *and* y_{Four}.

7

Interference due to insufficient CP: effective noise factor and analysis as a function of the reverberation time

Due to the temporal variation of the channel, the interference power due to insufficient CP varies over different OFDM packets. In this chapter, the time-varying interference is described using the concept of an *effective*, time-invariant (i.e., packet-independent) additive white Gaussian noise (AWGN). This description allows to determine directly the performance loss factor (in reference to the situation where no delay spread is present). The channel is considered as time-invariant per OFDM packet. In this chapter, the interference due to insufficient CP is also referred to as *multipath noise*.

Based on the theory of room electromagnetics, the effective spectral interference power is analyzed in terms of the reverberation time, resulting into a closed-form expression for the effective noise factor. Simplified interference determination methods are evaluated for IEEE 802.11 based on channel measurements in large conference rooms.

This chapter is structured as follows. In Section 7.1, the concept of the effective AWGN is derived theoretically. The interference power is analytically investigated in terms of the reverberation time in Section 7.2. Section 7.3 reports on the channel measurements in large conference rooms and the data processing. Experimental validation of the concept of the effective noise and the analytical results are provided in Sections 7.4 and 7.5, respectively. In Section 7.6, experimental values of the effective noise factor and loss factor are obtained for IEEE 802.11 in large conference rooms. Conclusions are drawn in Section 7.7.

7.1 Determination of the loss factor due to multipath noise: concept of an effective AWGN

7.1.1 Multipath noise described in terms of a packet-dependent AWGN

Based on the OFDM signal model proposed in Section 2.1, the symbol error vector (at the demapper) is composed of a contribution due to the hardware-related AWGN (including thermal noise), $\Delta\tilde{Y}_{\mathrm{AWGN},m,k,i'}$, and a contribution due to insufficient CP, $\Delta\tilde{Y}_{\mathrm{delay},m,k,i'}$:

$$\Delta\tilde{Y}_{m,k,i'} = \Delta\tilde{Y}_{\mathrm{AWGN},m,k,i'} + \Delta\tilde{Y}_{\mathrm{delay},m,k,i'} \ , \tag{7.1}$$

where m is the OFDM packet index, k is the OFDM symbol index and i' is the index of the subcarrier at which the error is detected.

The *instantaneous* signal-to-noise ratio (SNR) is defined as the ratio between (i) the (errorless) signal power at the demapper (of the receiver), averaged over all constellation points and (ii) the averaged error power (at the demapper) due to the thermal noise entering the receiver input:

$$\mathrm{SNR}_{m,i'} = \frac{\langle|\tilde{X}_{m,k,i'}|^2\rangle_k}{\langle|\Delta\tilde{Y}_{\mathrm{therm},m,k,i'}|^2\rangle_k} \tag{7.2}$$

$$= \frac{P_{\mathrm{T,subc}}|C_m(\omega_{i'})|^2 D_{\mathrm{FFT}}}{k_{\mathrm{B}}T} \tag{7.3}$$

In Eq. 7.2, $\langle\cdot\rangle_k$ indicates an averaging over all OFDM symbols k in the mth OFDM packet. $\tilde{X}_{m,k,i'}$ are the errorless (normalized) data symbols and $\Delta\tilde{Y}_{\mathrm{therm},m,k,i}$ is the (normalized) error vector due to the thermal noise entering the receiver input. The SNR is called *instantaneous* because it is based on one channel realization (per OFDM packet). In Eq. 7.3, the SNR is expressed as the ratio between the instantaneous received power per subcarrier and the thermal noise power per subcarrier. In Eq. 7.3, $C_m(\omega_i)$ is the channel response at (angular) frequency $\omega_{i'}$ of subcarrier i' (during the mth OFDM packet), k_{B} is the Boltzmann constant, T is the room temperature (i.e., 290 K according to the IEEE Standard [67]) and $P_{\mathrm{T,subc}}$ is the transmit power per subcarrier (averaged over all constellation points).

To obtain a certain packet error rate (PER) (i.e., the probability that one data packet corresponding to one OFDM packet is incorrectly received after channel decoding), a certain minimum SNR is required to ensure that the signal strength is large enough compared to the symbol error vector magnitude. In the case where only error $\Delta\tilde{Y}_{\mathrm{AWGN},m,k,i'}$ is present, the minimum required SNR, $\mathrm{SNR}_{\mathrm{min,AWGN}}$, is usually expressed as follows:

$$\mathrm{SNR}_{\mathrm{min,AWGN}} = F_{\mathrm{AWGN}}\mathrm{SNR}_{\mathrm{min,therm}} \tag{7.4}$$

In Eq. 7.4, $\mathrm{SNR}_{\mathrm{min,therm}}$ is the minimum required SNR in the case where only error $\Delta\tilde{Y}_{\mathrm{therm},m,k,i'}$ (i.e., due to thermal noise) is present and F_{AWGN} is the noise factor.

In the case where only error $\Delta\tilde{Y}_{\mathrm{delay},m,k,i'}$ is present, the minimum required SNR, $\mathrm{SNR}_{\mathrm{min,delay},m,i'}$, is analogously expressed introducing a factor $F_{\mathrm{delay},m,i'}$:

$$\mathrm{SNR}_{\mathrm{min,delay},m,i'} = F_{\mathrm{delay},m,i'}\,\mathrm{SNR}_{\mathrm{min,therm}} \tag{7.5}$$

Thus, the multipath noise at a subcarrier i' can be described by an additional packet-dependent AWGN term, characterized by a noise factor $F_{\mathrm{delay},m,i'}$. $F_{\mathrm{delay},m,i'}$ and $\mathrm{SNR}_{\mathrm{min,delay},m,i'}$ may vary over different OFDM packets and subcarriers due to the temporal variation of the channel and the frequency-selectivity of the multipath noise, respectively.

If $F_{\mathrm{delay},m,i'}$ is much larger than F_{AWGN}, $\Delta\tilde{Y}_{\mathrm{AWGN},m,k,i'}$ is negligible compared to $\Delta\tilde{Y}_{\mathrm{delay},m,k,i'}$ and vice versa. Therefore, the minimum required SNR corresponding to the total error vector is approximated by:

$$\mathrm{SNR}_{\mathrm{min,tot},m,i'} = (F_{\mathrm{AWGN}} + F_{\mathrm{delay},m,i'})\,\mathrm{SNR}_{\mathrm{min,therm}}. \tag{7.6}$$

Assuming that the channel coding is done per single OFDM packet, the required PER is achieved when the actual SNR at the receiver is higher than $\mathrm{SNR}_{\mathrm{min,tot},m,i'}$. This is, from Eq. 7.3, equivalent to

$$P_{\mathrm{T,subc}}|C_m(\omega_{i'})|^2 \geq \mathrm{SNR}_{\mathrm{min,tot},m,i'}\frac{k_{\mathrm{B}}T}{D_{\mathrm{FFT}}}. \tag{7.7}$$

The outage probability (p_{out}), i.e., the probability that the required PER is not achieved for a single OFDM packet, is determined by evaluation of Eq. 7.7 over all OFDM packets m.

7.1.2 Multipath noise described in terms of an *effective* AWGN

From Eqs. 7.6 and 7.7, the outage probability is obtained by evaluating the cumulative distribution function (CDF) of $\mathrm{SINR}_{m,i'}$, defined as

$$\mathrm{SINR}_{m,i'} = \frac{D_{\mathrm{FFT}}P_{\mathrm{T,subc}}}{k_{\mathrm{B}}T}\frac{|C_m(\omega_{i'})|^2}{F_{\mathrm{AWGN}} + F_{\mathrm{delay},m,i'}}, \tag{7.8}$$

at $\mathrm{SINR}_{m,i'} = \mathrm{SNR}_{\mathrm{min,therm}}$. In this CDF, the variation of $\mathrm{SINR}_{m,i'}$ is considered over all OFDM packets m. $\mathrm{SINR}_{m,i'}$ corresponds to the (instantaneous) signal-to-interference-plus-noise ratio (SINR) as detected at the demapper at subcarrier i' and during the mth OFDM packet.

As the channel response, varying over different OFDM packets m, is approximately uniformly distributed in the complex plane around zero for a sufficiently small channel response magnitude, it follows that the CDF of $|C_m(\omega_{i'})|^2$ is in

good approximation proportional to $|C_m(\omega_{i'})|^2$ for a sufficiently small channel response magnitude:

$$\mathrm{CDF}(|C_m(\omega_{i'})|^2) \approx M(\omega_{i'})|C_m(\omega_{i'})|^2, \tag{7.9}$$

where $M(\omega_{i'})$ is a proportionality factor depending on $\omega_{i'}$. Further, it is assumed that $F_{\mathrm{delay},m,i'}$ and $|C_m(\omega_{i'})|^2$ are uncorrelated over different OFDM packets and that $F_{\mathrm{delay},m,i'}$ follows roughly an exponential distribution. Under these assumptions, it can be mathematically shown from Eqs. 7.8 and 7.9 that the CDF tail of $\mathrm{SINR}_{m,i'}$, i.e., for a sufficiently low (dB-scaled) SINR, is in good approximation given by

$$\mathrm{CDF}(\mathrm{SINR}_{m,i'}) \approx M(\omega_{i'}) \frac{k_B T}{D_{\mathrm{FFT}} P_{\mathrm{T,subc}}} \langle F_{\mathrm{AWGN}} + F_{\mathrm{delay},m,i'} \rangle_m \mathrm{SINR}_{m,i'}\,, \tag{7.10}$$

where the average $\langle \cdot \rangle_m$ is taken over all OFDM packets m. Note that in Eq. 7.10, $\mathrm{SINR}_{m,i'}$ is linear-scaled. Consequently, the CDF tail of $\mathrm{SINR}_{m,i'}$ remains unchanged when considering $\langle F_{\mathrm{delay},m,i'} \rangle_m$ instead of $F_{\mathrm{delay},m,i'}$ in Eq. 7.8. Assuming that $\mathrm{SNR}_{\mathrm{min,therm}}$ falls in this CDF tail (i.e., $p_{\mathrm{out}} \ll 1$), it can be concluded that the multipath noise at a subcarrier i' can be described by an additional, *effective* AWGN term with the following time-invariant noise factor $F_{\mathrm{delay,eff},i'}$:

$$F_{\mathrm{delay,eff},i'} = \langle F_{\mathrm{delay},m,i'} \rangle_m\,. \tag{7.11}$$

This is an effective value, i.e., with respect to the actual reception quality, described by the outage probability with respect to a required PER.

Alternatively, the actual reception quality can also be described by a performance loss factor, L_{delay}: the same reception quality would be obtained when the transmit power is reduced with a factor L_{delay}^{-1} in the (hypothetical) situation where per subcarrier, the channel is considered as frequency-flat (without delay spread). From Eq. 7.8, L_{delay} is the ratio between the total noise factor, $F_{\mathrm{AWGN}} + F_{\mathrm{delay,eff},i'}$, and F_{AWGN}:

$$L_{\mathrm{delay}} = 1 + \frac{F_{\mathrm{delay,eff},i'}}{F_{\mathrm{AWGN}}}. \tag{7.12}$$

Assuming that $F_{\mathrm{delay,eff},i'}$ is approximately constant over all subcarriers i' (due to the averaging over all OFDM packets), the same loss factor applies to the whole bandwidth and can be included in link budget analysis.

For a realistic OFDM system, the loss factor due to multipath noise interference is derived analogously. The resulting loss factor is given by Eq. 7.12, where F_{AWGN} is replaced by $F \times L_{\mathrm{impl}}$. Here, F and L_{impl} are the conventional noise factor and the (linear-scaled) implementation loss of the realistic system, respectively. As the error vector due to insufficient CP considered in this dissertation is based on an idealized OFDM system (Section 2.1) and no additional errors are considered, e.g., due to frequency synchronization algorithms in the realistic system, it is expected that the resulting loss factor is a lower limit for realistic OFDM systems.

7.2 Analysis of the spectral interference power and the effective noise factor in terms of the reverberation time

7.2.1 Determination of the effective noise factor in terms of the interference coefficient

Assuming that $\Delta\tilde{Y}_{\mathrm{delay},m,k,i'}$, varying over different OFDM symbols k, behaves as a complex Gaussian variable and considering that the error vector due to thermal noise is also a complex Gaussian variable, the packet-dependent noise factor is simply determined as the ratio between the averaged error power due to multipath noise and the averaged error power due to thermal noise:

$$F_{\mathrm{delay},m,i'} = \frac{\langle|\Delta\tilde{Y}_{\mathrm{delay},m,k,i'}|^2\rangle_k}{\langle|\Delta\tilde{Y}_{\mathrm{therm},m,k,i'}|^2\rangle_k}. \tag{7.13}$$

From Eq. 7.11, Eq. 7.13 and the analytical relationship between the error vector and the interference coefficient for IEEE 802.11 (Eq. 2.26), it follows that the effective noise factor is given by

$$F_{\mathrm{delay,eff},i'} = \frac{2D_{\mathrm{FFT}}P_{\mathrm{T,subc}}}{k_{\mathrm{B}}T} \sum_{i=-N_{\mathrm{subc}}}^{N_{\mathrm{subc}}} \langle|y_{\mathrm{corr},m}(\omega_i) + y_{\mathrm{Four},i'-i,m}(\omega_i)|^2\rangle_m \,, \tag{7.14}$$

where the OFDM packet index m is now included into the notation of the interference coefficients ($y_{\mathrm{corr},m}(\omega_i)$ and $y_{\mathrm{Four},i'-i,m}(\omega_i)$) and the number of subcarriers used for transmission equals $2N_{\mathrm{subc}}+1$. In Eq. 7.14, it is assumed that the data symbols $\tilde{X}_{m,k,i}$ are uncorrelated. Both ICI and ISI (between two consecutive OFDM symbols) are included in Eq. 7.14. Note that for other physical standards, an expression similar to Eq. 7.14 can be obtained based on the more general analytical relationship between the error vector and the interference coefficient (Eq. 2.8), taking into account more ISI terms.

7.2.2 APDP-based expressions for the effective interference power and the effective noise factor

In Eq. 7.14, $\langle|y_{\mathrm{corr},m}(\omega_i) + y_{\mathrm{Four},i'-i,m}(\omega_i)|^2\rangle_m$ is estimated by the following sum: $\langle|y_{\mathrm{corr},m}(\omega_i)|^2\rangle_m + \langle|y_{\mathrm{Four},i'-i,m}(\omega_i)|^2\rangle_m$. Assuming that these effective (i.e., time-averaged) interference power terms are independent on the frequency (ω_i) over a certain frequency band, $[f_{\mathrm{band},1}, f_{\mathrm{band},2}]$, it follows from Eq. 7.14 that the effective noise factor can be determined in terms of the frequency-averaged

interference power terms:

$$F_{\mathrm{delay,eff},i'} = \frac{2D_{\mathrm{FFT}}P_{\mathrm{T,subc}}}{k_{\mathrm{B}}T}\Big((2N_{\mathrm{subc}}+1)\langle|y_{\mathrm{corr},m}(\omega_{\mathrm{s}})|^2\rangle_{m,\omega_{\mathrm{s}}} + \sum_{i=-N_{\mathrm{subc}}}^{N_{\mathrm{subc}}}\langle|y_{\mathrm{Four},i'-i,m}(\omega_{\mathrm{s}})|^2\rangle_{m,\omega_{\mathrm{s}}}\Big), \tag{7.15}$$

where $\langle\,\cdot\,\rangle_{m,\omega_{\mathrm{s}}}$ indicates an averaging over all OFDM packets m and over all source subcarrier frequencies, ω_{s}, in the aforementioned frequency band.

From Section 3.7, the frequency-averaged interference power terms can be estimated based on the averaged power-delay profile (APDP) and the weighting functions, $g_{\mathrm{corr}}(\tau)$ and $g_{\mathrm{Four},i'-i}(\tau)$:

$$\langle|y_{\mathrm{corr},m}(\omega_{\mathrm{s}})|^2\rangle_{m,\omega_{\mathrm{s}}} \approx R_{\mathrm{win}}^{-1}\sum_{k=0}^{N-1}|g_{\mathrm{corr}}(\tau_k-\tau_{\mathrm{int},0})|^2\langle|c_{\mathrm{IDFT}}(k)|^2\rangle_{m,\omega_{\mathrm{win}}} \tag{7.16}$$

$$\langle|y_{\mathrm{Four},i'-i,m}(\omega_{\mathrm{s}})|^2\rangle_{m,\omega_{\mathrm{s}}} \approx R_{\mathrm{win}}^{-1}\sum_{k=0}^{N-1}|g_{\mathrm{Four},i'-i}(\tau_k-\tau_{\mathrm{int},0})|^2 \times\langle|c_{\mathrm{IDFT}}(k)|^2\rangle_{m,\omega_{\mathrm{win}}} \tag{7.17}$$

where $\tau_k = k\Delta f_{\mathrm{win}}^{-1}$ and N is the ratio between the window width (Δf_{win}) and the frequency resolution of the channel response. For the near-optimal FFT window positioning proposed in Section 2.1.3, $\tau_{\mathrm{int},0} = \tau_{\mathrm{min}} + D_{\mathrm{CP}} + D_{\mathrm{FFT}} + D_{\mathrm{FFT}}\,N_{\mathrm{sample}}^{-1}$. The power-delay profile coefficients, $|c_{\mathrm{IDFT}}(k)|^2$ (defined in Section 3.4.1), are averaged over all packets m and, in the case of a moving window, over the window centre frequency, ω_{win}, ranging over the whole frequency band. Further, a Hann window is considered, implying that R_{win} equals $3/8$.

7.2.3 Analytical expressions for the interference power and the effective noise factor

Based on the theory of room electromagnetics for indoor channels [5], the tail of the APDP is described by an exponential decay:

$$\langle|c_{\mathrm{IDFT}}(k)|^2\rangle_{m,\omega_{\mathrm{win}}} = |c_{\mathrm{RE}}|^2\exp\big(-\frac{\tau_k-\tau_{\mathrm{min}}}{\tau_{\mathrm{r}}}\big), \tag{7.18}$$

where $|c_{\mathrm{RE}}|^2$ is a proportionality factor. It is assumed that this applies for the relevant part of the channel impulse response, i.e., where the weighting functions (after the cut-off if applied) are non-zero. τ_{min} is the delay of the first arriving propagation path and τ_{r} is the reverberation time.

Substituting Eq. 7.18 into Eqs. 7.16 and 7.17, the spectral interference power terms can be analytically determined as a function of the reverberation time, which

is referred to as *analytical method*. Assuming that $D_{\mathrm{FFT}} \gg \tau_{\mathrm{r}}$, the Fourier-type spectral interference power normalized to the zero subcarrier separation term is a function of $|i' - i|\Delta\omega_{\mathrm{subc}}\tau_{\mathrm{r}}$, where $\Delta\omega_{\mathrm{subc}}$ is the (angular) subcarrier frequency spacing (i.e., $2\pi/D_{\mathrm{FFT}}$). It is found that the tail of (normalized) spectral interference power is approximately determined by

$$\frac{\langle |y_{\mathrm{Four},i'-i,m}(\omega_{\mathrm{s}})|^2 \rangle_{m,\omega_{\mathrm{s}}}}{\langle |y_{\mathrm{Four},0,m}(\omega_{\mathrm{s}})|^2 \rangle_{m,\omega_{\mathrm{s}}}} \approx (|i' - i|\Delta\omega_{\mathrm{subc}}\tau_{\mathrm{r}})^{-2} \tag{7.19}$$

which holds with a deviation smaller than 1 dB for $|i' - i|\Delta\omega_{\mathrm{subc}}\tau_{\mathrm{r}} > 2$. This is illustrated in Fig. 7.1. Thus, the (Fourier-type) spectral interference profile has a frequency width of the order of the inverse of the reverberation time. The profile decay follows an inverse-square law as a function of the subcarrier separation and is extended over a frequency width of a few times τ_{r}^{-1}.

Assuming that $D_{\mathrm{FFT}} \gg \tau_{\mathrm{r}}$, the following closed-form analytical expressions can be derived for (i) the correction-type interference power, (ii) the Fourier-type interference power at a zero subcarrier separation and (iii) the total Fourier-type interference power:

$$\left\langle |y_{\mathrm{corr},m}(\omega_{\mathrm{s}})|^2 \right\rangle_{m,\omega_{\mathrm{s}}} \approx \frac{2}{3N_{\mathrm{sample}}^2} I_{\mathrm{diff}}\tau_{\mathrm{r}} \exp\Big(-\frac{D_{\mathrm{CP}} + D_{\mathrm{FFT}}\, N_{\mathrm{sample}}^{-1}}{\tau_{\mathrm{r}}}\Big) \tag{7.20a}$$

$$\left\langle |y_{\mathrm{Four},0,m}(\omega_{\mathrm{s}})|^2 \right\rangle_{m,\omega_{\mathrm{s}}} \approx \frac{16}{3} I_{\mathrm{diff}} \frac{\tau_{\mathrm{r}}^3}{D_{\mathrm{FFT}}^2} \exp\Big(-\frac{D_{\mathrm{CP}} + D_{\mathrm{FFT}}\, N_{\mathrm{sample}}^{-1}}{\tau_{\mathrm{r}}}\Big) \tag{7.20b}$$

$$\Big\langle \sum_{\Delta i=-\infty}^{\infty} |y_{\mathrm{Four},\Delta i,m}(\omega_{\mathrm{s}})|^2 \Big\rangle_{m,\omega_{\mathrm{s}}} \approx \frac{8}{3} I_{\mathrm{diff}} \frac{\tau_{\mathrm{r}}^2}{D_{\mathrm{FFT}}} \exp\Big(-\frac{D_{\mathrm{CP}} + D_{\mathrm{FFT}}\, N_{\mathrm{sample}}^{-1}}{\tau_{\mathrm{r}}}\Big). \tag{7.20c}$$

This approximation holds with a deviation of the averaged power lower than 0.5 dB for $\tau_{\mathrm{r}} < 0.2 D_{\mathrm{FFT}}$. Eq. 7.20c is obtained based on Eq. 2.29 (Section 2.4), where an infinite number of subcarriers is considered. In Eqs. 7.20a–7.20c, $|c_{\mathrm{RE}}|^2$ is expressed by I_{diff} [Hz] $= |c_{\mathrm{RE}}|^2 \Delta f_{\mathrm{win}}$, which is not dependent on the window width (Δf_{win}). Indeed, as the time resolution of the APDP is the inverse of Δf_{win}, $|c_{\mathrm{RE}}|^2$ is inversely proportional to Δf_{win}. Note that in the notation of I_{diff}, "diff" refers to the so-called diffuse (dense) multipath character of the channel [38].

While the correction-type interference power is independent on the subcarrier separation, the Fourier-type interference power is centred around a zero subcarrier separation with a frequency width of the order of the inverse of the reverberation time. The nominal number of subcarriers contributing equally to the total Fourier-type interference power is then the ratio between the total interference and the spectral interference power at zero subcarrier separation. The former is determined by Eq. 7.20c, assuming that the bandwidth exceeds the spectral interference width. From Eqs. 7.20c and 7.20b, the nominal number of subcarriers involved

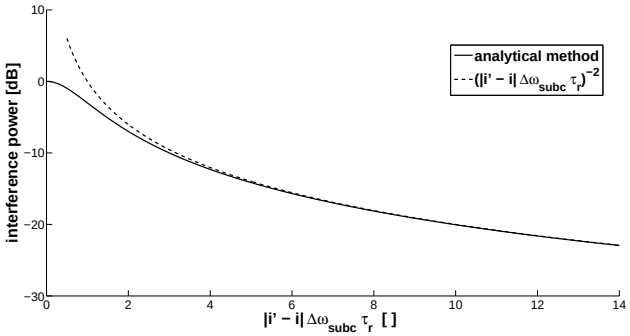

Figure 7.1: The Fourier-type effective spectral interference power (normalized to the zero subcarrier separation term) is calculated analytically (solid line). The tail of the interference profile is well described by the theoretical inverse-square law (Eq. 7.19) (dash line). The frequency width of the spectral interference is of the order of the inverse of the reverberation time.

in the Fourier-type interference equals $D_{\mathrm{FFT}}/(2\tau_{\mathrm{r}})$ (after rounding up) and the corresponding frequency width equals $(2\tau_{\mathrm{r}})^{-1}$.

7.2.4 Per-packet complex Gaussian behavior of the error vector due to multipath noise

In Section 7.2.1, it has been assumed that, considered per OFDM packet, the error vector due to multipath noise, $\Delta\tilde{Y}_{\mathrm{delay},m,k,i'}$, behaves as a complex Gaussian variable, allowing to determine the (packet-dependent) noise factor as in Eq. 7.13. More specifically, the complementary cumulative distribution function (CCDF) of the error vector magnitude should follow this behavior at the relevant level, being of the order of the required transmission symbol error rate (SER) (i.e., the probability that a data symbol error occurs at the demapper). When the number of data symbols which contribute to the error vector in a non-negligible way, is sufficiently large, the error vector behaves as a complex Gaussian variable (central limit theorem). For IEEE 802.11, where there is only ISI between two consecutive OFDM symbols, this implies a sufficiently large spectral interference width. Considering a frequency width of $(2\tau_{\mathrm{r}})^{-1}$, the number of uncorrelated interference terms (including ICI and ISI), M, is 12 for a (high) reverberation time of 267 ns, while it is 104 for a reverberation time of 31 ns.

To get an idea of how realistic the assumption of a complex Gaussian behavior is, the CCDF of the error vector magnitude for a QPSK[1] constellation is deter-

[1] Quadrature Phase-Shift Keying

mined, based on the following expression:

$$\Delta\tilde{Y}_{\mathrm{delay}} = \sum_{k=1}^{M} \tilde{X}_k \, y_0, \tag{7.21}$$

where y_0 is a complex-valued constant and $\tilde{X}_k$ are uncorrelated data symbols. When comparing this CCDF with the CCDF of a theoretical complex Gaussian variable at a CCDF level of the order of 10^{-2} (i.e., SER estimated from the maximum EVM specification for IEEE 802.11a [14]), we find that the deviation in power is much smaller than 1 dB for 104 terms and smaller than 0.75 dB for 12 terms. It can be concluded that the assumption that the error vector due to multipath noise behaves as a complex Gaussian variable is acceptable (i.e., with a power deviation less than 1 dB), even for a high reverberation time of 267 ns.

7.2.5 Closed-form analytical expression for the effective noise factor

The total Fourier-type interference power appearing in Eq. 7.15 is estimated as composed of $\min(2N_{\mathrm{subc}}+1, D_{\mathrm{FFT}}/(2\tau_{\mathrm{r}}))$ terms with the same power as at a zero subcarrier separation. Here, $\min(\,\cdot\,,\,\cdot\,)$ represents the minimum of the arguments. Consequently, using Eqs. 7.20a and 7.20b, Eq. 7.15 yields the following analytical expression for the effective noise factor, $F_{\mathrm{delay,eff}}$:

$$\begin{aligned} F_{\mathrm{delay,eff}} = \frac{4}{3} \frac{D_{\mathrm{FFT}}\, P_{\mathrm{T,subc}}}{k_{\mathrm{B}} T} I_{\mathrm{diff}} \tau_{\mathrm{r}} \exp\Big(-\frac{D_{\mathrm{CP}} + D_{\mathrm{FFT}}\, N_{\mathrm{sample}}^{-1}}{\tau_{\mathrm{r}}}\Big) \\ \times \left(\frac{(2N_{\mathrm{subc}}+1)}{N_{\mathrm{sample}}^2} + 8 \min\Big(2N_{\mathrm{subc}}+1, \frac{D_{\mathrm{FFT}}}{2\tau_{\mathrm{r}}}\Big) \Big(\frac{\tau_{\mathrm{r}}}{D_{\mathrm{FFT}}}\Big)^2 \right) \end{aligned} \tag{7.22}$$

Note that in the notation for the effective noise factor the subcarrier index i' is omitted, as no essential subcarrier dependence is considered.

7.3 Measurements and data processing

Measurements were executed in two large conference rooms with a virtual single-input multiple-output (SIMO) system. In this setup, the Tx and Rx antenna, both vertically polarized broadband omnidirectional Electro-Metrics antennas of type EM-6116, were connected to a Rohde & Schwarz ZVR vector network analyzer, which measured the scattering parameter S_{21} as a function of the frequency. A coaxial cable with two amplifiers was used to realize the Tx-Rx separation. The Rx antenna was attached to a two-dimensional positioning system.

The measurements were done in the frequency range 2.5 – 3 GHz. 801 frequency points were used, which allows to resolve power delay profiles for delays up to 1.6 µs (larger than an 800 ns CP). A 23×23 Rx array was used, with a separation of 1.5 cm.

In room A, repeated reception problems were reported with an IEEE 802.11a audio conference system. This system has a SISO[2] configuration without antenna diversity. According to the manufacturer, these problems occur specifically in this conference room and cannot be attributed to interference sources after spectral analysis.

The following positions of Tx and the Rx array were chosen in room A (Fig. 7.2): Tx at position 1 (usual position of the access point during meetings) and Rx at position 2 (case 1a) (and vice versa (case 1b)), and Tx at position 1 and Rx at position 3 (case 2a) (and vice versa (case 2b)). At position 1, the height of the antenna (Tx or Rx) was always 1.8 m, while at positions 2 and 3, the antenna height was always 1.2 m. The Tx-Rx separation was 8.9 m for case 1a-b and 6.9 m for case 2a-b.

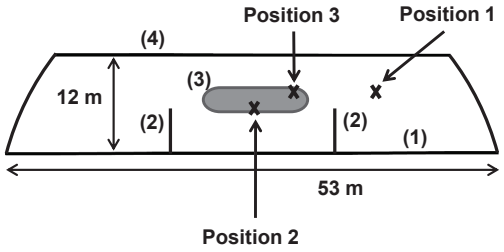

Figure 7.2: Floor plan of room A. The conference table is indicated by (3). Measurements were executed at Tx/Rx positions 1 – 3.

The wall behind position 2 (indicated as (1) in Fig. 7.2) and the two dividing walls ((2) in Fig. 7.2) contain about 30 metal HVAC (Heating, Ventilation, and Air Conditioning) plates (with dimensions 1 m by 1.5 m). The wall at the other side ((4) in Fig. 7.2) consists of windows only. The ceiling, which looks like a part of an ellipsoid, contains a metal wire mesh, with a separation of about 1 cm. The dimensions of the room are 12 m × 53 m and the ceiling has a maximal height of

[2] single-input single-output

13 m. Fig. 7.3 shows a picture of room A taken from the left-hand side on the floor plan (Fig. 7.2).

Figure 7.3: Conference room A

For comparison, measurements were also executed in conference room B (Fig. 7.4). The dimensions are 10 m $\times$ 32 m and the ceiling, which is approximately a horizontal plane, has a height of about 6 m. Tx is positioned around the conference table (in the middle of the room) as an access point at a height of 2.1 m. The Rx array is set at 2 positions (case 3a and 3b, resp.) at the conference table at a height of 1.5 m. Only one wall contains windows (8 windows with dimensions 2 m $\times$ 3 m). The Tx-Rx separation was 9.7 m and 8.3 m for case 3a and 3b, respectively. For all measurements (rooms A and B), there was a line-of-sight condition.

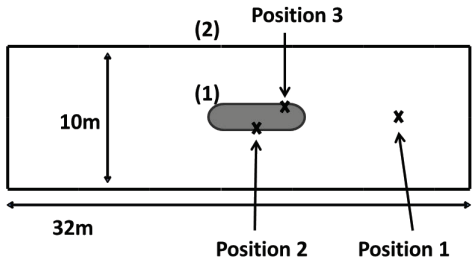

Figure 7.4: Floor plan of conference room B. The conference table is indicated by (1). Tx is set at position 1 and the Rx array is placed at positions 2 and 3, respectively.

The interference coefficients, $y_{\mathrm{corr},m}(\omega_\mathrm{s})$ and $y_{\mathrm{Four},i'-i,m}(\omega_\mathrm{s})$, are calculated over a frequency band of $[2.65, 2.85]$ GHz using windowing method III-Hann. The moving Hann window has a center frequency varying from 2.65 GHz to 2.85 GHz and a window width of 300 MHz. The calculation is carried out for typical IEEE 802.11 OFDM parameters and a 20 MHz bandwidth.

7.4 Experimental validation with respect to the concept of an effective AWGN

In this section, the description of the multipath noise by an *effective* AWGN, which has been theoretically shown for a sufficiently low outage probability (p_{out}) (Section 7.1), is validated experimentally for realistic values of p_{out}. For this validation, $\mathrm{SINR}_{m,i'}$ (defined by Eq. 7.8) is considered as a performance metric. First, $\mathrm{SINR}_{m,i'}$ is determined exactly based on Eq. 7.13, assuming uncorrelated data symbols, and Eq. 2.26 (Section 2.2). Secondly, $\mathrm{SINR}_{m,i'}$ is determined based on the effective noise factor, $\langle F_{\mathrm{delay},m,i'}\rangle_m$, used instead of the packet-dependent noise factor, $F_{\mathrm{delay},m,i'}$, in Eq. 7.8. In this validation, we focus on the interference detected at a zero subcarrier index i'. Typical IEEE 802.11 parameters are used: a total transmit power of $20\ \mathrm{dBm}$ and a (conventional) noise factor (F_{AWGN}) of $15\ \mathrm{dB}$.

The variation of $F_{\mathrm{delay},m,0}$ over different OFDM packets m (due to the temporal variation of the channel) is considered by the variation over the spatial small-scale Rx position. In both cases, $F_{\mathrm{delay},m,0}$ is based on a high number of diverse propagation paths arriving after several reflections or diffractions in the room and interfering in a varying way. Moreover, it is assumed that the sample set $\{F_{\mathrm{delay},m,0}, C_m(\omega_0)\}$ is statistically independent on the carrier frequency in the range 2.65 – 2.85 GHz. Hence, the validation is done using a sample set, $\{F_{\mathrm{delay},m,0}, C_m(\omega_0)\}$, including a variation over all OFDM packets m as well as over the frequency band 2.65 – 2.85 GHz.

For all cases in room A and 400 / $800\ \mathrm{ns}$ CP, the CDF of $\mathrm{SINR}_{m,0}$ is calculated exactly, as well as based on the effective noise factor. We find that the maximum power deviation for a CDF level $p_{\mathrm{out}} < 20\%$ is maximum $0.6\ \mathrm{dB}$ and $1\ \mathrm{dB}$ for $p_{\mathrm{out}} < 50\%$. This is illustrated for case 1b and $800\ \mathrm{ns}$ CP ((1) and (2) in Fig. 7.5). This shows that the concept of the effective AWGN is applicable for realistic values of p_{out} (i.e., $< 50\%$): the packet-dependent multipath noise is described by an additional effective AWGN with a noise factor ($F_{\mathrm{delay,eff}}$) being the averaged packet-dependent noise factor: $F_{\mathrm{delay,eff}} = \langle F_{\mathrm{delay},m,0}\rangle_m$.

In the theoretical derivation of the effective AWGN (Section 7.1), it has been assumed that $F_{\mathrm{delay},m,i'}$ and $|C_m(\omega_{i'})|^2$ are uncorrelated. For all cases in room A and 400 / $800\ \mathrm{ns}$ CP, it is found that the maximum power deviation between the measured CDF and the CDF assuming a perfect decorrelation ((1) and (3), resp., in Fig. 7.5) is smaller than $0.9\ \mathrm{dB}$ for $p_{\mathrm{out}} < 50\%$. Indeed, $F_{\mathrm{delay},m,i'}$ is based on a high number of propagation paths with several reflections or diffractions, while the channel response is mainly determined by the first arriving few paths. A second assumption made in Section 7.1.2 is that $F_{\mathrm{delay},m,i'}$ follows roughly an exponential distribution, which is also validated experimentally for room A. This is demonstrated in Fig. 7.6 for case 1b and $800\ \mathrm{ns}$ CP.

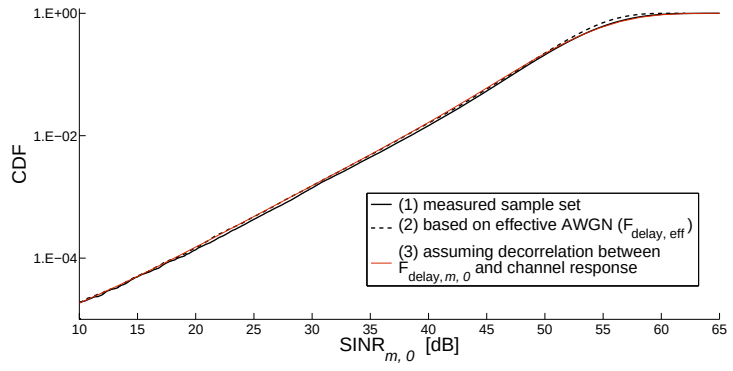

Figure 7.5: Based on a virtual SIMO measurement, the CDF of $\mathrm{SINR}_{m,0}$ *(curve (1)) is determined for* 800 ns *CP. For an outage probability smaller than 50%, an excellent agreement is found with the CDF based on the effective noise factor (*$F_{\mathrm{delay,eff}}$*) (curve (2)). CDF (3) is determined assuming a decorrelation between the packet-dependent noise factor (*$F_{\mathrm{delay},m,0}$*) and the channel response.*

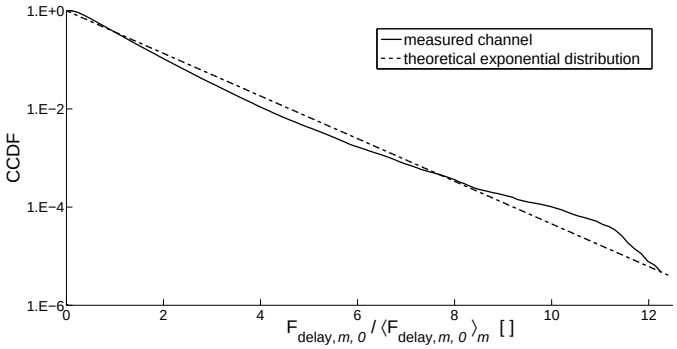

Figure 7.6: The complementary CDF (CCDF) of the ratio between $F_{\mathrm{delay},m,0}$ *and its average (solid line) is determined for* 800 ns *CP. This is compared with the theoretical CCDF (dashed line) assuming* $F_{\mathrm{delay},m,0}$ *as an exponentially distributed variable.*

7.5 Experimental validation with respect to the APDP-based and the analytical determination method

7.5.1 Validation of the frequency-independence of the packet-averaged interference power

In Section 7.2.1, it has been assumed that the packet-averaged spectral interference power terms, $\langle|y_{\mathrm{corr},m}(\omega_\mathrm{s})|^2\rangle_m$ and $\langle|y_{\mathrm{Four},i'-i,m}(\omega_\mathrm{s})|^2\rangle_m$, are independent on the frequency (ω_s). In Fig. 7.7, these are shown as a function of the frequency for case 1b (room A), 800 ns CP and a subcarrier separation ($|i'-i|$) of 0, 5, 10 and 15. Very similar results are obtained for the other cases for room A and $400/800$ ns CP. The maximum variation of the interference power terms over a channel bandwidth of 20 MHz is about ± 2 dB. The average decrease of the power terms over the considered frequency range is only less than 3 dB. It can be concluded that the packet-averaged spectral interference power terms, $\langle|y_{\mathrm{corr},m}(\omega_\mathrm{s})|^2\rangle_m$ and $\langle|y_{\mathrm{Four},i'-i,m}(\omega_\mathrm{s})|^2\rangle_m$, can be considered as frequency-independent, allowing to derive the APDP-based expression for the interference power (Section 7.2.2).

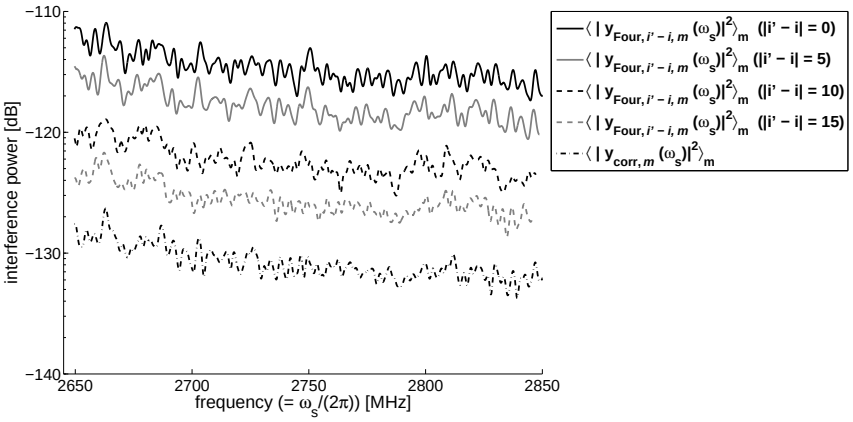

Figure 7.7: The packet-averaged interference power terms, $\langle|y_{\mathrm{corr},m}(\omega_\mathrm{s})|^2\rangle_m$ and $\langle|y_{\mathrm{Four},i'-i,m}(\omega_\mathrm{s})|^2\rangle_m$, are experimentally determined as a function of the frequency for a subcarrier separation ($|i'-i|$) of 0, 5, 10 and 15. Only a small variation over the considered frequency band is found.

7.5.2 Validation of the APDP-based and the analytical method for the determination of the effective interference power

Most rigorously, the frequency-averaged effective spectral interference power terms, $\langle |y_{\mathrm{corr},m}(\omega_\mathrm{s})|^2 \rangle_{m,\omega_\mathrm{s}}$ and $\langle |y_{\mathrm{Four},i'-i,m}(\omega_\mathrm{s})|^2 \rangle_{m,\omega_\mathrm{s}}$ are determined from the measured samples of the interference coefficient (*samples-based* method). Further, two simplified methods have been proposed. Firstly, the *APDP-based* method is based on the measured APDP and a weighting function (Eqs. 7.16 and 7.17). Secondly, the *analytical* method is based on the theory of room electromagnetics (Eq. 7.18), where the reverberation time and the proportionality factor are to be determined from the APDP.

For the validation of the analytical method, τ_r and I_diff are determined from the virtual SIMO measurements in rooms A and B (Table 7.1). These parameters are determined using linear regression of the APDP in log-lin scale. For room A, the fitting according to Eq. 7.18 is based on the delay interval starting at $\tau_\mathrm{min} + D_\mathrm{CP} + D_\mathrm{FFT}\, N_\mathrm{sample}^{-1}$ and with a duration of 4 times τ_r. For room B, the fitting is based on the delay interval $[200, 400]$ ns, because the APDP cannot be detected for higher delays due to the measurement noise level. In room A, τ_r varies from 109 ns to 116 ns for 400 ns CP and from 129 ns to 137 ns for 800 ns CP. This is strikingly higher than in room B, where a τ_r of $35 - 36$ ns is found. In room A, I_diff is found to be $6 - 12$ Hz and $3 - 4$ Hz for 400 ns and 800 ns, resp., and $12 - 21$ Hz in room B.

Table 7.1: Measured APDP tail parameters: reverberation time (τ_r) and proportionality factor (I_diff)

		D_CP [ns]	τ_r [ns]	I_diff [Hz]
room A	case 1a	400	110 ± 3	9 ± 3
		800	134 ± 4	3 ± 1
	case 1b	400	113 ± 4	6 ± 2
		800	131 ± 4	3 ± 1
	case 2a	400	109 ± 3	12 ± 4
		800	137 ± 4	3 ± 1
	case 2b	400	116 ± 4	9 ± 3
		800	129 ± 4	4 ± 1
room B	case 3a	400	35 ± 2	12 ± 6
	case 3b	400	36 ± 2	21 ± 8

The spectral interference power terms, $\langle |y_{\mathrm{corr},m}(\omega_\mathrm{s})|^2 \rangle_{m,\omega_\mathrm{s}}$ and $\langle |y_{\mathrm{Four},i'-i,m}(\omega_\mathrm{s})|^2 \rangle_{m,\omega_\mathrm{s}}$, are calculated for a subcarrier separation ($|i'-i|$) ranging from 0 to 19 based on the (i) samples-based, (ii) APDP-based and (iii) analytical method. The Fourier-type interference power is shown in Fig. 7.8 for

case 1b and 800 ns CP. The theoretical inverse-square law of the spectral interference profile (Eq. 7.19 in Section 7.2.3) is also included, where the factor $\langle |y_{\mathrm{Four},0,m}(\omega_{\mathrm{s}})|^2 \rangle_{m,\omega_{\mathrm{s}}}$ is based on the analytical method. The agreement between the samples-based and the APDP-based method is excellent: for all cases for room A and $400/800$ ns CP, the deviation of all interference power terms is maximum 0.3 dB. The agreement between the analytical and the samples-based method is good: for all cases for room A and $400/800$ ns CP, the deviation of $\langle |y_{\mathrm{corr},m}(\omega_{\mathrm{s}})|^2 \rangle_{m,\omega_{\mathrm{s}}}$ is maximum 1.9 dB and the deviation of $\langle |y_{\mathrm{Four},i'-i,m}(\omega_{\mathrm{s}})|^2 \rangle_{m,\omega_{\mathrm{s}}}$ for $0 \leq |i'-i| \leq 19$ is maximum 1.3 dB (Fig. 7.8).

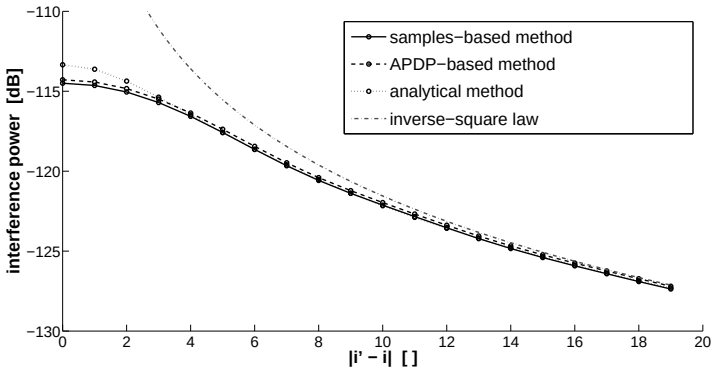

Figure 7.8: The Fourier-type spectral interference power, $\langle |y_{\mathrm{Four},i'-i,m}(\omega_{\mathrm{s}})|^2 \rangle_{m,\omega_{\mathrm{s}}}$, is experimentally determined as a function of the subcarrier separation ($|i'-i|$) based on the samples-based, APDP-based and analytical method, showing good agreement. The theoretical inverse-square law is also included.

7.6 Effective noise factor and loss factor for IEEE 802.11 in large conference rooms

The effective noise factor, $F_{\mathrm{delay,eff}}$, is determined for rooms A and B (Table 7.2) using the analytical method (Eq. 7.22), where τ_{r} and I_{diff} are determined from the APDP (Table 7.1). For room B, the values of τ_{r} and I_{diff} corresponding to 400 ns CP are also used for 800 ns CP. As an additional validation, $F_{\mathrm{delay,eff}}$ in room A is also determined using the samples-based method, based on Eq. 7.14, where the interference power is additionally averaged over the considered frequency band, 2.65 – 2.85 GHz. The following IEEE 802.11 OFDM parameters are used: an FFT size (N_{sample}) of 64 (i.e., a 20 MHz bandwidth) and a transmit power (P_{T}) of 20 dBm. The number of subcarriers used for transmission is considered 52.

For all cases in room A and $400/800$ ns CP, the deviation of $F_{\mathrm{delay,eff}}$ between the samples-based and the analytical method is maximum 1.1 dB (Table 7.2), which is an excellent agreement. For 800 ns CP, $F_{\mathrm{delay,eff}}$ is (averaged over all cases) 22.5 dB and -56.9 dB in room A and B, respectively. For 400 ns CP, $F_{\mathrm{delay,eff}}$ is 36.4 dB and -7.9 dB, respectively. As F_{delay} is proportional to the transmit power, $F_{\mathrm{delay,eff}}$ is even 10 dB higher for a transmit power of 30 dBm (maximum allowed EIRP[3] in 5 GHz band [68]). Compared to room B, $F_{\mathrm{delay,eff}}$ in room A is about 44 dB and 80 dB higher for 400 ns and 800 ns CP, respectively. This is due to the higher reverberation time in room A (averaged 122 ns vs 35 ns in room B), mainly via the factor $\exp(-D_{\mathrm{CP}}/\tau_{\mathrm{r}})$ in Eq. 7.22.

The corresponding loss factor, L_{delay}, is determined based on Eq. 7.12 for a transmit power of 20 / 30 dBm and a noise factor F_{AWGN} of 15 dB (Table 7.2). For room A, the $F_{\mathrm{delay,eff}}$ values from the samples-based method are used. As in room B, $F_{\mathrm{delay,eff}}$ is much lower than F_{AWGN}, L_{delay} is about 0 dB. In room A and for a 20 dBm transmit power, L_{delay} is (averaged) 21.4 dB and 8.3 dB for 400 ns and 800 ns CP, respectively. For a 30 dBm transmit power, L_{delay} is even about 10 dB higher (up to 19 dB for 800 ns CP). This shows that the interference due to insufficient CP causes a severe performance degradation in room A.

As $F_{\mathrm{delay,eff}}$ is strongly dependent on the CP length (Table 7.2), a possible way-out to reduce L_{delay} is to include a long CP option in the physical standard. In [47], a variable guard interval algorithm has already been presented for dynamic multipath channels. Based on Eq. 7.22, when switching D_{CP} from 800 ns to 1600 ns, L_{delay} in room A would be reduced from (averaged) 8 / 18 dB for a transmit power of 20 / 30 dBm, resp., to a zero loss. However, due to the larger overhead, the physical data rate would decrease by 17%. To keep the data rate unchanged, D_{FFT} should increase proportionally to D_{CP}. However, this implies a higher FFT processor size and a lower resistance against the Doppler effect [1].

Another strategy to mitigate the multipath noise is using a directive transmit antenna, properly oriented in the room, in order to reduce the multipath component. Another approach makes use of SINR-based antenna selection. The (packet-dependent) noise factor is expected to be uncorrelated between two antennas with

[3] Equivalent Isotropically Radiated Power

Table 7.2: The effective noise factor ($F_{\mathrm{delay,eff}}$) is determined for a transmit power (P_{T}) of 20 dBm *using the (i) samples-based and (ii) analytical method. The loss factor (L_{delay}) is given for a transmit power of* $20 - 30$ dBm.

room	Tx/Rx position	D_{CP} [ns]	$F_{\mathrm{delay,eff}}$ [dB]		L_{delay} [dB] (at $P_{\mathrm{T}} = 20 - 30$ dBm)
			(i)	(ii)	
A	case 1a	400	36.1	36.0	21.1 - 31.1
		800	22.2	23.1	8.0 - 17.3
	case 1b	400	35.0	34.6	20.0 - 30.0
		800	21.6	20.9	7.5 - 16.7
	case 2a	400	37.0	36.9	22.0 - 32.0
		800	23.9	23.1	9.4 - 19.0
	case 2b	400	37.4	36.3	22.4 - 32.4
		800	22.4	22.3	8.1 - 17.5
B	case 3a	400	-	-10.0	0.0 - 0.1
		800	-	-59.6	0.0 - 0.0
	case 3b	400	-	-5.8	0.0 - 0.4
		800	-	-54.1	0.0 - 0.0

a separation of the order of the wavelength, as it is based on a dense set of physically distinct propagation paths. Hence, an additional gain is obtained by selecting the antenna with the highest SINR. Further, channel equalization techniques with ISI/ICI cancellation [39, 69] can also reduce the multipath noise. In [70], interference cancellation based on ICI/ISI-aware beamforming is proposed. Finally, another strategy is more robust channel coding [39].

7.7 Conclusions

The effect of variations of both the received signal and the interference due to insufficient CP (i.e., multipath noise) over subsequent OFDM bursts is taken into account for slowly time-varying channels. The time-varying interference is described as a time-invariant, effective additive white Gaussian noise, which directly results into a loss factor. It is theoretically and experimentally motivated that this effective noise corresponds to the linear-scaled time-average of the interference power. Further, the spectral interference profile and the effective noise factor are analytically described in terms of the reverberation time based on the room electromagnetics theory. It is found that the frequency width of the spectral interference is typically of the order of the inverse of the reverberation time. Experimental validation is performed based on channel sounding in a large conference room. A loss factor up to 19 dB is found for IEEE 802.11 with a 800 ns CP and a 30 dBm transmit power, showing that the multipath noise may severely affect the system performance.

8

Path loss model and prediction of range, power and throughput for IEEE 802.11 in large conference rooms

In literature, both experimentally and theoretically determined propagation models have been reported for Wireless LAN in different indoor environments [30] - [36]. However, almost no path loss (PL) models can be found which are applicable for large conference rooms. The IEEE 802.11 TGn channel model could be applicable [29]. However, this model applies to very different types of environment (from residential to large space (indoors - outdoors)), and possibly does not take into account the specific geometry of large conference rooms (e.g., hemicycles). The path loss modeling in the TGac channel model is taken over from the TGn channel model [37].

In this chapter, a PL model for large conference rooms is determined, based on PL measurements. This model will be compared with the TGn channel model. Further, the influence of humans (during a meeting) on the PL model will be characterized. Based on the proposed PL model, the effect of typical IEEE 802.11n features (including frequency, bandwidth and MIMO antenna configuration) on the required number of access points, total power consumption (due to radiation) and maximum (physical) throughput will be investigated, with the focus on large conference rooms. This evaluation will be compared again with the TGn channel model.

The outline of this chapter is as follows. Section 8.1 describes the PL measurements. In Section 8.2, the PL models are presented and discussed, including the influence of the presence of humans. Section 8.3 gives an analysis of the influ-

ence of IEEE 802.11n features on the range, power consumption and throughput. Conclusions are provided in Section 8.4.

8.1 Measurement configurations and setups

8.1.1 Path loss measurement

The path loss measurements were carried out in a large conference room in the European Parliament in Brussels. This room has a hemicycle geometry and contains about 350 seats (Fig. 8.1). The height of the ceiling is 7 to 8 m. The measurements were done at frequencies 2.4 and 5.4 GHz, corresponding to the two bands for IEEE 802.11.

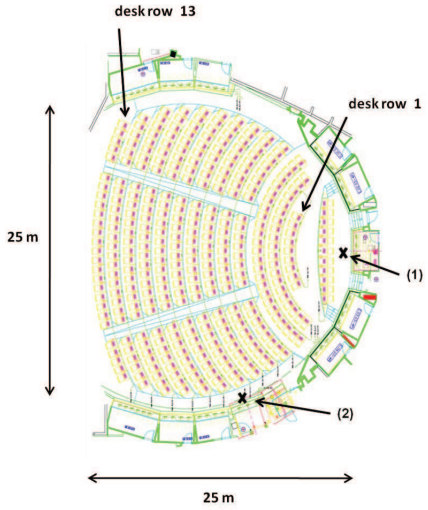

Figure 8.1: Plan of a conference room in the European Parliament (Brussels), where path loss measurements were carried out.

Two transmitter (Tx) positions are considered. The first one is near the centre of the hemicycle ((1) in Fig. 8.1), at a height of 2 m and at a distance of 1 m from the wall. The second position is at the side of the room ((2) in Fig. 8.1), at a height of 3.5 m and about 10 cm from the wall. The Tx positions were chosen to obtain a line-of-sight condition for all the seats. The receiver (Rx) was positioned just above the desks (i.e., the actual position of the clients). The measured trajectories, which the receiver moved along, included all rows of desks. The total length of all trajectories was about 285 m. The receiver was moved with a speed corresponding to averaged 6 samples per wavelength.

Note that the PL measurements were executed over an area with a large azimuth range (seen from the transmit antenna) up to 134°. As the transmit antenna was always positioned near the walls of the room, a variation of environment was achieved over the different azimuth angles. This contributes strongly to the representativeness of the measurement data sets and obtained PL models.

As measurement equipment at the Tx side, a Rohde & Schwarz signal gen-

erator SMJ100A is used, connected to an omnidirectional transmitting antenna (type MAT-JAYBEAM MA431Z00 for 2.4 GHz and European Antennas EVD2-5300/1285 for 5.4 GHz). The equipment at the Rx side included a receiving antenna (of the same type as Tx), connected to the Hewlett Packard spectrum analyzer 8561B, and a tachometer. The spectrum analyzer and the tachometer were connected to a laptop, which saved the received power and the distance along the Rx trajectory as a function of time.

During the measurements, no people were present in the room. There was no permission to execute measurements during meetings in the European Parliament. However, the presence of people may have an influence on the developed PL model.

8.1.2 PL measurement in a university auditorium

To investigate the influence of humans on the PL model, PL measurements were carried out in a university auditorium during a lecture and repeated in the absence of people. The area of this auditorium (Fig. 8.2) is $12\ \mathrm{m} \times 20\ \mathrm{m}$ and the height of the ceiling is $4.6\ \mathrm{m}$. There are 17 desk rows of 16 seats. During the lecture, about 80 people were present. The occupation of the seats was nearly homogeneous. The measurement equipment and the frequencies were the same as for the conference room in the European Parliament (Section 8.1.1). Tx was positioned in front of the auditorium (in the corner, $1.7\ \mathrm{m}$ from the walls) at a height of $2.2\ \mathrm{m}$ (Fig. 8.2). The height of Rx was $1.2\ \mathrm{m}$ (i.e., above the desks). The measured Rx trajectories were row 8, 11, 13 and 16 (Fig. 8.2). These rows were left unoccupied to provide passage of the measurement equipment.

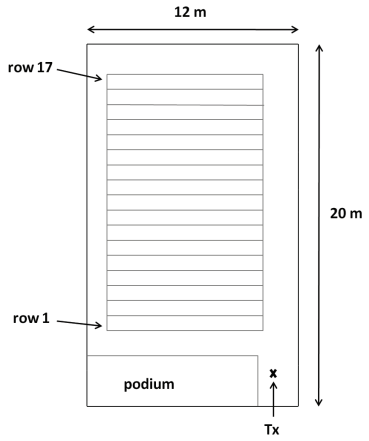

Figure 8.2: Plan of a university auditorium where path loss measurements were carried out.

8.2 Path loss model

8.2.1 Development of the path loss model

The path loss (PL) [dB] is determined as

$$\mathrm{PL} = -\langle P_\mathrm{R} \rangle + P_\mathrm{T} + G_\mathrm{T} + G_\mathrm{R} - L_\mathrm{T} - L_\mathrm{R}, \tag{8.1}$$

where $\langle P_\mathrm{R} \rangle$ is the averaged received power (P_R) [dBm], P_T is the transmit power [dBm], G_T (G_R) is the transmitter (receiver) gain [dBi], and L_T (L_R) is the transmitter (receiver) feeder loss [dB].

From the measurement data, the P_R samples and their corresponding position (distance along measured trajectory) are obtained. To calculate $\langle P_\mathrm{R} \rangle$, the P_R samples are averaged over a distance of 10λ, where λ is the wavelength, to cancel out small-scale fading [36].

During the measurements, a transmit power of 15 dBm is used. The losses of the cables are determined experimentally: L_T is 4.1 dB at 2.4 GHz and 7.6 dB at 5.4 GHz, L_R is 2.2 dB at 2.4 GHz and 3.5 dB at 5.4 GHz.

The gain (G) of the transmitter and receiver is expressed as follows:

$$G = G_\mathrm{max} + F(\theta), \tag{8.2}$$

where G_max is the (maximal) gain [dBi] in the horizontal plane, and $F(\theta)$ [dB], defined by $G - G_\mathrm{max}$, depends on the elevation angle, θ. It is necessary to consider an angle-dependent gain, since angles θ (between Tx and Rx) up to 47° are present (in the conference room in the European Parliament), and the 3 dB beamwidth is 40° and 80° for the 2.4 GHz and 5.4 GHz antenna, respectively. For the antennas used at 2.4 GHz, the values of G_max and $F(\theta)$ are available in the datasheet of the manufacturer. For the dipole antennas used at 5.4 GHz, G_max can be found in the datasheet, but there is no data available for $F(\theta)$. Therefore, $F(\theta)$ is determined by a theoretical approximation, applying to thin wire dipole antennas, proposed in [71]:

$$F(\theta) = 20 \log \left(\frac{\cos(k\,L\,\sin(\theta)) - \cos(k\,L)}{\cos(\theta)(1 - \cos(k\,L))} \right), \tag{8.3}$$

where k is defined by $2\pi/\lambda$, and $2L$ is the length of the antenna. The 3 dB beamwidth (available in the datasheet) allows to determine the parameter kL in Eq. 8.3: $kL = 1.426$.

The PL samples are calculated using Eq.8.1, in positions (along the trajectory) with a separation of $\lambda/40$ (i.e., as a moving average). PL models are determined for the large conference room (European Parliament) for the different cases (two frequencies, two Tx positions).

8.2.2 Path loss model: results and discussion

For the large conference room (European Parliament), the path loss [dB] is described as a function of the distance (d) [m] between Tx and Rx by a one-slope

model with one standard deviation, σ [dB]:

$$\mathrm{PL} = \mathrm{PL}_0 + 10\,n\,\log(d) + X_\sigma, \tag{8.4}$$

where PL_0 is the mean path loss at a distance of 1 m, n is the PL exponent and X_σ [dB] is a normally distributed variable with 0 dB median and standard deviation σ. These parameters, determined by the method of least squares, are shown in Table 8.1, as well as the Tx-Rx separation where the PL could be experimentally determined. The determined PL exponents vary from 1.2 to 1.7, which is lower than the free-space PL exponent of 2. This can be explained by reflections at the walls, the ceiling and the floor. This gives an additional, rather homogeneous contribution to the free-space received power, which lowers the PL exponent. The same explanation was given in [72], where PL exponents of 1.5 to 1.7 were reported for a class room. Also in [36], PL exponents of 1.3 to 1.7 were found in factory buildings for wood and metal processing (in line-of-sight condition) and attributed to multipath propagation.

Table 8.1: Parameters of PL model, based on PL measurements in a large conference room.

frequency	Tx position	n	PL_0 [dB]	d_{br} [m]	σ [dB]	considered Tx-Rx separation
2.4 GHz	front	1.4	43	3.9	2.0	5 - 24 m
	side	1.7	40	1.2	2.2	5 - 26 m
	all	1.6	42	2.5	2.1	
5.4 GHz	front	1.2	51	3.0	2.3	5 - 24 m
	side	1.2	53	4.9	2.2	5 - 27 m
	all	1.2	52	3.9	2.4	

For all cases, it is found that it is possible to describe the path loss accurately by a one-slope model with a standard deviation of about 2 dB. This is illustrated in Fig. 8.3, where percentiles as a function of the Tx-Rx distance (i.e., based on PL samples at a Tx-Rx distance varying over 4 m) are shown. The median can be modeled by a one-slope model, with a deviation less than 1 dB. The shift between the 75th percentile and the median is almost constant, which indicates a single standard deviation.

Assuming that, for a short Tx-Rx separation, the dominant path arriving at Rx is the line-of-sight path, the median of the PL samples should equal the free-space PL for short Tx-Rx separation (as also proposed in the TGn model [29]). In this case, it is useful to express the PL model with a breakpoint [29]:

$$\mathrm{PL} = \mathrm{PL}_{\mathrm{free},0} + 10\,n\,\log(d/d_{\mathrm{br}}) + X_\sigma, \tag{8.5}$$

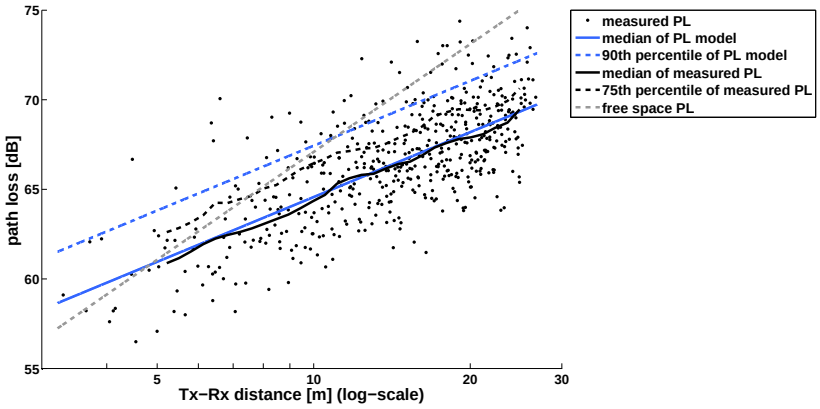

Figure 8.3: Measured PL and PL model in a large conference room (at 5.4 GHz*, Tx position at the side). Percentiles based on the measured PL samples show that the PL can be described accurately by a one-slope model with a single standard deviation. For clarity, only PL samples of positions separated by* 10λ *are shown.*

where d_{br} is the breakpoint distance [m] between Tx and Rx where the one-slope model intersects with the free-space path loss, and $\mathrm{PL}_{\mathrm{free},0}$ is the free-space path loss [dB] at distance d_{br}. The corresponding breakpoint parameters, shown in Table 8.1, vary from 1 to 5 m. These breakpoints are smaller than the minimal considered Tx-Rx separation of 5 m (Table 8.1), in agreement with the fact that the PL samples can be accurately modeled by a one-slope model.

The expression using a breakpoint (Eq. 8.5) gives more insight in the frequency (f) dependency of the PL model than the expression in terms of an intercept, PL_0. Firstly, the PL is proportional to λ^{-2} (where λ is the wavelength) via the term $\mathrm{PL}_{\mathrm{free},0}$ (first contribution). This is due to the interaction between the electromagnetic field and the antenna. Secondly, the frequency has also an influence on the interaction between the electromagnetic field and the environment, which is reflected in the path loss exponent, the breakpoint distance (i.e., transition from free-space PL to different attenuation mechanism) and σ (i.e., standard deviation due to large-scale fading) (second contribution). The influence of the frequency on these parameters is determined in Table 8.1. The two effects of the frequency on the PL have been compared by calculating the ratio, r, of the first and the second contribution:

$$r = \frac{20\ \log(5.4/2.4)}{\left|\mathrm{PL}_{5.4\ \mathrm{GHz}}(d) - \mathrm{PL}_{2.4\ \mathrm{GHz}}(d) - 20\ \log(5.4/2.4)\right|}, \tag{8.6}$$

where $\mathrm{PL}_{5.4\ \mathrm{GHz}}(d)$ and $\mathrm{PL}_{2.4\ \mathrm{GHz}}(d)$ are the 90th percentile PL [dB] at 5.4 GHz and 2.4 GHz, resp., calculated using the proposed PL models (Table 8.1) at a Tx-Rx separation d. This ratio (r) is found to be minimal 2.7 for Tx in front of the

room, and minimal 3.8 for Tx on the side. This shows that the first contribution (PL proportional to λ^{-2}) is stronger than the second one. This explains that the PL_0 values (listed in Table 8.1) are higher at 5.4 GHz than at 2.4 GHz.

According to the IEEE 802.11 TGn channel model [29], the PL can be modeled by the free-space PL for $d < d_{\mathrm{br}}$, and by a one-slope model with exponent 3.5 for $d > d_{\mathrm{br}}$. The TGn model predicts a breakpoint of 20 m for 'Large office' (type of environment 'E') and 30 m for 'Large space (indoors - outdoors)' (type of environment 'F'). Compared to the TGn channel model, the PL model proposed here has a lower breakpoint and a lower PL exponent for $d > d_{\mathrm{br}}$. This results in much lower PL values. This is illustrated in Fig. 8.4, where the proposed PL models (PL median) and the TGn PL models for types of environment 'E' and 'F' are shown for 2.4 GHz. The PL median of the proposed models is up to 6 dB and 8 dB lower than the PL median of the TGn model at 2.4 GHz and 5.4 GHz, respectively. Consequently, the range predicted by link budget analysis based on the proposed PL model is up to a factor 1.6 higher than the range based on the TGn model at 2.4 GHz (Fig. 8.4) and a factor 2.3 higher at 5.4 GHz. Assuming that the required number of access points (#AP) is inversely proportional to the square of the range, #AP decreases by a factor 2.7 and 5.1, resp., according to the proposed PL model. It can be concluded that the proposed PL model is significantly different compared to the TGn path loss model for range prediction in large conference rooms.

Besides the influence of the specific environment, the deviation between the proposed path loss model and TGn model can be possibly explained by the different way of de-embedding the antenna radiation pattern. The proposed model is developed by compensating the received power by the antenna gain in line-of-sight condition. However, in the case of multipath propagation, non-line-of-sight propagation paths generally have a different antenna gain. Consequently, when de-embedding the antenna gain per propagation path, a different path loss value may be obtained.

8.2.3 Influence of humans on the PL model

Based on the PL measurement in the university auditorium, one-slope PL models are obtained in the same way as described in Section 8.2.1. In Table 8.2, the parameters of these PL models are listed for the case of the empty room and the room with a lecture at 2.4 GHz and 5.4 GHz. Fig. 8.5 shows the median of these PL models. At 2.4 GHz, the PL exponent (n) during the lecture is almost a factor 2 higher than in the empty room (Table 8.2) and the intercept PL_0 is about 8 dB lower. The latter is due to a higher PL exponent, while the PL during the lecture intersects with the PL in the empty room at a Tx-Rx separation of about 10 m (Fig. 8.5). At 5.4 GHz, the deviation of the PL median between the lecture and the empty room is smaller than 0.5 dB (Fig. 8.5), which is negligible for range prediction. At both 2.4 GHz and 5.4 GHz, the difference of the standard deviation (σ) between the lecture and the empty room is also negligible (< 0.2 dB) (Table 8.2).

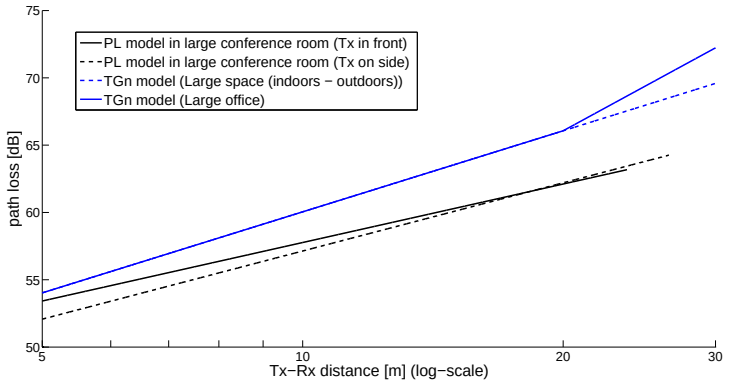

Figure 8.4: Comparison of proposed PL models (PL median), developed for conference rooms, with the TGn PL models for 'Large office' and 'Large space (indoors - outdoors)' at 2.4 GHz.

These findings can be explained as follows. At 2.4 GHz, the PL exponent in the empty room is lower than the free-space PL exponent (i.e., 2) due to multipath propagation (as mentioned before). In the presence of humans, the PL exponent increases towards 2 due to the absorption by the human body (Table 8.2). This occurs from a Tx-Rx separation of about 10 m (Fig. 8.5). This might be related to the Tx-Rx separation at which the crowded area starts. During the lecture, the minimal distance between Tx and the humans was about 4 m. At 5.4 GHz, the PL exponent in the empty room is about 2 (Table 8.2), which is almost the same during the lecture.

For the large conference room in the European Parliament, it can be similarly expected that the attenuation increases in the crowded area, which results in a higher PL exponent (towards 2). Consequently, the intercept PL_0 is expected to decrease in the presence of humans, since the minimal distance between Tx and the humans is larger than 1 m.

Table 8.2: Parameters of PL model in a university auditorium in the absence of humans and during a lecture at 2.4 GHz *and* 5.4 GHz.

		n	PL_0 [dB]	σ [dB]
2.4 GHz	empty room	0.99	47.7	0.94
	lecture	1.76	39.8	0.91
5.4 GHz	empty room	2.04	43.4	1.15
	lecture	1.88	45.4	1.32

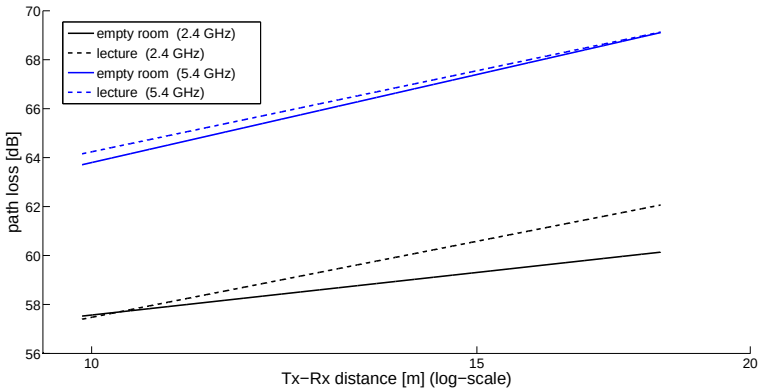

Figure 8.5: PL model in a university auditorium in the absence of humans and during a lecture at 2.4 GHz *and* 5.4 GHz.

8.3 Range, power consumption and throughput of IEEE 802.11n in large conference rooms

8.3.1 Calculation of the range, number of access points and power consumption

In this section, an evaluation of the following parameters is made, with the focus on large conference rooms: SISO (Single-Input Single-Output) vs. MIMO 2×2:1 / MIMO 2×2:2 (i.e., one and two spatial streams, resp.), 2.4 GHz vs. 5 GHz band and 20 vs. 40 MHz bandwidth. The evaluated parameters are the required number of access points (#AP), the required total radiated power consumption (P) and the maximum possible (physical) throughput ($\mathrm{TP}_{\max}$). The evaluation is based on the TGn model as well as the proposed PL model, which allows to thoroughly compare the two models. It is assumed that the access points are positioned according to a fixed range, which is achieved by tuning the transmit power. A guard interval of 800 ns is considered. The data rate varies from 6.5 Mbps (BPSK 1/2) to 65 Mbps (64-QAM 5/6) for SISO or MIMO 2×2:1 and from 13 Mbps (BPSK 1/2) to 130 Mbps (64-QAM 5/6) for MIMO 2×2:2 [73].

The evaluation is based on link budget analysis [74]:

$$P_{\mathrm{T}} - P_{\mathrm{R,sens}} + G_{\mathrm{T}} + G_{\mathrm{R}} - L_{\mathrm{T}} - L_{\mathrm{R}} = \mathrm{PL}_{\mathrm{med}}(R) + M_{\mathrm{S}} + M_{\mathrm{F}}, \qquad (8.7)$$

where $P_{\mathrm{R,sens}}$ is the receiver sensitivity [dBm], $\mathrm{PL}_{\mathrm{med}}(\,\cdot\,)$ is the (median) PL model as a function of the Tx-Rx distance, R [m] is the range, M_{S} [dB] is the shadowing margin and M_{F} [dB] is the temporal fading margin. The required number of access points (#AP) is then calculated as

$$\#\mathrm{AP} = S/(\pi R^2), \qquad (8.8)$$

where S [m^2] is the area of the room. The required total power consumption, P [mW], due to radiation, is calculated as

$$P = \#\mathrm{AP}\, P_{\mathrm{T}}. \qquad (8.9)$$

For the calculations, receiver sensitivities of an IEEE 802.11n reference receiver are used, as specified in the IEEE 802.11n standard [26]. Compared to SISO, the sensitivities are decreased by 6 dB for MIMO 2×2:1 (due to diversity gain) and are assumed to be the same for MIMO 2×2:2 [75]. Compared to a bandwidth of 20 MHz, the sensitivities are increased by 3 dB for 40 MHz.

The calculation is done for a G_{T} (G_{R}) of 2 dBi and a L_{T} (L_{R}) of 0 dB. A 5.8 dB margin for temporal fading is used (95% temporal availability), based on K-factors varying from -12 dB to -6 dB, as proposed in [76] for large office environments. A coverage percentage of 90% is considered to determine M_{S} [28].

In the evaluation, the maximum allowed EIRP (Equivalent Isotropically Radiated Power) in Europe is taken into account. This is 20 dBm in the 2.4 GHz band. In the 5 GHz band, this is 23 dBm up to channel 64 (further referred to as "5.2 GHz" band) and 30 dBm from channel 100 (further referred to as "5.5 GHz" band) [77] [68]. Channels 65 to 99 are not used in IEEE 802.11n.

8.3.2 Results and discussion

These calculations allow to make an evaluation as shown in Tables 8.3 and 8.4. Both tables apply to 2.4 GHz, SISO, 20 MHz bandwidth and a 30 m fixed range (unless otherwise mentioned in the tables). The results in Table 8.3 are obtained using the TGn model for environment 'E' ('Large office') as well as 'F' ('Large space (indoors - outdoors)'). The results in Table 8.4 are calculated using the proposed PL model (Table 8.1), considering two different Tx positions. Note that for 5.2 GHz and 5.5 GHz, the PL model for 5.4 GHz is adjusted according to the (linear-scaled) PL varying proportional to f^2 (Section 8.2.2).

*Table 8.3: The effect of different link parameters on #AP, total radiated power consumption (P) (expressed by a multiplication factor) and $\mathrm{TP}_{\max}$, assuming a fixed range of 30 m (unless otherwise mentioned). This calculation is based on the **TGn model** for environment 'E' and 'F', resp. (indicated by (1)).*

	#AP	P [mW]	$\mathrm{TP}_{\max}$ [Mbps]
2.4 → 5.2 GHz	=	× 4.7	65 → 39 – 58.5 (1)
2.4 → 5.5 GHz	=	× 5.3	65 → 65
SISO → MIMO 2×2:1	=	× 0.25	65 → 65
SISO → MIMO 2×2:2	=	=	65 → 130
20 → 40 MHz	=	× 2.0	65 → 81 – 135 (1)
range: 30 → 15 m	× 4	× 0.35 – 0.41 (1)	65 → 65

*Table 8.4: The effect of different link parameters on #AP, total radiated power consumption (P) (expressed by a multiplication factor) and $\mathrm{TP}_{\max}$, assuming a fixed range of 30 m (unless otherwise mentioned). This calculation is based on the **proposed PL model** for the two Tx positions: in front and at the side, resp. (indicated by (1)).*

	#AP	P [mW]	$\mathrm{TP}_{\max}$ [Mbps]
2.4 → 5.2 GHz	=	× 2.7 – 3.3 (1)	65 → 65
2.4 → 5.5 GHz	=	× 2.7 – 3.3 (1)	65 → 65
SISO → MIMO 2×2:1	=	× 0.25	65 → 65
SISO → MIMO 2×2:2	=	=	65 → 130
20 → 40 MHz	=	× 2.0	65 → 135
range: 30 → 15 m	× 4	× 1.5 – 1.2 (1)	65 → 65

8.3.2.1 Effect of the frequency

At a higher frequency (5.2 / 5.5 GHz vs. 2.4 GHz), the required total radiated power consumption (P) [mW] increases by a factor 3 to 5 (for the same modulation type) (Tables 8.3 and 8.4). Indeed, at a higher frequency, there is a higher PL, which requires a higher transmit power (P_{T}) to maintain the same range. The PL increases with the frequency, due to the interaction between electromagnetic field and antenna (i.e., linear-scaled PL proportional to f^2), which has a stronger effect than the interaction between electromagnetic field and environment (Section 8.2.2). The latter explains the different effect on the radiated power consumption according to the TGn model (with a multiplication factor of 5 approximately) and the proposed PL model (with a multiplication factor of 3 approximately).

A higher frequency (5.2 / 5.5 GHz vs. 2.4 GHz) has two different effects on the maximum possible throughput ($\mathrm{TP}_{\max}$). Firstly, due to the higher PL at a higher frequency, a higher transmit power (P_{T}) is required for a certain MCS. When this transmit power exceeds the maximum allowed radiated power, this MCS is no longer possible and $\mathrm{TP}_{\max}$ decreases. Secondly, the maximum allowed radiated power is higher at a higher frequency, which can have an increasing effect on $\mathrm{TP}_{\max}$. The total effect on $\mathrm{TP}_{\max}$ can be decreasing or increasing. According to the TGn model (Table 8.3), $\mathrm{TP}_{\max}$ at 5.2 GHz is lower than at 2.4 GHz. This decrease of $\mathrm{TP}_{\max}$ is stronger for environment 'E' than for 'F' due to the higher PL (Section 8.2.2). Compared to 2.4 GHz, $\mathrm{TP}_{\max}$ keeps the maximum value of 65 Mbps at 5.5 GHz. This is due to the EIRP limit of 30 dBm, which is higher than the 23 dBm limit at 5.2 GHz. According to the proposed PL model (Table 8.4), $\mathrm{TP}_{\max}$ keeps the maximum value of 65 Mbps at both 5.2 and 5.5 GHz. This can be explained by the lower PL according to the proposed PL model.

8.3.2.2 Effect of configuration and bandwidth

According to the TGn model and the proposed PL model, the total radiated power consumption (P) [mW] decreases by a factor 4 for MIMO 2×2:1 (vs. SISO) (Tables 8.3 and 8.4). P remains unchanged for MIMO 2×2:2 (vs. SISO) and increases by a factor 2 for 40 MHz bandwidth (vs. 20 MHz). Indeed, from Eqs. 8.7 and 8.9, and taking into account that the number of access points (#AP) is fixed, it is clear that the increase of P [dBm] equals the increase of the receiver sensitivity ($P_{\mathrm{R,sens}}$ [dBm]), irrespective of the PL model.

Compared to SISO, MIMO 2×2:1 can generally result in an increased $\mathrm{TP}_{\max}$, when for SISO, the required transmit power (to obtain the fixed range) exceeds the maximum allowed radiated power. Indeed, the lower sensitivity $P_{\mathrm{R,sens}}$ of MIMO 2×2:1 allows to achieve the fixed range using a lower transmit power. In particular, it can be seen in Tables 8.3 and 8.4 that the maximum data rate of 65 Mbps remains unchanged. Compared to SISO, $\mathrm{TP}_{\max}$ doubles for MIMO 2×2:2, due to the two spatial streams (multiplexing).

A higher bandwidth (40 MHz vs. 20 MHz) has two different effects on the maximum possible throughput $\mathrm{TP}_{\max}$. Firstly, $\mathrm{TP}_{\max}$ increases approximately by

a factor 2 (e.g., from 65 to 135 Mbps). Secondly, the higher receiver sensitivity can have a decreasing effect on $\mathrm{TP}_{\max}$ (as explained before). The latter effect occurs according to the TGn model (environment 'E') (Table 8.3), while this effect does not occur according to the proposed PL model (Table 8.4). This different prediction can be explained by the lower PL according to the proposed PL model.

8.3.2.3 Effect of the range

For a lower fixed range of 15 m (vs. 30 m), the required number of access points increases by a factor 4 (Eq. 8.8). The total radiated power (P) decreases (by a factor 2.4 to 2.9) according to the TGn model, while P increases (by a factor 1.2 to 1.5) according to the proposed PL model. This can be explained as follows. From Eq. 8.7, it is clear that the transmit power [mW] is proportional to R^n, where R is the range and n the PL exponent. Consequently, it follows from Eqs. 8.8 and 8.9 that P is proportional to R^{n-2}. Thus, a higher fixed range (R) has an increasing (decreasing) effect on P, when the PL exponent n is higher (lower) than 2. According to the TGn model, the PL exponent is 2 to 3.5, which indeed results in an increasing effect on P (for increasing range). According to the proposed PL model, the PL exponent is lower than 2 (Table 8.1), which results in a decreasing effect on P (for increasing range).

A lower fixed range can generally result in an increased maximum possible throughput $\mathrm{TP}_{\max}$. However, in this case, the maximum data rate of 65 Mbps remains unchanged (Tables 8.3 and 8.4).

The mentioned contradiction between the two PL models on the power consumption is further illustrated in Figs. 8.6 and 8.7, which show the required total radiated power consumption (P) as a function of the transmit power (P_{T}) according to the TGn model (environment 'F') and the proposed PL model (Tx position in front), respectively. The calculation is done for 2.4 GHz and 5.5 GHz, SISO, 20 MHz bandwidth, modulation scheme 64-QAM 5/6 (65 Mbps) and an area of $10,000$ m^2 (very large hall). The calculation is based on Eqs. 8.7 – 8.9, where the number of access points (#AP) has been rounded up to an integer. It can be seen that there is indeed an overall increasing or stagnating trend of P vs. P_{T} according to the TGn model (Fig. 8.6) and an overall decreasing trend according to the proposed PL model (Fig. 8.7). Indeed, since P_{T} [mW] is proportional to R^n, it is clear from Eqs. 8.8 and 8.9 that P is proportional to $P_{\mathrm{T}}^{-2/n+1}$. Consequently, the overall trend is increasing (or stagnating) for a PL exponent higher than (or equal to) 2 (TGn model) and decreasing for a PL exponent lower than 2 (proposed PL model). The effect of rounding up the number of access points (i.e., the tooth profile in Figs. 8.6 and 8.7) can be explained as follows. First, P [mW] increases linearly with increasing P_{T} [mW], because the number of access points remains constant. Then, when the range has been increased sufficiently so that one access point can be left out, P falls back to the $P_{\mathrm{T}}^{-2/n+1}$ relationship (Figs. 8.6 and 8.7). This effect is negligible when the number of access points is sufficiently high (i.e., for low P_{T}) (Figs. 8.6 and 8.7). Note that when only one access point is required (i.e., for sufficiently high P_{T}), P [mW] increases linearly with P_{T} [mW] (e.g.,

Fig. 8.7).

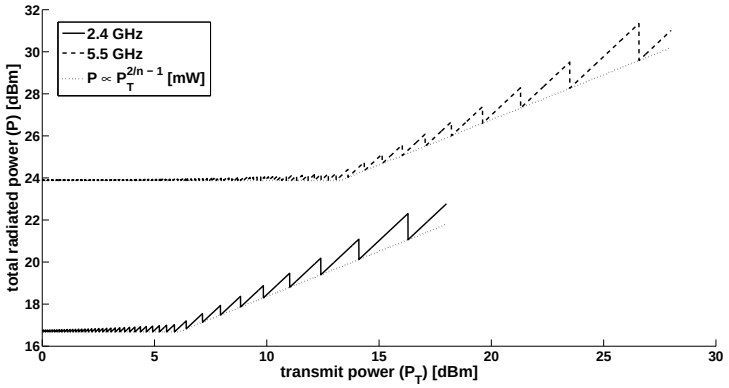

*Figure 8.6: Total radiated power consumption (P) as a function of the transmit power (P_{T}) at the 2.4 GHz and 5.5 GHz band. The calculation is based on the **TGn model**. An overall stagnating or increasing trend of P vs. P_{T} is found. The dotted line indicates the overall trend (P [mW] proportional to $P_{\mathrm{T}}^{-2/n+1}$).*

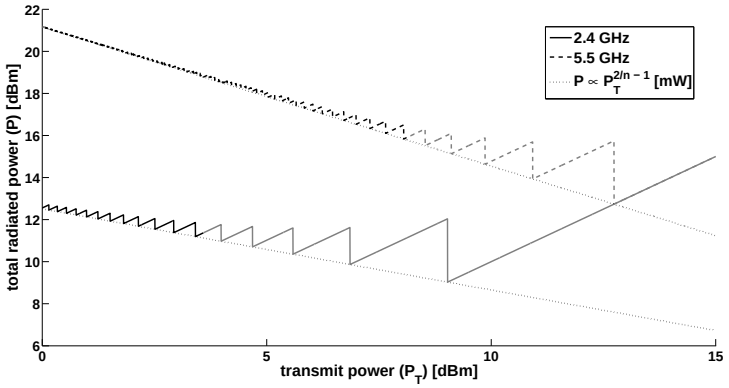

*Figure 8.7: Total radiated power consumption (P) as a function of the transmit power (P_{T}) at the 2.4 GHz and 5.5 GHz band. The calculation is based on the **proposed PL model**. An overall decreasing relation of P vs. P_{T} is found. The dotted line indicates the overall trend (P [mW] proportional to $P_{\mathrm{T}}^{-2/n+1}$). The grey line indicates that the PL model is out of the region where the PL could be experimentally determined.*

8.3.3 Summary

Finally, this evaluation can be summarized as follows. At a higher frequency (5.2 / 5.5 GHz vs. 2.4 GHz), a higher total radiated power (P) is required. The effect on the maximum possible throughput ($\mathrm{TP}_{\max}$) can be decreasing or increasing (due to a higher EIRP limit at a higher frequency). A MIMO 2×2 configuration has only advantages: a lower P and a possibly higher $\mathrm{TP}_{\max}$ when using MIMO 2×2:1, a doubled $\mathrm{TP}_{\max}$ and an unchanged P when using MIMO 2×2:2. A higher bandwidth (40 MHz vs. 20 MHz) requires a higher P and may have an additional decreasing effect on the doubled $\mathrm{TP}_{\max}$. A higher fixed range requires a lower number of access points, but can have a decreasing effect on $\mathrm{TP}_{\max}$. The effect on P can be decreasing or increasing, depending on the PL exponent.

8.4 Conclusions

A path loss (PL) model is developed for IEEE 802.11 in large conference rooms based on PL measurements. The PL can be described accurately by a one-slope model. In the absence of humans, PL exponents varying from 1.2 to 1.7 are found, which is lower than the PL exponents proposed by the TGn channel model (2 to 3.5). Based on PL measurements in the presence of humans, the PL exponent increases towards 2.

The effect of the frequency (2.4 / 5 GHz), configuration (SISO vs. MIMO 2×2) and bandwidth (20 MHz vs. 40 MHz) on the required number of access points, total radiated power consumption, and maximum (physical) throughput has been investigated. This has been done by link budget calculation, based on the proposed PL model as well as the TGn channel model.

The predictions of the two PL models differ essentially in two aspects. Firstly, the TGn model predicts limitations on the maximum throughput at a (fixed) range of 30 m, while the proposed PL model does not. This is due to a lower PL according to the proposed PL model. Secondly, according to the TGn model, a higher (fixed) range requires a higher (or unchanged) radiated power consumption, while the proposed PL model predicts a lower required power consumption. This is due to a PL exponent higher than (or equal to) 2 according to the TGn model and a PL exponent lower than 2 according to the proposed PL model. The proposed PL model can be used as a refinement of the TGn/ac channel model specifically for large conference rooms.

9

Conclusions, applications and future work

9.1 Conclusions

9.1.1 Interference due to insufficient CP: detection methodology based on frequency-domain channel sounding

9.1.1.1 Time window

For IEEE 802.11, where the FFT duration is typically much larger than the reverberation time of an indoor channel, the delay interval causing interference can be shortened by cutting off the weighting function, resulting into a smaller required time window. Based on the room electromagnetics theory, a parametric analysis shows that, to suppress the relative error power below -14 dB, the cut-off must be applied at a delay exceeding the CP length by at least 6.6 times the reverberation time. This requirement is most critically determined by the Fourier-type interference coefficient at a zero subcarrier separation, which is the most important spectral interference term. Experimental validation of this theoretical requirement is provided based on a measured indoor channel.

9.1.1.2 Windowing methods and window-related errors

The following windowing methods are presented in this dissertation, classified depending on the window positioning and the profile. Methods of type I and II are based on a fixed and moving window, resp., and on a conventional weighting function, which is dependent on both the source and the detecting subcarrier for the Fourier-type interference coefficient. For method types I and II, a Hann window (method *I-Hann* and *II-Hann*, resp.) and a rectangular window are considered (method *I-rect* and *II-rect*, resp.). In addition, a Hann window with window correction is studied (method *I-HC* and *II-HC*, resp.). Method type III, which is introduced in this dissertation, is based on the decomposition of the Fourier-type interference coefficient in terms of a generalized (frequency-dependent) interference coefficient, which is evaluated at the source and detecting subcarrier separately. For method type III, a Hann and a rectangular window are considered (*III-Hann* and *III-rect*, resp.).

Based on a channel measurement in a large exposition hall, the performance of the windowing methods is evaluated with respect to the measurement range requirement for a 241 MHz frequency band. The required measurement range is determined from a convergence analysis procedure specifically for the window-related error types only, i.e., due to (i) non-uniform windowing, (ii) a non-zero time resolution and (iii) direct and aliased leakage. To determine the *spectral* interference, method III-Hann is found most appealing, especially for a higher bandwidth (e.g., 160 MHz). Only an excess measurement range due to the resolution error is required, which is of the order of the inverse of the reverberation time. Other methods based on a Hann window require an excess of the order of the bandwidth (methods II-Hann, I-HC, II-HC) or even the frequency band (method I-Hann) due to the error of non-uniform windowing. Proportionality factors are determined

experimentally. Methods using a rectangular window suffer from leakage for a higher CP, which is most critically determined by the spectral Fourier-type interference coefficient at a zero subcarrier separation (i.e., the most important spectral term). In the case studied, method I-rect requires an excess measurement range of 661 MHz for 800 ns CP.

To determine the *total* interference, method III-Hann is also very attractive. Methods II-Hann and I-HC are very useful too, requiring an excess measurement range of the order of the spectral interference width. Typically, this is of the order of the inverse of the reverberation time. Note that method I-HC is less attractive to determine the interference as a function of the frequency because of a non-uniformly distributed error. Other methods based on a Hann window still require an excess of the order of the bandwidth (method II-HC) or the frequency band (method I-Hann). Methods using a rectangular window may suffer from leakage, especially at a higher CP. In the case studied, method I-rect requires an excess measurement range of 321 MHz for 800 ns CP.

For the error due to a non-zero time resolution, an estimation for the relative error power is derived for the correction-type coefficient based on the room electromagnetics theory. This theoretical error power serves as a reference for the Fourier-type coefficient, for which the resolution error power is typically strongly reduced for a small subcarrier separation. Using a Hann window (without window correction) or method III-rect, the resolution error power is found inversely proportional to the product of the reverberation time and the window width. For method III-Hann and III-rect, the proportionality factor is -6.5 dB and -6.7 dB, respectively. However, for methods I-rect and II-rect, the resolution error power is rather determined by the excess of the window with respect to the evaluation frequency, than to the window width itself. Interestingly, the window width required to suppress the resolution error becomes smaller when the reverberation time is larger, i.e., when the interference becomes more significant. Experimental verification based on a measured indoor channel shows that the theoretical error power is a good order estimation.

The limitations on the measurement range requirement through leakage are more generally investigated in terms of a maximum measurable signal-to-interference ratio ($\mathrm{SIR}_{\max}$), defined based on the total interference power originating from any OFDM symbol (i.e., including ISI and ICI). To measure an interference power as low as the thermal noise level, $\mathrm{SIR}_{\max}$ should not be smaller than the signal-to-noise ratio (SNR) that is actually detected by the OFDM receiver. To reach a $\mathrm{SIR}_{\max}$ of 100 dB, method III-Hann requires for 400 ns CP a window width of 79 MHz and 53 MHz for direct and aliased leakage, resp., and 46 MHz and 162 MHz for 800 ns CP. In contrast, the performance of methods using a rectangular window is dramatically poor and the improvement through increasing the window width is slight. For method I-rect, even an extremely high window width of 1500 MHz results into $\mathrm{SIR}_{\max}$ limitations of 65 dB and 60 dB due to direct and aliased leakage, resp., for 400 ns CP and 67 dB and 50 dB, resp., for 800 ns CP.

9.1.1.3 Measurement noise

The influence of the windowing methods on the error power due to measurement noise is investigated experimentally. It is found that in the range of convergence (i.e., for a measurement range larger than the requirement based on window-related errors), there is largely no essential influence. Further, the measurement error is investigated spectrally, showing that (for IEEE 802.11) the Fourier-type interference coefficient at a zero subcarrier separation is most critical to suppress the measurement noise by averaging of the channel reponse. Finally, the inversely proportional relationship between the measurement error power and the number of sweeps is experimentally validated for 800 ns CP, providing a practical procedure to determine the required number of sweeps for averaging.

9.1.1.4 Processing time

The performance of the windowing methods is also investigated with respect to the processing time required to determine the interference coefficient. It is found that especially for a high bandwidth, the total processing time for method type III is much lower than for type I and II at a realistic measurement range. At the *required* measurement range, the processing time for method III-Hann is found to be largely two orders of magnitude lower than for the other methods.

9.1.2 Interference due to insufficient CP: effective noise and relation with reverberation time

The effect of variations of both the received signal and the interference due to insufficient CP (i.e., multipath noise) over subsequent OFDM bursts is taken into account for slowly time-varying channels. The time-varying interference is described as a time-invariant, effective additive Gaussian noise, which directly results into a loss factor. It is theoretically and experimentally motivated that this effective noise corresponds to the linear-scaled time-average of the interference power. Further, the spectral and the total interference are analytically described in terms of the reverberation time based on the room electromagnetics theory. It is found that the spectral interference width is typically of the order of the inverse of the reverberation time. Experimental validation is performed based on channel sounding in a large conference room. A loss factor up to 19 dB is found for 800 ns CP and a 30 dBm transmit power, showing that the interference due to insufficient CP may severely affect the system performance.

9.1.3 Path loss modeling in large indoor environments

A path loss (PL) model is developed for IEEE 802.11 in large conference rooms based on PL measurements. The PL can be described accurately by a one-slope model. In the absence of humans, PL exponents varying from 1.2 to 1.7 are found, which is lower than the PL exponents proposed by the TGn channel model (2 to

3.5). Based on PL measurements in the presence of humans, the PL exponent increases towards 2.

The effect of the frequency (2.4 / 5 GHz), configuration (SISO vs. MIMO 2×2) and bandwidth (20 MHz vs. 40 MHz) on the required number of access points, total radiated power consumption, and maximum (physical) throughput has been investigated. This has been done by link budget calculation, based on the proposed PL model as well as the TGn channel model. The predictions of the two PL models differ essentially in two aspects. Firstly, the TGn model predicts limitations on the maximum throughput at a (fixed) range of 30 m, while the proposed PL model does not. This is due to a lower PL according to the proposed PL model. Secondly, according to the TGn model, a higher (fixed) range requires a higher (or unchanged) radiated power consumption, while the proposed PL model predicts a lower required power consumption. This is due to a PL exponent higher than (or equal to) 2 according to the TGn model and a PL exponent lower than 2 according to the proposed PL model. The proposed PL models can be used as a refinement of the TGn/ac channel model specifically for large conference rooms.

9.2 Applications and future work

9.2.1 Characterization of the interference due to insufficient CP

A complete measurement procedure based on frequency-domain channel sounding is developed for accurate detection of the interference due to insufficient CP for OFDM over time-dispersive and slowly time-varying channels. The measurement procedure is in principle applicable to general OFDM technologies, as far as frequency domain channel sounding is practically feasible. E.g., for IEEE 802.11ad (at 60 GHz), a VNA-based setup may be no longer adequate due to the need for a phase-stable cable between Tx and Rx and wideband channel sounding with synchronization or stable clock references may be needed. Compared to IEEE 802.11a/g/n/ac, some differences should be taken into account for IEEE 802.11ad, which has a 194 ns FFT period and a 48.4 ns CP length [16]. Firstly, more ISI terms (between non-consecutive OFDM symbols) may become important and the overall weighting function for the total interference will tend to a more uniform profile. Secondly, the theory of room electromagnetics may be not applicable from an excess delay as small as the CP length.

Although the proposed characterization procedure is based on frequency-domain channel sounding, there are also implications on time-domain channel sounding based on (time-domain) cross-correlation. Based on the frequency domain, the issue of the time resolution and the dynamic range is dealt with by the windowing method. For time-domain channel sounding, the autocorrelation function of the pseudo-random sequence is equivalent to the (continuous) inverse Fourier transform of the window for frequency-domain channel sounding. In both cases, the channel impulse response (i.e., complex envelope) is detected as a convolution of the actual (baseband) channel impulse response and the aforementioned time-domain pulse. Firstly, this implies that, to determine the spectral interference due to insufficient CP over a given frequency band, the spectrum of the pseudo-random sequence should properly cover the frequency band with a certain excess of the order of the inverse of the reverberation time. This is needed to ensure a sufficiently small time resolution, including near the edges of the frequency band. Secondly, the chip size (L) should be sufficiently large to obtain the required time window. Thirdly, the chip size should be large enough to achieve a sufficiently large dynamic range. As the dynamic range for an *m*-sequence equals $20\log(L)$ [59], the maximum SIR limitation ($\mathrm{SIR}_{\max}$) varies (in linear scale) proportional to L^2, assuming that the time window exceeds the (fixed) interference delay interval. This may result in a high required chip size (i.e., of the order of 10^4 or higher), which imposes high sequence generator requirements and a time window (i.e., proportional to L) exceeding many times the actual required time window of interest.

The proposed characterization procedure allows frequency-dependent monitoring of the signal-to-interference-plus-noise ratio (SINR) including multipath noise (Section 2.5), which is a performance metric with respect to the channel

capacity [78] and is related to the EVM specifications in physical standards [26]. Using windowing method III-Hann, this is possible over a large frequency band (e.g., with a width of the order of GHz) with an excess measurement range only of the order of the inverse of the reverberation time. Other important characteristics based on the frequency-dependent received signal power and interference power are the (i) signal-to-interference ratio (SIR), indicating the maximum achievable channel capacity (i.e., for an arbitrarily large transmit power), (ii) the SINR loss (compared to the situation without multipath noise), which corresponds essentially to the loss factor (Section 7.1) and (iii) the multipath noise factor (Section 7.1), describing the multipath noise in reference to the thermal noise level. Note that the SIR is independent on the transmit power, contrary to the SINR, the loss factor and the multipath noise factor.

These characteristics allow to optimize several system parameters. Firstly, it contributes to better CP selection for realistic channels by optimization of the channel capacity, which is based on the SINR and the loss factor due to CP-related overhead [18]. Secondly, the effect of the antenna radiation pattern can be evaluated in terms of the SINR, investigating e.g., the potential interference mitigation effect of beamforming. The loss factor due to insufficient CP can be included in link budget analysis, which is important for better network planning and transmit power control (Section 9.2.2).

9.2.2 Implications to link budget analysis

In link budget analysis, the range for a certain modulation and coding scheme is determined based on the requirement that the outage probability (with respect to a given PER) is lower than a critical value, being typically about 5% [28]. When describing the multipath noise by an effective noise factor, the statistics of the instantaneous SINR remain unchanged for a CDF level lower than about 50%, as found in Chapter 7. As the critical outage probability falls within this range, the concept of the effective noise is applicable to link budget analysis. Therefore, the corresponding loss factor, L_{delay} (Eq. 7.12), can be included in the link budget relation (Eq. 8.7) as an additional margin.

The effect of including the loss factor due to multipath noise in link budget analysis can be described based on Fig. 9.1, which shows schematically the range as a function of the transmit power. As the effective noise factor is proportional to the transmit power (Eq. 7.14), the effect of the multipath noise is negligible for a sufficiently small transmit power. In this case, the range (R) increases with the transmit power (P_{T} [mW]) according to $R \propto P_{\mathrm{T}}^{1/n}$, where n is the path loss exponent. For a sufficiently high transmit power, the effective noise factor ($F_{\mathrm{delay,eff}}$) becomes more dominant than the conventional noise factor (F_{AWGN}) due to hardware-related impairments and thermal noise. In this case, the SINR remains unchanged when increasing the transmit power and consequently, the reception quality and the range as well.

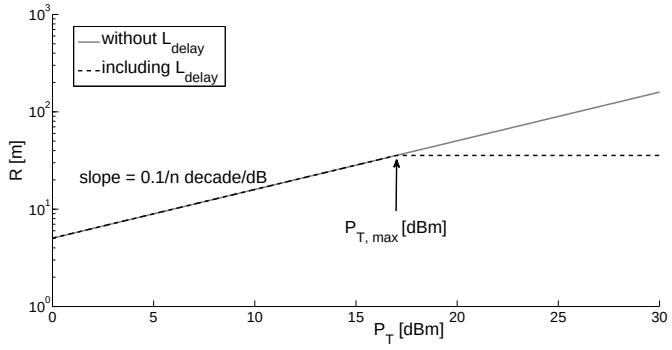

Figure 9.1: A schematical plot of the range (R) as a function of the transmit power (P_{T}) based on link budget analysis without and including the loss factor due to multipath noise (L_{delay}). The range increases with P_{T} according to the path loss exponent (n). As a result of the loss factor, there is a stagnation of the range from a certain transmit power ($P_{\mathrm{T,max}}$).

Realistic $P_{\mathrm{T,max}}$ values may be lower than the maximum allowed EIRP[1]. For conference room A (Chapter 7) and considering an F_{AWGN} of 15 dB, a $P_{\mathrm{T,max}}$ of -1 dBm and 13 dBm is found for 400 ns and 800 ns CP, respectively. These values are smaller than the maximum allowed EIRP for WLAN application, being 20 dBm in the 2.4 GHz band and $23/30$ dBm in the 5 GHz band [68]. Thus, the multipath noise may have an important influence on transmit power control. From a certain level ($P_{\mathrm{T,max}}$), increasing the transmit power no longer provides an improvement of the reception quality and the range remains unchanged. Further increasing of the transmit power would only result into a higher power consumption and an increased co-channel and adjacent channel interference.

9.2.3 Implications to channel modeling

A complete channel model should include channel components with an excess delay larger than the CP length. For IEEE 802.11a/g/n/ac indoors, the time window should be extended over an excess delay of at least 6.6 times the reverberation time to reproduce the spectral interference power with a deviation smaller than 1 dB (Section 3.8). A loss factor due to insufficient CP up to 19 dB was detected in a large conference room at 800 ns CP and a 30 dBm transmit power (Section 7.6), showing that the multipath noise may considerably affect the system performance. Based on the analytical expression for the multipath noise factor (Section 7.2) and a 30 dBm transmit power, the noise factor already exceeds 10 dB when the reverberation time is larger than 44 / 78 ns for 400 / 800 ns CP, resp. , which are realistic values for indoor scenarios.

The channel components with an excess delay larger than the CP length can be

[1] Equivalent Isotropically Radiated Power

modeled based on an exponentially decaying APDP with uncorrelated Rayleigh fading, as far as the room electromagnetics theory is applicable (Section 1.1.1.2). As the analytical determination method of the interference (Section 7.2), based on the room electromagnetics theory, has been experimentally validated (Section 7.5), this motivates that the room electromagnetics theory is applicable to properly model the interference due to insufficient CP for IEEE 802.11 indoor channels. However, it should be noted that the room electromagnetics theory requires that the time-domain channel is sufficiently dense compared to the time resolution. From a window width of 200 MHz, it has been observed that the APDP tail may show a specular structure instead of a purely exponential decay (Fig. 6.3 in Section 6.2). For channel modeling over a higher frequency band, the room electromagnetics theory could be applied with respect to a moving window with a limited window width, resulting into a frequency-dependent reverberation time and multipath intensity factor.

9.2.4 Implications to frequency-domain equalization

The proposed interference characterization method also allows the detection of the spectral interference between all individual OFDM symbols and subcarriers. The spectral (frequency-averaged) interference power profile is an important characteristic with respect to frequency-domain equalization (FEQ) for interference cancellation, as the required number of taps is related to the spectral interference width. Based on the room electromagnetics theory, the spectral interference profile has been analytically determined in terms of the reverberation time (Section 7.2), revealing that the nominal number of subcarriers involved in the interference (per ISI/ICI term) equals half the ratio between the FFT duration and the reverberation time (after rounding up).

The FEQ operation on the FFT output is directly related to the interference coefficient, $y_{\mathrm{tot},i'-i,\Delta k}(\omega_i)$, describing the interference from the ith subcarrier to the i'th subcarrier between two OFDM symbols with an index separation of Δk (Section 2.2). The structure of the interference coefficient matrix (per Δk) can be reduced to a representation based on the generalized interference coefficient, $\tilde{y}_{\Delta k}(\omega_i)$, and the Fourier-type interference coefficient at a zero separation, $y_{\mathrm{Four},0,\Delta k}(\omega_i)$ (Section 3.4.3). Using a moving window (i.e., windowing method type III) with a window width of the order of the inverse of the reverberation, these two interference coefficient vectors can be accurately determined from the channel frequency response for a given FFT window positioning. These results have a potential application to a per-tone multitap FEQ scheme, as proposed in [79], where the taps are determined based on maximization of the SINR by solving a minimum mean-square-error problem.

9.2.5 Future research

Other future work in connection with this dissertation can be carried out in the following research domains:

- experimental characterization of the interference due to insufficient CP for IEEE 802.11ad and IEEE 802.15.3c. This is interesting because of the frequency-selective nature of the 60 GHz channel and the GHz-bandwidth.
- investigation of the influence of the antenna small-scale position and polarization on the interference due to insufficient CP. By measuring the effect on the SINR, the gain of antenna diversity for multiple-antenna systems can be experimentally characterized.
- investigation of the applicability of the concept of an effective noise factor to spatial or polarized MIMO systems.

References

[1] H. Steendam and M. Moeneclaey, "Analysis and optimization of the performance of OFDM on frequency-selective time-selective fading channels," *IEEE Trans. Commun.*, vol. 47, no. 12, pp. 1811–1819, Dec. 1999.

[2] A. Molisch, *Wireless communications*, 2nd ed. Hoboken, NJ, USA: Wiley, 2011.

[3] T. van Waterschoot, V. Le Nir, J. Duplicy, and M. Moonen, "Analytical expressions for the power spectral density of CP-OFDM and ZP-OFDM signals," *IEEE Signal Process. Lett.*, vol. 17, no. 4, pp. 371–374, Apr. 2010.

[4] K.-W. Yip, T.-S. Ng, and Y.-C. Wu, "Impacts of multipath fading on the timing synchronization of IEEE 802.11a wireless LANs," in *Proc. IEEE Int. Conf. Communications (ICC)*, New York City, NY, USA, Apr. 28-May 2 2002, pp. 517–521.

[5] J. Andersen, J. Nielsen, G. Pedersen, G. Bauch, and M. Herdin, "Room electromagnetics," *IEEE Antennas and Propagation Magazine*, vol. 49, no. 2, pp. 27–33, 2007.

[6] A. A. M. Saleh and R. A. Valenzuela, "A statistical model for indoor multipath propagation," *IEEE J. Select. Areas Commun.*, vol. SAC-5, no. 2, pp. 138–145, Feb. 1987.

[7] E. Tanghe, "Experimental statistical channel modelling for advanced wireless communication systems in indoor environments," Ph.D. dissertation, Ghent University, Belgium, 2011.

[8] J. Andersen, K. L. Chee, M. Jacob, G. Pedersen, and T. Kürner, "Reverberation and absorption in an aircraft cabin with the impact of passengers," *IEEE Trans. Antennas Propag.*, vol. 60, no. 5, pp. 2472–2480, May 2012.

[9] A. Bamba *et al.*, "Experimental assessment of specific absorption rate using room electromagnetics," *IEEE Trans. Electromagn. Compat.*, vol. 54, no. 4, pp. 747–757, Aug. 2012.

[10] G. Steinböck, T. Pedersen, B. H. Fleury, W. Wang, and R. Raulefs, "Experimental validation of the reverberation effect in room electromagnetics," *IEEE Trans. Antennas Propag.*, vol. 63, no. 5, pp. 2041–2053, May 2015.

[11] A. Ali, T. Khanzada, and A. Omar, "Adaptive guard interval length for OFDM-based WLAN systems in frequency selective channels," in *Proc. European Conf. Wireless Techn. (EuWIT)*, Amsterdam, The Netherlands, Oct. 2008, pp. 115–118.

[12] S.-W. Kim and K. H. Tchah, "Performance analysis of adaptive equalizer design for OFDM wireless LAN," *IEEE Trans. Consumer Electron.*, vol. 50, no. 2, pp. 512–516, May 2004.

[13] W. Zhong and Z. Mao, "Efficient time-domain residual ISI cancellation for OFDM-based WLAN systems," *IEEE Trans. Consumer Electron.*, vol. 52, no. 2, pp. 321–326, May 2006.

[14] *Part 11: Wireless LAN Medium Access Control (MAC) and Physical Layer (PHY) specifications. High-speed Physical Layer in the 5 GHz Band*, IEEE Std. 802.11a-1999(R2003), Jun. 2006.

[15] K. Takizawa, M. Kyrö, K. Haneda, H. Hagiwara, and P. Vainikainen, "Performance evaluation of 60 GHz radio systems in hospital environments," in *Proc. IEEE Int. Conf. Communications (ICC)*, Ottawa, Canada, Jun. 2012, pp. 3219–3295.

[16] *Part 11: Wireless LAN Medium Access Control (MAC) and Physical Layer (PHY) specifications. Amendment 3: Enhancements for Very High Throughput in the 60 GHz Band*, IEEE Std. 802.11ad-2012, Dec. 2012.

[17] *Part 15.3: Wireless Medium Access Control (MAC) and Physical Layer (PHY) specifications for high rate Wireless Personal Area Networks (WPANs). Amendment 2: Millimeter-wave-based alternative Physical Layer extension*, IEEE Std 802.15.3c-2009, Oct. 2009.

[18] M. Batariere, K. Baum, and T. Krauss, "Cyclic prefix length analysis for 4G systems," in *Proc. IEEE Veh. Technol. Conf. (VTC Fall)*, Los Angeles, CA, Sep. 2004, pp. 543–547.

[19] S. Srikanth, P. Murugesa Pandian, and X. Fernando, "Orthogonal frequency division multiple access in WiMAX and LTE: A comparison," *IEEE Commun. Mag.*, vol. 50, no. 9, pp. 153–161, Sep. 2012.

[20] *Part 16: Air Interface for Broadband Wireless Access Systems. Amendment 3: Advanced Air Interface*, IEEE Std 802.16m-2011, May 2011.

[21] Z. Liu and T. C. Yang, "On the design of cyclic prefix length for time-reversed OFDM," *IEEE Trans. Wireless Commun.*, vol. 11, no. 10, pp. 3723–3733, Oct. 2012.

[22] F. Lindqvist and A. Fertner, "Frequency domain echo canceller for DMT-based systems," *IEEE Signal Process. Lett.*, vol. 18, no. 12, pp. 713–716, Dec. 2012.

[23] H. Gassara, F. Rouissi, and A. Ghazel, "Statistical characterization of the indoor low-voltage narrowband power line communication channel," *IEEE Trans. Electromagn. Compat.*, vol. 56, no. 1, pp. 123–131, Feb. 2014.

[24] D. J. F. Barros and J. M. Kahn, "Optimized dispersion compensation using orthogonal frequency-division multiplexing," *J. Lightwave Technol.*, vol. 26, no. 16, pp. 2889–2898, Aug. 2008.

[25] *Part 11: Wireless LAN Medium Access Control (MAC) and Physical Layer (PHY) specifications. Amendment 4: Further Higher Data Rate Extension in the 2.4 GHz Band*, IEEE Std. 802.11g-2003, Jun. 2003.

[26] *Part 11: Wireless LAN Medium Access Control (MAC) and Physical Layer (PHY) specifications. Amendment 5: Enhancements for Higher Throughput*, IEEE Std. 802.11n-2009, Oct. 2009.

[27] *Part 11: Wireless LAN Medium Access Control (MAC) and Physical Layer (PHY) specifications. Amendment 4: Enhancements for Very High Throughput for Operation in Bands below 6 GHz*, IEEE Std. 802.11ac-2013, Dec. 2013.

[28] S. Saunders and A. Aragón-Zavala, *Antennas and propagation for wireless communication systems*, 2nd ed. Chichester, U.K.: John Wiley & Sons Ltd, 2007.

[29] V. Erceg *et al.*, "TGn channel models," IEEE, Tech. Rep., May 2004.

[30] J. Tarng and T. Liu, "Effective models in evaluating radio coverage on single floors of multifloor buildings," *Vehicular Technology, IEEE Transactions on*, vol. 48, no. 3, pp. 782–9, 1999.

[31] N. Papadakis, A. Economou, J. Fotinopoulou, and P. Constantinou, "Radio propagation measurements and modeling of indoor channels at 1800 MHz," *Wireless Personal Communications*, vol. 9, no. 2, pp. 95–111, 1999.

[32] S. Phaiboon, P. Phokharatkul, and S. Somkuarnpanit, "New upper and lower bounds line of sight path loss model for mobile propagation in buildings," *AEU - International Journal of Electronics and Communications*, vol. 62, no. 3, pp. 207–215, 2008.

[33] T. R. Liu and J. H. Tarng, "Modeling and measurement of 2.44-GHz radio out-of-sight propagation on single floors," *Microwave and Optical Technology Letters*, vol. 14, no. 1, pp. 56–59, 1997.

[34] K. W. Cheung, J.-M. Sau, and R. Murch, "A new empirical model for indoor propagation prediction," *Vehicular Technology, IEEE Transactions on*, vol. 47, no. 3, pp. 996–1001, 1998.

[35] C.-M. Chen, C.-C. Chiu, C.-H. Chen, and Y.-C. Chen, "A novel propagation-prediction model for small rooms with metallic furniture," *Microwave and Optical Technology Letters*, vol. 44, no. 3, pp. 281–4, 2005.

[36] E. Tanghe *et al.*, "The industrial indoor channel: large-scale and temporal fading at 900, 2400, and 5200 MHz," *IEEE Transactions on Wireless Communications*, vol. 7, no. 7, pp. 2740–51, 2008.

[37] G. Breit *et al.*, "TGac channel model addendum," IEEE, Tech. Rep., Sep. 2009.

[38] F. Quitin, "Channel modeling for polarized MIMO systems," Ph.D. dissertation, Université libre de Bruxelles – Université catholique de Louvain, 2011.

[39] E. Viterbo and K. Fazel, "How to combat long echoes in OFDM transmission schemes: sub-channel equalization and more powerful channel coding," in *Proc. IEEE Global Telecommun. Conf. (GLOBECOM)*, vol. 3, Singapore, Nov. 1995, pp. 2069–2074.

[40] J. Seoane, S. Wilson, and S. Gelfand, "Analysis of intertone and interblock interference in OFDM when the length of the cyclic prefix is shorter than the length of the impulse response of the channel," in *Proc. IEEE Global Telecommun. Conf. (GLOBECOM)*, vol. 1, Phoenix, AZ, Nov. 1997, pp. 32–36.

[41] G. Pantos, A. Kanatas, and P. Constantinou, "Performance evaluation of OFDM transmission over a challenging urban propagation environment," *IEEE Trans. Broadcast.*, vol. 49, no. 1, pp. 87–96, Mar. 2003.

[42] H. Steendam, "Parameter optimization for OFDM systems in doubly-selective fading channels with line-of-sight components," *IEEE Trans. Wireless Commun.*, vol. 6, no. 5, pp. 1626–1630, May 2007.

[43] V. D. Nguyen and H.-P. Kuchenbecker, "Intercarrier and intersymbol interference analysis of OFDM systems on time-invariant channels," in *Proc. IEEE Int. Symp. Pers. Indoor Mobile Radio Commun. (PIMRC)*, vol. 4, Lisboa, Portugal, Sep. 2002, pp. 1482–1487.

[44] ——, "Intercarrier and intersymbol interference analysis of OFDM systems on time-varying channels," in *Proc. IEEE Workshop Signal Process. Adv. Wireless Commun. (SPAWC)*, Rome, Italy, Jun. 2003, pp. 140–144.

[45] P. Bello, "Characterization of randomly time-variant linear channels," *IEEE Trans. Commun. Syst.*, vol. CS-11, no. 4, pp. 360–393, Dec. 1963.

[46] W. Henkel, G. Taubock, P. Odling, P. Borjesson, and N. Petersson, "The cyclic prefix of OFDM/DMT - an analysis," in *Proc. IEEE Int. Zurich Semin. Broadband Commun.*, Zurich, Switzerland, Feb. 2002, pp. 22–1–22–3.

[47] S. S. Das, E. D. Carvalho, and R. Prasad, "Variable guard interval orthogonal frequency division multiplexing in dynamic channel condition," in *Proc. IEEE Int. Symp. Pers. Indoor Mobile Radio Commun. (PIMRC)*, Helsinki, Finland, Sep. 2006, pp. 1–5.

[48] J. Montojo and L. Milstein, "Effects of imperfections on the performance of OFDM systems," *IEEE Trans. Commun.*, vol. 57, no. 7, pp. 2060–2070, Jul. 2009.

[49] V. Kotzsch, W. Rave, and G. Fettweis, "ISI analysis in network MIMO OFDM systems with insufficient cyclic prefix length," in *Proc. IEEE Int. Symp. Wireless Comm. Systems (ISWCS)*, York, U.K., Sep. 2010, pp. 189–193.

[50] "IEEE 802.11 Wireless LAN PHY Layer (RF) operation and measurement," Agilent Technologies, Tech. Rep., Apr. 2002.

[51] "WLAN 802.11a/b/g/n/ac X-Series measurement application N9077A & W9077A," Agilent Technologies, Tech. Rep., Jun. 2014.

[52] J. Parsons, D. Demery, and A. Turkmani, "Sounding techniques for wideband mobile radio channels: A review," *Commun. Speech Vis., IEE Proc. I*, vol. 138, no. 5, pp. 437–446, Oct. 1991.

[53] T. Zwick, T. J. Beukema, and H. Nam, "Wideband channel sounder with measurements and model for the 60 GHz indoor radio channel," *IEEE Trans. Veh. Technol.*, vol. 54, no. 4, pp. 1266–1277, Jul. 2005.

[54] D. Chizhik, J. Ling, P. W. Wolniansky, R. A. Valenzuela, N. Costa, and K. Huber, "Multiple-input-multiple-output measurements and modeling in Manhattan," *IEEE J. Sel. Areas Commun.*, vol. 21, no. 3, pp. 321–331, Apr. 2003.

[55] J. Jemai and T. Kürner, "Broadband WLAN channel sounder for IEEE 802.11b," *IEEE Trans. Veh. Technol.*, vol. 57, no. 6, pp. 3381–3392, Nov. 2008.

[56] Q. Chen, "Wideband channel sounding techniques for dynamic spectrum access networks," Ph.D. dissertation, University of Kansas, 2009.

[57] C. Oestges, D. Vanhoenacker-Janvier, and B. Clerckx, "Wide-band SIMO 1 $\times$ 2 measurements and characterization of outdoor wireless channels at 1.9 GHz," *IEEE Trans. Veh. Technol.*, vol. 53, no. 4, pp. 1190–1202, Jul. 2004.

[58] R. J. Pirkl and G. D. Durgin, "Optimal sliding correlator channel sounder design," *IEEE Trans. Wireless Commun.*, vol. 7, no. 9, pp. 3488–3497, Sep. 2008.

[59] S. Haese, C. Moullec, P. Coston, and K. Sayegrigh, "High resolution spread spectrum channel sounder for wireless communications systems," in *IEEE Int. Conf. Personal Wireless Communications (ICPWC)*, Jaipur, India, Feb. 1999, pp. 170–173.

[60] R. Thomä, D. Hampicke, A. Richter, G. Sommerkorn, A. Schneider, U. Trautwein, and W. Wirnitzer, "Identification of time-variant directional mobile radio channels," *IEEE Trans. Instrum. Meas.*, vol. 49, no. 2, pp. 357–364, Apr. 2000.

[61] T. Zwick, D. Hampicke, A. Richter, G. Sommerkorn, R. Thomä, and W. Wiesbeck, "A novel antenna concept for double-directional channel measurements," *IEEE Trans. Veh. Technol.*, vol. 53, no. 2, pp. 527–537, Mar. 2004.

[62] J. Gomes, A. Silva, and S. Jesus, "OFDM demodulation in underwater time-reversed shortened channels," in *Proc. IEEE OCEANS*, Quebec City, QC, Canada, Sep. 2008, pp. 1–8.

[63] Y. S. Cho, J. Kim, W. Y. Yang, and C. G. Kang, *MIMO-OFDM wireless communications with MATLAB*. Hoboken, NJ, USA: Wiley, 2010, pp. 121–142.

[64] M. Krondorf, "Analytical methods for multicarrier performance evaluation," Ph.D. dissertation, Technischen Universität Dresden, 2009.

[65] M. Speth, S. A. Fechtel, G. Fock, and H. Meyr, "Optimum receiver design for wireless broad-band systems using OFDM - Part I," *IEEE Trans. Commun.*, vol. 47, no. 11, pp. 1668–1677, Apr. 1999.

[66] M. Zargari *et al.*, "A single-chip dual-band tri-mode CMOS transceiver for IEEE 802.11a/b/g Wireless LAN," *Solid-State Circuits, IEEE Journal of*, vol. 39, no. 12, pp. 2239 – 49, 2004.

[67] "Agilent fundamentals of RF and microwave noise figure measurements," Agilent Technologies, Tech. Rep., 2010.

[68] Belgian Institute for Postal services and Telecommunications. [Online]. Available: http://www.bipt.be

[69] J. Lee, T. Ohtsuki, and M. Nakagawa, "Performance of turbo equalized double window cancellation and combining in large delay spread channels," in *Personal, Indoor and Mobile Radio Communications, 2009 IEEE 20th International Symposium on*, Tokyo, JP, Sep. 2009, pp. 226 – 230.

[70] X. Sun, Q. Wang, L. Cimini, L. Greenstein, and D. Chan, "ICI/ISI-aware beamforming for MIMO-OFDM wireless systems," *IEEE Transactions on Wireless Communications*, vol. 11, no. 1, pp. 378–385, 2012.

[71] D. De Zutter and F. Olyslager, *Applied electromagnetics*. Ghent, Belgium:Ghent University, 2005.

[72] J. Dabin, A. Haimovich, and H. Grebel, "A statistical ultra-wideband indoor channel model and the effects of antenna directivity on path loss and multipath propagation," *IEEE Journal on Selected Areas in Communications*, vol. 24, no. 4, pp. 752–8, 2006.

[73] Wikipedia. [Online]. Available: en.wikipedia.org/wiki/IEEE_802.11n

[74] E. Tanghe *et al.*, "Statistical validation of WLAN range calculated with propagation models for industrial environments by chipset-level received signal strength measurements," *IET Science, Measurement and Technology*, vol. 3, no. 3, pp. 244–255, 2009.

[75] A. Sibille, "Time-domain diversity in ultra-wideband MIMO communications," *EURASIP Journal on Advances in Signal Processing*, vol. 2005, no. 3, pp. 316–327, 2005.

[76] R. J. C. Bultitude, "Measurement, characterization and modeling of indoor 800/900 MHz radio channels for digital communications," *IEEE Commun. Mag.*, vol. 25, no. 6, pp. 5–12, 1987.

[77] Wikipedia. [Online]. Available: en.wikipedia.org/wiki/List_of_WLAN_channels

[78] A. M. Tonello, S. D'Alessandro, and L. Lampe, "Cyclic prefix design and allocation in bit-loaded OFDM over power line communication channels," *IEEE Trans. Commun.*, vol. 58, no. 11, pp. 3265–3276, Nov. 2010.

[79] K. Van Acker, G. Leus, M. Moonen, O. van de Wiel, and T. Pollet, "Per tone equalization for DMT-based systems," *IEEE Trans. Commun.*, vol. 49, no. 1, pp. 109–119, Jan. 2001.

A

Derivation of CIR-based weighting functions for the interference coefficient due to insufficient CP

This chapter presents a detailed derivation of the weighting functions to determine the interference coefficient due to insufficient CP on the basis of the continuous channel impulse response, $c_{\mathrm{tot}}(\tau)$. The derivation is based on the OFDM signal model described in Section 2.1. Note that $c_{\mathrm{tot}}(\tau)$ refers to the cascade of the propagation channel and the channel select filter. Considering the linearity of the signal model, the FFT output (at the receiver) at the k'th OFDM symbol and the i'th subcarrier can be divided up into contributions from the different data symbols at a respective OFDM symbol k and subcarrier i. This contribution is proportional to the data symbol, $\tilde{X}_{k,i}$, and the interference coefficient. The corresponding interference process is characterized by an OFDM symbol separation, $\Delta k = k' - k$, and a subcarrier separation $\Delta i = i' - i$. Fig. A.1 shows schematically the transmit and received signal corresponding to (i) an arbitrary data symbol $\tilde{X}_{k,i}$ and (ii) the data symbol $\tilde{X}_{k',i'}$ that is aimed to be detected by the receiver. The FFT window (at the receiver) to detect the k'th OFDM symbol is positioned at a general start instant $t_{k',0}$. From Eq. 2.1, the transmit signal (in complex representation) corresponding to the data symbol $\tilde{X}_{k,i}$ is given by (omitting the OFDM packet index m

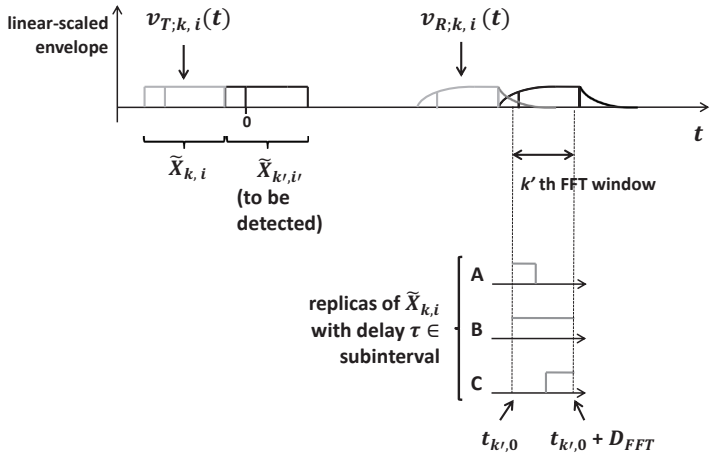

Figure A.1: Transmit and received OFDM signal corresponding to data symbols $\tilde{X}_{k,i}$ and $\tilde{X}_{k',i'}$ are schematically shown. The received signal is a superposition of replicas of the transmit signal with different delays, which are classified into 3 subintervals types depending on the extent of overlap with the FFT window: type A (left-hand partial overlap), type B (complete overlap) and type C (right-hand partial overlap).

for reasons of clarity):

$$\begin{aligned} v_{\mathrm{T};k,i}(t) =& g_{\mathrm{T}} \tilde{X}_{k,i} \exp(j\omega_{\mathrm{c}} t) \exp\Big(j2\pi D_{\mathrm{FFT}}^{-1} i(t+\Delta k) D_{\mathrm{CP}}\Big) \\ & \times \Bigg(\mathrm{U}\Big(t + D_{\mathrm{CP}} + \Delta k (D_{\mathrm{FFT}} + D_{\mathrm{CP}})\Big) \\ & - \mathrm{U}\Big(t - D_{\mathrm{FFT}} + \Delta k (D_{\mathrm{FFT}} + D_{\mathrm{CP}})\Big) \Bigg) \end{aligned} \tag{A.1}$$

The Δkth *interference delay interval* is defined as the interval involving all delays that contribute to the FFT output through an interference process with an OFDM symbol separation Δk. This interference delay interval can be divided up into 3 subintervals of type A, B and C, defined by:

$$\begin{cases} (\mathrm{A}) & \tau \in [\tau_{\mathrm{int},1,\Delta k}; \tau_{\mathrm{int},1,\Delta k} + D_{\mathrm{FFT}}] \\ (\mathrm{B}) & \tau \in [\tau_{\mathrm{int},1,\Delta k} + D_{\mathrm{FFT}}; \tau_{\mathrm{int},1,\Delta k} + D_{\mathrm{FFT}} + D_{\mathrm{CP}}] \\ (\mathrm{C}) & \tau \in [\tau_{\mathrm{int},1,\Delta k} + D_{\mathrm{FFT}} + D_{\mathrm{CP}}; \tau_{\mathrm{int},1,\Delta k} + 2D_{\mathrm{FFT}} + D_{\mathrm{CP}}] \end{cases} \tag{A.2}$$

where the start delay of the interference delay interval is defined by

$$\tau_{\mathrm{int},1,\Delta k} = t_{k',0} - D_{\mathrm{FFT}} + \Delta k (D_{\mathrm{FFT}} + D_{\mathrm{CP}}) \tag{A.3}$$

The meaning of these subintervals is illustrated in Fig. A.1. A delay from subinterval A leads to a *left-hand partial* overlap between the received replica of the

transmit signal and the FFT window. A delay from subinterval B results into a *complete* overlap and a delay from subinterval C gives a *right-hand partial* overlap.

The contribution to the FFT output at the k'th OFDM symbol and i'th subcarrier and originating from the kth OFDM symbol and ith subcarrier, $Y_{k',i';k,i}$, is usually determined by a decomposition of the received signal (over the FFT interval) into a Fourier series. However, due to the delay-dispersive channel, the received signal is no longer identical at both edges of the FFT interval (contrary to the transmit signal). For this reason, $Y_{k',i';k,i}$ is divided into two terms: (i) a discrete Fourier transform (DFT) with a symmetrical weighting at the borders of the FFT interval, $Y_{k',i';k,i;\mathrm{Four}}$, and (ii) a correction term, $Y_{k',i';k,i;\mathrm{corr}}$:

$$Y_{k',i';k,i} = Y_{k',i';k,i;\mathrm{Four}} + Y_{k',i';k,i;\mathrm{corr}} \tag{A.4}$$

where

$$\begin{aligned} Y_{k',i';k,i;\mathrm{Four}} = & \sum_{l=1}^{N_{\mathrm{sample}}-1} v_{\mathrm{R};k,i}(t_{k',l}) \exp(-j2\pi i'\, l/N_{\mathrm{sample}}) \\ & + \frac{v_{\mathrm{R};k,i}(t_{k',0}) + v_{\mathrm{R};k,i}(t_{k',N_{\mathrm{sample}}})}{2} \end{aligned} \tag{A.5}$$

and

$$Y_{k',i';k,i;\mathrm{corr}} = \frac{v_{\mathrm{R};k,i}(t_{k',0}) - v_{\mathrm{R},k,i}(t_{k',N_{\mathrm{sample}}})}{2} \tag{A.6}$$

where the time samples $t_{k',l}$ are determined by $t_{k',l} = t_{k',0} + lD_{\mathrm{FFT}}\, N_{\mathrm{sample}}^{-1}$ and $v_{\mathrm{R};k,i}(t)$ is the contribution from the kth OFDM symbol and ith subcarrier to the received down-converted I/Q signal ($v_{\mathrm{R,I/Q},m}(t)$ in Section 2.1):

$$v_{\mathrm{R};k,i}(t) = \exp(-j\omega_{\mathrm{c}}t)\Big(c_{\mathrm{tot}}(\tau) * v_{\mathrm{T};k,i}(t)\Big) \tag{A.7}$$

From Eq. A.5, $Y_{k',i';k,i;\mathrm{Four}}$ can be determined in terms of the Fourier series coefficients, $Z_{k',i';k,i}$:

$$Y_{k',i';k,i;\mathrm{Four}} = N_{\mathrm{sample}} \sum_{n=-\infty}^{\infty} Z_{k',i'+nN_{\mathrm{sample}};k,i} \tag{A.8}$$

where

$$Z_{k',i';k,i} = D_{\mathrm{FFT}}^{-1} \int_{t_{k',0}}^{t_{k',0}+D_{\mathrm{FFT}}} v_{\mathrm{R};k,i}(t) \exp(-j2\pi i'\,(t - t_{k',0})/D_{\mathrm{FFT}})\,\mathrm{d}t \tag{A.9}$$

The Fourier series coefficient, $Z_{k',i';k,i}$, will be related to a so-called *Fourier-type interference coefficient* and the correction term, $Y_{k',i';k,i;\mathrm{corr}}$, will be related to a so-called *correction-type interference coefficient*.

A.1 Weighting function for Fourier series coefficients (*Fourier-type interference coefficient*)

In this section, the Fourier series coefficient, $Z_{k',i';k,i}$, is analytically related to the channel impulse reponse. $Z_{k',i';k,i}$ is divided up into 3 terms each originating from delays from subinterval A, B and C, resp., of the interference delay interval. These terms are denoted by $Z_{k',i';k,i;A}$, $Z_{k',i';k,i;B}$ and $Z_{k',i';k,i;C}$, respectively.

A.1.1 $Z_{k',i';k,i;A}$

From Eqs. A.1, A.7 and A.9, $Z_{k,i';k',i;\mathrm{A}}$ is written as

$$Z_{k,i';k',i;\mathrm{A}} = g_{\mathrm{T}}\tilde{X}_{k,i}\exp\Big(j2\pi D_{\mathrm{FFT}}^{-1} i\tau_{\mathrm{int},1,\Delta k}\Big)\int_{-\infty}^{\infty} c_{\mathrm{tot}}(\tau)\exp(-j\omega_i\tau) \times \underbrace{\left(D_{\mathrm{FFT}}^{-1}\int_{t_{k',0}}^{t_{k',0}+\Delta t_{\mathrm{A}}} \exp\Big(-j2\pi D_{\mathrm{FFT}}^{-1}\Delta i(t-t_{k',0})\Big)\,\mathrm{d}t\right)}_{I_{\mathrm{A}}}\mathrm{d}\tau \tag{A.10}$$

where ω_i is the (angular) frequency of subcarrier i and Δt_{A} is defined as

$$\Delta t_{\mathrm{A}} = \tau - \tau_{\mathrm{int},1,\Delta k} \tag{A.11}$$

Δt_{A} indicates the duration of overlap between the received replica of the transmit signal (corresponding to $\tilde{X}_{k,i}$) and the FFT window (Fig. A.1). From Eq. A.10, the weighting function is obtained by the integral I_{A}:

$$I_{\mathrm{A}} = \frac{\tau - \tau_{\mathrm{int},0,\Delta k} + D_{\mathrm{FFT}}}{D_{\mathrm{FFT}}} \quad (\text{for } \Delta i = 0) \tag{A.12}$$

$$I_{\mathrm{A}} = \frac{j}{2\pi\Delta i}\Big(\exp\big(-j2\pi D_{\mathrm{FFT}}^{-1}\Delta i(\tau - \tau_{\mathrm{int},1,\Delta k})\big) - 1\Big) \quad (\text{for } \Delta i \neq 0) \tag{A.13}$$

$$= g_{0,\Delta i}(\tau - \tau_{\mathrm{int},0,\Delta k} + D_{\mathrm{FFT}}) \quad (\text{for } \Delta i \neq 0) \tag{A.14}$$

where $g_{0,\Delta i}(\tau)$ is defined by Eq. 2.11 and $\tau_{\mathrm{int},0,\Delta k}$ is defined by

$$\tau_{\mathrm{int},0,\Delta k} = \tau_{\mathrm{int},1,\Delta k} + D_{\mathrm{FFT}} \tag{A.15}$$

A.1.2 $Z_{k',i';k,i;B}$

Analogously, $Z_{k',i';k,i;\mathrm{B}}$ is given by Eq. A.10 where $\Delta t_{\mathrm{A}} = D_{\mathrm{FFT}}$ due to the complete overlap of the FFT window (Fig. A.1). The corresponding integral, I_{B}, is then

$$I_{\mathrm{B}} = 1 \qquad (\Delta i = 0) \tag{A.16}$$

$$I_{\mathrm{B}} = 0 \qquad (\Delta i \neq 0) \tag{A.17}$$

A.1.3 $Z_{k',i';k,i;C}$

Analogously to $Z_{k',i';k,i;A}$, the corresponding integral for $Z_{k',i';k,i;C}$, I_{C}, is determined by

$$I_{\mathrm{C}} = D_{\mathrm{FFT}}^{-1} \int_{t_{k',0}+\Delta t_{\mathrm{C}}}^{t_{k',0}+D_{\mathrm{FFT}}} \exp\Big(-j2\pi D_{\mathrm{FFT}}^{-1}\Delta i(t-t_{k',0})\Big)\,\mathrm{d}t \tag{A.18}$$

$$= -D_{\mathrm{FFT}}^{-1} \int_{t_{k',0}}^{t_{k',0}+\Delta t_{\mathrm{C}}} \exp\Big(-j2\pi D_{\mathrm{FFT}}^{-1}\Delta i(t-t_{k',0})\Big)\,\mathrm{d}t \tag{A.19}$$

From Eq. A.19, I_{C} is determined by

$$I_{\mathrm{C}} = \frac{-\tau + \tau_{\mathrm{int},0,\Delta k} + D_{\mathrm{CP}}}{D_{\mathrm{FFT}}} \quad (\text{for } \Delta i = 0) \tag{A.20}$$

$$I_{\mathrm{C}} = -g_{0,\Delta i}(\tau - \tau_{\mathrm{int},0,\Delta k} - D_{\mathrm{CP}}) \quad (\text{for } \Delta i \neq 0) \tag{A.21}$$

where

$$\Delta t_{\mathrm{C}} = \tau - \tau_{\mathrm{int},0,\Delta k} - D_{\mathrm{CP}} \tag{A.22}$$

A.1.4 Determination of $Y_{k',i';k,i;\mathrm{Four}}$

Substituting Eq. A.10 into Eq. A.8 and expressing the integrals I_{A}, I_{B} and I_{C} by the weighting functions as determined in Eqs. A.12 and A.14, Eqs. A.16 and A.17 and Eqs. A.20 and A.21, resp., $Y_{k',i';k,i;\mathrm{Four}}$ is written as

$$Y_{k',i';k,i;\mathrm{Four}} = g_{\mathrm{T}} N_{\mathrm{sample}} \tilde{X}_{k,i} \exp\Big(j2\pi D_{\mathrm{FFT}}^{-1} i \tau_{\mathrm{int},1,\Delta k}\Big) \times \sum_{n=-\infty}^{\infty} \int_{-\infty}^{\infty} g_{\mathrm{Four},\Delta i}(\tau - \tau_{\mathrm{int},0,\Delta k}) c_{\mathrm{tot}}(\tau) \exp(-j\omega_i \tau)\,\mathrm{d}\tau \tag{A.23}$$

where $g_{\mathrm{Four},\Delta i}(\tau)$ is the weighting function defined in Section 2.2.1 (Table 2.2).

A.2 Weighting function for the correction term, $Y_{k',i';k,i;\mathrm{corr}}$ (*correction-type interference coefficient*)

Substituting Eq. A.1 into Eq. A.7, the received signal sampled at the start and end instant of the FFT interval is resp. given by

$$\begin{aligned} v_{\mathrm{R};k,i}(t_{k',0}) = g_{\mathrm{T}}\tilde{X}_{k,i}\exp\Big(j2\pi D_{\mathrm{FFT}}^{-1} i\tau_{\mathrm{int},1,\Delta k}\Big) \\ \times \int_{-\infty}^{\infty}\Big(\mathrm{U}(\tau-\tau_{\mathrm{int},1,\Delta k}) - \mathrm{U}(\tau-\tau_{\mathrm{int},1,\Delta k}-D_{\mathrm{CP}}-D_{\mathrm{FFT}})\Big) \\ \times c_{\mathrm{tot}}(\tau)\exp(-j\omega_i\tau)\,\mathrm{d}\tau \end{aligned} \tag{A.24}$$

and

$$\begin{aligned} v_{\mathrm{R};k,i}(t_{k',0}+D_{\mathrm{FFT}}) = g_{\mathrm{T}}\tilde{X}_{k,i}\exp\Big(j2\pi D_{\mathrm{FFT}}^{-1} i\tau_{\mathrm{int},1,\Delta k}\Big) \\ \times \int_{-\infty}^{\infty}\Big(\mathrm{U}(\tau-\tau_{\mathrm{int},1,\Delta k}-D_{\mathrm{CP}}-D_{\mathrm{FFT}}) - \mathrm{U}(\tau-\tau_{\mathrm{int},1,\Delta k}-D_{\mathrm{CP}}-2D_{\mathrm{FFT}})\Big) \\ \times c_{\mathrm{tot}}(\tau)\exp(-j\omega_i\tau)\,\mathrm{d}\tau \end{aligned} \tag{A.25}$$

From Eqs. A.24 and A.25, it follows that

$$\begin{aligned} Y_{k',i';k,i;\mathrm{corr}} = g_{\mathrm{T}}N_{\mathrm{sample}}\tilde{X}_{k,i}\exp\Big(j2\pi D_{\mathrm{FFT}}^{-1} i\tau_{\mathrm{int},1,\Delta k}\Big) \\ \times \int_{-\infty}^{\infty} g_{\mathrm{corr}}(\tau-\tau_{\mathrm{int},0,\Delta k})c_{\mathrm{tot}}(\tau)\exp(-j\omega_i\tau)\,\mathrm{d}\tau \end{aligned} \tag{A.26}$$

where $g_{\mathrm{corr}}(\tau)$ is a weighting function defined in Section 2.2.1 (Table 2.1).

A.3 Error vector due to insufficient CP

The equalized constellation error vector due to insufficient CP, $\Delta\tilde{Y}_{\mathrm{delay},k',i';k,i}$, at the k'th OFDM symbol and the i'th subcarrier and originating from OFDM symbol k and subcarrier i, is determined by

$$\Delta\tilde{Y}_{\mathrm{delay},k',i';k,i} = \frac{Y_{k',i';k,i} - Y_{\mathrm{ideal},k',i'}}{H_{k',i'}} \tag{A.27}$$

The errorless (unequalized) FFT output, $Y_{\mathrm{ideal},k',i'}$, is determined by the FFT output at the k'th OFDM symbol and the i'th subcarrier assuming an *infinite* CP length. In this case, the channel behaves as frequency-flat, which yields that

$$Y_{\mathrm{ideal},k',i'} = g_{\mathrm{T}} \tilde{X}_{k',i'} N_{\mathrm{sample}} \exp\Big(j2\pi D_{\mathrm{FFT}}^{-1} i' \tau_{\mathrm{int},1,0}\Big) C_{\mathrm{tot}}(\omega_{i'}) \tag{A.28}$$

where $C_{\mathrm{tot}}(\omega_{i'})$ is channel frequency response. Assuming an idealized channel estimation, the one-tap channel equalization coefficient $H_{k',i'}$ is determined by

$$H_{k',i'} = Y_{\mathrm{ideal},k',i'} / \tilde{X}_{k',i'} \tag{A.29}$$

Finally, $\Delta\tilde{Y}_{\mathrm{delay},k',i';k,i}$ is determined from Eqs. A.27, A.28, A.29 and substituting the two FFT output terms $Y_{k',i';k,i;\mathrm{Four}}$ and $Y_{k',i';k,i;\mathrm{corr}}$ by Eqs. A.23 and A.26, respectively. As an **overall conclusion**, the equalized constellation error vector is determined as follows:

$$\begin{aligned}\Delta\tilde{Y}_{\mathrm{delay},k',i';k,i} = {} & \frac{\tilde{X}_{k,i}}{C_{\mathrm{tot}}(\omega_{i'})} \exp\Big(j2\pi D_{\mathrm{FFT}}^{-1}(i\tau_{\mathrm{int},1,\Delta k} - i'\tau_{\mathrm{int},1,0})\Big) \\ & \times \left(y_{\mathrm{corr},k'-k}(\omega_i) + \sum_{n=-\infty}^{\infty} y_{\mathrm{Four},i'-i+nN_{\mathrm{sample}},k'-k}(\omega_i) \right)\end{aligned} \tag{A.30}$$

In Eq. A.30, the Fourier-type interference coefficient, $y_{\mathrm{Four},\Delta i,\Delta k}(\omega)$, is defined by means of the weighting function $g_{\mathrm{Four},\Delta i}(\tau)$:

$$\begin{cases} y_{\mathrm{Four},\Delta i,\Delta k}(\omega) = \int\limits_{-\infty}^{\infty} g_{\mathrm{Four},\Delta i}(\tau - \tau_{\mathrm{int},0,\Delta k}) c_{\mathrm{tot}}(\tau) \exp(-j\omega\tau)\,\mathrm{d}\tau \\ \qquad\qquad \big(\text{for } \{\Delta i;\Delta k\} \neq \{0;0\}\big) \\ y_{\mathrm{Four},\Delta i,\Delta k}(\omega) = \int\limits_{-\infty}^{\infty} \big(g_{\mathrm{Four},\Delta i}(\tau - \tau_{\mathrm{int},0,\Delta k}) - 1\big) c_{\mathrm{tot}}(\tau) \exp(-j\omega\tau)\,\mathrm{d}\tau \\ \qquad\qquad \big(\text{for } \Delta i = \Delta k = 0\big) \end{cases} \tag{A.31}$$

In Eq. A.30, the correction-type interference coefficient, $y_{\mathrm{corr},\Delta k}(\omega)$, is defined by means of the weighting funtion $g_{\mathrm{corr}}(\tau)$:

$$y_{\mathrm{corr},\Delta k}(\omega) = \int\limits_{-\infty}^{\infty} g_{\mathrm{corr}}(\tau - \tau_{\mathrm{int},0,\Delta k}) c_{\mathrm{tot}}(\tau) \exp(-j\omega\tau)\,\mathrm{d}\tau \tag{A.32}$$